

**Characterization of Carotid Plaque Vulnerability using Quantitative Ultrasound and
Strain Imaging**

By

Xiao Wang

A dissertation submitted in partial fulfillment of
the requirements for the degree of

Doctor of Philosophy

(Medical Physics)

at the

UNIVERSITY OF WISCONSIN–MADISON

2015

Date of final oral examination: 6/4/2015

The dissertation is approved by the following members of the Final Oral Committee:

Tomy Varghese, Professor, Medical Physics
Robert J. Dempsey, Professor, Neurological Surgery
Carol C. Mitchell, Assistant Professor, Medicine
Timothy J. Hall, Professor, Medical Physics
James E. Holden, Professor, Medical Physics

©Copyright by Xiao Wang 2015
All Rights Reserved

*For my loving husband Chi and my lovely son Russell
For my dearest parents*

Abstract

Characterization of Carotid Plaque Vulnerability using Quantitative Ultrasound and Strain Imaging

Xiao Wang

Under the supervision of Professor Tomy Varghese and Professor Robert J. Dempsey

At the University of Wisconsin-Madison

Stroke is the leading cause of serious, long-term disability and the fourth leading cause of death in the United States. In addition to clinically recognized stroke, "silent" strokes may occur, and are five times more prevalent. Silent strokes are not detected based on classical transient ischemic attack (TIA) symptoms and therefore difficult to prevent. It is also likely that these "silent" strokes may cause accumulated cognitive decline, due to cerebral micro-emboli caused by instability in carotid vulnerable plaque. Thus it is important to characterize carotid plaque and assess its vulnerability.

Plaque instability may be characterized by increased strain variations over a cardiac cycle with arterial pulsation. Therefore, strain imaging to detect plaque vulnerability based on regions with large strain fluctuations, may be able to determine plaque regions at increased risk for rupture. In this dissertation, accumulated axial, lateral and shear strain indices were correlated with cognitive function assessed on human subjects. Significant correlation of these maximum strain indices and cognitive function was demonstrated, indicating the feasibility of using strain indices to predict cognitive decline. Carotid plaque along with adventitia layer was segmented to identify vulnerable regions. Ultrasound strain imaging may therefore be a useful surrogate in the clinic to

detect vulnerability of plaque and assess potential risk of silent stroke.

Statistical distributions of strain indices in different groups of patients and volunteers were also evaluated, followed by comparison of strain indices to trans-cranial Doppler (TCD) results. In addition to strain estimation along longitudinal scanning planes, an algorithm was developed to estimate radial and circumferential strain in a cross-sectional view of *in vivo* carotid artery using noninvasive ultrasound.

Carotid plaque can also be characterized using quantitative ultrasound (QUS), to assess the acoustic properties of tissue. Differences in acoustic properties may reflect difference in tissue composition. A novel approach is proposed whereby localized calcified, fibrous and lipid regions within heterogeneous plaque using a region-to-region registration with 3D histology and 3D attenuation coefficient was performed. QUS may also provide improved characterization of vulnerable plaque composition using direct localization of plaque regions and structure to histology.

Acknowledgements

First of all I would like to thank my advisor, Professor Tomy Varghese. He gave me the opportunity to study medical physics here and introduced me to ultrasound research. His insightful ideas were the origination and directions of my research. Not only did he guide me in my academic life, but he gave me a lot of life advice and showed me patiently how to become a successful researcher.

I would like to express my gratitude to Professor Robert Dempsey. He performed excellent surgeries on these patients and saved real lives. He is also a great leader of the Plaque Study group. His deep knowledge in neurosurgery was the clinical foundation of this dissertation.

I want to specially thank Professor Carol Mitchell. She was my closest work mate in these four and a half years. I wouldn't be able to show those beautiful ultrasound images in this dissertation without her steady hands on the ultrasound transducers. She was also very patient and segmented all the plaques for me. We solved the mystery of changing the size of Q-box on SuperSonic Aixplorer together.

I greatly appreciate Professor Timothy Hall for his help and support, especially for letting me use his ultrasound machines. I would also like to thank Professor James Holden. He is such a great educator, and I will never forget the calm and elegant approach he used in his lectures.

I would like to sincerely thank Professor James Zagzebski. He is no doubt a wonderful mentor. I really enjoyed all the discussions with him. I would like to thank Professor Ernest Madsen and Gary Frank for the technical support and all the beautiful phantoms they made.

I would like to express my gratitude to all the members of the Plaque Study group: to Dr. Shahriar Salamat who spent a lot of time sitting in front of microscopes and segmenting pathology images; to Dr. Daren Jackson for sharing his thoughts in cognitive function and discussion on our publications; to Dr. Stephanie Wilbrand for her great organized coordination of patients and each research sub-group; and to all other members for working on the plaque research together.

I would like to thank all the ultrasound group members; they are Dr. Matt McCormick, Dr. Ryan Dewall, Dr. Nick Rubert, Dr. Haiyan Xu, Dr. Eenas Omari, Dr. Chi Ma, Wenqi Ge, Atul Ingle, Kayvan Samimi and Wenjun Yang. Special thanks go to Dr. Matt McCormick, who laid a good foundation for Plaque Study research.

I would also like to thank all my friends here in Madison, Wisconsin and far away. With their company, I didn't not only survive but actually enjoyed many a cold winter in this forbidden north land.

I owe my parents, Professor Qingyun Wang and Professor Ling Feng, a great debt of gratitude for their unconditional love and selfless support, and all the good things I inherited from them. They encouraged me to be a better me. I want to specially thank my mom who took very good care of my son when I was writing this dissertation late at night in WIMR.

I want to dedicate this dissertation to my husband, Dr. Chi Ma, who was also an ultrasound group member. His love and support was my biggest motivation. I'm truly grateful that he took very good care of the family, even though he needed to drive a long way back from Mayo Clinic in Rochester, Minnesota every week. And my naughty son Russell, who is always a happy baby, is a blessing in my life. I love you both so much.

Contents

Abstract	ii
Acknowledgements	iv
Contents	vi
List of Figures	xi
List of Tables	xvii
Chapter 1 : Introduction	1
1.1 Motivation	1
1.2 Organization of the Dissertation	2
1.3 References	4
Chapter 2 : Literature Review	7
2.1 Clinical Significance	7
2.1.1 Stroke and Carotid Plaque Vulnerability	7
2.1.2 Silent Stroke and Cognition	9
2.1.3 Cognitive Function Assessments	10
2.1.4 Carotid Artery Stiffness	11
2.2 Carotid Plaque Characterization with Ultrasound Imaging	12
2.2.1 Ultrasound Strain Imaging	12
2.2.2 Ultrasound Strain Definition	16
2.2.3 Quantitative Ultrasound Imaging	17
2.2.4 Trans-cranial Doppler	19
2.2.5 Pulse Wave Imaging	20
2.2.6 Shear Wave Imaging	22
2.3 References	23
Chapter 3 : Correlation of Ultrasound Strain Indices with Cognitive Function Assessed using RBANS	34

3.1	Introduction	34
3.2	Materials and Methods	35
	3.2.1 Data Acquisition	35
	3.2.2 Estimation of Strain Indices	38
	3.2.3 RBANS Scores	40
3.3	Results	41
	3.3.1 Accumulated Axial, Lateral and Shear Strain over a Cardiac Cycle	41
	3.3.2 Correlation with RBANS Scores	44
3.4	Discussion	52
3.5	Improved Correlation with Inclusion of Adventitial Layer	55
	3.5.1 Comparison of the Strain Indices with and without Adventitia	55
	3.5.2 Improvement in Correlation with RBANS	68
3.6	Shear Strain within the Adventitia	74
3.7	Conclusions	75
3.8	References	76

Chapter 4 : Correlation of Strain Indices with NINDS-CSN VCI Harmonization

	Standards 60-Minute Protocol	80
4.1	Introduction	80
4.2	Materials and Methods	80
	4.2.1 Data Acquisition	80
	4.2.2 Strain Indices Estimation	81
	4.2.3 Cognition Assessment	81
	4.2.4 Correlation Analysis	83
4.3	Results	83
4.4	Discussion	87
4.5	Conclusions	88
4.6	References	88

	Chapter 5 : Receiver Operating Characteristic Analysis of Strain Indices as a Classifier for Cognitive Impairment	90
--	--	-----------

5.1	Introduction	90
5.2	Materials and Methods	91
	5.2.1 Data Acquisition	91
	5.2.2 Strain Indices Estimation	92
	5.2.3 Cognition Assessment	94
	5.2.4 Statistics and ROC Analysis	95
5.3	Results	96
	5.3.1 Correlation Study	96
	5.3.2 ROC Analysis	100
5.4	Discussion	110
5.5	Conclusions	112
5.6	References	112

Chapter 6 : Statistics of Strain Indices versus Plaque Study Patients and Volunteers

114

6.1	Introduction	114
6.2	Materials and Methods	115
	6.2.1 Data Acquisition on Human Subjects	115
	6.2.2 Data Acquisition on Human Volunteers	116
	6.2.3 Statistical Methods	117
6.3	Results	118
	6.3.1 Strain Indices Histograms	118
	6.3.2 Statistics of Strain Indices for Different Clinical Groups	121
	6.3.3 Comparison with Human Volunteers	146
6.4	Discussion	152
6.5	Conclusions	152
6.6	References	153

Chapter 7 : Trans-cranial Doppler versus Ultrasound Strain Indices

155

7.1	Introduction	155
7.2	Materials and Methods	156

7.2.1	Data Acquisition	156
7.2.2	Statistical Analysis	157
7.3	Results	158
7.3.1	HITS	158
7.3.2	Correlations of MCA Velocities with Strain Indices and ICA Velocities	159
7.4	Discussion	161
7.5	Conclusions	162
7.6	References	162
Chapter 8 : Estimation of Carotid Radial and Circumferential Strain		165
8.1	Introduction	165
8.2	Materials and Methods	166
8.2.1	Data Acquisition	166
8.2.2	Polar grid generation	168
8.2.3	Radial and Circumferential Displacement Estimation	168
8.2.4	Radial and Circumferential Strain Generation	169
8.3	Results	170
8.3.1	Radial and Circumferential Displacements	170
8.3.2	Radial and Circumferential Strain Tensor Images	173
8.4	Discussion	176
8.5	Conclusions	177
8.6	References	177
Chapter 9 : Characterization of Carotid Plaque with Histology and Quantitative Ultrasound		179
9.1	Introduction	179
9.2	Materials and Methods	181
9.2.1	Attenuation Estimation	181
9.2.2	Histology Reconstruction	184
9.3	Results	186

9.3.1	Alignment of Attenuation Volumes to Histology	186
9.3.2	Attenuation Coefficients in Different Regions	188
9.4	Discussion	188
9.5	Conclusions	189
9.6	References	190
Chapter 10 : Conclusions and Future Work		192
10.1	Contributions of this Dissertation	192
10.2	Future Directions	194

List of Figures

- Figure 3.1:** B-mode image (a) and segmented plaque on B-mode image (b). 38
- Figure 3.2:** Axial strain values overlaid on the B-mode image (a). Mean values in the small ROI and entire plaque are shown in (b), and their standard deviations in (c). 42
- Figure 3.3:** Lateral strain values overlaid on the B-mode image (a). Mean values in the small ROI and entire plaque are shown in (b), and their standard deviations in (c). 43
- Figure 3.4:** Shear strain values overlaid on the B-mode image (a). Mean values in the small ROI and entire plaque are shown in (b), and their standard deviations in (c). 44
- Figure 3.5:** Linear least square fits of total RBANS score with maximum (a), absolute minimum (b), and peak-to-peak (c) axial strain averaged over the small ROI. \circ = Symptomatic, \times = asymptomatic, \square = questionable, the dotted line represents the linear fit for symptomatic, dashed line the linear fit for asymptomatic, and the solid line denotes the linear fit for all patients. 46
- Figure 3.6:** Linear least square fits of total RBANS score with maximum (a), absolute minimum (b), and peak-to-peak (c) lateral strain averaged over the small ROI. \circ = Symptomatic, \times = asymptomatic, \square = questionable, the dotted line represents the linear fit for symptomatic, dashed line the linear fit for asymptomatic, and the solid line denotes the linear fit for all patients. 47
- Figure 3.7:** Linear least square fits of total RBANS score with maximum (a), absolute minimum (b), and peak-to-peak (c) shear strain averaged over the small ROI. \circ = Symptomatic, \times = asymptomatic, \square = questionable, the dotted line represents the linear fit for symptomatic, dashed line the linear fit for asymptomatic, and the solid line denotes the linear fit for all patients. 48
- Figure 3.8:** Linear least square fits of total RBANS score with the maximum axial (a), lateral (b) and shear (c) strain averaged over the entire plaque. \circ = Symptomatic, \times = asymptomatic, \square = questionable, the dotted line represents the linear fit for symptomatic, dashed line the linear fit for asymptomatic, and the solid line denotes the linear fit for all patients. 50
- Figure 3.9:** Linear least square fit of the total RBANS score with peak-to-peak axial (a),

lateral (b) and shear (c) strain averaged over the entire plaque. \circ = Symptomatic, \times = asymptomatic, \square = questionable, the dotted line represents the linear fit for symptomatic, dashed line the linear fit for asymptomatic, and the solid line denotes the linear fit for all patients. 51

Figure 3.10: B-mode image (a) and segmented plaque on B-mode image using the plaque-only segmentation (b) and the plaque-with-adventitia segmentation (c). 57

Figure 3.11: Axial strain values overlaid on the B-mode image using the plaque-only segmentation (a) and the plaque-with-adventitia segmentation (b) on a symptomatic plaque. 59

Figure 3.12: Axial strain values overlaid on the B-mode image using the plaque-only segmentation (a) and the plaque-with-adventitia segmentation (b) on an asymptomatic plaque. 60

Figure 3.13: Lateral strain values overlaid on the B-mode image using the plaque-only segmentation (a) and the plaque-with-adventitia segmentation (b) on a symptomatic plaque. 61

Figure 3.14: Lateral strain values overlaid on the B-mode image using the plaque-only segmentation (a) and the plaque-with-adventitia segmentation (b) on an asymptomatic plaque. 62

Figure 3.15: Shear strain values overlaid on the B-mode image using the plaque-only segmentation (a) and the plaque-with-adventitia segmentation (b) on a symptomatic plaque. 63

Figure 3.16: Shear strain values overlaid on the B-mode image using the plaque-only segmentation (a) and the plaque-with-adventitia segmentation (b) on an asymptomatic plaque. 64

Figure 3.17: Accumulated axial (a), lateral (b) and shear (c) strain over two cardiac cycles with plaque-only and plaque-with-wall segmentation on a symptomatic (i) and an asymptomatic patient (ii). 66

Figure 3.18: Accumulated axial (a), lateral (b) and shear (c) strain over two cardiac cycles in carotid artery wall on healthy human volunteer (i) and (ii). 67

Figure 3.19: Linear least-squares fits of RBANS Total score with maximum axial (a), and maximum lateral (b) strain averaged over the small region of interest. \circ =

Symptomatic, x = asymptomatic, □ = questionable, the dotted line represents the linear fit for symptomatic, dashed line the linear fit for asymptomatic, and the solid line denotes the linear fit for all patients. 69

Figure 3.20: Linear least-squares fits of RBANS Total score with maximum (a), and peak-to-trough (b) shear strain averaged over the small region of interest. ○ = Symptomatic, x = asymptomatic, □ = questionable, the dotted line represents the linear fit for symptomatic, dashed line the linear fit for asymptomatic, and the solid line denotes the linear fit for all patients. 71

Figure 5.1: B-mode image reconstructed from RF data (A) and segmented plaque with adventitia on the B-mode image (B). 93

Figure 5.2: Axial (A), lateral (B) and shear (C) strain images in the segmented region overlaid on the B-mode image. 97

Figure 5.3: Linear least-squares fits of the z-scores with maximum axial strain (A), maximum lateral strain (B) and maximum shear strain (C). ○ = Symptomatic, x = asymptomatic, □ = questionable, the dotted line represents the linear fit for symptomatic, dashed line the linear fit for asymptomatic, and the solid line denotes the linear fit for all patients. 99

Figure 5.4: Three-dimensional scatter plot of maximum axial, lateral and shear strain indices plotted against each other. ○ = Higher cognition group ($z < 0$), * = lower cognition group ($z \geq 0$). 101

Figure 5.5: Three-dimensional scatter plot of z-score, maximum axial strain and maximum lateral strain plotted against each other. ○ = Symptomatic group, * = asymptomatic group. 102

Figure 5.6: Three-dimensional scatter plot of z-score, maximum lateral strain and maximum shear strain plotted against each other. ○ = Symptomatic group, * = asymptomatic group. 103

Figure 5.7: Three-dimensional scatter plot of z-score, maximum shear strain and maximum axial strain plotted against each other. ○ = Symptomatic group, * = asymptomatic group. 104

Figure 5.8: ROC curves using individual strain indices or features (A) and combined features (B) for all patients. 105

Figure 5.9: ROC curves using individual features (A) and combined features (B) for symptomatic patients.	107
Figure 5.10: ROC curves using individual features (A) and combined features (B) for asymptomatic patients.	109
Figure 6.1: Histogram and fitted curve for maximum and peak-to-peak axial strain (a), lateral strain (b) and shear strain (c) for all patients.	119
Figure 6.2: Normal distribution fitted histogram of maximum axial strain (a), lateral strain (b) and shear strain (c).	120
Figure 6.3: Comparison of histograms with fitted curve for maximum axial strain for symptomatic group and asymptomatic group.	122
Figure 6.4: Comparison of histograms with fitted curve for maximum lateral strain for symptomatic group and asymptomatic group.	123
Figure 6.5: Comparison of histograms with fitted curve for maximum shear strain for symptomatic group and asymptomatic group.	124
Figure 6.6: Three-dimensional scatter plot of maximum axial, lateral and shear strain indices plotted against each other. \circ = Symptomatic group, $*$ = asymptomatic group.	125
Figure 6.7: Comparison of histograms with fitted curve for maximum axial strain for diabetes group and the no diabetes group.	127
Figure 6.8: Comparison of histograms with fitted curve for maximum lateral strain for diabetes group and the no diabetes group.	128
Figure 6.9: Comparison of histograms with fitted curve for maximum shear strain for diabetes group and the no diabetes group.	129
Figure 6.10: Three-dimensional scatter plot of maximum axial, lateral and shear strain indices plotted against each other. \circ = Diabetes group, $*$ = no diabetes group.	130
Figure 6.11: Comparison of histograms with fitted curve for maximum axial strain for hypertension and no hypertension group respectively.	132
Figure 6.12: Comparison of histograms with fitted curve for maximum lateral strain for hypertension and no hypertension group respectively.	133
Figure 6.13: Comparison of histograms with fitted curve for maximum shear strain for hypertension and no hypertension group respectively.	134
Figure 6.14: Three-dimensional scatter plot of maximum axial, lateral and shear strain	

- indices plotted against each other. \circ = Hypertension group, $*$ = no hypertension group. 135
- Figure 6.15:** Comparison of histograms with fitted curve for maximum axial strain for hyperlipidemia group and no hyperlipidemia group. 137
- Figure 6.16:** Comparison of histograms with fitted curve for maximum lateral strain for hyperlipidemia group and no hyperlipidemia group. 138
- Figure 6.17:** Comparison of histograms with fitted curve for maximum shear strain for hyperlipidemia group and no hyperlipidemia group. 139
- Figure 6.18:** Three-dimensional scatter plot of maximum axial, lateral and shear strain indices plotted against each other. \circ = Hyperlipidemia group, $*$ = no hyperlipidemia group. 140
- Figure 6.19:** Comparison of histograms with fitted curve for maximum axial strain for smoker group and non-smoker group. 142
- Figure 6.20:** Comparison of histograms with fitted curve for maximum lateral strain for smoker group and non-smoker group. 143
- Figure 6.21:** Comparison of histograms with fitted curve for maximum shear strain for smoker group and non-smoker group. 144
- Figure 6.22:** Three-dimensional scatter plot of maximum axial, lateral and shear strain indices plotted against each other. \circ = Smoker group, $*$ = non-smoker group. 145
- Figure 6.23:** Comparison of histograms for maximum axial strain (a), lateral strain (b) and shear strain (c) for patient group and volunteer group. 147
- Figure 6.24:** Three-dimensional scatter plot of maximum axial, lateral and shear strain indices plotted against each other. \circ = Patient group, $*$ = volunteer group. 148
- Figure 6.25:** Bivariate histograms of age and maximum axial strain (a), lateral strain (b) and shear strain (c) for patient group and volunteer group. 149
- Figure 6.26:** Three-dimensional scatter plot of maximum axial, lateral and shear strain indices plotted against each other. \circ = Patients in 40s, $+$ = patients in 50s, $*$ = patients in 60s, Δ = patients in 70s, \square = patients in 80s. 150
- Figure 6.27:** Three-dimensional scatter plot of maximum axial, lateral and shear strain indices plotted against each other. \circ = Patients in 40s, $+$ = patients in 50s, $*$ = patients in 60s, Δ = patients in 70s. 151

Figure 7.1: A classical HITS labeled on the TCD display.	159
Figure 8.1: B-mode image reconstructed from RF data (a) and segmented plaque with adventitia on the B-mode image (b).	167
Figure 8.2: Radial displacement images at systole (a) and end-diastole (b) in the segmented region.	171
Figure 8.3: Circumferential displacement images at systole (a) and end-diastole (b) in the segmented region.	172
Figure 8.4: Radial strain images at systole (a) and end-diastole (b) in the segmented region.	174
Figure 8.5: Circumferential strain images at systole (a) and end-diastole (b) in the segmented region.	175
Figure 9.1: 3D B-mode and QUS attenuation coefficient volumes for a plaque specimen.	184
Figure 9.2: Pathology microscopic slides and color-coded segmentation of different plaque regions.	186
Figure 9.3: Alignment of attenuation images with color-coded histology slides for the previously shown sample.	187
Figure 9.4: Alignment of attenuation images with color-coded histology slides for another sample.	187

List of Tables

Table 3.1: Characteristics of the human subject population utilized in this study.	36
Table 3.2: Correlations of RBANS Total score for plaque-only and plaque-with-adventitia segmentation. Significant correlations are marked in bold.	72
Table 3.3: Correlations of the specific component scores in RBANS total with maximum strain indices. Significant correlations are marked in bold.	73
Table 4.1: Significant correlations of each sub-test score to maximum strain indices for all patients (n = 51).	84
Table 4.2: Significant correlations of each sub-test score to maximum strain indices for symptomatic group (n = 31).	85
Table 4.3: Significant correlations of each sub-test score to maximum strain indices for asymptomatic group (n = 20).	85
Table 4.4: Significant correlations of each sub-test score to maximum strain indices for diabetes group (n = 14).	86
Table 4.5: Significant correlations of each sub-test score to maximum strain indices for hypertension group (n = 43).	86
Table 4.6: Significant correlations of each sub-test score to maximum strain indices for hyperlipidemia group (n = 40).	87
Table 4.7: Significant correlations of each sub-test score to maximum strain indices for smoker group (n = 37).	87
Table 5.1: Correlation of z-score to maximum strain indices.	100
Table 5.2: Sensitivity, specificity, area under curve (AUC) and 95% confidence intervals (CI) for individual features and combined features for all patients.	106
Table 5.3: Sensitivity, specificity, area under curve (AUC) and 95% confidence intervals (CI) for individual features and combined features for symptomatic patients.	108
Table 5.4: Sensitivity, specificity, area under curve (AUC) and 95% confidence intervals (CI) for individual features and combined features for asymptomatic patients.	110
Table 6.1: Mean and standard deviation of the normal distribution fit for maximum axial, lateral and shear strain indices.	121

Table 6.2: Sensitivity and specificity for the classification of symptomatic patients for individual and combined features.	126
Table 6.3: Sensitivity and specificity of classification of patients with diabetes for individual features and combined features.	131
Table 6.4: Sensitivity and specificity of classification of patients with hypertension for individual features and combined features.	136
Table 6.5: Sensitivity and specificity of classification of patients with hyperlipidemia for individual features and combined features.	141
Table 6.6: Sensitivity and specificity of classification of patients with tobacco usage for individual features and combined features.	146
Table 7.1: Correlations of maximum strain indices with MCA PSV on surgical side and non-surgical side for patients with HITS.	160
Table 7.2: Correlations of ICA PSV with MCA PSV on surgical side and non-surgical side for patients with HITS.	160
Table 9.1: Attenuation coefficients in different regions.	188

Chapter 1 : Introduction

1.1 Motivation

Stroke is the leading cause of serious, long-term disability and the fourth leading cause of mortality in the United States [1]. Over 700,000 strokes are reported each year and more than 130,000 people die each year from strokes in the United States [2]. Treatment of disabilities due to strokes also significantly adds to health care costs [2]. Twice as many stroke patients may also experience vascular cognitive impairment [3]. In addition, at least 5 “silent” strokes occur for each clinically recognized stroke [4]. Silent strokes, without clinical symptoms, have been associated with cognitive impairment [5]. Vascular cognitive impairment is the second leading cause of dementia after Alzheimer’s disease [6]. Instability in vulnerable plaque can generate cerebral micro-emboli, which may be related to both stroke and eventual cognitive abnormality.

Plaques are not randomly distributed in vessel walls. Symptomatically sensitive areas for plaque deposition include coronary and carotid arteries and the descending aorta [7-12]. Carotid plaque and its relationship to stroke has been an area of considerable research focus due to the devastating effects of emboli. In addition to stenosis, emboli in the carotid vessels may be more critical due to the smaller vessels and critical regions of the cerebral vasculature [13]. Carotid stenosis by itself may not result in emboli; however, the structural stability of the deposited plaque is a more direct indicator for emboli. Even small emboli may produce devastating and clinically relevant

consequences, therefore, it is clinically important to identify not only the presence of atherosclerotic plaques, but also those plaques that are biochemically or functionally more likely to produce emboli [14]. Emboli might be generated from rupture of vulnerable plaque, thus it is important to assess plaque vulnerability [15].

For superficial arteries, ultrasound imaging can become a viable screening modality for assessing plaque geometry and the extent of stenosis. Strain imaging [16] to detect plaque vulnerability based on identifying localized regions with large strain fluctuations, with arterial pulsation, may be able to determine risk for cognitive impairment. Plaque instability may be characterized by these increased strain variations over a cardiac cycle. Accumulated strain tensor indices over a cardiac cycle within a pulsating carotid plaque may be a viable biomarker for the diagnosis of plaque instability. In addition to strain imaging, quantitative ultrasound (QUS) imaging, which assesses the variation in acoustic properties such as the attenuation coefficient, may enable characterization of tissue composition in heterogeneous carotid plaque [17] and assist in the classification of vulnerable plaque [18].

1.2 Organization of the Dissertation

In Chapter 2, we discuss in more detail the clinical significance of stroke, silent stroke and vascular cognitive impairment. The importance of the characterization of carotid vulnerable plaque is emphasized. Previous work on the characterization of carotid plaque using ultrasound strain imaging and quantitative ultrasound is reviewed.

In Chapters 3 through 5 we evaluate the distribution and variation of maximum and peak-to-trough axial, lateral and shear strains indices estimated from *in vivo* carotid

plaques in patients scheduled for a carotid endarterectomy (CEA) using noninvasive ultrasound imaging. We also examine the relationship between these strain indices and cognitive function. Chapter 3 focuses on the correlations between our strain indices and cognitive function measured using a Repeatable Battery for the Assessment of Neuropsychological Status (RBANS) in an initial group of patients. A improved segmentation method is also proposed in Chapter 3 that includes the adventitial layer that provides better correlations with our strain indices. Chapter 4 evaluates the strain indices in a second larger group of patients and correlate maximum strain indices to cognition scores obtained with National Institute of Neurological Disorder and Stroke-Canadian Stroke Network (NINDS-CSN) Vascular Cognitive Impairment Harmonization Standards 60-minute protocol. Chapter 5 combines strain indices and cognition results of the two groups of patients and evaluates correlations between strain indices and cognitive function, as well as examine the feasibility of using strain indices to classify patients with cognitive impairment using Receiver Operating Characteristic (ROC) analysis.

Chapter 6 conducts a statistical analysis on the variation in the strain indices among all patients and volunteers. Statistical distributions of maximum axial, lateral and shear strain indices for symptomatic patients are compared to those for asymptomatic patients. Strain distributions for patients with diabetes, hypertension, hyperlipidemia and tobacco smoking groups are compared to those without the condition. Strain and age distributions were also compared between patients and a limited study on volunteers.

Micro-emboli generated by plaque rupture may be visualized using trans-cranial Doppler (TCD) monitoring. Chapter 7, provide a comparison of middle cerebral artery (MCA) velocities measured using TCD with ultrasound strain indices and internal carotid

artery (ICA) velocities in patients with emboli observed with TCD monitoring.

So far strain indices were estimated in a longitudinal scan of the carotid artery. A more straightforward and intuitive interpretation of deformation may be obtained by looking at the radial and circumferential strain along a cross-sectional view. In Chapter 8 we present radial and circumferential strain indices estimation using a Lagrangian description for cross-sectional scans of *in vivo* carotid artery using noninvasive ultrasound.

Chapter 9 presents QUS based evaluation of excised plaque using the attenuation coefficient as a parameter of interest. A novel approach is proposed to characterize localized calcified, fibrous and lipid regions within heterogeneous plaque using a region-to-region registration with three-dimensional (3D) histology and 3D attenuation coefficient maps obtained using QUS methods.

Finally, Chapter 10 describes the contributions of this dissertation and suggests possible avenues for future work on the characterization of carotid plaque vulnerability.

1.3 References

1. Kochanek, K.D., Xu, J., Murphy, S.L., Minino, A.M., and Kung, H.C., *Deaths: final data for 2009*. Natl Vital Stat Rep, 2011. **60**(3): p. 1-116.
2. Mozaffarian, D., Benjamin, E.J., Go, A.S., Arnett, D.K., Blaha, M.J., Cushman, M., de Ferranti, S., Despres, J.P., Fullerton, H.J., Howard, V.J., Huffman, M.D., Judd, S.E., Kissela, B.M., Lackland, D.T., Lichtman, J.H., Lisabeth, L.D., Liu, S., Mackey, R.H., Matchar, D.B., McGuire, D.K., Mohler, E.R., 3rd, Moy, C.S., Muntner, P., Mussolino, M.E., Nasir, K., Neumar, R.W., Nichol, G., Palaniappan, L., Pandey, D.K., Reeves, M.J., Rodriguez, C.J., Sorlie, P.D., Stein, J., Towfighi, A., Turan, T.N., Virani, S.S., Willey, J.Z., Woo, D., Yeh, R.W., and Turner, M.B., *Heart disease and stroke statistics--2015 update: a report from the American Heart Association*. Circulation, 2015. **131**(4): p. e29-322.
3. Hachinski, V., Iadecola, C., Petersen, R.C., Breteler, M.M., Nyenhuis, D.L., Black, S.E., Powers, W.J., DeCarli, C., Merino, J.G., Kalaria, R.N., Vinters, H.V.,

- Holtzman, D.M., Rosenberg, G.A., Wallin, A., Dichgans, M., Marler, J.R., and Leblanc, G.G., *National Institute of Neurological Disorders and Stroke-Canadian Stroke Network vascular cognitive impairment harmonization standards*. *Stroke*, 2006. **37**(9): p. 2220-41.
4. Vermeer, S.E., Prins, N.D., den Heijer, T., Hofman, A., Koudstaal, P.J., and Breteler, M.M., *Silent brain infarcts and the risk of dementia and cognitive decline*. *N Engl J Med*, 2003. **348**(13): p. 1215-22.
 5. Elias, M.F., Sullivan, L.M., D'Agostino, R.B., Elias, P.K., Beiser, A., Au, R., Seshadri, S., DeCarli, C., and Wolf, P.A., *Framingham stroke risk profile and lowered cognitive performance*. *Stroke*, 2004. **35**(2): p. 404-9.
 6. Battistin, L. and Cagnin, A., *Vascular cognitive disorder. A biological and clinical overview*. *Neurochem Res*, 2010. **35**(12): p. 1933-8.
 7. Persson, A.V., Robichaux, W.T., and Silverman, M., *The natural history of carotid plaque development*. *Arch Surg*, 1983. **118**(9): p. 1048-52.
 8. Avril, G., Batt, M., Guidoin, R., Marois, M., Hassen-Khodja, R., Daune, B., Gagliardi, J.M., and Le Bas, P., *Carotid endarterectomy plaques: correlations of clinical and anatomic findings*. *Ann Vasc Surg*, 1991. **5**(1): p. 50-4.
 9. Park, A.E., McCarthy, W.J., Pearce, W.H., Matsumura, J.S., and Yao, J.S., *Carotid plaque morphology correlates with presenting symptomatology*. *J Vasc Surg*, 1998. **27**(5): p. 872-8; discussion 878-9.
 10. Montauban van Swijndregt, A.D., Elbers, H.R., Moll, F.L., de Letter, J., and Ackerstaff, R.G., *Cerebral ischemic disease and morphometric analyses of carotid plaques*. *Ann Vasc Surg*, 1999. **13**(5): p. 468-74.
 11. Schulz, U.G. and Rothwell, P.M., *Association between arterial bifurcation anatomy and angiographic plaque ulceration among 4,627 carotid stenoses*. *Cerebrovasc Dis*, 2003. **15**(4): p. 244-51.
 12. Galili, O., Herrmann, J., Woodrum, J., Sattler, K.J., Lerman, L.O., and Lerman, A., *Adventitial vasa vasorum heterogeneity among different vascular beds*. *J Vasc Surg*, 2004. **40**(3): p. 529-35.
 13. Dempsey, R.J., Vemuganti, R., Varghese, T., and Hermann, B.P., *A review of carotid atherosclerosis and vascular cognitive decline: a new understanding of the keys to symptomatology*. *Neurosurgery*, 2010. **67**(2): p. 484-93; discussion 493-4.
 14. Golledge, J., Greenhalgh, R.M., and Davies, A.H., *The symptomatic carotid plaque*. *Stroke*, 2000. **31**(3): p. 774-81.
 15. Carr, S., Farb, A., Pearce, W.H., Virmani, R., and Yao, J.S., *Atherosclerotic plaque rupture in symptomatic carotid artery stenosis*. *J Vasc Surg*, 1996. **23**(5): p. 755-65; discussion 765-6.
 16. Ophir, J., Céspedes, I., Ponnekanti, H., Yazdi, Y., and Li, X., *Elastography: a quantitative method for imaging the elasticity of biological tissues*. *Ultrason Imaging*, 1991. **13**(2): p. 111-34.

17. Barzilai, B., Saffitz, J.E., Miller, J.G., and Sobel, B.E., *Quantitative ultrasonic characterization of the nature of atherosclerotic plaques in human aorta*. *Circ Res*, 1987. **60**(3): p. 459-63.
18. Lee, D.J., Sigel, B., Swami, V.K., Justin, J.R., Gahtan, V., O'Brien, S.P., Dwyer-Joyce, L., Feleppa, E.J., Roberts, A.B., and Berkowitz, H.D., *Determination of carotid plaque risk by ultrasonic tissue characterization*. *Ultrasound Med Biol*, 1998. **24**(9): p. 1291-9.

Chapter 2 : Literature Review

2.1 Clinical significance

2.1.1 Stroke and carotid plaque vulnerability

Stroke is the leading cause of serious, long-term disability and the fourth leading cause of death in the United States. Stroke etiologies and vascular risk factors are different in young adult patients and older patients, and mortality or clinical outcome is not independently associated with age [1]. Carotid plaque and possible embolic stroke are strongly linked through emboli generated by plaque rupture. Carotid stenosis by itself may not result in emboli; however, the structural stability of the deposited plaque is a more direct indicator of emboli. Micro-emboli generated from the rupture of vulnerable carotid plaque can flow into the vasculature of the brain and cause ischemic events resulting in stroke, vascular cognitive impairment or both [2]. Vulnerable plaques are unstable and can be an origination point for emboli. In general, softer plaques that are prone to increased deformations over a cardiac cycle are hypothesized to be vulnerable and pre-disposed to shedding emboli. In historical classification, vulnerable plaques are plaques that have a thin fibrous cap or fissured cap covering the foamy or necrotic core, with the presence of overt hemorrhage, ulceration or thrombus [3-4]. A panel of proteins expressed or retained in atherosclerotic plaques excised from human carotid artery has been found to be more abundant in vulnerable unstable plaques defined by the histology criteria [4] than stable plaques using proteomics, and therefore may be involved in the

plaque rupture process [5]. It is possible that plaque vulnerability is enhanced when the plaque undergoes significant strain variations and fatigue over the arterial pulsation of the cardiac cycle.

Carotid plaque composition is also related to coronary artery disease. Patients with acute myocardial infarction and coronary artery disease, frequently have unstable carotid plaques [6]. Complex carotid plaques with thrombi, ulceration, irregularity, predominantly echolucent or hypoechoic areas, and heterogeneity within echolucent areas, are associated with complex coronary plaques, and have higher prevalence in acute coronary syndromes than stable coronary artery disease [7]. Low integrated backscatter on echolucent plaques indicates lipid-rich lesions or unstable plaques. Echolucent or hypoechoic carotid plaques have been shown to predict the presence of complex coronary plaque, and also future coronary events in patients with stable coronary artery disease [8]. Studies have shown that irregularity on plaque surface in symptomatic carotid artery plaque predicts contralateral carotid plaque irregularity. Patients with plaque surface irregularity on both arteries tend to have previous myocardial infarction, and non-stroke vascular death [9].

Generally carotid endarterectomies (CEA) are performed on patients when the stenosis is greater than 70%, regardless of plaque composition [10]. Risk models of CEA on symptomatic carotid stenosis have been studied, since treatment decisions are based on the likelihood benefits and risks of CEA for individual patients [11]. It has been shown that CEA lowers death and morbidity rates for most patients, but risks are higher for patients with a smoking history, substantial angina, contralateral occlusion, or pre-operative transient ischemic attacks (TIA) [12]. Studies have shown that there is only

moderate benefit with CEA for patients with <70% stenosis in 5 years, but durable benefit for patients with >70% stenosis over 8 years, and there is no benefit for patients with <50% stenosis [13]. Clinical trials conducted indicated that CEA is highly beneficial for symptomatic patients with 70-99% stenosis [14], but studies also showed that symptomatic patients with 70 - 99% carotid stenosis may not benefit from CEA [15].

2.1.2 Silent stroke and cognition

In addition to clinically recognized stroke, "silent" strokes may occur, and are five times more prevalent [16]. Silent strokes are not detected based on classical TIA symptoms and therefore difficult to prevent. It is likely that these "silent" strokes may be associated with accumulated cognitive decline. For every patient suffering a stroke, twice as many people will experience vascular cognitive impairment [17]. Studies have suggested that silent strokes may occur with concurrent subclinical micro-emboli [18] and have been associated with cognitive impairment [19]. The pathophysiology of silent strokes includes microvascular degeneration, either in the brain or in the feeding vessel walls, and embolic disorders [20-21]. The focus has been on the possibility of physical abnormalities within diseased carotid vessels as measurable markers of microvascular pathology and potential sources of microemboli [22-23]. Cerebral micro-emboli due to instability in carotid vulnerable plaque can lead to cognitive impairment [24], and thus it is important to characterize carotid plaque and assess its vulnerability. It has also been suggested that increased strain in plaque may correlate with cognitive abnormalities [25], suggesting that it is important to identify patients with vulnerable plaques to help prevent future stroke and cognitive impairment. Studies have shown that the risk of silent stroke is positively related to the extent of carotid stenosis for both symptomatic and asymptomatic

patients [26].

Vascular cognitive impairment [27], on the other hand, may also be predicted by arterial aging and stiffening [28]. There is evidence that cerebral micro-emboli have a significant correlation with vascular dementia and are associated with a faster decline of cognitive function [29-30]. Correlations have also been found between the number of intra-operative micro-emboli detected by trans-cranial Doppler and the post-operational cognitive measures [24, 31-32]. Vascular risk factors including diabetes, hypertension, dyslipidemia, smoking and atherosclerosis have also been associated with Alzheimer's disease [33]. Research has also focused on controlling cardiovascular risk factors to prevent or slow the progression of mixed dementia, coexistence of Alzheimer's disease and vascular dementia, since cognition improved after treatment will eventually decline [34].

2.1.3 Cognitive function assessments

The syndrome of dementia, either Alzheimer's or vascular cognitive impairment, involves cognitive decline with memory impairment and deterioration in at least one other cognitive function [35]. Definition of cognitive function includes the processes of how a person perceives, registers, stores, retrieves, and uses information [36]. The purpose of cognitive assessment is to evaluate an individual's cognitive abilities and to screen for the presence of cognitive impairment [37]. Assessing cognitive function is essential for early detection and prompt treatment of cognitive impairment, since undetected cognitive impairment is related to greater mobility and mortality [38]. Several cognition tests have been utilized in the clinic to screen for dementia and cognitive impairment [39], and for cognition assessment in elderly patients [37].

To assess cognitive impairment, the Repeatable Battery for the Assessment of Neuropsychological Status (RBANS) [40] has been widely used as a cognition test protocol. RBANS takes less than 30 minutes, and it evaluates five cognitive domains. RBANS has been reported to be effective at both characterizing cognitive decline in older patients and screening for dementia in younger patients [40]. This cognition test was later extended by providing age and education-corrected scaled scores in the subtests [41].

The National Institute of Neurological Disorder and Stroke—Canadian Stroke Network (NINDS-CSN) Vascular Cognitive Impairment Harmonization Standards in 2006 suggested different neuropsychological protocols for evaluation of cognition [17]. As a substitute for RBANS, the NINDS Vascular Cognitive Impairment Harmonization Standards has been suggested for the neuropsychological assessment of vascular cognitive impairment [28]. This cognitive function assessment protocol has been incorporated into stroke patient care in the clinic and has demonstrated clinical feasibility [42].

2.1.4 Carotid artery stiffness

In addition to the acoustic properties of carotid plaque, the wall stiffness of carotid artery can also be an index in the prediction of stroke. Van Popele et al. [43] conducted the Rotterdam Study and found that both aortic and common carotid artery stiffness had strong positive association with atherosclerosis. Mattace-Raso et al. [44] demonstrated that aortic pulse wave velocity (PWV), which measures arterial stiffness along with carotid distensibility, strongly predicted coronary heart disease and stroke in the Rotterdam Study. Laurent et al. [45-46] assessed aortic stiffness in patients with essential hypertension by measuring carotid-femoral PWV and found that stiffness is an

independent predictor of cardiovascular mortality and fatal stroke. Tsivgoulis et al. [47] evaluated common carotid artery (CCA) distensibility, the change of CCA diameter during the cardiac cycle, and found that increased CCA stiffness was associated with ischemic stroke. Eigenbrodt et al. [48] showed that CCA diameter was positively and significantly associated with age among middle-aged, black and white men and women with no pre-existing disease, no plaques or shadowing, and no major vascular risk factors. Nikic et al. [49] evaluated CCA intima-media thickness (IMT) in patients with incident ischemic brain infarctions and in controls without cerebrovascular disease, and found that mean CCA IMT was significantly higher in patients than in controls. Sharma et al. [50] conducted a cohort study involving over 2000 individuals, they found that subclinical atherosclerosis determined by carotid IMT, carotid plaque score, and coronary artery calcium score in the absence of clinical cardiovascular event are significantly associated with parameters of left ventricular dyssynchrony as a marker of subclinical regional myocardial dysfunction. Paini et al. [51] compared carotid artery stiffness at the site of plaque to the upstream adjacent CCA, and showed that an inward bending strain pattern, defined by stiffer carotid artery at the level of plaque than proximal CCA, would associate with type 2 diabetes and dyslipidemia. Several ultrasound-based techniques have been introduced to quantify arterial stiffness, including pulse wave imaging [52] and shear wave imaging [53-54].

2.2 Carotid plaque characterization with ultrasound imaging

2.2.1 Ultrasound strain imaging

Characterization of carotid plaque plays an important role in detecting plaque

vulnerability to rupture. Ultrasound is a noninvasive option for imaging superior shallow vessels such as the carotid artery. B-mode images are commonly used clinically, but they are not sufficient to identify the vulnerability of plaque since they can only differentiate specific plaque types from normal tissue; but it is difficult to differentiate thrombus from surrounding lipidic plaque [55].

Plaque instability may be characterized by increased strain variations over a cardiac cycle with arterial pulsation. Therefore, strain imaging to detect plaque vulnerability based on regions with large strain fluctuations, may be able to determine risk of plaque rupture, which can lead to cognitive impairment. Thus ultrasound strain imaging [56] may be a useful surrogate in the clinic to detect vulnerability of plaque and assess potential risk of silent stroke. Ultrasound strain imaging has been utilized to estimate the mechanical deformation of plaque, and can therefore assist in characterization of plaque vulnerability [57]. Most of the research on plaque characterization has focused on high-frequency intravascular ultrasound (IVUS) characterization of coronary arteries because of its high spatial resolution. Intravascular elastography has been shown to identify vulnerable plaque both *in vitro* and *in vivo*. Fibrous tissue present with lower mean radial strain (0 - 0.2%) when compared to lipidic tissue (1 - 2%) [58-61]. Schaar et al. [62] used strain imaging and histology separately to identify vulnerable plaque, and plotted strain values against histology indices. They showed intravascular elastography to be a good diagnostic tool due to the high sensitivity of 88% and 89% specificity using a receiver operator characteristic (ROC) analysis for a strain threshold of 1.26% [62].

There are fewer studies of noninvasive carotid plaque imaging using elastography, and strain imaging [63-74]. Maurice et al. [63] proposed a Von Mises parameter to

characterize mechanical properties of the vessel wall and utilized a Lagrangian speckle model estimator to calculate the strain tensor in order to estimate axial, lateral, shear and radial strain in the plaque and to characterize the vessel wall. They indicated that their method was reproducible, since the correlation of strain values between left and right common carotid arteries was significant. Schmitt et al. [64] implemented a Lagrangian model to estimate strain tensors for both cross-sectional and longitudinal imaging views. They found that axial strain and axial shear strain provide plaque size information, along with composition and mechanical properties. Ribbers et al. [67] calculated the radial and circumferential strain in two ways; from axial and shear strain and from principle strain. The strain patterns obtained agree with the theory, but zero-strain zones were observed at the diagonal boundaries. Hansen et al. [69] improved this technique and was able to use an angle-compounding technique to reduce noise artifacts and obtain better radial and circumferential strain estimations from only the axial strain. Wan et al. [75] calculated radial and circumferential strain in a vessel phantom using reflection model-based corrected B-mode images. Majdouline et al. [76] investigated the condition of the plaque and associated shear strain elasticity index (SSE), with its absolute value statistically higher in plaques with increased vulnerability. Since ultrasound beams align with the axial direction during scanning, it is natural to study the plaque in a longitudinal imaging plane. Idzenga et al. [70] were able to examine the longitudinal shear strain in carotid artery utilizing radiofrequency (RF) data instead of B-mode data. Mercure et al. [77] corrected the under-estimation of axial strain in plaques using a kinematics constraints based local angle compensation method. Naim et al. [78] found that strain index can index the presence of a lipid core with high sensitivity and moderate specificity, using

clinical findings from high resolution magnetic resonance imaging (MRI). Liu et al. [79] recently utilized a two-level, RF data based real-time tissue elastography (RTE) to identify vulnerable carotid atherosclerotic plaques. They showed that ultrasonic RTE has the potential to characterize composition of carotid plaques *in vivo* and identify plaques that are vulnerable to rupture. Widman et al. [80] demonstrated that it is feasible to track radial and longitudinal strain of plaque in the carotid artery using speckle tracking strain using a validation experiment by sonomicrometry in a plaque phantom.

In our laboratory, Shi et al. [71] developed a multi-level tracking algorithm to calculate displacement and strain and indicated that axial strain and lateral displacement parameters can separate soft from calcified plaque. They therefore hypothesized that this differentiation could help identify vulnerable plaque using cumulated strain indices. McCormick et al. [73-74] developed a robust strain estimation algorithm based on a hierarchical framework utilizing a Lagrangian description and applied Bayesian regularization to estimate all components of the displacement vector and strain tensor within the two-dimensional (2D) imaging plane for plaque characterization. Accumulated strain indices derived from the strain tensor were utilized to assess the vulnerability of carotid plaque based on increased deformation over a cardiac cycle [71, 81].

Other ultrasound based elasticity imaging methods have also been widely investigated in assessing plaque vulnerability and identifying plaque prone to rupture [82-84], and may assist in the prediction of embolism and resulting stroke. Kim et al. [82] showed that ultrasound-induced thermal strain images correspond well with B-mode images on arterial wall structure and could distinguish fatty tissue from muscle with a temperature change of less than 2 degrees, and therefore demonstrated the potential of

ultrasound-induced thermal strain imaging with small temperature increases for plaque characterization. Doherty et al. [83] performed parametric analysis using Finite Element Method (FEM) models to simulate acoustic radiation force impulse (ARFI) imaging on carotid plaques, and found that ARFI imaging could differentiate a softer lipid pool from surrounding stiffer tissue and the fibrous cap. As for safety concerns, they noted that the stresses induced by ARFI imaging are orders of magnitude lower than stresses induced due to blood pressure. Korukonda et al. [84] studied sparse-array elastography and compared it to plane-wave imaging and compounded-plane-wave imaging on simulated vessel and vessel phantoms. They concluded that the performance of sparse-array imaging was comparable to plane-wave and compounded-plane-wave imaging on phantoms. Hansen et al. [85] recently extended their strain compounding technique to plane wave based ultrafast ultrasonic imaging.

2.2.2 Ultrasound strain definition

Strain is the gradient of displacement. Axial strain is defined as $e_y = \frac{\partial d_y}{\partial y}$, lateral strain is defined as $e_x = \frac{\partial d_x}{\partial x}$, and shear strain is defined as $e_{xy} = \frac{1}{2} \left(\frac{\partial d_y}{\partial x} + \frac{\partial d_x}{\partial y} \right)$, where d_y and d_x represent the axial and lateral displacements respectively. In axial direction, positive displacement indicates that the object is moving away from the transducer, while negative displacement indicates that the object is moving towards the transducer; in lateral direction, positive displacement indicates that the object is moving to the right while negative displacement indicates that the object is moving to the left. Strain over a cardiac cycle could be represented by accumulated strain, which is the gradient of accumulation of incremental frame-to-frame displacements. The accumulated

displacements for axial and lateral directions are defined as:

$$D_y^N = \sum_{i=2}^N d_y^i$$

$$D_x^N = \sum_{i=2}^N d_x^i$$

where d_y^i and d_x^i are the incremental axial and lateral displacements estimated at the i^{th} frame, the accumulated displacements D_y^N and D_x^N are the accumulated axial and lateral displacements integrated from the 2nd frame to the N^{th} frame. The accumulated strains can then be calculated as:

$$E_y^N = \frac{\partial D_y^N}{\partial y}$$

$$E_x^N = \frac{\partial D_x^N}{\partial x}$$

$$E_{xy}^N = \frac{1}{2} \left(\frac{\partial D_y^N}{\partial x} + \frac{\partial D_x^N}{\partial y} \right)$$

where E_y^N , E_x^N , and E_{xy}^N represents axial, lateral and shear strains respectively. Positive strains indicate tissue expansion, while negative strain indicates tissue compression.

2.2.3 Quantitative ultrasound imaging

Carotid plaque is primarily composed of cholesterol, calcium, and fibrous tissue [86]. Heterogeneous plaques are difficult to characterize using conventional ultrasound B-mode imaging [55]. Differences in acoustic properties, which can be assessed using quantitative ultrasound (QUS) or elasticity imaging methods, may reflect difference in

tissue composition [87]. Therefore QUS has been widely used to assess acoustic properties of tissue, such as the integrated attenuation, attenuation coefficient and integrated backscatter coefficient, in order to characterize and classify plaque and the classification is often compared to pathology patterns.

Characterization of carotid plaque may play an important role in detecting plaque vulnerability to rupture [88]. Plaque analysis using parameters such as the integrated attenuation, attenuation coefficient and integrated backscatter have been reported [55, 87-100]. The integrated attenuation is defined as the integral value of attenuation coefficient over the frequency bandwidth. It was found that on freshly excised aorta walls, the integrated attenuation gradually increased from normal, fibrous, fibrofatty to calcified tissue, and the slope of fibrous tissue was lower than that of normal tissue at a center frequency of 10 MHz [89]. IVUS was used on excised femoral and iliac artery segments at 20MHz, and it was shown that attenuation can differentiate fibrous plaque from non-fibrous plaque and normal vessel wall, although there was no correlation with pathology [90]. Studies that could distinguish between thrombus and non-thrombus tissue both *in vivo* and *ex vivo* using backscatter slope, intercept and total power of the spectrum were also presented [55, 88, 91]. Bridal et al. [92-94] measured the integrated attenuation, attenuation slope and integrated backscatter from 5MHz up to 56MHz, and classified lipid and calcified plaque from normal tissue by comparison to histology. Abdominal aorta was also examined at 10MHz and the study showed that integrated backscatter can classify calcified, fibrous, fibrofatty and normal regions in atherosclerotic plaque [87]. Nair et al. [97] built a classification tree model using autoregressive spectral analysis and developed a real-time automated tissue characterization approach using IVUS images on

coronary plaques. Their results correspond well with histology classifications and have potential for virtual histology evaluations and plaque vulnerability assessments [95-97]. Properties related to tissue scatterers such as scatterer size and spacing have also caught a lot of attention. Roth et al. [98] proposed a parameter called the relative Fourier energy, that is the normalized power spectrum of the demodulated ultrasound echo signal, determined by the scatterer distribution. They used this parameter to separate fibrofatty and calcified tissue from normal tissue and got a significant correlation with histology classification [98].

In our laboratory, Shi et al. [99-100] reported on the equivalent scatterer size and attenuation coefficient for calcified and soft regions of *ex vivo* carotid plaque in the frequency range of 2.5 to 7.5 MHz. Calcified regions have an equivalent scatterer size range of 120-180 μm , with attenuation coefficients between 1.4-2.5dB/cm/MHz, while for softer regions the equivalent scatterer sizes distribution is in the 280-470 μm range and the attenuation coefficients range from 0.3-1.3dB/cm/MHz [99-100].

2.2.4 Trans-cranial Doppler

Trans-cranial Doppler (TCD) measures the velocity of blood flow in middle cerebral arteries (MCA). During the monitoring process, a high intensity transient signal (HITS) can occur in the recordings, which may reflect the propagation of micro-emboli [101-103]. TCD signatures that could separate signal of micro-emboli, both gaseous and solid, from artifacts has been provided [101]. The TCD signals of embolic source has been found to be transient and high intensity, and therefore TCD could be a sensitive detector of clinically silent emboli [102]. Several optimization approaches have been attempted to automate the detection of micro-emboli [103]. A real HITS should satisfy all of the

following criteria: the Doppler signal is less than 300 milliseconds, the amplitude of the signal is at least 3dB higher than the background blood flow signal, the signal is unidirectional within the velocity spectrum, and an audible “snap”, “chirp” or “moan” is present [104]. It has been shown that HITS occurs in 30% of symptomatic patients [105], and is more likely to be present in stroke-related symptomatic patients than TIA-related symptomatic patients or asymptomatic patients [106].

2.2.5 Pulse wave imaging

When the heart contracts, the volumetric change induced by the inflowing blood generates a pressure pulse wave propagating through the arteries. PWV has been considered as one of the most important indices quantify arterial stiffness. PWV can be expressed by the Moens-Korteweg equation:

$$PWV = \sqrt{\frac{Eh}{2R\rho}}$$

where E denotes the Young's modulus of the artery wall along the circumferential direction, h is the thickness of the wall, R is the inner radius of the artery, ρ is the density of the wall material. This relationship holds true when the artery wall is thin and not embedded in an elastic medium, and assuming the perturbations of the artery are small [107]. PWV increases with an increase in the artery stiffness according to the equation above.

Traditionally, PWV is measured using the "foot-to-foot" velocity, which is considered as the gold standard. For example, in carotid-femoral PWV measurement, waveforms in right common carotid artery and right femoral artery are recorded and the

time delay (Δt) at the feet of these two waveforms are calculated. PWV can then be calculated using the physical distance (ΔD) between the two measurement points as, $PWV = \Delta t / \Delta D$ [108]. Because the pulse wave propagates at a relative high speed (meters/second), time delay measurement could potentially induce considerable uncertainty in final PWV value. One way to compensate time delay measurement error is to calculate PWV over a larger distance. This method, however, results in a global value and doesn't take into account local inhomogeneities in arterial stiffness [109].

Pulse wave imaging has also been developed for MRI [110-111] and ultrasound [52, 112-114] as non-invasive imaging methods to measure regional PWV, rather than global value measured with the traditional method. When compared with ultrasound based methods, MRI based analysis is limited by patient selection, lower temporal resolution, in addition to its higher cost.

Several high temporal rate ultrasound imaging techniques have been developed to achieve both quantitative visualization and estimation of PWV. Luo et al. [52] measured PWV in the human carotid artery in 8 healthy volunteers using an ultrasound system with a high frame rate of 8000 fps enabled using an ECG-gated synchronized acquisition. Couade et al. [112] developed an ultrafast ultrasound imaging system that enabled a 1000 fps full-view imaging. They measured 25 PWV in 25 healthy volunteers. Hasegawa et al. [113] measured PWV in 3 healthy subjects using high frame rate ultrasound imaging achieved by plane wave transmission and parallel beam forming. Nagaoka et al. [114] measured PWV in 4 healthy young males and 1 healthy young female with high speed ultrasound achieved by plane wave transmission and spatial compounding. These methods generated PWV in good agreement with that reported in the literature.

2.2.6 Shear wave imaging

Shear wave imaging has also been demonstrated to be a feasible option for assessing arterial stiffness. Nightingale et al. [115] showed that shear wave images generated using ARFI on *ex vivo* human breast tissue and *in vivo* human male abdomen all matched well following modulus reconstruction and comparison to B-mode images. The challenge lay in the small magnitude of displacement generated by induced radiation force [115-116]. Dumont et al. [117] combined ARFI-based shear wave imaging with ARFI-based spectral Doppler imaging to estimate wall shear rate, vascular wall displacement, spectral Doppler velocity and transverse wave velocity in tissue-mimicking phantoms, and the results showed reasonable agreement with other research groups. Couade et al.[53] validated that the elasticity of arterial wall is exhibited from shear wave propagation in an artery phantom and in the common carotid artery of one healthy volunteer. Behler et al. [118] proposed the use of reflected shear wave imaging (RSWI) and obtained parametric images on 3 porcine iliac arteries with plaques, and showed that RSWI could identify lipid, calcium and collagen regions in atherosclerotic plaque. Deffieux et al. [119] implemented this technology with a directional filter, which was previously applied in magnetic resonance elastography, to reduce the artifact since errors might be induced in shear wave velocity estimation from the propagation of the reflected shear waves. However, higher pressures associated with ultrasound radiation in shear wave imaging may induce the rupture of plaque in a diseased artery. The impact of adverse biological effects with shear wave imaging in clinical studies needs further investigation [120]. Ramnarine et al.[54] recently conducted a study involving eighty-one patients and demonstrated that shear wave elastography (SWE) is able to quantify carotid plaque

elasticity and provide clinically relevant information to help identify unstable carotid plaques.

2.3 References

1. Arnold, M., Halpern, M., Meier, N., Fischer, U., Haefeli, T., Kappeler, L., Brekenfeld, C., Mattle, H.P., and Nedeltchev, K., *Age-dependent differences in demographics, risk factors, co-morbidity, etiology, management, and clinical outcome of acute ischemic stroke*. *J Neurol*, 2008. **255**(10): p. 1503-7.
2. Whisnant, J.P., Basford, J.R., Bernstein, E.F., Cooper, E.S., Dyken, M.L., Easton, J.D., Little, J.R., Marler, J.R., Millikan, C.H., Petito, C.K., Price, T.R., Raichle, M.E., Robertson, J.T., Thiele, B., Walker, M.D., and Zimmerman, a.R.A., *Special report from the National Institute of Neurological Disorders and Stroke. Classification of cerebrovascular diseases III*. *Stroke*, 1990. **21**(4): p. 637-76.
3. Sary, H.C., *Composition and classification of human atherosclerotic lesions*. *Virchows Arch A Pathol Anat Histopathol*, 1992. **421**(4): p. 277-90.
4. Sary, H.C., Chandler, A.B., Dinsmore, R.E., Fuster, V., Glagov, S., Insull, W., Jr., Rosenfeld, M.E., Schwartz, C.J., Wagner, W.D., and Wissler, R.W., *A definition of advanced types of atherosclerotic lesions and a histological classification of atherosclerosis. A report from the Committee on Vascular Lesions of the Council on Arteriosclerosis, American Heart Association*. *Circulation*, 1995. **92**(5): p. 1355-74.
5. Lepedda, A.J., Cigliano, A., Cherchi, G.M., Spirito, R., Maggioni, M., Carta, F., Turrini, F., Edelstein, C., Scanu, A.M., and Formato, M., *A proteomic approach to differentiate histologically classified stable and unstable plaques from human carotid arteries*. *Atherosclerosis*, 2009. **203**(1): p. 112-8.
6. Rossi, A., Franceschini, L., Fusaro, M., Cicoira, M., Eleas, A.A., Golia, G., Bonapace, S., Santini, F., Sangiorgi, G., Zardini, P., and Vassanelli, C., *Carotid atherosclerotic plaque instability in patients with acute myocardial infarction*. *Int J Cardiol*, 2006. **111**(2): p. 263-6.
7. Triposkiadis, F., Sitafidis, G., Kostoulas, J., Skoularigis, J., Zintzaras, E., and Fezoulidis, I., *Carotid plaque composition in stable and unstable coronary artery disease*. *Am Heart J*, 2005. **150**(4): p. 782-9.
8. Honda, O., Sugiyama, S., Kugiyama, K., Fukushima, H., Nakamura, S., Koide, S., Kojima, S., Hirai, N., Kawano, H., Soejima, H., Sakamoto, T., Yoshimura, M., and Ogawa, H., *Echolucent carotid plaques predict future coronary events in patients with coronary artery disease*. *J Am Coll Cardiol*, 2004. **43**(7): p. 1177-84.
9. Rothwell, P.M., Villagra, R., Gibson, R., Donders, R.C., and Warlow, C.P., *Evidence of a chronic systemic cause of instability of atherosclerotic plaques*. *Lancet*, 2000. **355**(9197): p. 19-24.

10. Hanley, D., Gorelick, P.B., Elliott, W.J., Broder, M.S., Saver, J.L., Kidwell, C.S., Fagan, S.C., Wilson, A., Lennihan, L., Schwer, W.A., Rubenstein, L.Z., Crowell, R.M., Haines, S.J., Lopez, C.C., Zorowitz, R., and Dubois, R.W., *Determining the appropriateness of selected surgical and medical management options in recurrent stroke prevention: a guideline for primary care physicians from the National Stroke Association work group on recurrent stroke prevention*. J Stroke Cerebrovasc Dis, 2004. **13**(5): p. 196-207.
11. Rothwell, P.M., Mehta, Z., Howard, S.C., Gutnikov, S.A., and Warlow, C.P., *Treating individuals 3: from subgroups to individuals: general principles and the example of carotid endarterectomy*. Lancet, 2005. **365**(9455): p. 256-65.
12. Duncan, J.M., Reul, G.J., Ott, D.A., Kincade, R.C., and Davis, J.W., *Outcomes and risk factors in 1,609 carotid endarterectomies*. Tex Heart Inst J, 2008. **35**(2): p. 104-10.
13. Barnett, H.J., Taylor, D.W., Eliasziw, M., Fox, A.J., Ferguson, G.G., Haynes, R.B., Rankin, R.N., Clagett, G.P., Hachinski, V.C., Sackett, D.L., Thorpe, K.E., Meldrum, H.E., and Spence, J.D., *Benefit of carotid endarterectomy in patients with symptomatic moderate or severe stenosis*. North American Symptomatic Carotid Endarterectomy Trial Collaborators. N Engl J Med, 1998. **339**(20): p. 1415-25.
14. *Beneficial effect of carotid endarterectomy in symptomatic patients with high-grade carotid stenosis*. N Engl J Med, 1991. **325**(7): p. 445-53.
15. Rothwell, P.M. and Warlow, C.P., *Prediction of benefit from carotid endarterectomy in individual patients: a risk-modelling study*. European Carotid Surgery Trialists' Collaborative Group. Lancet, 1999. **353**(9170): p. 2105-10.
16. Vermeer, S.E., Prins, N.D., den Heijer, T., Hofman, A., Koudstaal, P.J., and Breteler, M.M., *Silent brain infarcts and the risk of dementia and cognitive decline*. N Engl J Med, 2003. **348**(13): p. 1215-22.
17. Hachinski, V., Iadecola, C., Petersen, R.C., Breteler, M.M., Nyenhuis, D.L., Black, S.E., Powers, W.J., DeCarli, C., Merino, J.G., Kalara, R.N., Vinters, H.V., Holtzman, D.M., Rosenberg, G.A., Wallin, A., Dichgans, M., Marler, J.R., and Leblanc, G.G., *National Institute of Neurological Disorders and Stroke-Canadian Stroke Network vascular cognitive impairment harmonization standards*. Stroke, 2006. **37**(9): p. 2220-41.
18. Dempsey, R.J., Vemuganti, R., Varghese, T., and Hermann, B.P., *A review of carotid atherosclerosis and vascular cognitive decline: a new understanding of the keys to symptomology*. Neurosurgery, 2010. **67**(2): p. 484-93; discussion 493-4.
19. Elias, M.F., Sullivan, L.M., D'Agostino, R.B., Elias, P.K., Beiser, A., Au, R., Seshadri, S., DeCarli, C., and Wolf, P.A., *Framingham stroke risk profile and lowered cognitive performance*. Stroke, 2004. **35**(2): p. 404-9.
20. Fleg, J.L., Stone, G.W., Fayad, Z.A., Granada, J.F., Hatsukami, T.S., Kolodgie, F.D., Ohayon, J., Pettigrew, R., Sabatine, M.S., Tearney, G.J., Waxman, S.,

- Domanski, M.J., Srinivas, P.R., and Narula, J., *Detection of high-risk atherosclerotic plaque: report of the NHLBI Working Group on current status and future directions*. JACC Cardiovasc Imaging, 2012. **5**(9): p. 941-55.
21. AlMuhanna, K., Zhao, L., Kowalewski, G., Beach, K.W., Lal, B.K., and Sikdar, S., *Investigation of cerebral hemodynamics and collateralization in asymptomatic carotid stenoses*. Conf Proc IEEE Eng Med Biol Soc, 2012: p. 5618-21.
 22. Fleiner, M., Kummer, M., Mirlacher, M., Sauter, G., Cathomas, G., Krapf, R., and Biedermann, B.C., *Arterial neovascularization and inflammation in vulnerable patients: early and late signs of symptomatic atherosclerosis*. Circulation, 2004. **110**(18): p. 2843-50.
 23. Tureyen, K., Vemuganti, R., Salamat, M.S., and Dempsey, R.J., *Increased angiogenesis and angiogenic gene expression in carotid artery plaques from symptomatic stroke patients*. Neurosurgery, 2006. **58**(5): p. 971-7; discussion 971-7.
 24. Russell, D., *Cerebral microemboli and cognitive impairment*. J Neurol Sci, 2002. **203-204**: p. 211-4.
 25. Rocque, B.G., Jackson, D., Varghese, T., Hermann, B., McCormick, M., Kliewer, M., Mitchell, C., and Dempsey, R.J., *Impaired cognitive function in patients with atherosclerotic carotid stenosis and correlation with ultrasound strain measurements*. J Neurol Sci, 2012. **322**(1-2): p. 20-4.
 26. Norris, J.W. and Zhu, C.Z., *Silent stroke and carotid stenosis*. Stroke, 1992. **23**(4): p. 483-5.
 27. O'Brien, J.T., Erkinjuntti, T., Reisberg, B., Roman, G., Sawada, T., Pantoni, L., Bowler, J.V., Ballard, C., DeCarli, C., Gorelick, P.B., Rockwood, K., Burns, A., Gauthier, S., and DeKosky, S.T., *Vascular cognitive impairment*. Lancet Neurol, 2003. **2**(2): p. 89-98.
 28. Gorelick, P.B., Scuteri, A., Black, S.E., Decarli, C., Greenberg, S.M., Iadecola, C., Launer, L.J., Laurent, S., Lopez, O.L., Nyenhuis, D., Petersen, R.C., Schneider, J.A., Tzourio, C., Arnett, D.K., Bennett, D.A., Chui, H.C., Higashida, R.T., Lindquist, R., Nilsson, P.M., Roman, G.C., Sellke, F.W., and Seshadri, S., *Vascular contributions to cognitive impairment and dementia: a statement for healthcare professionals from the american heart association/american stroke association*. Stroke, 2011. **42**(9): p. 2672-713.
 29. Purandare, N., Voshaar, R.C., Hardicre, J., Byrne, J., McCollum, C., and Burns, A., *Cerebral emboli and depressive symptoms in dementia*. Br J Psychiatry, 2006. **189**: p. 260-3.
 30. Purandare, N., Voshaar, R.C., Morris, J., Byrne, J.E., Wren, J., Heller, R.F., McCollum, C.N., and Burns, A., *Asymptomatic spontaneous cerebral emboli predict cognitive and functional decline in dementia*. Biol Psychiatry, 2007. **62**(4): p. 339-44.
 31. Stump, D.A., Rogers, A.T., Hammon, J.W., and Newman, S.P., *Cerebral emboli and cognitive outcome after cardiac surgery*. J Cardiothorac Vasc Anesth, 1996.

- 10(1)**: p. 113-8; quiz 118-9.
32. Braekken, S.K., Reinvang, I., Russell, D., Brucher, R., and Svennevig, J.L., *Association between intraoperative cerebral microembolic signals and postoperative neuropsychological deficit: comparison between patients with cardiac valve replacement and patients with coronary artery bypass grafting*. J Neurol Neurosurg Psychiatry, 1998. **65(4)**: p. 573-6.
 33. Deschaintre, Y., Richard, F., Leys, D., and Pasquier, F., *Treatment of vascular risk factors is associated with slower decline in Alzheimer disease*. Neurology, 2009. **73(9)**: p. 674-80.
 34. Langa, K.M., Foster, N.L., and Larson, E.B., *Mixed dementia: emerging concepts and therapeutic implications*. JAMA, 2004. **292(23)**: p. 2901-8.
 35. Association, A.P., *Diagnostic and statistical manual of mental disorders, (DSM-5®)*. 2013: American Psychiatric Pub.
 36. Foreman, M.D., Fletcher, K., Mion, L.C., and Trygstad, L., *Assessing cognitive function*. in Geriatric protocol for best practice, 2003: p. 99-115.
 37. Woodford, H.J. and George, J., *Cognitive assessment in the elderly: a review of clinical methods*. QJM, 2007. **100(8)**: p. 469-84.
 38. Inouye, S.K., Foreman, M.D., Mion, L.C., Katz, K.H., and Cooney, L.M., Jr., *Nurses' recognition of delirium and its symptoms: comparison of nurse and researcher ratings*. Arch Intern Med, 2001. **161(20)**: p. 2467-73.
 39. Cullen, B., O'Neill, B., Evans, J.J., Coen, R.F., and Lawlor, B.A., *A review of screening tests for cognitive impairment*. J Neurol Neurosurg Psychiatry, 2007. **78(8)**: p. 790-9.
 40. Randolph, C., Tierney, M.C., Mohr, E., and Chase, T.N., *The Repeatable Battery for the Assessment of Neuropsychological Status (RBANS): preliminary clinical validity*. J Clin Exp Neuropsychol, 1998. **20(3)**: p. 310-9.
 41. Duff, K., Patton, D., Schoenberg, M.R., Mold, J., Scott, J.G., and Adams, R.L., *Age- and education-corrected independent normative data for the RBANS in a community dwelling elderly sample*. Clin Neuropsychol, 2003. **17(3)**: p. 351-66.
 42. Han, D.Y., Anderson, A.J., Jones, J.E., Hermann, B.P., and Sattin, J.A., *Neuropsychology in Multidisciplinary Stroke Care: Clinical Feasibility of the NINDS-CSN Vascular Cognitive Impairment Harmonization Standards*. International Scholarly Research Notices, 2014. **2014**: p. 6.
 43. van Popele, N.M., Grobbee, D.E., Bots, M.L., Asmar, R., Topouchian, J., Reneman, R.S., Hoeks, A.P., van der Kuip, D.A., Hofman, A., and Witteman, J.C., *Association between arterial stiffness and atherosclerosis: the Rotterdam Study*. Stroke, 2001. **32(2)**: p. 454-60.
 44. Mattace-Raso, F.U., van der Cammen, T.J., Hofman, A., van Popele, N.M., Bos, M.L., Schalekamp, M.A., Asmar, R., Reneman, R.S., Hoeks, A.P., Breteler, M.M., and Witteman, J.C., *Arterial stiffness and risk of coronary heart disease and stroke: the Rotterdam Study*. Circulation, 2006. **113(5)**: p. 657-63.

45. Laurent, S., Boutouyrie, P., Asmar, R., Gautier, I., Laloux, B., Guize, L., Ducimetiere, P., and Benetos, A., *Aortic stiffness is an independent predictor of all-cause and cardiovascular mortality in hypertensive patients*. Hypertension, 2001. **37**(5): p. 1236-41.
46. Laurent, S., Katsahian, S., Fassot, C., Tropeano, A.I., Gautier, I., Laloux, B., and Boutouyrie, P., *Aortic stiffness is an independent predictor of fatal stroke in essential hypertension*. Stroke, 2003. **34**(5): p. 1203-6.
47. Tsvigoulis, G., Vemmos, K., Papamichael, C., Spengos, K., Daffertshofer, M., Cimboneriu, A., Zis, V., Lekakis, J., Zakopoulos, N., and Mavrikakis, M., *Common carotid arterial stiffness and the risk of ischaemic stroke*. Eur J Neurol, 2006. **13**(5): p. 475-81.
48. Eigenbrodt, M.L., Bursac, Z., Rose, K.M., Couper, D.J., Tracy, R.E., Evans, G.W., Brancati, F.L., and Mehta, J.L., *Common carotid arterial interadventitial distance (diameter) as an indicator of the damaging effects of age and atherosclerosis, a cross-sectional study of the Atherosclerosis Risk in Community Cohort Limited Access Data (ARICLAD), 1987-89*. Cardiovasc Ultrasound, 2006. **4**: p. 1.
49. Nikic, P., Savic, M., Jakovljevic, V., and Djuric, D., *Carotid atherosclerosis, coronary atherosclerosis and carotid intima-media thickness in patients with ischemic cerebral disease: Is there any link?* Exp Clin Cardiol, 2006. **11**(2): p. 102-6.
50. Sharma, R.K., Donekal, S., Rosen, B.D., Tattersall, M.C., Volpe, G.J., Ambale-Venkatesh, B., Nasir, K., Wu, C.O., Polak, J.F., Korcarz, C.E., Stein, J.H., Carr, J., Watson, K.E., Bluemke, D.A., and Lima, J.A., *Association of subclinical atherosclerosis using carotid intima-media thickness, carotid plaque, and coronary calcium score with left ventricular dyssynchrony: The multi-ethnic Study of Atherosclerosis*. Atherosclerosis, 2015. **239**(2): p. 412-8.
51. Painsi, A., Boutouyrie, P., Calvet, D., Zidi, M., Agabiti-Rosei, E., and Laurent, S., *Multi-axial mechanical characteristics of carotid plaque: analysis by multiarray echotracking system*. Stroke, 2007. **38**(1): p. 117-23.
52. Luo, J., Li, R.X., and Konofagou, E.E., *Pulse wave imaging of the human carotid artery: an in vivo feasibility study*. IEEE Trans Ultrason Ferroelectr Freq Control, 2012. **59**(1): p. 174-81.
53. Couade, M., Pernot, M., Prada, C., Messas, E., Emmerich, J., Bruneval, P., Criton, A., Fink, M., and Tanter, M., *Quantitative assessment of arterial wall biomechanical properties using shear wave imaging*. Ultrasound Med Biol, 2010. **36**(10): p. 1662-76.
54. Ramnarine, K.V., Garrard, J.W., Kanber, B., Nduwayo, S., Hartshorne, T.C., and Robinson, T.G., *Shear wave elastography imaging of carotid plaques: feasible, reproducible and of clinical potential*. Cardiovasc Ultrasound, 2014. **12**: p. 49.
55. Noritomi, T., Sigel, B., Swami, V., Justin, J., Gahtan, V., Chen, X., Feleppa, E.J., Roberts, A.B., and Shirouzu, K., *Carotid plaque typing by multiple-parameter*

- ultrasonic tissue characterization*. *Ultrasound Med Biol*, 1997. **23**(5): p. 643-50.
56. Ophir, J., Cespedes, I., Ponnekanti, H., Yazdi, Y., and Li, X., *Elastography: a quantitative method for imaging the elasticity of biological tissues*. *Ultrason Imaging*, 1991. **13**(2): p. 111-34.
 57. Varghese, T., *Quasi-Static Ultrasound Elastography*. *Ultrasound Clin*, 2009. **4**(3): p. 323-338.
 58. de Korte, C.L., van der Steen, A.F., Cespedes, E.I., and Pasterkamp, G., *Intravascular ultrasound elastography in human arteries: initial experience in vitro*. *Ultrasound Med Biol*, 1998. **24**(3): p. 401-8.
 59. de Korte, C.L., Pasterkamp, G., van der Steen, A.F., Woutman, H.A., and Bom, N., *Characterization of plaque components with intravascular ultrasound elastography in human femoral and coronary arteries in vitro*. *Circulation*, 2000. **102**(6): p. 617-23.
 60. de Korte, C.L., van der Steen, A.F., Cepedes, E.I., Pasterkamp, G., Carlier, S.G., Mastik, F., Schoneveld, A.H., Serruys, P.W., and Bom, N., *Characterization of plaque components and vulnerability with intravascular ultrasound elastography*. *Phys Med Biol*, 2000. **45**(6): p. 1465-75.
 61. de Korte, C.L. and van der Steen, A.F., *Intravascular ultrasound elastography: an overview*. *Ultrasonics*, 2002. **40**(1-8): p. 859-65.
 62. Schaar, J.A., De Korte, C.L., Mastik, F., Strijder, C., Pasterkamp, G., Boersma, E., Serruys, P.W., and Van Der Steen, A.F., *Characterizing vulnerable plaque features with intravascular elastography*. *Circulation*, 2003. **108**(21): p. 2636-41.
 63. Maurice, R.L., Ohayon, J., Fretigny, Y., Bertrand, M., Soulez, G., and Cloutier, G., *Noninvasive vascular elastography: theoretical framework*. *IEEE Trans Med Imaging*, 2004. **23**(2): p. 164-80.
 64. Schmitt, C., Soulez, G., Maurice, R.L., Giroux, M.F., and Cloutier, G., *Noninvasive vascular elastography: toward a complementary characterization tool of atherosclerosis in carotid arteries*. *Ultrasound Med Biol*, 2007. **33**(12): p. 1841-58.
 65. Maurice, R.L., Daronat, M., Ohayon, J., Stoyanova, E., Foster, F.S., and Cloutier, G., *Non-invasive high-frequency vascular ultrasound elastography*. *Phys Med Biol*, 2005. **50**(7): p. 1611-28.
 66. Maurice, R.L., Soulez, G., Giroux, M.F., and Cloutier, G., *Noninvasive vascular elastography for carotid artery characterization on subjects without previous history of atherosclerosis*. *Med Phys*, 2008. **35**(8): p. 3436-43.
 67. Ribbers, H., Lopata, R.G., Holewijn, S., Pasterkamp, G., Blankensteijn, J.D., and de Korte, C.L., *Noninvasive two-dimensional strain imaging of arteries: validation in phantoms and preliminary experience in carotid arteries in vivo*. *Ultrasound Med Biol*, 2007. **33**(4): p. 530-40.
 68. Hansen, H.H., Lopata, R.G., and de Korte, C.L., *Noninvasive carotid strain imaging using angular compounding at large beam steered angles: validation in*

- vessel phantoms*. IEEE Trans Med Imaging, 2009. **28**(6): p. 872-80.
69. Hansen, H.H., Lopata, R.G., Idzenga, T., and de Korte, C.L., *An angular compounding technique using displacement projection for noninvasive ultrasound strain imaging of vessel cross-sections*. Ultrasound Med Biol, 2010. **36**(11): p. 1947-56.
 70. Idzenga, T., Holewijn, S., Hansen, H.H., and de Korte, C.L., *Estimating cyclic shear strain in the common carotid artery using radiofrequency ultrasound*. Ultrasound Med Biol, 2012. **38**(12): p. 2229-37.
 71. Shi, H., Mitchell, C.C., McCormick, M., Kliewer, M.A., Dempsey, R.J., and Varghese, T., *Preliminary in vivo atherosclerotic carotid plaque characterization using the accumulated axial strain and relative lateral shift strain indices*. Phys Med Biol, 2008. **53**(22): p. 6377-94.
 72. Shi, H. and Varghese, T., *Two-dimensional multi-level strain estimation for discontinuous tissue*. Phys Med Biol, 2007. **52**(2): p. 389-401.
 73. McCormick, M., Rubert, N., and Varghese, T., *Bayesian regularization applied to ultrasound strain imaging*. IEEE Trans Biomed Eng, 2011. **58**(6): p. 1612-20.
 74. McCormick, M., Varghese, T., Wang, X., Mitchell, C., Kliewer, M.A., and Dempsey, R.J., *Methods for robust in vivo strain estimation in the carotid artery*. Phys Med Biol, 2012. **57**(22): p. 7329-53.
 75. Wan, J.J., He, F.L., Zhao, Y.F., Zhang, H.M., Zhou, X.D., and Wan, M.X., *Non-Invasive Vascular Radial/Circumferential Strain Imaging and Wall Shear Rate Estimation Using Video Images of Diagnostic Ultrasound*. Ultrasound in Medicine and Biology, 2014. **40**(3): p. 622-636.
 76. Majdoulina, Y., Ohayon, J., Keshavarz-Motamed, Z., Roy Cardinal, M.H., Garcia, D., Allard, L., Lerouge, S., Arsenault, F., Soulez, G., and Cloutier, G., *Endovascular shear strain elastography for the detection and characterization of the severity of atherosclerotic plaques: in vitro validation and in vivo evaluation*. Ultrasound Med Biol, 2014. **40**(5): p. 890-903.
 77. Mercure, E., Destrempe, F., Roy Cardinal, M.H., Poree, J., Soulez, G., Ohayon, J., and Cloutier, G., *A local angle compensation method based on kinematics constraints for non-invasive vascular axial strain computations on human carotid arteries*. Comput Med Imaging Graph, 2014. **38**(2): p. 123-36.
 78. Naim, C., Cloutier, G., Mercure, E., Destrempe, F., Qin, Z., El-Abyad, W., Lanthier, S., Giroux, M.F., and Soulez, G., *Characterisation of carotid plaques with ultrasound elastography: feasibility and correlation with high-resolution magnetic resonance imaging*. Eur Radiol, 2013. **23**(7): p. 2030-41.
 79. Liu, F., Yong, Q., Zhang, Q., Liu, P., and Yang, Y., *Real-time tissue elastography for the detection of vulnerable carotid plaques in patients undergoing endarterectomy: a pilot study*. Ultrasound Med Biol, 2015. **41**(3): p. 705-12.
 80. Widman, E., Caidahl, K., Heyde, B., D'Hooge, J., and Larsson, M., *Ultrasound speckle tracking strain estimation of in vivo carotid artery plaque with in vitro*

- sonomicrometry validation*. *Ultrasound Med Biol*, 2015. **41**(1): p. 77-88.
81. Wang, X., Jackson, D.C., Varghese, T., Mitchell, C.C., Hermann, B.P., Kliewer, M.A., and Dempsey, R.J., *Correlation of cognitive function with ultrasound strain indices in carotid plaque*. *Ultrasound Med Biol*, 2014. **40**(1): p. 78-89.
 82. Kim, K., Huang, S.W., Hall, T.L., Witte, R.S., Chenevert, T.L., and O'Donnell, M., *Arterial vulnerable plaque characterization using ultrasound-induced thermal strain imaging (TSI)*. *IEEE Trans Biomed Eng*, 2008. **55**(1): p. 171-80.
 83. Doherty, J.R., Dumont, D.M., Trahey, G.E., and Palmeri, M.L., *Acoustic radiation force impulse imaging of vulnerable plaques: a finite element method parametric analysis*. *J Biomech*, 2013. **46**(1): p. 83-90.
 84. Korukonda, S., Nayak, R., Carson, N., Schifitto, G., Dogra, V., and Doyley, M.M., *Noninvasive vascular elastography using plane-wave and sparse-array imaging*. *IEEE Trans Ultrason Ferroelectr Freq Control*, 2013. **60**(2): p. 332-42.
 85. Hansen, H.H.G., Saris, A.E.C.M., Vaka, N.R., Nillesen, M.M., and de Korte, C.L., *Ultrafast vascular strain compounding using plane wave transmission*. *Journal of Biomechanics*, 2014. **47**(4): p. 815-823.
 86. Seeger, J.M. and Klingman, N., *The relationship between carotid plaque composition and neurologic symptoms*. *J Surg Res*, 1987. **43**(1): p. 78-85.
 87. Barzilai, B., Saffitz, J.E., Miller, J.G., and Sobel, B.E., *Quantitative ultrasonic characterization of the nature of atherosclerotic plaques in human aorta*. *Circ Res*, 1987. **60**(3): p. 459-63.
 88. Lee, D.J., Sigel, B., Swami, V.K., Justin, J.R., Gahtan, V., O'Brien, S.P., Dwyer-Joyce, L., Feleppa, E.J., Roberts, A.B., and Berkowitz, H.D., *Determination of carotid plaque risk by ultrasonic tissue characterization*. *Ultrasound Med Biol*, 1998. **24**(9): p. 1291-9.
 89. Picano, E., Landini, L., Distanto, A., Benassi, A., Sarnelli, R., and L'Abbate, A., *Fibrosis, lipids, and calcium in human atherosclerotic plaque. In vitro differentiation from normal aortic walls by ultrasonic attenuation*. *Circ Res*, 1985. **56**(4): p. 556-62.
 90. Wilson, L.S., Neale, M.L., Talhami, H.E., and Appleberg, M., *Preliminary results from attenuation-slope mapping of plaque using intravascular ultrasound*. *Ultrasound Med Biol*, 1994. **20**(6): p. 529-42.
 91. Noritomi, T., Sigel, B., Gahtan, V., Swami, V., Justin, J., Feleppa, E., and Shirouzu, K., *In vivo detection of carotid plaque thrombus by ultrasonic tissue characterization*. *J Ultrasound Med*, 1997. **16**(2): p. 107-11.
 92. Bridal, S.L., Fornes, P., Bruneval, P., and Berger, G., *Parametric (integrated backscatter and attenuation) images constructed using backscattered radio frequency signals (25-56 MHz) from human aortae in vitro*. *Ultrasound Med Biol*, 1997. **23**(2): p. 215-29.
 93. Bridal, S.L., Fornes, P., Bruneval, P., and Berger, G., *Correlation of ultrasonic attenuation (30 to 50 MHz and constituents of atherosclerotic plaque*. *Ultrasound*

- Med Biol, 1997. **23**(5): p. 691-703.
94. Bridal, S.L., Beyssen, B., Fornes, P., Julia, P., and Berger, G., *Multiparametric attenuation and backscatter images for characterization of carotid plaque*. *Ultrason Imaging*, 2000. **22**(1): p. 20-34.
 95. Nair, A., Kuban, B.D., Obuchowski, N., and Vince, D.G., *Assessing spectral algorithms to predict atherosclerotic plaque composition with normalized and raw intravascular ultrasound data*. *Ultrason Med Biol*, 2001. **27**(10): p. 1319-31.
 96. Nair, A., Kuban, B.D., Tuzcu, E.M., Schoenhagen, P., Nissen, S.E., and Vince, D.G., *Coronary plaque classification with intravascular ultrasound radiofrequency data analysis*. *Circulation*, 2002. **106**(17): p. 2200-6.
 97. Nair, A., Calvetti, D., and Vince, D.G., *Regularized autoregressive analysis of intravascular ultrasound backscatter: improvement in spatial accuracy of tissue maps*. *IEEE Trans Ultrason Ferroelectr Freq Control*, 2004. **51**(4): p. 420-31.
 98. Roth, S.L., Hastings, H.M., Evans, S.J., Esposito, M., Gladstone, C., Rathod, S., and Bodenheimer, M.M., *Spectral analysis of demodulated ultrasound returns: detection of scatterer periodicity and application to tissue classification*. *Ultrason Imaging*, 1997. **19**(4): p. 266-77.
 99. Shi, H., Varghese, T., Dempsey, R.J., Salamat, M.S., and Zagzebski, J.A., *Relationship between ultrasonic attenuation, size and axial strain parameters for ex vivo atherosclerotic carotid plaque*. *Ultrason Med Biol*, 2008. **34**(10): p. 1666-77.
 100. Shi, H., Varghese, T., Mitchell, C.C., McCormick, M., Dempsey, R.J., and Kliewer, M.A., *In vivo attenuation and equivalent scatterer size parameters for atherosclerotic carotid plaque: preliminary results*. *Ultrasonics*, 2009. **49**(8): p. 779-85.
 101. Spencer, M.P., Thomas, G.I., Nicholls, S.C., and Sauvage, L.R., *Detection of middle cerebral artery emboli during carotid endarterectomy using transcranial Doppler ultrasonography*. *Stroke*, 1990. **21**(3): p. 415-23.
 102. Droste, D.W. and Ringelstein, E.B., *Detection of high intensity transient signals (HITS): how and why?* *Eur J Ultrasound*, 1998. **7**(1): p. 23-9.
 103. Dittrich, R., Ritter, M.A., and Droste, D.W., *Microembolus detection by transcranial doppler sonography*. *Eur J Ultrasound*, 2002. **16**(1-2): p. 21-30.
 104. *Basic identification criteria of Doppler microembolic signals. Consensus Committee of the Ninth International Cerebral Hemodynamic Symposium*. *Stroke*, 1995. **26**(6): p. 1123.
 105. Zuromskis, T., Wetterholm, R., Lindqvist, J.F., Svedlund, S., Sixt, C., Jatuzis, D., Obelieniene, D., Caidahl, K., and Volkmann, R., *Prevalence of micro-emboli in symptomatic high grade carotid artery disease: a transcranial Doppler study*. *Eur J Vasc Endovasc Surg*, 2008. **35**(5): p. 534-40.
 106. Telman, G., Kouperberg, E., Hlebtovsky, A., Sprecher, E., Hoffman, A., and

- Beyar, R., *Determinants of micro-embolic signals in patients with atherosclerotic plaques of the internal carotid artery*. Eur J Vasc Endovasc Surg, 2009. **38**(2): p. 143-7.
107. Hermeling, E., Reesink, K.D., Reneman, R.S., and Hoeks, A.P., *Measurement of local pulse wave velocity: effects of signal processing on precision*. Ultrasound Med Biol, 2007. **33**(5): p. 774-81.
 108. Calabia, J., Torguet, P., Garcia, M., Garcia, I., Martin, N., Guasch, B., Faur, D., and Valles, M., *Doppler ultrasound in the measurement of pulse wave velocity: agreement with the Complior method*. Cardiovasc Ultrasound, 2011. **9**: p. 13.
 109. Xu, J., *Do we need a better approach for measuring pulse-wave velocity?* Ultrasound Med Biol, 2003. **29**(9): p. 1373.
 110. Bock, M., Schad, L.R., Muller, E., and Lorenz, W.J., *Pulsed-wave velocity measurement using a new real-time MR-method*. Magn Reson Imaging, 1995. **13**(1): p. 21-9.
 111. Taviani, V., Hickson, S.S., Hardy, C.J., McEniery, C.M., Patterson, A.J., Gillard, J.H., Wilkinson, I.B., and Graves, M.J., *Age-related changes of regional pulse wave velocity in the descending aorta using Fourier velocity encoded M-mode*. Magn Reson Med, 2011. **65**(1): p. 261-8.
 112. Couade, M., Pernot, M., Messas, E., Emmerich, J., Hagege, A., Fink, M., and Tanter, M., *Ultrafast imaging of the arterial pulse wave*. Irbm, 2011. **32**(2): p. 106-108.
 113. Hasegawa, H., Hongo, K., and Kanai, H., *Measurement of regional pulse wave velocity using very high frame rate ultrasound*. Journal of Medical Ultrasonics, 2013. **40**(2): p. 91-98.
 114. Nagaoka, R., Masuno, G., Kobayashi, K., Yoshizawa, S., Umemura, S., and Saijo, Y., *Measurement of regional pulse-wave velocity using spatial compound imaging of the common carotid artery in vivo*. Ultrasonics, 2015. **55**: p. 92-103.
 115. Nightingale, K., McAleavey, S., and Trahey, G., *Shear-wave generation using acoustic radiation force: in vivo and ex vivo results*. Ultrasound Med Biol, 2003. **29**(12): p. 1715-23.
 116. Nightingale, K., Soo, M.S., Nightingale, R., and Trahey, G., *Acoustic radiation force impulse imaging: in vivo demonstration of clinical feasibility*. Ultrasound Med Biol, 2002. **28**(2): p. 227-35.
 117. Dumont, D.M., Doherty, J.R., and Trahey, G.E., *Noninvasive assessment of wall-shear rate and vascular elasticity using combined ARFI/SWEI/spectral Doppler imaging system*. Ultrason Imaging, 2011. **33**(3): p. 165-88.
 118. Behler, R.H., Nichols, T.C., Merricks, E.P., and Gallippi, C.M. *Reflected shear wave imaging of atherosclerosis*. in *Ultrasonics Symposium (IUS), 2009 IEEE International*. 2009: IEEE.
 119. Deffieux, T., Gennisson, J.L., Bercoff, J., and Tanter, M., *On the effects of reflected waves in transient shear wave elastography*. IEEE Trans Ultrason

- Ferroelectr Freq Control, 2011. **58**(10): p. 2032-5.
120. Sarvazyan, A.P., Rudenko, O.V., Swanson, S.D., Fowlkes, J.B., and Emelianov, S.Y., *Shear wave elasticity imaging: a new ultrasonic technology of medical diagnostics*. Ultrasound Med Biol, 1998. **24**(9): p. 1419-35.

Chapter 3 : Correlation of Ultrasound Strain Indices with Cognitive Function Assessed using RBANS

3.1 Introduction

In this chapter¹, a hierarchical block-matching based motion tracking algorithm developed in our laboratory [1] is utilized to evaluate the distribution and variation of axial, lateral and shear strains indices estimated from noninvasive *in vivo* scans of carotid plaque. We focus on the correlation between multiple strain indices and cognitive function measured by Repeatable Battery for the Assessment of Neuropsychological Status (RBANS).

Plaque instability may lead to chronic embolization, which may contribute to progressive cognitive decline in patients. Accumulated strain tensor indices over a cardiac cycle within a pulsating carotid plaque may become a viable biomarker for the diagnosis of plaque instability. Increased axial and lateral deformation and strain in plaque [2] has been shown to correlate with cognitive changes [3-4], suggesting that it is important to identify patients with unstable or vulnerable plaques to help prevent future silent strokes and cognitive impairment. However, we found no significant correlation of

¹This chapter is adapted from Wang, X., Jackson, D.C., Varghese, T., Mitchell, C.C., Hermann, B.P., Kliewer, M.A., and Dempsey, R.J., *Correlation of cognitive function with ultrasound strain indices in carotid plaque*. *Ultrasound Med Biol*, 2014. **40**(1): p. 78-89.

Wang, X., Mitchell, C.C., Varghese, T., Jackson, D.C., Rocque, B.G., Hermann, B.P., and Dempsey, R.J., *Improved Correlation of Strain Indices with Cognitive Dysfunction with Inclusion of Adventitia Layer with Carotid Plaque*. *Ultrasonic Imaging*, doi:10.1177/0161734615589252.

shear strain indices with cognitive function if the strain was measured as an average over the entire plaque sample [4]. Since shear stress may develop at the interface between different tissue constituents with different stiffness inside the plaque [5], shear strain may be an important indicator in the pathogenesis of plaque rupture [6]. It has been previously reported that the shear strain in the adventitia of the common carotid artery presents with a cyclic behavior, induced by the pulsating blood pressure [7]. Other studies have shown that the intima-media layer in the vessel wall may have longitudinal movements introducing shear strain in the adventitia [8]. We have also shown previously that high strain values are observed at the plaque-adventitia interface during lateral motion in a human carotid artery [1-2].

Inclusion of the adventitial layer focuses our strain or instability measures on the plaque vessel wall interface hypothesized to be a region with increased shearing forces and measureable instability. Accumulated axial, lateral, and shear strain distribution in plaques identified with the plaque-with- adventitia segmentation was also estimated and correlated to RBANS scores. We compare the strain indices obtained with the inclusion of the adventitial layer and their correlations to cognitive function in human subjects to our results obtained with plaque only.

3.2 Materials and Methods

3.2.1 Data acquisition

Ultrasound imaging was performed on 24 patients, scheduled for a carotid endarterectomy procedure (CEA), and presented with significant plaque. Patients provided informed consent using a protocol approved by the University of Wisconsin-

Madison Institutional Review Board (IRB) prior to the ultrasound and strain imaging study. The patients ranged in age from 44 to 79, with a mean and standard deviation (SD) of 65.88 ± 8.74 respectively. These patients then underwent CEA at the University of Wisconsin-Madison Hospitals and Clinics. Additional details on the patients and the different measurements are presented in Table 3.1.

Clinical Classification	Subject Num	Sex	Age	BMI	Plaque Dimension (mm ²)	Total RBANS Score	Max Axial Strain	Max Lateral Strain	Max Shear Strain
Symptomatic	1	F	79	18.1	36.67	82	16	13.59	16.45
	2	M	72	28.5	28.95	63	28	20.90	34.96
	3	M	72	36.5	148.62	72	26	15.72	21.58
	4	F	72	28	28.81	68	11.2	12.92	32.22
	5	M	71	29	39.29	72	15.6	22.19	13.97
	6	M	57	29.5	72.26	72	3.6	2.44	3.31
	7	M	66	27.3	78.86	83	30	14.68	13.88
	8	M	68	35	28.65	91	14.7	7.05	4.96
	9	M	63	27.3	25.34	88	18.6	14.09	32.46
	10	M	44	35.1	75.63	100	12.88	5.15	25.79
	11	M	62	29.6	14.59	116	4.45	3.09	8.41
	12	M	75	27.3	46.59	121	5.58	7.23	9.52
	13	M	75	30.8	120.97	100	7.21	4.84	13.02
	14	M	61	27.2	49.68	88	25.85	4.73	11.20
	15	M	49	28.3	100.85	78	20.68	16.54	30.11
	16	M	59	25.1	31.25	95	7.2	4.48	18.56
	Mean \pm SD		65.31 \pm 9.71	28.91 \pm 4.33	57.94 \pm 38.46	86.81 \pm 6.63	15.47 \pm 8.74	10.60 \pm 6.46	18.15 \pm 10.25
Asymptomatic	17	F	61	35.9	24.59	78	45	19.40	27.24
	18	F	74	27.1	27.95	86	11.3	9.76	15.21
	19	F	71	29.3	35.53	71	18.4	5.12	8.68
	20	F	59	N/A	33.85	85	19.83	7.99	16.39
	21	F	60	25.3	45.08	92	10.88	10.65	21.36
	22	M	63	26.9	83.32	81	23.11	25.20	34.26
	23	F	75	30.4	35.64	91	12.48	8.50	13.89
		Mean \pm SD		66.14 \pm 6.94	29.15 \pm 3.77	40.85 \pm 19.82	83.43 \pm 7.41	20.14 \pm 11.92	12.38 \pm 7.19
Questionable	24	M	73	32.8	29.76	89	17	20.25	29.43
All	Mean \pm SD		65.88 \pm 8.74	29.14 \pm 4.08	51.78 \pm 33.93	85.92 \pm 4.06	16.90 \pm 9.57	11.52 \pm 6.70	19.04 \pm 9.68

Table 3.1: Characteristics of the human subject population utilized in this study.

RF echo signal data, along with clinical B-mode images and color-flow Doppler images, were acquired using a Siemens Antares ultrasound system (Siemens Ultrasound, Mountain View, CA, USA) equipped with a VFX 13-5 linear transducer. The transmit frequency of the transducer was set to 11.4 MHz with a single transmit focus set at the depth of plaque. The total depth of the B-mode image was 4 cm, and 508 A-lines in the lateral direction, with a total lateral width of 38 mm was acquired. RF data was digitized at a 40 MHz sampling frequency. At least two cardiac cycles of RF data were obtained.

Plaque regions were segmented by a radiologist at end-diastole using the Medical Imaging Interaction Toolkit (MITK). Two complete cardiac cycles were chosen, with plaque segmentation performed on the three end-diastolic frames. The plaque regions were segmented on B-mode images constructed from RF data, as shown in Figure 3.1. Clinical B-mode and color-flow Doppler images were also used by the radiologist to better define plaque borders. The plaque dimension reported in Table 3.1 was measured by averaging the area of the segmented region over the three end-diastolic frames.

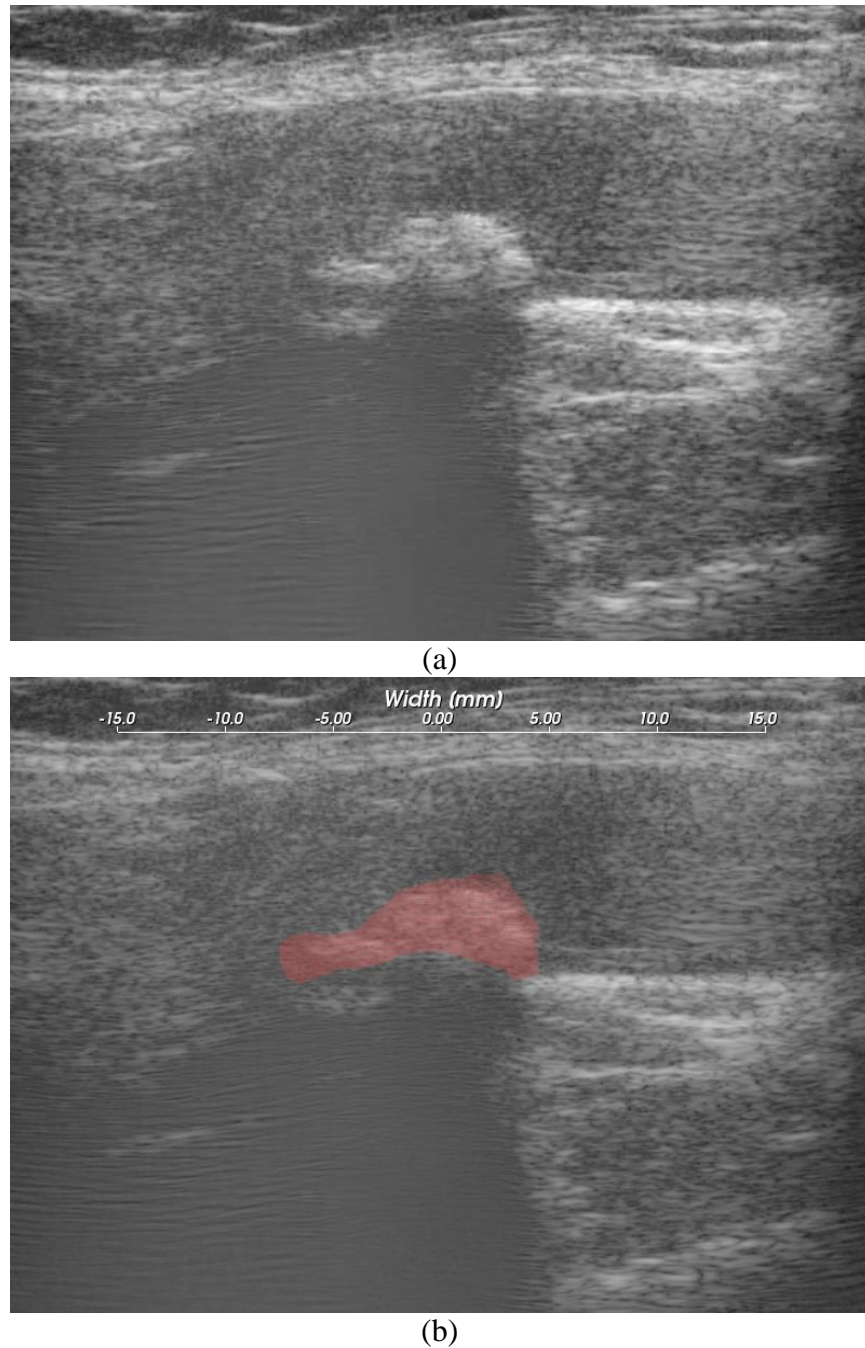


Figure 3.1: B-mode image (a) and segmented plaque on B-mode image (b).

3.2.2 Estimation of strain indices

A hierarchical block-matching based motion tracking algorithm developed in our laboratory [1], was utilized. Block matching between pre- and post-deformation frames

was performed using a hierarchical framework and normalized cross-correlation analysis performed over three iterations [9]. The matching block was 15×28 pixels at the top level, and 10×18 pixels at the bottom level. There was no overlap between the blocks. Along the axial or beam direction one pixel represents 0.02 mm, while on the lateral direction one pixel represents 0.075 mm. A dynamic frame skip method was utilized to obtain high quality motion tracking with a short frame skip during systole and a longer frame skip during end diastole. Incremental local displacements were tracked, estimated and then filtered with a 3×3 pixel median filter to remove outliers. Local strain was then assessed by applying a least-squares gradient over a 3×3 pixel radius from displacement estimates accumulated over a cardiac cycle using the end-diastolic frame as the reference frame.

We utilized this approach to estimate the accumulated axial, lateral, and shear strain distribution in plaques identified within the imaging plane. Shear strain was defined by the expression $e_{xy} = \frac{1}{2} \left(\frac{\partial d_y}{\partial x} + \frac{\partial d_x}{\partial y} \right)$, where x and y represent the lateral and axial directions respectively [1]. Strain estimates were computed inside the segmented plaque and overlaid on the B-mode images. Displacement and strain between consecutive frames calculated by the block-matching motion tracking algorithm were relatively small since the frame rates used were no less than 27 fps. We present accumulated strain indices over a cardiac cycle to better characterize the elasticity of plaque tissue.

From the accumulated strain calculated in each subsequent frame, a small region of interest (ROI) in the plaque with maximum strain was found. We limited this area to be within a 10 - 20 data points range, around the center of the ROI. The maximum strain of the selected plaque ROI in each frame was then obtained by averaging the strain values in

this small ROI to reduce noise. The corresponding minimum and peak-to-peak strain indices in the same ROI were also computed, as was the mean strain over the entire plaque. From the mean strains over two cardiac cycles, we estimated the maximum, minimum and peak-to-peak strain indices over the entire plaque region. Strain indices were then correlated with RBANS Total scores using Pearson's correlation coefficients.

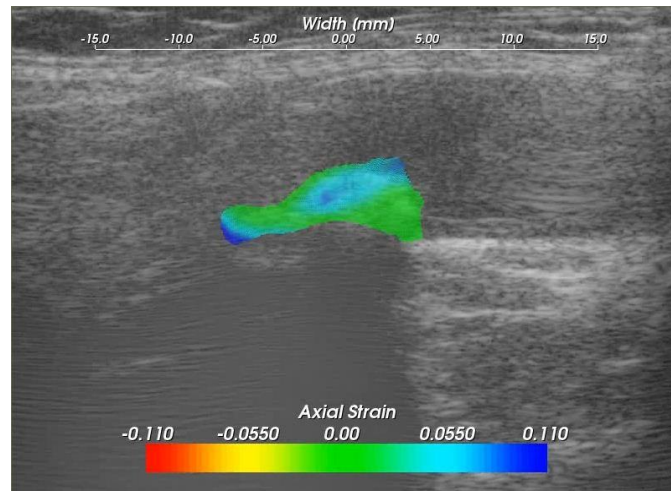
3.2.3 RBANS scores

The 24 patients were classified as symptomatic, asymptomatic or questionable based on clinical findings. A patient was classified as symptomatic if he or she presented with stroke or a transient ischemic attack (TIA), and was deemed asymptomatic otherwise. Carotid stenosis and indication for CEA for asymptomatic patients were based on other clinical symptoms or imaging studies performed; for example on patients presenting with cardiac conditions. Patients underwent objective cognitive assessment using a mental status screening measure (Repeatable Battery for the Assessment of Neuropsychological Status (RBANS)) which provides an index of overall cognitive status as well as five indices for specific cognitive abilities (Immediate Memory, Visuospatial/Constructional, Language, Attention, and Delayed Memory) [10]. All index scores are age-adjusted and normalized [11]. Plaque assessment using B-mode and strain imaging was conducted while blinded to the cognitive results. To reduce the number of comparisons only the total RBANS score was used to compare with all strain indices with a significance level of $p < 0.05$ using a *t*-test.

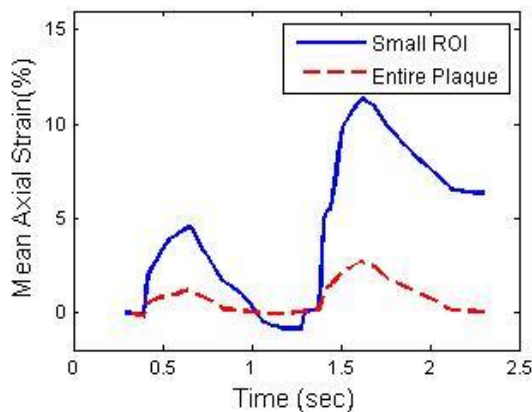
3.3 Results

3.3.1 Accumulated axial, lateral and shear strain over a cardiac cycle

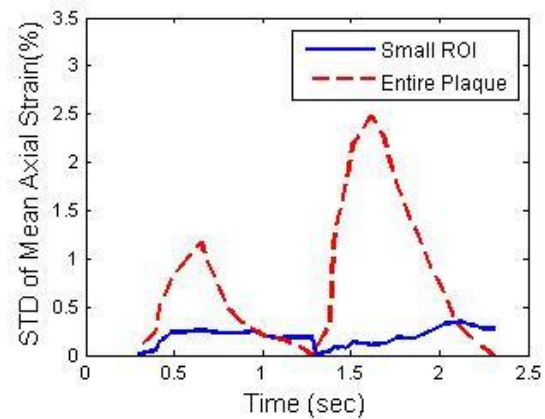
Figure 3.2 (a) shows a typical axial strain image for the plaque demarcated in Fig. 3.1. The axial strain magnitude and direction are depicted on the color bar overlaid on the gray-scale B-mode images. Axial strains were averaged in the small ROI and over the entire plaque, respectively. The mean axial strains and standard deviation (STD) are plotted in Fig. 3.2 (b) and (c). The strain curves depict the deformation over two cardiac cycles. The variation in the strain over the two cardiac cycles are not identical, as shown in Fig. 3.2 (b), because of the irregular and turbulent flow patterns caused by stenosis in the vessel due to the presence of plaque. Note that the mean axial strain computed over the entire plaque is significantly lower than that obtained within the small ROI. On the other hand, the STD over the entire plaque is significantly higher than that in the small ROI. This suggests that in this heterogeneous plaque, the axial strain estimate varies significantly. The maximum axial strain can get as high as 11%, but the mean peak axial strain is around 3%.



(a)



(b)



(c)

Figure 3.2: Axial strain values overlaid on the B-mode image (a). Mean values in the small ROI and entire plaque are shown in (b), and their standard deviations in (c).

In a similar manner, the variability in the lateral strain estimated in the same plaque is shown in Figure 3.3. The lateral strain presents with similar trends; in that it varies significantly inside the plaque so the mean value is much smaller, with a peak value of 2% compared to the maximum lateral strain of 9% in a small ROI, and the STD is also larger, as expected. The distribution of lateral strain inside the plaque suggests that the composition of plaque changes from region to region.

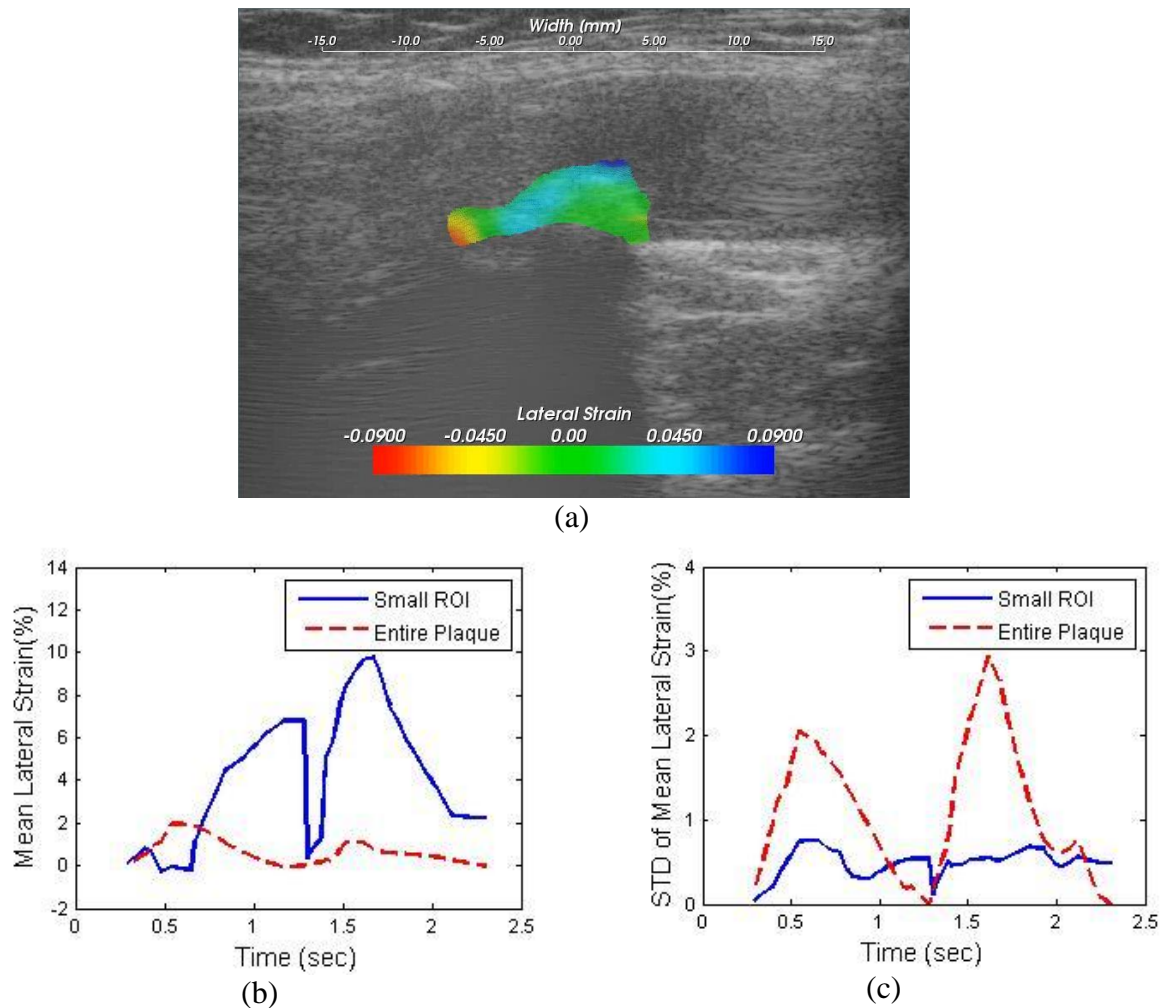


Figure 3.3: Lateral strain values overlaid on the B-mode image (a). Mean values in the small ROI and entire plaque are shown in (b), and their standard deviations in (c).

Finally the shear strain in the same plaque is shown in Figure 3.4. The mean shear strain of the entire plaque does not exhibit a cyclic behavior, when compared to axial and lateral strain estimates. The mean peak shear strain is only 1%, but the maximum shear strain in the ROI is around 15%. Observe that the variation in the shear strain is quite similar to that of the axial and lateral strain. The behaviors of the three strain indices indicate the variability in the strain estimates over different types of tissue within a single plaque. Since the mean strain in the small ROI has a lower standard deviation, we

consider the maximum strain averaged over the small ROI to be the maximum strain value within the entire plaque.

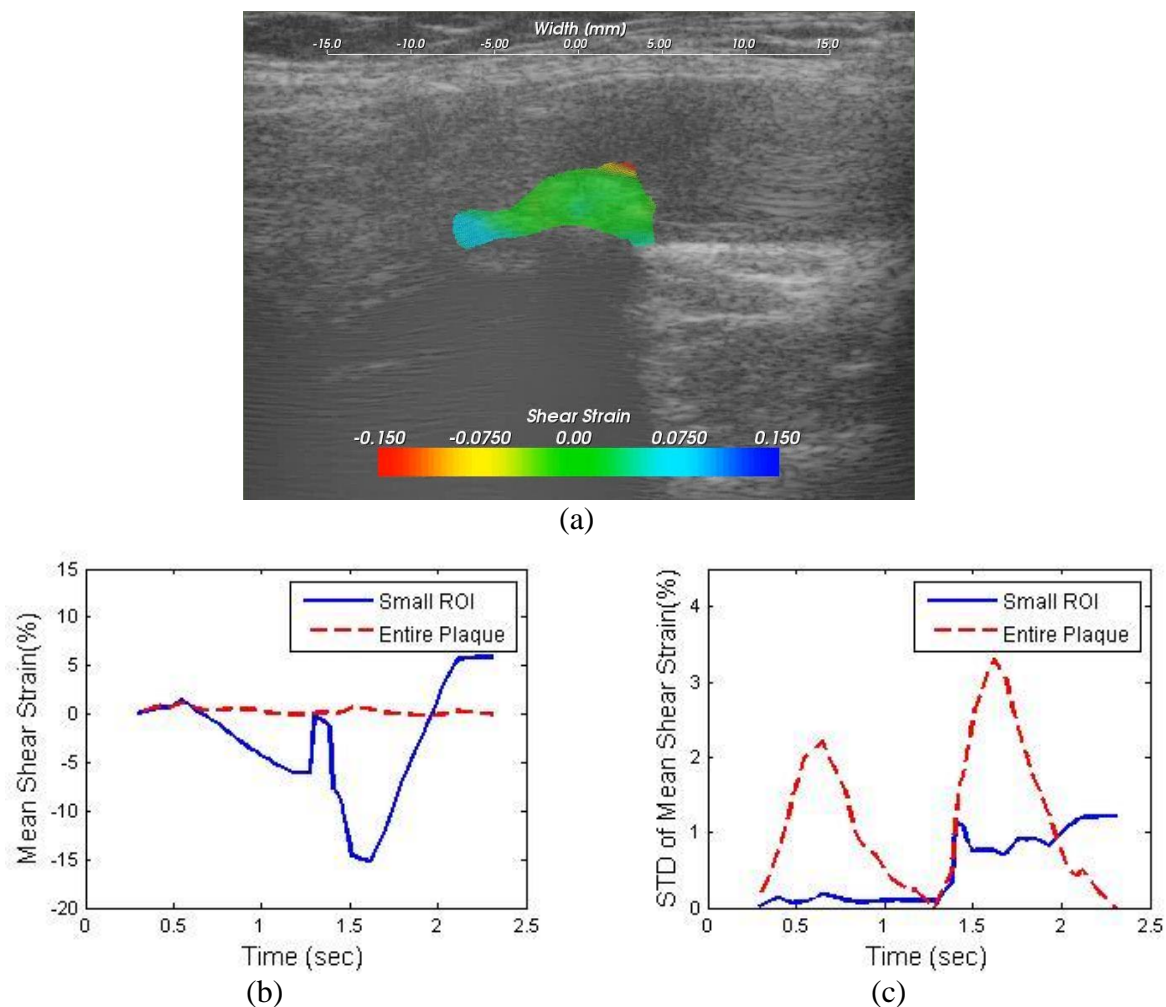


Figure 3.4: Shear strain values overlaid on the B-mode image (a). Mean values in the small ROI and entire plaque are shown in (b), and their standard deviations in (c).

3.3.2 Correlation with RBANS scores

The maximum, minimum and peak-to-peak strain indices over a small ROI with the largest deformation were then obtained from the mean strain value in the ROI. Figure 3.5 is a plot of total RBANS score versus axial strain indices. As indicated in Table 3.1, 16 out of 24 patients in this study were identified as symptomatic, 7 were asymptomatic and

1 was questionable. A linear fit was performed for symptomatic, asymptomatic and for all the patients respectively to show the correlation of the two variables. The strains shown in the plots are all scalar values; the maximum strain is always positive and the minimum strain is always negative. For better comparison, we use absolute value for the minimum axial strain values such all the indices are positive. The Pearson's coefficient (r) and the significance value (p) were also calculated for each correlation. Overall the total RBANS score appears lower with increasing strain indices. The maximum and peak-to-peak axial strain, also reveal correlation to the total RBANS score. The correlation or linear fit between the RBANS score for asymptomatic and symptomatic is improved for indices estimated within the ROI. However, the correlation of absolute minimum strain is weaker than the other two indices.

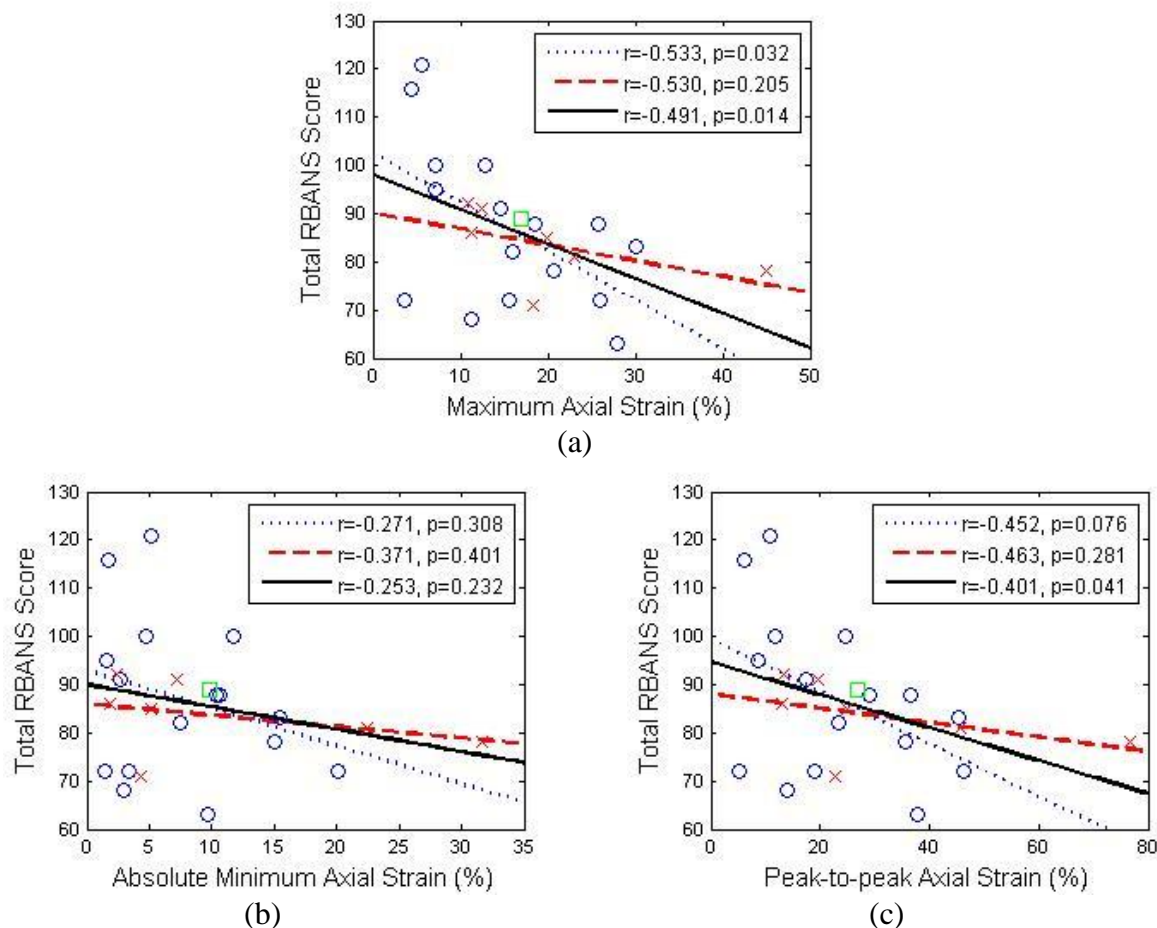


Figure 3.5: Linear least square fits of total RBANS score with maximum (a), absolute minimum (b), and peak-to-peak (c) axial strain averaged over the small ROI. \circ = Symptomatic, \times = asymptomatic, \square = questionable, the dotted line represents the linear fit for symptomatic, dashed line the linear fit for asymptomatic, and the solid line denotes the linear fit for all patients.

The association of RBANS Total score with the lateral strain indices is depicted in Figure 3.6 where a negative correlation between cognition and the strain indices is observed. The maximum and peak-to-peak lateral strain correlated significantly with cognition. Although the absolute minimum lateral strain shows a weaker correlation, it is not as weak as the absolute minimum axial strain. Note that the association between

cognition and strain is higher for strains within the ROI; however, we observe a decrease in the correlation with asymptomatic patients, along with a change in the correlation to a positive value.

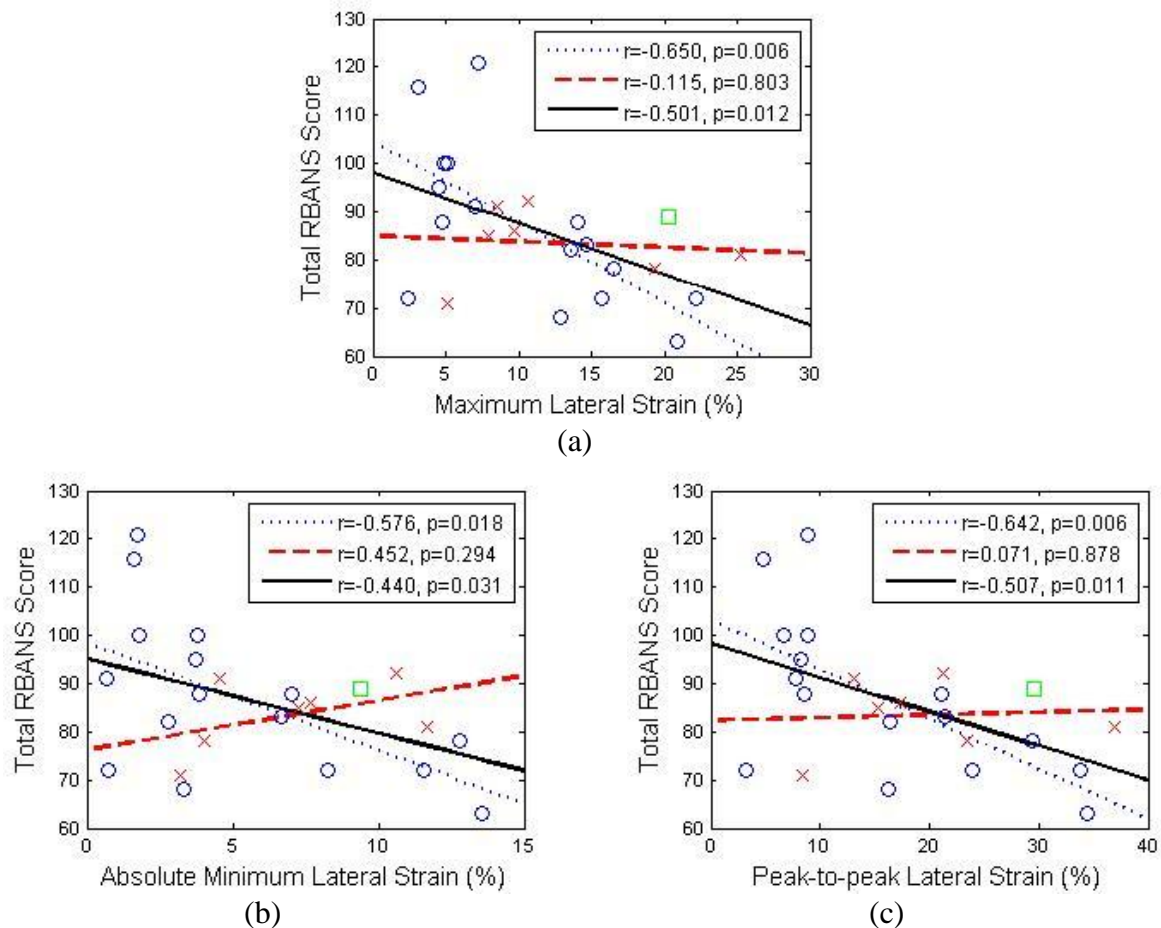


Figure 3.6: Linear least square fits of total RBANS score with maximum (a), absolute minimum (b), and peak-to-peak (c) lateral strain averaged over the small ROI. \circ = Symptomatic, \times = asymptomatic, \square = questionable, the dotted line represents the linear fit for symptomatic, dashed line the linear fit for asymptomatic, and the solid line denotes the linear fit for all patients.

Figure 3.7 demonstrates similar correlations with shear strain indices. Note that the correlation is much weaker for shear strain indices than the axial and lateral strain

indices. The absolute minimum shear strain reveals a positive correlation with RBANS Total score, as opposed to the negative correlations observed for the entire patient group for axial and lateral strain indices.

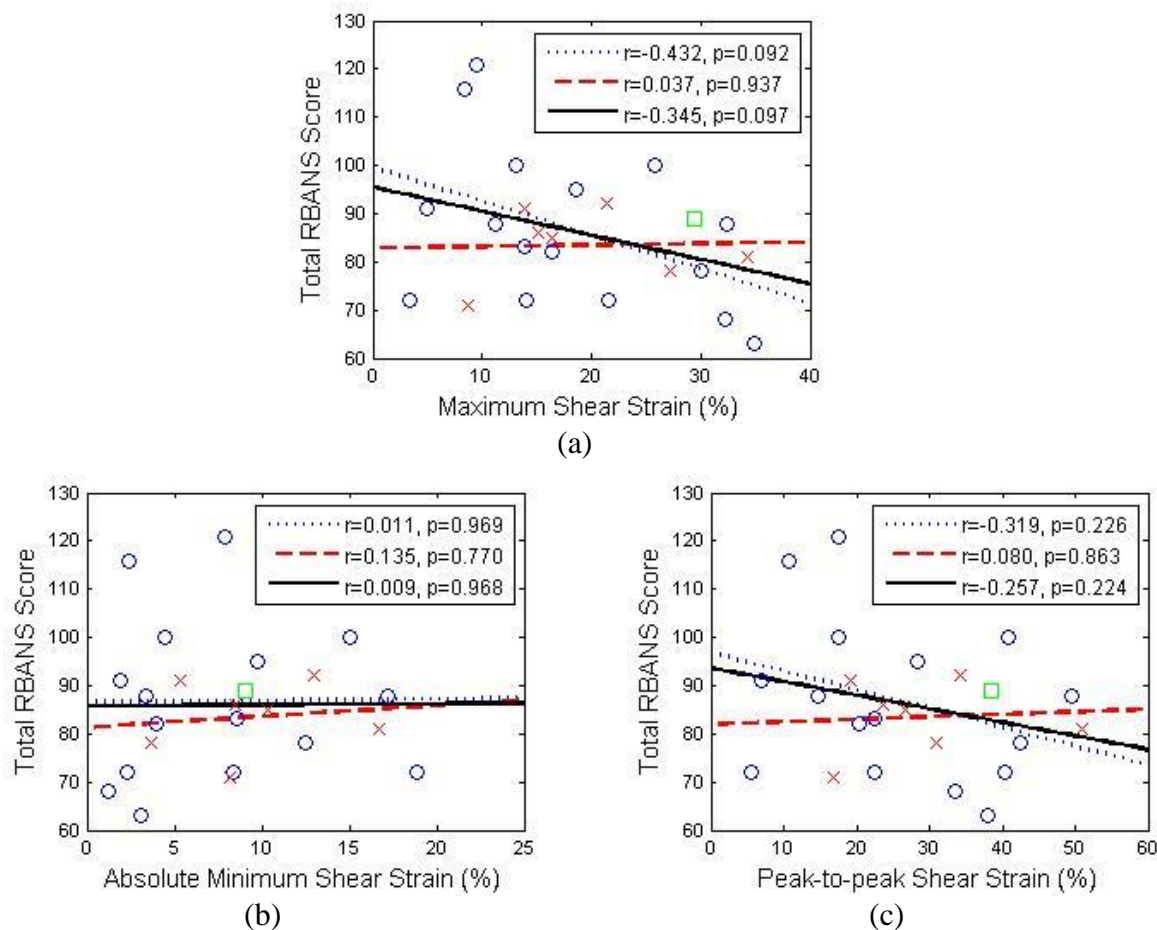


Figure 3.7: Linear least square fits of total RBANS score with maximum (a), absolute minimum (b), and peak-to-peak (c) shear strain averaged over the small ROI. \circ = Symptomatic, \times = asymptomatic, \square = questionable, the dotted line represents the linear fit for symptomatic, dashed line the linear fit for asymptomatic, and the solid line denotes the linear fit for all patients.

Observe from these plots that the correlation of the RBANS Total score to absolute minimum strain in the ROI is rather weak. Therefore only the maximum and peak-to-

peak mean strain over the entire plaque region was computed, in the rest of the plots. The linear correlation between RBANS Total score with maximum mean strain indices over the entire plaque is shown in Figure 3.8, while the peak-to-peak mean strain indices are shown in Figure 3.9. Note that when the strain estimates are averaged over the entire plaque region, the maximum and peak-to-peak axial strain shows only a weak correlation with RBANS Total score for all patients. Note that the linear fits for the symptomatic patients generally follow the trend, and dominates the results for the entire group of patients for the axial and shear strain indices. However, we do observe significant deviations between the symptomatic and asymptomatic patients for the linear fit for the lateral strain indices; but the correlation is rather weak.

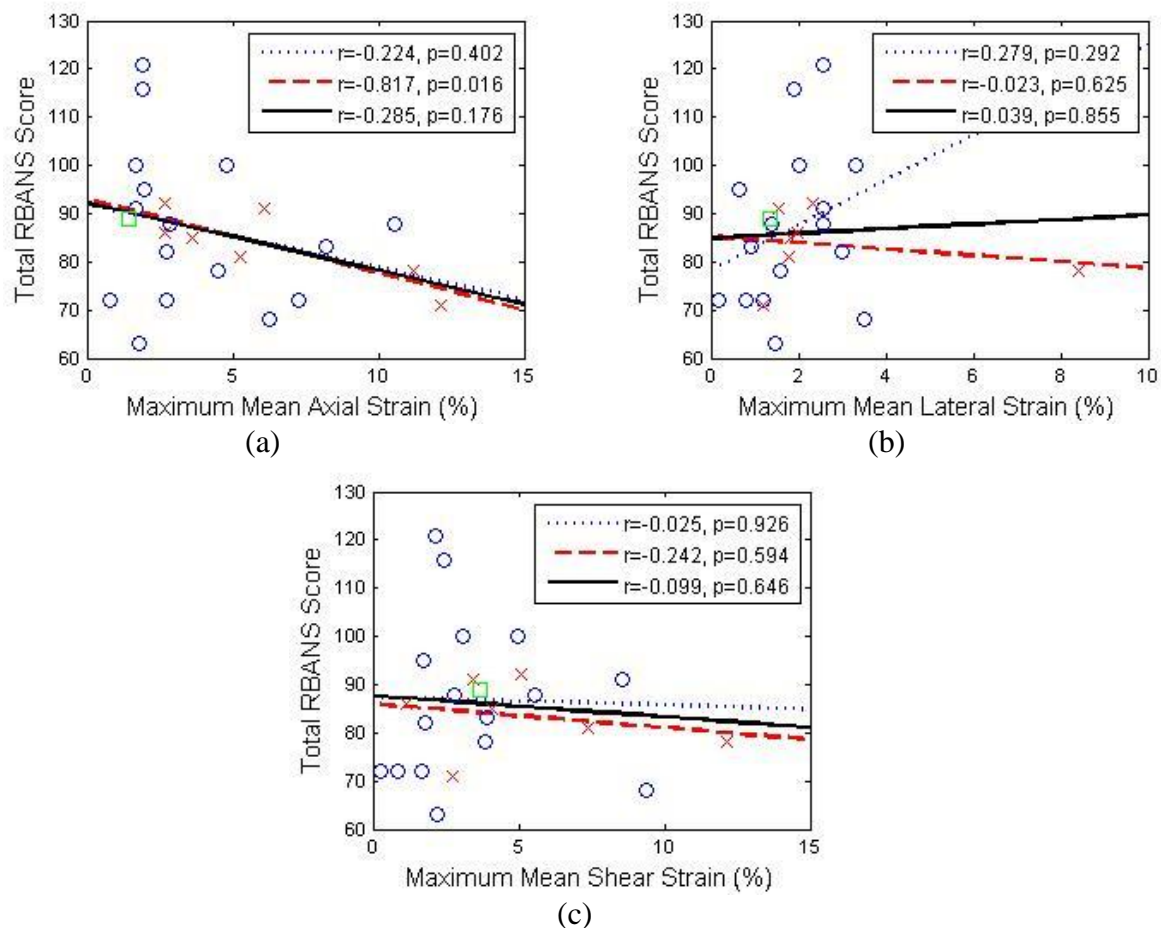


Figure 3.8: Linear least square fits of total RBANS score with the maximum axial (a), lateral (b) and shear (c) strain averaged over the entire plaque. \circ = Symptomatic, \times = asymptomatic, \square = questionable, the dotted line represents the linear fit for symptomatic, dashed line the linear fit for asymptomatic, and the solid line denotes the linear fit for all patients.

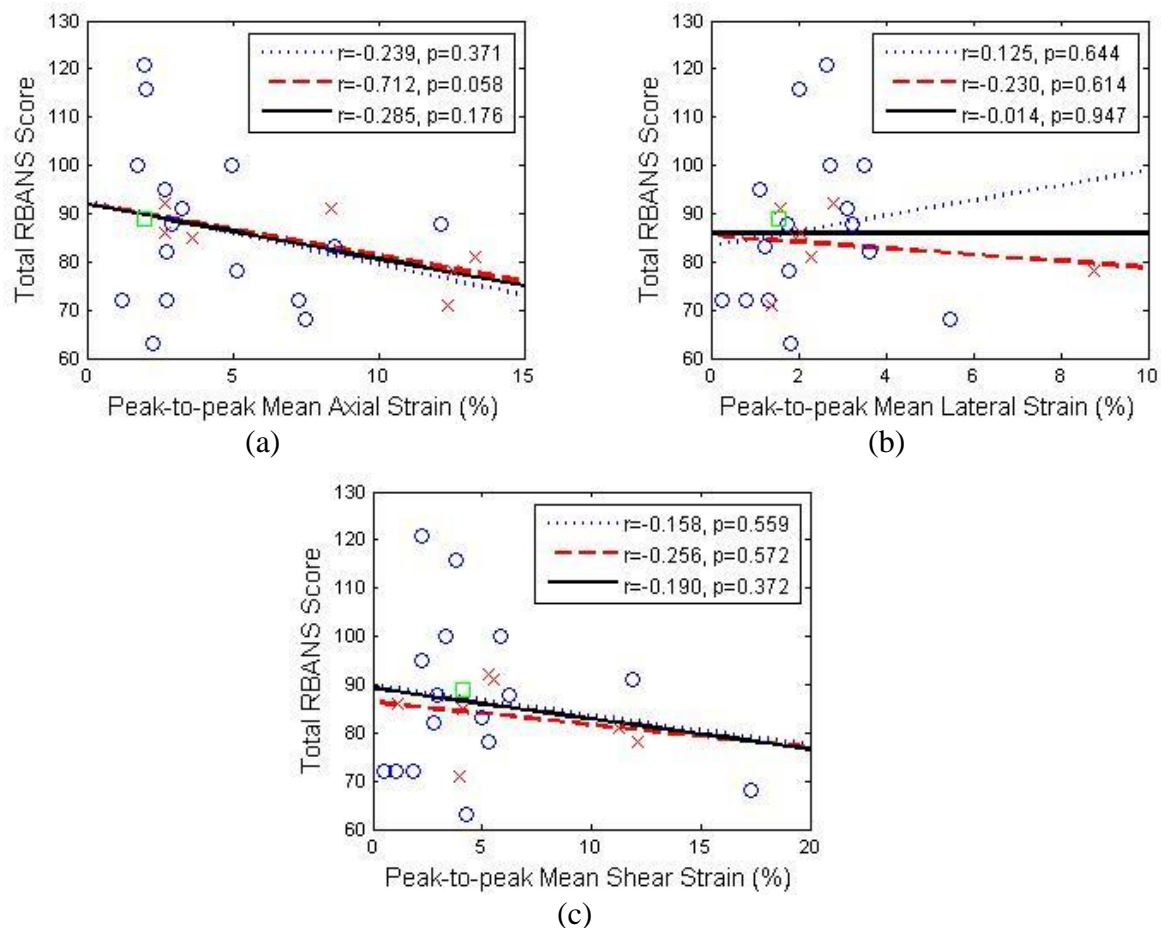


Figure 3.9: Linear least square fit of the total RBANS score with peak-to-peak axial (a), lateral (b) and shear (c) strain averaged over the entire plaque. \circ = Symptomatic, \times = asymptomatic, \square = questionable, the dotted line represents the linear fit for symptomatic, dashed line the linear fit for asymptomatic, and the solid line denotes the linear fit for all patients.

Overall, the mean strain indices for the 7 asymptomatic patients are slightly higher than that for the 16 symptomatic patients, and the mean RBANS score for the asymptomatic group is also lower than that for the symptomatic group. From the figures, we observe that there is no significant correlation between the RBANS Total score and strain indices averaged over the entire plaque region. However, the maximum and peak-

to-peak axial and lateral strains show some correlation with an r value around 0.5, and a significant p -value of less than 0.05. For the symptomatic group, the correlation for maximum and peak-to-peak strain indices is higher. However, the correlation for strain indices averaged over the entire plaque region is significantly higher for asymptomatic group.

3.4 Discussion

In this chapter we have shown that a relationship exists between cognitive function and the maximum and peak-to-peak axial and lateral strain indices. As the axial and lateral strain indices increase in plaque, there appears to be a corresponding poorer performance in the cognitive function for these patients. Since these strain indices primarily indicate the extent of deformation of plaque based on pulsatile flow in the carotid over the cardiac cycle, where larger deformations point to the presence of areas of softer plaques or variability in plaque composition over its length, larger deformations may therefore indicate an increased probability of plaque rupture in these softer plaques. Deformation of the carotid wall and plaque is caused by a combination of wall shear stress, wall tensile stress and cyclic force induced by the pulsatile blood pressure [12-15]. The buildup of plaque disrupts blood flow and results in hemodynamic changes such as high velocity jets that introduce shear stresses and turbulence which lead to blood pressure fluctuations over the length of the blood vessel [16-18]. Re-circulating flow, high shear stresses and increasing turbulence in turn can accelerate plaque rupture [19-23]. As a consequence of plaque rupture, micro-emboli or even emboli may flow into the brain and cause ischemic events leading to stroke or vascular dementia, which may result in or be accompanied by cognitive impairment. This study helps establish the relationship

between increasing strain indices in plaque and cognitive impairment through embolism.

Previous studies have shown that lateral strain estimation incurs more noise artifacts than axial strain because of the relative small dimensions of the plaque when compared to the lateral resolution of ultrasound system and their heterogeneous nature [2]. Shear strain may therefore include artifacts, since it is neither aligned, nor perpendicular to the ultrasound beam. This may explain the absence of a cyclic trend with the shear strain over a cardiac cycle. Axial strain indices overall provide the best correlation with RBANS Total score. Our improved algorithm allows for better tracking of the lateral deformation and thereby lateral strain estimation [1]. Lateral strain indices obtained using this algorithm, also show improved correlation with the RBANS Total score, although the correlation is not as good as that obtained using the axial strain indices as expected. The fact that lateral strain indices also show strong correlations with RBANS score especially for symptomatic patients indicate the utility of using lateral strains in this chapter.

Most plaques are heterogeneous and difficult to completely classify as either soft or calcified. Plaque stiffness variations, however, can be evaluated by the distribution of local axial and lateral strains within the plaque, from the estimated strain images. These stiffness variations suggest that regions with highest strains (maximum values) or deformations may tend to break off and detach from the rest of plaque. Due to heterogeneity, a plaque with lower mean strain values can still possess localized regions with very high strain, which may be prone to rupture. The lack of significant correlation between the total RBANS score with strain indices averaged over the entire plaque region, could therefore be due to local strain estimates from the small pockets of softer plaque embedded in large heterogeneous plaque regions, being averaged out over the

entire plaque.

Note that the correlation of maximum and peak-to-peak lateral strain to total RBANS score is much higher for symptomatic patients, but weaker for asymptomatic patients. The comparison of symptomatic and asymptomatic patients brings up a possible hypothesis, indicating that the rupture of carotid plaque for symptomatic patients may have already occurred with ongoing emboli, whereas for asymptomatic patients, the plaque is still intact. We hypothesize that ruptured plaque tend to have larger deformations in the lateral direction due to the possible fissures in plaque after rupture. On the other hand, for intact plaques, the fibrous cap may limit the lateral deformation of the entire plaque. However, lipidic regions within these plaques may break off and generate emboli eventually. This is consistent with our observation that asymptomatic patients have slightly higher axial than lateral strains within the plaque. Note the high correlation between RBANS Total score and axial strain indices averaged over the entire plaque region for asymptomatic patients, which are significantly higher. The RBANS correlation with the lateral strains indices for these patients are however significantly lower.

Since both symptomatic and asymptomatic patients were studied, the relationship between cognitive impairment and characterization of plaque may lead to further investigation of these patient groups. In addition to clinically recognized stroke, "silent" strokes may occur, and are five times more prevalent [24]. Silent strokes are not detected based on classical transient ischemic attack (TIA) symptoms and therefore difficult to prevent. It is likely that these "silent" strokes may be causing accumulated cognitive decline. Studies have suggested that silent stroke occurs with concurrent subclinical

emboli [25] and is better understood with cognitive impairment studies [26]. This is consistent with our study that some of the asymptomatic patients may have great potential of developing emboli. Thus ultrasound strain imaging may be a surrogate in the clinic to detect the potential risk of having a silent stroke.

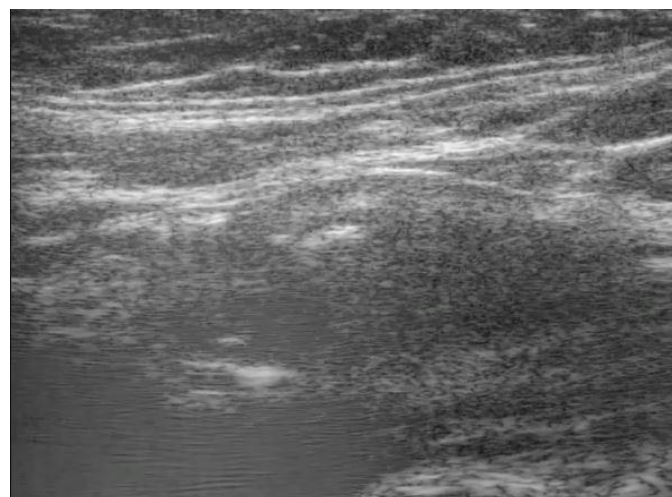
Despite the relationship described in this chapter, examination of a larger number of patients is required to further establish the correlation. Note that the correlation not being significant for the asymptomatic patients may also be due to the small sample size. In addition, the blood pressure for patients was not documented in this study. More detailed analysis of the different RBANS components may also be enlightening, for example, the correlation of each of the index scores in RBANS to the strain indices.

3.5 Improved correlation with inclusion of adventitia layer

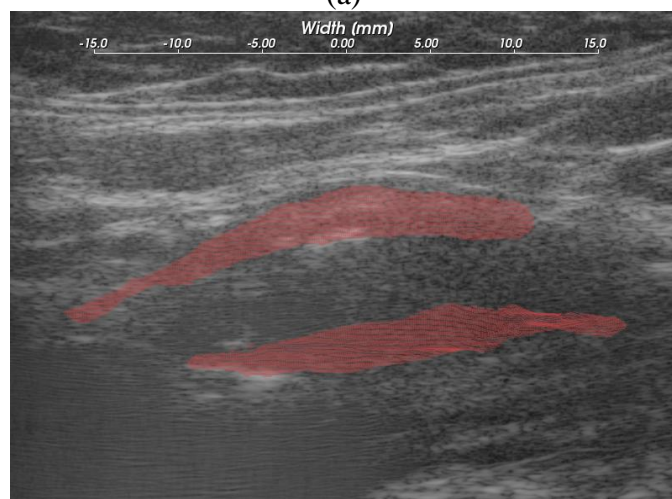
3.5.1 Comparison of the strain indices with and without adventitia

In the previous analysis reported in this chapter, the adventitia layer was not included with the plaque region during segmentation process (i.e. plaque-only segmentation). Using plaque-only segmentations in the carotid artery, we demonstrated that impaired cognitive function correlated significantly with maximum axial and lateral strain indices within a localized region of interest in plaque. However, in another study we observed large shear strains in the carotid artery wall in volunteers without plaque and in animal models [27]. Therefore, in this sub-section, we included the adventitia in the segmentation (i.e. plaque-with-adventitia segmentation) based on the hypothesis that increased shearing strains may be present in the adventitial layer or at the plaque-adventitia interface.

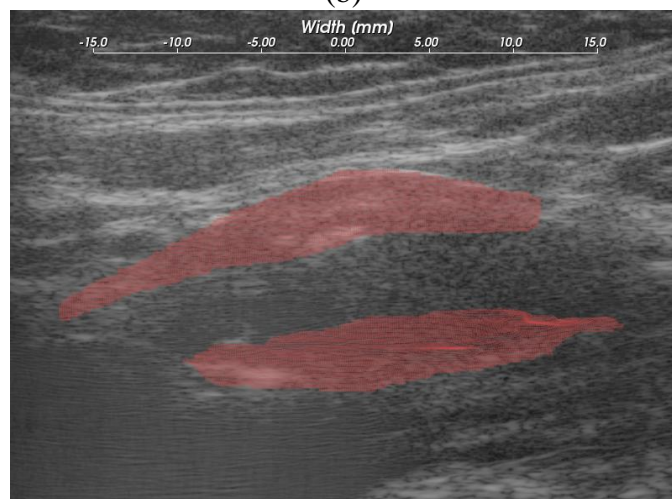
Plaque regions with adventitia were segmented by a radiologist on the B-mode images constructed from RF data, as shown in Figure 3.10. In the previous work we used the plaque-only segmentation, i.e. plaque was separated from artery wall on the plaque-adventitia interface, as shown in Figure 3.10(b). In this section we propose including the adventitia layer in the demarcation of plaque, denoted as the plaque-with-adventitia segmentation in Figure 3.10(c).



(a)



(b)



(c)

Figure 3.10: B-mode image (a) and segmented plaque on B-mode image using the plaque-only segmentation (b) and the plaque-with-adventitia segmentation (c).

Figure 3.11 and Figure 3.12 shows the comparison of axial strain images using the two segmentation methods on carotid plaque for a symptomatic patient segmented in Figure 3.10. Accumulated axial strain estimates overlaid on the B-mode image using the plaque-only segmentation are illustrated in Figure 3.11(a) and the plaque-with-adventitia segmentation in Figure 3.11(b). For the plaque-with-adventitia segmentation, the axial strain distribution in the adventitia is also shown in addition to the strain in the plaque. Although large accumulated axial strain values around 10% were found in the adventitia region, this did not exceed the maximum axial strain in the plaque. An asymptomatic case is also presented in Figures 3.12(a) and 3.12(b). The asymptomatic plaque shows less heterogeneity, but similar trends can still be observed.

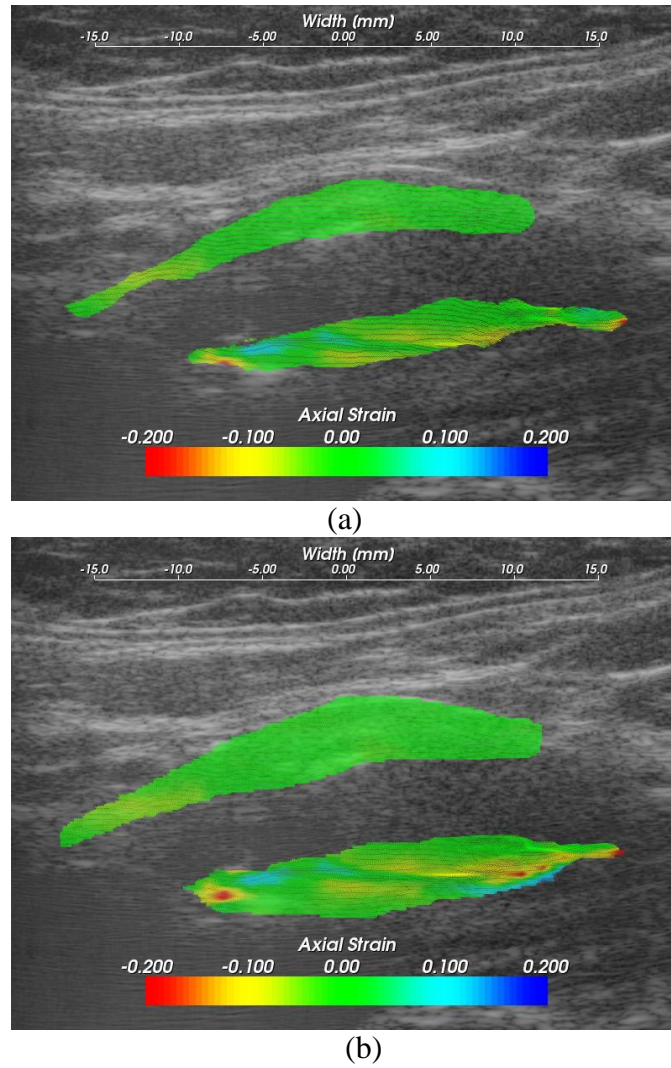


Figure 3.11: Axial strain values overlaid on the B-mode image using the plaque-only segmentation (a) and the plaque-with-adventitia segmentation (b) on a symptomatic plaque.

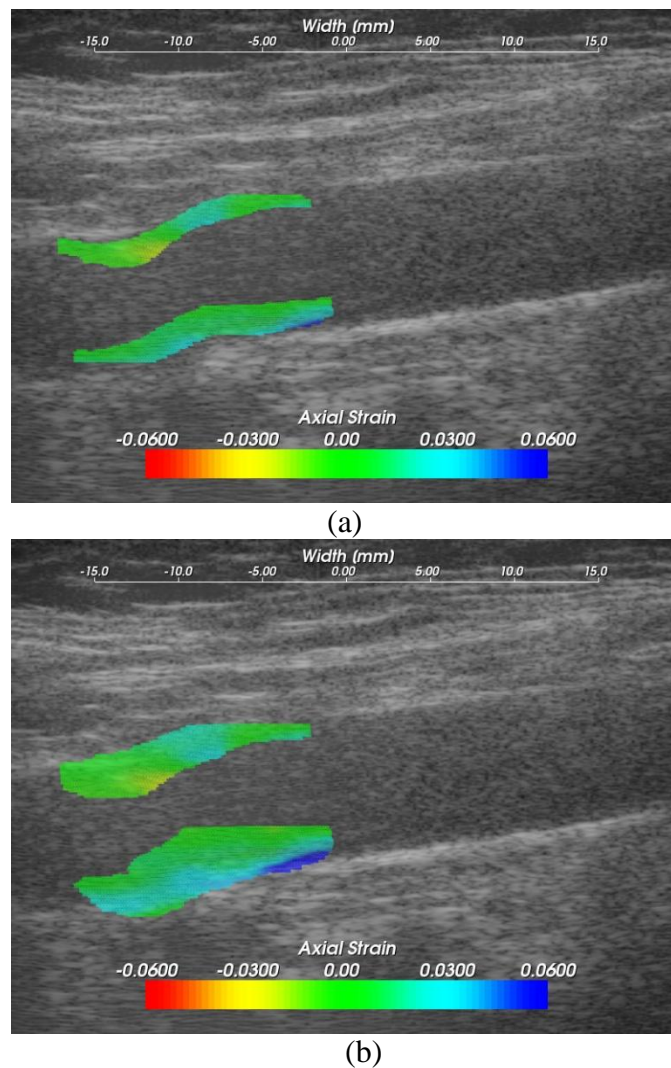


Figure 3.12: Axial strain values overlaid on the B-mode image using the plaque-only segmentation (a) and the plaque-with-adventitia segmentation (b) on an asymptomatic plaque.

In a similar manner, accumulated lateral strain images on the same symptomatic plaque with the two segmentation methods are illustrated in Figures 3.13(a) and 3.13(b). The extended region also has lateral strain values as large as 10%. We hypothesize that large strains in the lateral direction could arise from soft plaque deformation with blood flow, especially around stenosis. However, similar to the case with the accumulated axial strain, the maximum accumulated lateral strain does not change for the plaque even after

including the adventitia layer. For the patient with asymptomatic plaque large lateral strains were observed closer to adventitia, as shown in Figures 3.14(a) and 3.14(b).

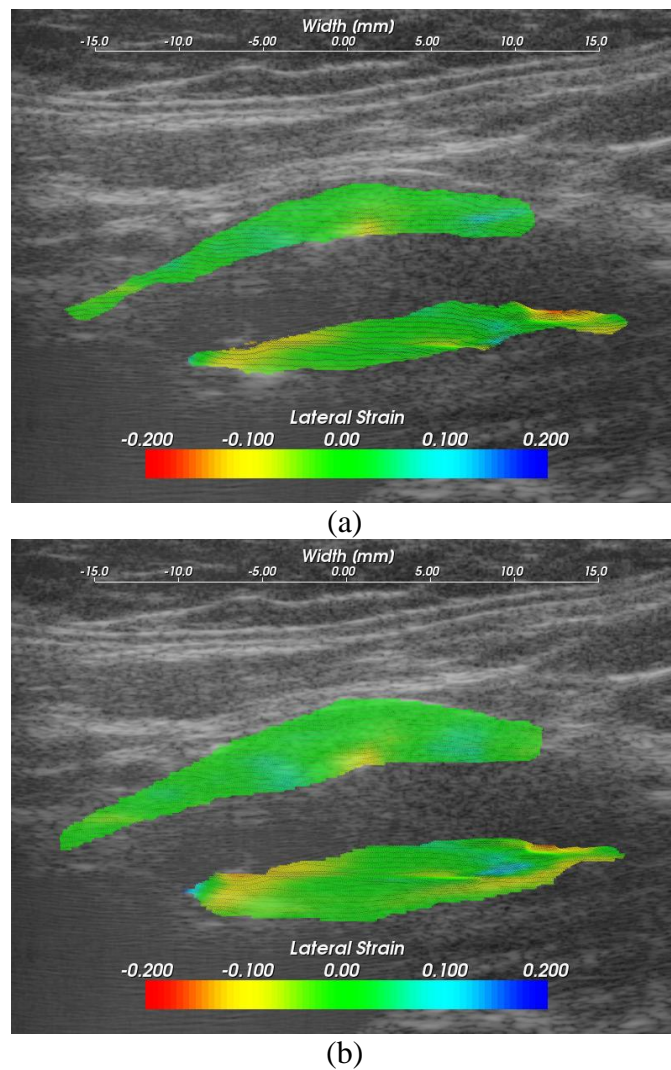


Figure 3.13: Lateral strain values overlaid on the B-mode image using the plaque-only segmentation (a) and the plaque-with-adventitia segmentation (b) on a symptomatic plaque.

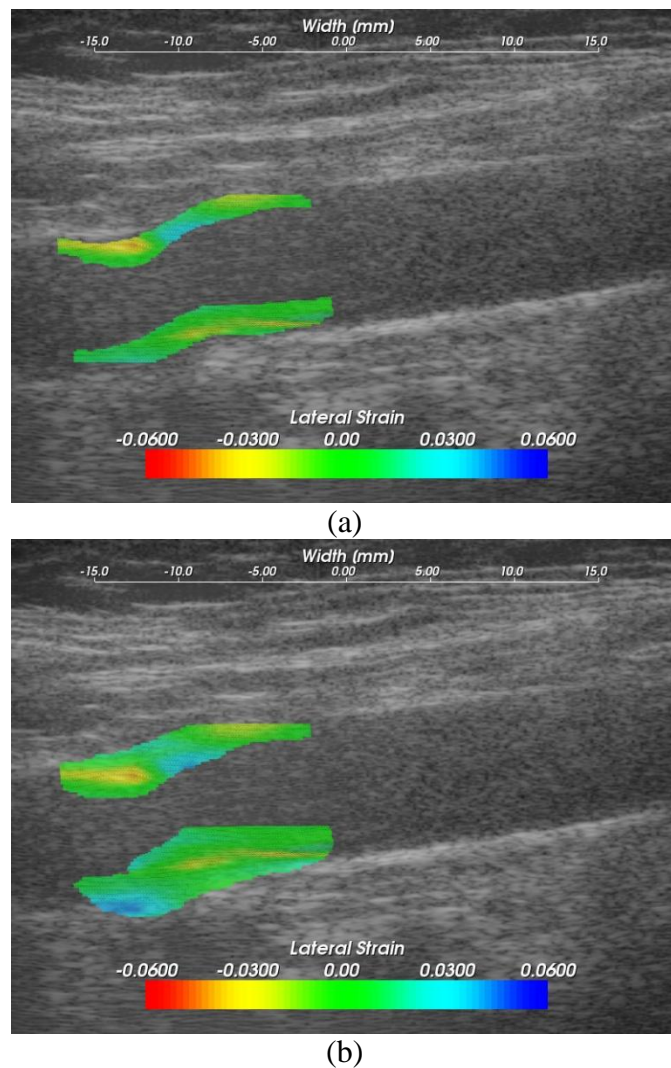


Figure 3.14: Lateral strain values overlaid on the B-mode image using the plaque-only segmentation (a) and the plaque-with-adventitia segmentation (b) on an asymptomatic plaque.

Finally, accumulated shear strain images for the same symptomatic patient with the two segmentation methods are shown in Figures 3.15(a) and 3.15(b) respectively. Notice that in the extended adventitial layer we now observe large accumulated shear strain values on the order of approximately 20% shear strain. Therefore the maximum accumulated shear strain for this patient is located near the adventitia layer instead of within the plaque. Similarly large shear strains were revealed after including the

adventitia layer in the segmentation in the asymptomatic plaque shown in Figures 3.16(a) and 3.16(b). Note also that the increased accumulated shear strain in the adventitia could be due to the presence of both large accumulated axial and lateral shear strains in this region.

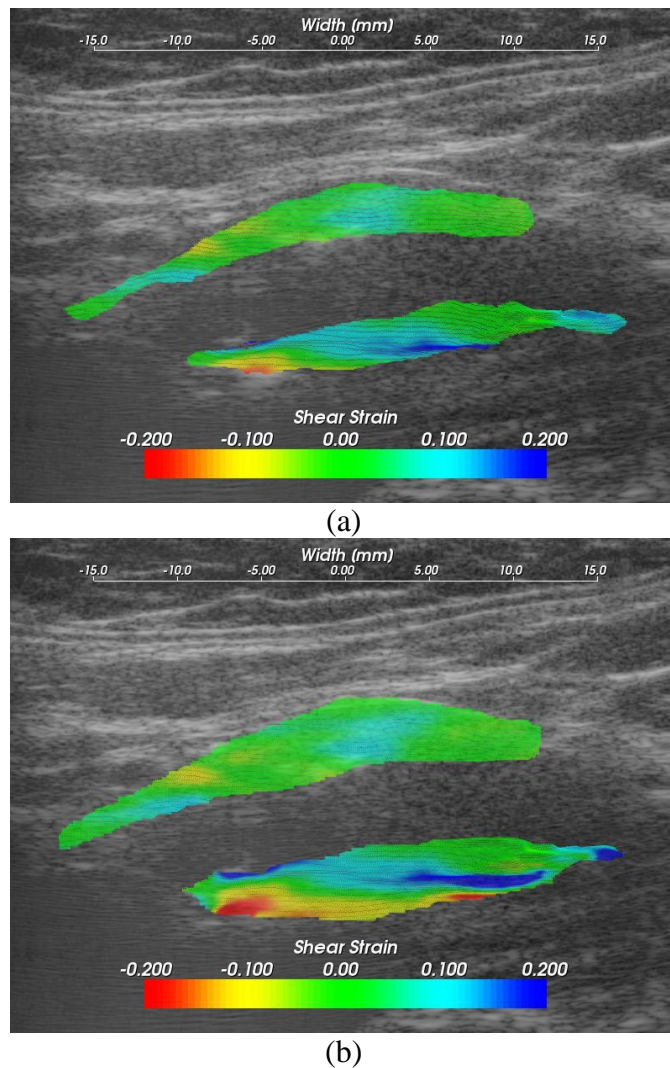


Figure 3.15: Shear strain values overlaid on the B-mode image using the plaque-only segmentation (a) and the plaque-with-adventitia segmentation (b) on a symptomatic plaque.

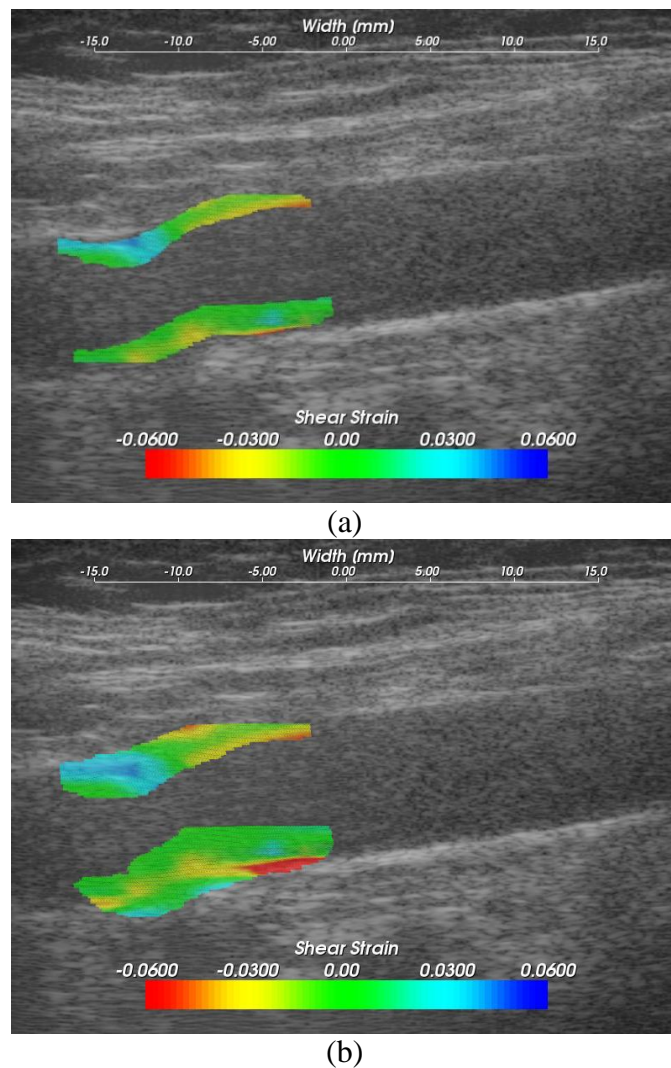


Figure 3.16: Shear strain values overlaid on the B-mode image using the plaque-only segmentation (a) and the plaque-with-adventitia segmentation (b) on an asymptomatic plaque.

Variations in accumulated strain estimates after including the adventitia layer in the segmentation are demonstrated in Figure 3.17. Accumulated axial, lateral and shear strains over two cardiac cycles for both plaque-only and plaque-with-adventitia segmentation on a symptomatic and asymptomatic patient are shown in Figures 3.17(a), 3.17(b) and 3.17(c) respectively. Note that the absolute values of the strain increases with the inclusion of the adventitia for both symptomatic and asymptomatic patient.

Accumulated axial, lateral and shear strain plots over two cardiac cycles in the carotid artery wall of two healthy human volunteers are also shown in Figure 3.18(a), 3.18(b) and 3.18(c) respectively. Note that the segmented region in this case, is only the vessel wall since no visible plaque was present. A cyclic variation in the accumulated strain tensor plots is clearly observed for both healthy vessels with normal blood flow. Observe the clear difference in the accumulated strain tensor estimates between that observed with a volunteer in Fig. 3.18, versus that for patients in Fig. 3.17. Irregular and turbulent flow patterns in the carotid arteries of patients with plaque introduce the non-periodic patterns observed in Fig. 3.17. Similar results has also been obtained and published by our lab on swine models[27].

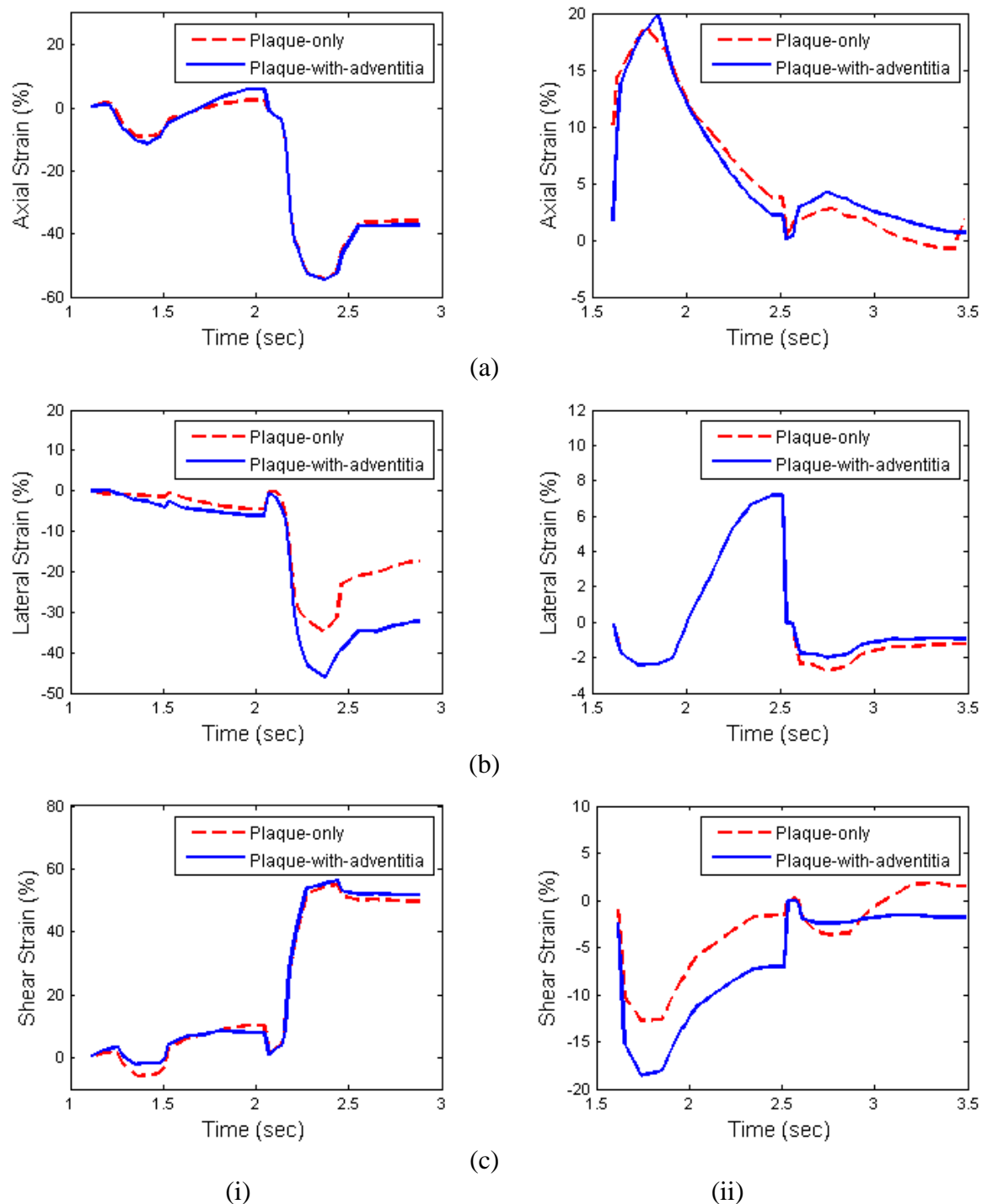


Figure 3.17: Accumulated axial (a), lateral (b) and shear (c) strain over two cardiac cycles with plaque-only and plaque-with-wall segmentation on a symptomatic (i) and an asymptomatic patient (ii).

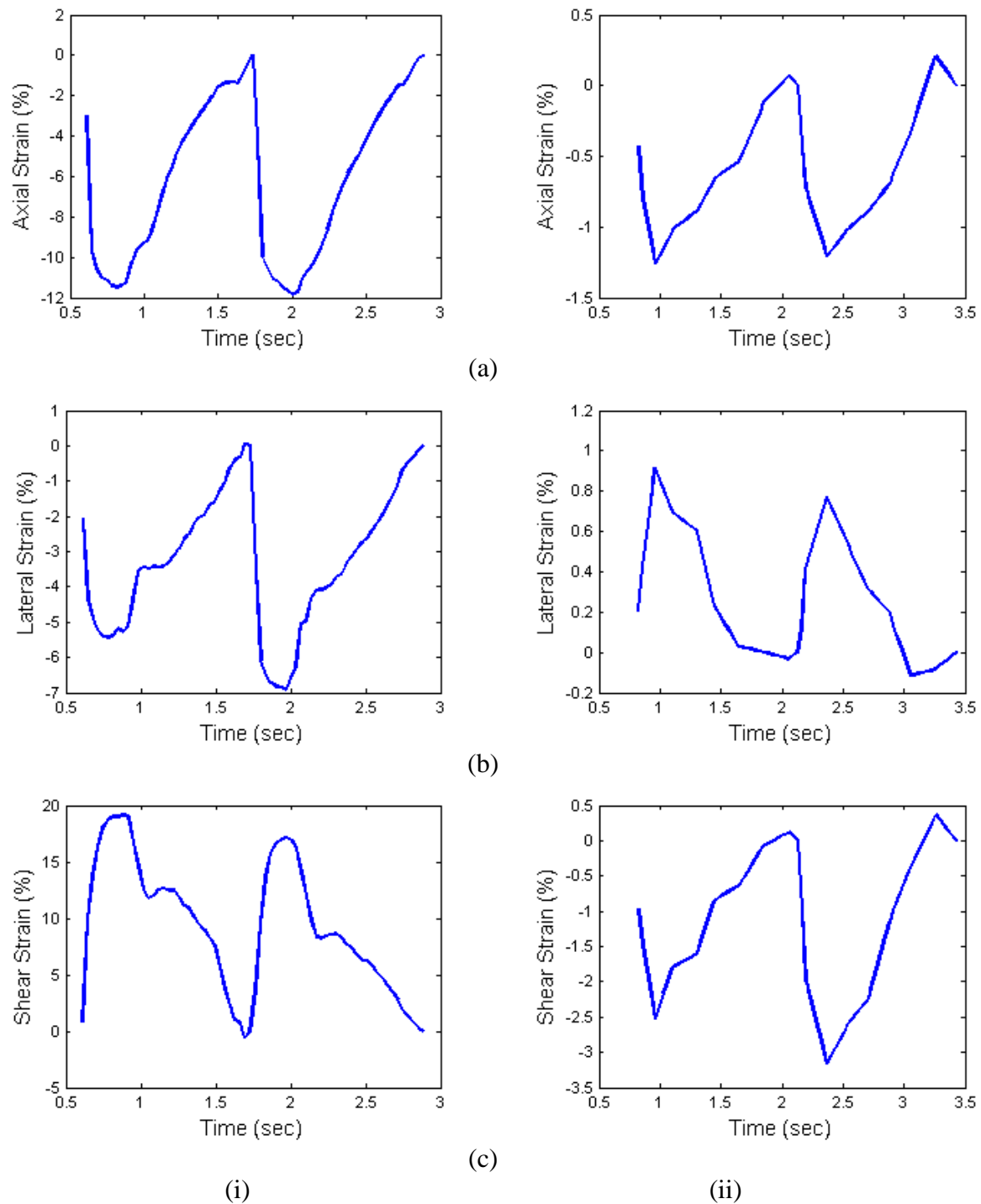
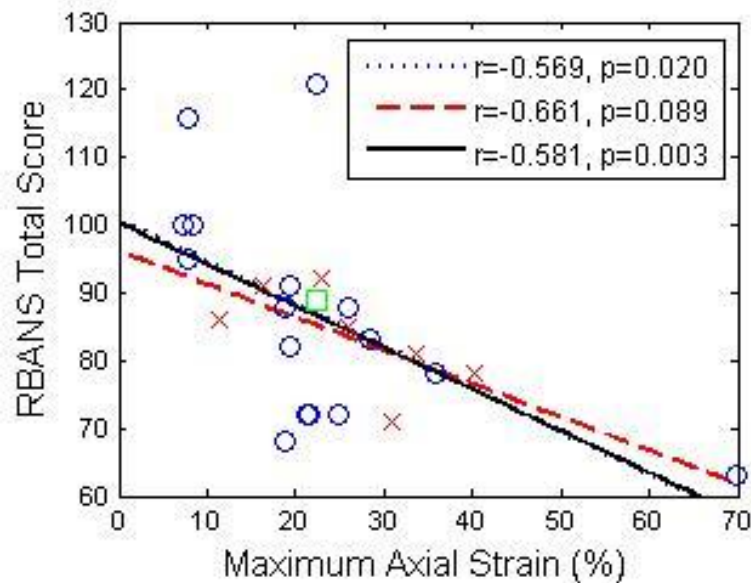


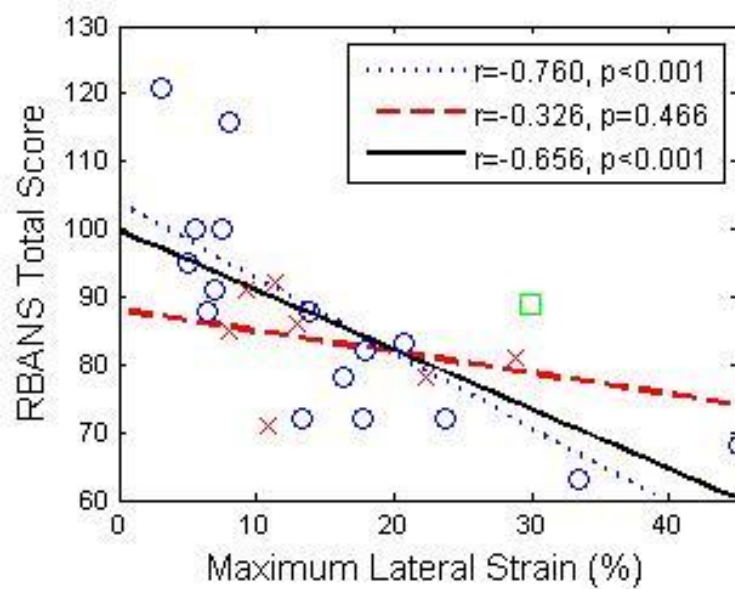
Figure 3.18: Accumulated axial (a), lateral (b) and shear (c) strain over two cardiac cycles in carotid artery wall on healthy human volunteer (i) and (ii).

3.5.2 Improvement in correlation with RBANS

The maximum and peak-to-trough strain indices over a small ROI with the largest deformation were obtained from the mean strain values within this ROI and then correlated with RBANS Total score. Note that the strain indices are absolute values. Figure 3.19 depicts the correlation of the RBANS Total score with maximum axial and lateral strain. As indicated before, the 16 symptomatic patients were plotted separately from the 7 asymptomatic patients. The uncertain one was also shown in the plot. A linear fit was performed for the two groups respectively, and also for all patients combined. The strains in the plots are all in scalar values. Pearson coefficient (r) and significance (p) values were also obtained for each correlation. Overall the RBANS Total score worsened with increasing strain indices for all the subjects, the same pattern identified in our previous work using plaque-only segmentation. For the maximum axial strain, the r values for the symptomatic group and for all patients combined improved from -0.533 and -0.491 to -0.569 and -0.581 respectively. For the maximum lateral strain, the r values for the symptomatic group and for all patients combined improved from -0.650 and -0.501 to -0.760 and -0.656 respectively. The correlations for the symptomatic group and for all patients combined were already significant in the previous results. Still, the p value decreased. Note that $p < 0.001$ for the correlation of RBANS Total score to maximum lateral strain for the symptomatic group and for all patients combined. Minimum strain indices are not provided since we did not observe any significant improvement in the correlations for minimum strain from that described in our previous work.



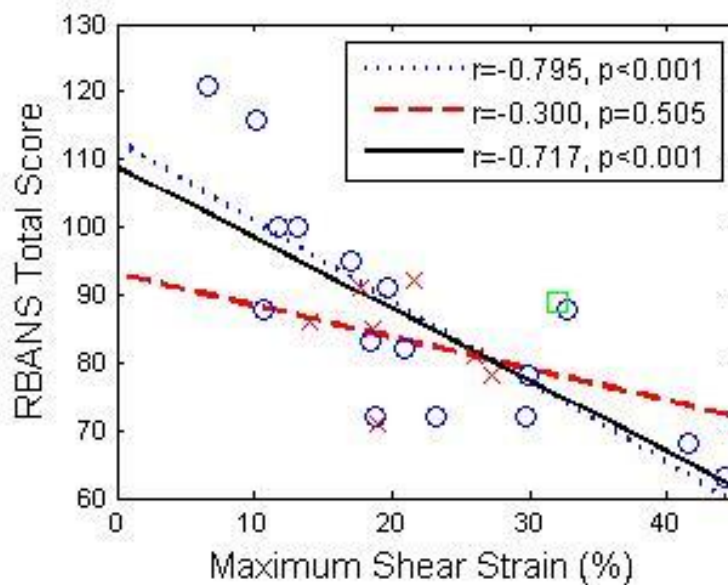
(a)



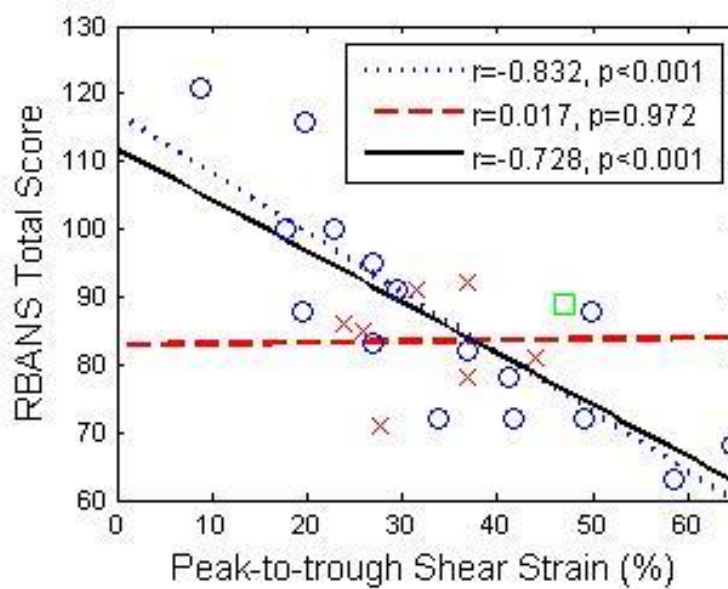
(b)

Figure 3.19: Linear least-squares fits of RBANS Total score with maximum axial (a), and maximum lateral (b) strain averaged over the small region of interest. \circ = Symptomatic, \times = asymptomatic, \square = questionable, the dotted line represents the linear fit for symptomatic, dashed line the linear fit for asymptomatic, and the solid line denotes the linear fit for all patients.

The correlation of RBANS Total score with shear strain indices is illustrated in Figure 3.20. Here we show both maximum and peak-to-trough shear strain indices. The correlations with the plaque-with-adventitia segmentation exhibits significant improvement when compared to the previous results. The correlation coefficients r for maximum shear strain were -0.432 and -0.345 for the symptomatic group and for all patients combined using the plaque-only segmentation, while with the plaque-with-adventitia segmentation, the correlation coefficients improved to -0.795 and -0.717. Similarly, the correlation coefficients r for peak-to-trough shear strain improved from -0.319 and -0.257 to -0.832 and -0.728 for the symptomatic group and for all patients combined. The p values also decreased, now making the correlations significant for the symptomatic group and for all patients combined, which was not the case previously. This aspect is noteworthy since no significant correlation for shear strain indices was observed in the previous results.



(a)



(b)

Figure 3.20: Linear least-squares fits of RBANS Total score with maximum (a), and peak-to-trough (b) shear strain averaged over the small region of interest. \circ = Symptomatic, \times = asymptomatic, \square = questionable, the dotted line represents the linear fit for symptomatic, dashed line the linear fit for asymptomatic, and the solid line denotes the linear fit for all patients.

A comparison of the RBANS Total scores obtained with plaque-only and plaque-with-adventitia, along with correlations to maximum accumulated strain indices are shown in Table 3.2. Since the correlation with RBANS Total score improved significantly with the inclusion of adventitia, we also report on the correlation of maximum accumulated strain indices to each of the component subscales of the RBANS utilizing the plaque-with-adventitia segmentation in Table 3.3. Significant correlations are marked in bold. Note that the two areas of cognition that show significant correlation for the symptomatic group and for all patients combined are Immediate Memory and Delayed Memory. Immediate Memory also shows significant correlation for asymptomatic patients. For asymptomatic patients there is also significant correlation of Attention to maximum axial strain and shear strain indices respectively.

		Maximum Axial Strain	Maximum Lateral Strain	Maximum Shear Strain
RBANS Total (Plaque-only)	Symptomatic	$r=-0.533$, $p=0.032$	$r=-0.650$, $p=0.006$	$r=-0.432$, $p=0.092$
	Asymptomatic	$r=-0.530$, $p=0.205$	$r=-0.115$, $p=0.803$	$r=0.037$, $p=0.937$
	All	$r=-0.491$, $p=0.014$	$r=-0.501$, $p=0.012$	$r=-0.345$, $p=0.097$
RBANS Total (Plaque-with-adventitia)	Symptomatic	$r=-0.569$, $p=0.020$	$r=-0.760$, $p<0.001$	$r=-0.795$, $p<0.001$
	Asymptomatic	$r=-0.661$, $p=0.089$	$r=-0.326$, $p=0.466$	$r=-0.300$, $p=0.505$
	All	$r=-0.581$, $p=0.003$	$r=-0.656$, $p<0.001$	$r=-0.717$, $p<0.001$

Table 3.2: Correlations of RBANS Total score for plaque-only and plaque-with-adventitia segmentation. Significant correlations are marked in bold.

		Maximum Axial Strain	Maximum Lateral Strain	Maximum Shear Strain
Immediate Memory	Symptomatic	$r=-0.592$, $p=0.014$	$r=-0.740$, $p<0.001$	$r=-0.752$, $p<0.001$
	Asymptomatic	$r=-0.852$, $p=0.008$	$r=-0.568$, $p=0.167$	$r=-0.722$, $p=0.052$
	All	$r=-0.620$, $p=0.001$	$r=-0.566$, $p=0.004$	$r=-0.602$, $p=0.002$
Visuospatial / Constructional	Symptomatic	$r=-0.191$, $p=0.476$	$r=-0.575$, $p=0.018$	$r=-0.611$, $p=0.011$
	Asymptomatic	$r=0.195$, $p=0.670$	$r=-0.047$, $p=0.919$	$r=0.266$, $p=0.557$
	All	$r=-0.162$, $p=0.448$	$r=-0.506$, $p=0.011$	$r=-0.521$, $p=0.009$
Language	Symptomatic	$r=-0.321$, $p=0.222$	$r=-0.202$, $p=0.452$	$r=-0.258$, $p=0.332$
	Asymptomatic	$r=-0.143$, $p=0.756$	$r=-0.509$, $p=0.227$	$r=-0.022$, $p=0.962$
	All	$r=-0.187$, $p=0.381$	$r=-0.158$, $p=0.459$	$r=-0.132$, $p=0.539$
Attention	Symptomatic	$r=-0.044$, $p=0.870$	$r=-0.077$, $p=0.776$	$r=-0.056$, $p=0.837$
	Asymptomatic	$r=-0.838$, $p=0.011$	$r=-0.303$, $p=0.499$	$r=-0.758$, $p=0.036$
	All	$r=-0.083$, $p=0.699$	$r=-0.090$, $p=0.674$	$r=-0.095$, $p=0.657$
Delayed Memory	Symptomatic	$r=-0.609$, $p=0.011$	$r=-0.762$, $p<0.001$	$r=-0.744$, $p<0.001$
	Asymptomatic	$r=-0.345$, $p=0.438$	$r=0.119$, $p=0.796$	$r=0.079$, $p=0.864$
	All	$r=-0.549$, $p=0.005$	$r=-0.559$, $p=0.004$	$r=-0.604$, $p=0.002$

Table 3.3: Correlations of the specific component scores in RBANS total with maximum strain indices. Significant correlations are marked in bold.

3.6 Shear strain within the adventitia

Cognitive function quantified by the RBANS Total score exhibits a negative correlation with maximum accumulated axial, lateral and shear strain indices when measured at the interface between normal adventitial wall and plaque. As the deformation or strain increases, the instability of plaque also increases concomitantly, expediting its possible rupture, resulting in embolism, and eventually leading to cognitive decline. The associations between strain and cognition reported in this work were significant for the symptomatic group and for all patients combined, suggesting a relationship between increasing strain indices in the carotid plaque and cognitive impairment through embolism. For the asymptomatic group, the correlations were not significant, partly due to the smaller size and reduced power. Despite the statistically significant correlation presented in this chapter, a larger sample size is essential to further establish this relationship.

The improved strain-cognition correlation shown here supports our hypothesis that increased shear strains may exist in the adventitia layer or at the plaque-adventitia border. Our results are consistent with the evidence of shear strain in adventitia reported in the literature [7-8]. Compared to the plaque-only segmentation, the plaque-with-adventitia segmentation provides more information on the strain distribution in and around the plaque. The correlation coefficients between both the maximum accumulated axial strain and maximum lateral strain with cognitive function increased, though these changes were not as dramatic as those obtained for the accumulated shear strain indices. For the symptomatic group and for all patients combined, the maximum and peak-to-trough shear strain indices demonstrated significant correlation with cognitive function after including

adventitia, which suggests that large shear strain values in the adventitia should be considered in the characterization of carotid plaque. These results also suggest that plaque residual wall interface is of importance in the etiology of a symptomatic disorder, just as they suggest that carotid plaque instability is an important etiology of cognitive vascular decline.

Shear strain within the arterial wall has been studied extensively since it may be responsible for plaque formation and rupture. As people age, their artery walls stiffen, thus the shear strain may also increase between the vascular arterial layers. The adventitia layer is associated with plaque progression and thrombus formation since angiogenesis, a possible factor in facilitating plaque rupture, originates from adventitia-media interface [28-31]. Significant shear can occur between adventitia and media, resulting in the tearing of the vasa vasorum, which arises from the adventitia to supply the media layer. Rupture of vasa vasorum can produce micro-hemorrhage into a plaque, leaving fissures that can cause instability, local thrombosis and embolism [32-34].

The plaque-with-adventitia segmentation method not only takes the shearing at plaque boundaries into account, but also is an easier and more convenient method for radiologists since it is difficult to distinguish plaque from adventitia in ultrasound B-mode images in many instances. For the plaque-only method, intima-media was also included since it is almost inseparable from plaque.

3.7 Conclusions

In summary, the results reveal a significant relationship between the maximum and peak-to-peak axial, lateral and shear strain indices in carotid plaque with cognitive

function. Since ultrasound strain indices may assist in the identification of plaques prone to rupture, which in turn causes emboli; it plays an important role in characterizing plaque and detecting vulnerability of plaque. This correlation study indicates that these microemboli may be related to cognitive impairment. While silent stroke is strongly linked with cognitive impairment, it suggests that ultrasound strain imaging can play an important role in predicting embolism and resulting cognitive impairment, as well as preventing potential silent strokes.

The recent results also demonstrate the feasibility and advantage of the plaque-with-adventitia segmentation method over the plaque-only segmentation method. As this is the interface of microvascular abnormalities essential for plaque growth and instability, it is likely to be the area where one could most easily noninvasively image for plaque instability using these techniques.

3.8 References

1. McCormick, M., Varghese, T., Wang, X., Mitchell, C., Kliewer, M.A., and Dempsey, R.J., *Methods for robust in vivo strain estimation in the carotid artery*. *Phys Med Biol*, 2012. **57**(22): p. 7329-53.
2. Shi, H., Mitchell, C.C., McCormick, M., Kliewer, M.A., Dempsey, R.J., and Varghese, T., *Preliminary in vivo atherosclerotic carotid plaque characterization using the accumulated axial strain and relative lateral shift strain indices*. *Phys Med Biol*, 2008. **53**(22): p. 6377-94.
3. Rocque, B.G., Jackson, D., Varghese, T., Hermann, B., McCormick, M., Kliewer, M., Mitchell, C., and Dempsey, R.J., *Impaired cognitive function in patients with atherosclerotic carotid stenosis and correlation with ultrasound strain measurements*. *J Neurol Sci*, 2012. **322**(1-2): p. 20-4.
4. Wang, X., Jackson, D.C., Varghese, T., Mitchell, C.C., Hermann, B.P., Kliewer, M.A., and Dempsey, R.J., *Correlation of cognitive function with ultrasound strain indices in carotid plaque*. *Ultrasound Med Biol*, 2014. **40**(1): p. 78-89.
5. Falk, E., Shah, P.K., and Fuster, V., *Coronary plaque disruption*. *Circulation*, 1995. **92**(3): p. 657-71.

6. Gertz, S.D. and Roberts, W.C., *Hemodynamic shear force in rupture of coronary arterial atherosclerotic plaques*. Am J Cardiol, 1990. **66**(19): p. 1368-72.
7. Idzenga, T., Holewijn, S., Hansen, H.H., and de Korte, C.L., *Estimating cyclic shear strain in the common carotid artery using radiofrequency ultrasound*. Ultrasound Med Biol, 2012. **38**(12): p. 2229-37.
8. Cinthio, M., Ahlgren, A.R., Bergkvist, J., Jansson, T., Persson, H.W., and Lindstrom, K., *Longitudinal movements and resulting shear strain of the arterial wall*. Am J Physiol Heart Circ Physiol, 2006. **291**(1): p. H394-402.
9. McCormick, M., Rubert, N., and Varghese, T., *Bayesian regularization applied to ultrasound strain imaging*. IEEE Trans Biomed Eng, 2011. **58**(6): p. 1612-20.
10. Randolph, C., Tierney, M.C., Mohr, E., and Chase, T.N., *The Repeatable Battery for the Assessment of Neuropsychological Status (RBANS): preliminary clinical validity*. J Clin Exp Neuropsychol, 1998. **20**(3): p. 310-9.
11. Duff, K., Patton, D., Schoenberg, M.R., Mold, J., Scott, J.G., and Adams, R.L., *Age- and education-corrected independent normative data for the RBANS in a community dwelling elderly sample*. Clin Neuropsychol, 2003. **17**(3): p. 351-66.
12. Lee, R.T., *Atherosclerotic lesion mechanics versus biology*. Z Kardiol, 2000. **89 Suppl 2**: p. 80-4.
13. Gao, H. and Long, Q., *Effects of varied lipid core volume and fibrous cap thickness on stress distribution in carotid arterial plaques*. J Biomech, 2008. **41**(14): p. 3053-9.
14. Richardson, P.D., Davies, M.J., and Born, G.V., *Influence of plaque configuration and stress distribution on fissuring of coronary atherosclerotic plaques*. Lancet, 1989. **2**(8669): p. 941-4.
15. van der Wal, A.C. and Becker, A.E., *Atherosclerotic plaque rupture--pathologic basis of plaque stability and instability*. Cardiovasc Res, 1999. **41**(2): p. 334-44.
16. Kefayati, S. and Poepping, T.L., *Transitional flow analysis in the carotid artery bifurcation by proper orthogonal decomposition and particle image velocimetry*. Med Eng Phys, 2013. **35**(7): p. 898-909.
17. Slager, C.J., Wentzel, J.J., Gijzen, F.J., Schuurbijs, J.C., van der Wal, A.C., van der Steen, A.F., and Serruys, P.W., *The role of shear stress in the generation of rupture-prone vulnerable plaques*. Nat Clin Pract Cardiovasc Med, 2005. **2**(8): p. 401-7.
18. DePaola, N., Gimbrone, M.A., Jr., Davies, P.F., and Dewey, C.F., Jr., *Vascular endothelium responds to fluid shear stress gradients*. Arterioscler Thromb, 1992. **12**(11): p. 1254-7.
19. Bluestein, D., Niu, L., Schoepfoerster, R.T., and Dewanjee, M.K., *Fluid mechanics of arterial stenosis: relationship to the development of mural thrombus*. Ann Biomed Eng, 1997. **25**(2): p. 344-56.
20. Poepping, T.L., Rankin, R.N., and Holdsworth, D.W., *Flow patterns in carotid bifurcation models using pulsed Doppler ultrasound: effect of concentric vs.*

- eccentric stenosis on turbulence and recirculation*. *Ultrasound Med Biol*, 2010. **36**(7): p. 1125-34.
21. Stein, P.D. and Sabbah, H.N., *Measured turbulence and its effect on thrombus formation*. *Circ Res*, 1974. **35**(4): p. 608-14.
 22. Loree, H.M., Kamm, R.D., Atkinson, C.M., and Lee, R.T., *Turbulent pressure fluctuations on surface of model vascular stenoses*. *Am J Physiol*, 1991. **261**(3 Pt 2): p. H644-50.
 23. Reininger, A.J., Reininger, C.B., Heinzmann, U., and Wurzinger, L.J., *Residence time in niches of stagnant flow determines fibrin clot formation in an arterial branching model--detailed flow analysis and experimental results*. *Thromb Haemost*, 1995. **74**(3): p. 916-22.
 24. Vermeer, S.E., Prins, N.D., den Heijer, T., Hofman, A., Koudstaal, P.J., and Breteler, M.M., *Silent brain infarcts and the risk of dementia and cognitive decline*. *N Engl J Med*, 2003. **348**(13): p. 1215-22.
 25. Dempsey, R.J., Vemuganti, R., Varghese, T., and Hermann, B.P., *A review of carotid atherosclerosis and vascular cognitive decline: a new understanding of the keys to symptomology*. *Neurosurgery*, 2010. **67**(2): p. 484-93; discussion 493-4.
 26. Elias, M.F., Sullivan, L.M., D'Agostino, R.B., Elias, P.K., Beiser, A., Au, R., Seshadri, S., DeCarli, C., and Wolf, P.A., *Framingham stroke risk profile and lowered cognitive performance*. *Stroke*, 2004. **35**(2): p. 404-9.
 27. Ge, W., Krueger, C.G., Weichmann, A., Shanmuganayagam, D., and Varghese, T., *Displacement and strain estimation for evaluation of arterial wall stiffness using a familial hypercholesterolemia swine model of atherosclerosis*. *Med Phys*, 2012. **39**(7): p. 4483-92.
 28. Hiyama, T., Tanaka, T., Endo, S., Komine, K., Kudo, T., Kobayashi, H., and Shiokawa, Y., *Angiogenesis in atherosclerotic plaque obtained from carotid endarterectomy: association between symptomatology and plaque morphology*. *Neurol Med Chir (Tokyo)*, 2010. **50**(12): p. 1056-61.
 29. ten Kate, G.L., Sijbrands, E.J., Valkema, R., ten Cate, F.J., Feinstein, S.B., van der Steen, A.F., Daemen, M.J., and Schinkel, A.F., *Molecular imaging of inflammation and intraplaque vasa vasorum: a step forward to identification of vulnerable plaques?* *J Nucl Cardiol*, 2010. **17**(5): p. 897-912.
 30. Lawrence-Brown, M., Stanley, B.M., Sun, Z., Semmens, J.B., and Liffman, K., *Stress and strain behaviour modelling of the carotid bifurcation*. *ANZ J Surg*, 2011. **81**(11): p. 810-6.
 31. Idzenga, T., Pasterkamp, G., and de Korte, C., *Shear strain in the adventitial layer of the arterial wall facilitates development of vulnerable plaques*. *Bioscience Hypotheses*, 2009. **2**(5): p. 339-342.
 32. Lusby, R.J., Ferrell, L.D., Ehrenfeld, W.K., Stoney, R.J., and Wylie, E.J., *Carotid plaque hemorrhage. Its role in production of cerebral ischemia*. *Arch Surg*, 1982.

- 117(11):** p. 1479-88.
33. McCarthy, M.J., Loftus, I.M., Thompson, M.M., Jones, L., London, N.J., Bell, P.R., Naylor, A.R., and Brindle, N.P., *Angiogenesis and the atherosclerotic carotid plaque: an association between symptomatology and plaque morphology*. *J Vasc Surg*, 1999. **30(2)**: p. 261-8.
 34. Vicenzini, E., Giannoni, M.F., Puccinelli, F., Ricciardi, M.C., Altieri, M., Di Piero, V., Gossetti, B., Valentini, F.B., and Lenzi, G.L., *Detection of carotid adventitial vasa vasorum and plaque vascularization with ultrasound cadence contrast pulse sequencing technique and echo-contrast agent*. *Stroke*, 2007. **38(10)**: p. 2841-3.

Chapter 4 : Correlation of Strain Indices with NINDS-CSN VCI Harmonization Standards 60-Minute Protocol

4.1 Introduction

In this chapter, we estimate strain indices in a second group of patients and correlate maximum strain indices to cognition scores obtained with a new cognition test protocol as a substitute for RBANS. We use National Institute of Neurological Disorder and Stroke-Canadian Stroke Network (NINDS-CSN) Vascular Cognitive Impairment Harmonization Standards [1] as a test protocol for a standardized cognitive assessment. NINDS-CSN Vascular Cognitive Impairment Harmonization Standards recommended common standards for the study of vascular cognitive impairment as a first step, and agreed that additional methodologies would be in need to integrate all specific sub-tests [2].

4.2 Materials and Methods

4.2.1 Data acquisition

Ultrasound imaging and cognition tests were performed on 51 patients (28 male and 23 female) with significant plaque prior to a carotid endarterectomy (CEA) procedure at the University of Wisconsin-Madison Hospitals and Clinics. Patients were enrolled in the study after providing informed consent using a protocol approved by the University of Wisconsin-Madison Institutional Review Boards (IRB). The age of the patients ranged

from 43 to 85, with a mean and standard deviation of 69.96 ± 9.24 respectively.

Ultrasound radiofrequency (RF) echo signal data was acquired using a Siemens S2000 ultrasound system (Siemens Ultrasound, Mountain View, CA, USA) equipped with an 18L6 linear array transducer, along with clinical B-mode images and color-flow Doppler images on these patients. The transmit frequency was 11.4 MHz with a single transmit focus set at the depth of the plaque. The sampling frequency was 40 MHz, with at least two cardiac cycles of RF data acquired.

4.2.2 Strain indices estimation

Plaque regions with adventitia were segmented by a radiologist/research sonographer for end-diastole frames using the Medical Imaging Interaction Toolkit (MITK), as previously shown in Chapter 3. The segmented regions were automatically tracked over two complete cardiac cycles using the same hierarchical block-matching motion tracking algorithm developed in our laboratory [3], using the segmented end-diastolic frame as the initial frame of the sequence. Details of our algorithm were presented in Chapter 3. Maximum accumulated strain over two cardiac cycles was obtained with the absolute value of the maximum strain used in our analysis.

4.2.3 Cognition assessment

Cognition assessment was also performed before CEA, using NINDS-CSN Vascular Cognitive Impairment Harmonization Standards 60-minute protocol, which consisted of several scores evaluating executive/activation, visuospatial, language/lexical retrieval, memory/learning, neuropsychiatric/depression symptoms, and pre-morbid status [1].

A raw score and a t-score, which is a standardized scaled score, were generated in

each sub-tests, however, only the t-scores were used in our analysis. “ANMLT” denotes the t-score provided for a Semantic Fluency test, in other words, a test that involves listing Animals, which evaluates language and executive function. “COWAT” represents the t-score for Phonemic Fluency, which also evaluates language and executive function. WAIS-IV Digit Symbol scaled score (“WAISIVDigitSymbolSS”) evaluates speeded motor function. WAIS-IV Block Design scaled score (“WAISIVBlockDesignSS”) evaluates visuospatial and motor function. WAIS-IV Information scaled score (“WAISIVInformationSS”) evaluates general information and verbal IQ. WAIS-IV Digit Span scaled score (“WAISIVDigitSpanSS”) evaluates working memory and attention. “TMTAT” and “TMTBT” were the t-scores generated in Trail-Making Test A and Trail-Making Test B, respectively. Trail-Making Test A evaluates motor and visual attention, whereas Trail-Making Test B also evaluates executive function in addition to motor and visual attention. “CESDR” is the raw score obtained in the Center for Epidemiologic Studies-Depression Scale test which is a screening test for depression and depressive disorders. The Hopkins Verbal Learning Test provides a total recall t-score (“HVLTRTRT”) which evaluates verbal learning and immediate verbal memory, and a delayed recall t-score (“HVLTRDRT”) which evaluates verbal learning and delayed verbal memory. The Rey Complex Figure Test includes a copy test, a immediate recall test, and a delayed recall test. The “RCFTCopyTime” evaluates visuospatial learning. The 3-second delay t-score (“RCFT3DelayT”) evaluates visuospatial learning and immediate spatial memory. The 30-second delay t-score (“RCFT30DelayT”) evaluates visuospatial learning and delayed spatial memory. The Boston Naming Test only provides the Confrontation Naming raw score (“ConfrontationNamingRaw”) which

evaluates language. Finally, the North American Reading Test evaluates pre-morbid status, including pre-morbid verbal IQ (“NARTREstimatedVIQ”), pre-morbid performance IQ (“NARTREstimatedPIQ”) and pre-morbid full-scale IQ (“NARTREstimatedFSIQ”).

4.2.4 Correlation analysis

Ultrasound imaging and cognition assessment were conducted separately and were blinded to each other. Since no overall or total score was provided by NINDS-CSN Vascular Cognitive Impairment Harmonization Standards, we conducted a correlation study on each sub-test with a scaled score. Maximum strain indices were correlated to the sub-test scaled scores using a Pearson’s correlation coefficient r and a significance level of $p < 0.05$ using a two-tailed t -test. Correlation analysis was performed for all patients, and also in each clinically relevant group of patients separately. Patients were classified as symptomatic or asymptomatic group based on the same clinical criteria as described in Chapter 3. In this group of patients, 31 patients were symptomatic, and 20 were asymptomatic. Patients were also classified based on specific vascular risk factors including diabetes, hypertension, hyperlipidemia and tobacco usage. Among 51 patients, 14 patients had diabetes, 43 had hypertension, 40 had hyperlipidemia, and 37 were smokers, or previous smokers, or used other tobacco products.

4.3 Results

Correlation coefficients and significance values of maximum axial, lateral and shear strain indices with each sub-test score for all patients are listed in Table 4.1. Among all correlations, we only listed significant correlations with the absolute value of $r > 0.5$ and

$p < 0.05$. Note that WAISIVDigitSymbolSS and TMTBT have negative correlations with maximum strain indices, while on the other hand RCFTCopyTime has positive association with maximum strain indices, indicating that the cognition score appears to trend lower with increasing strain indices. Note that the RCFTCopyTime is the time that takes to copy a figure, therefore the longer the copy time, the lower the cognition score. The significant correlations suggest that strain is associated with motor, speeded motor function, executive function, visual attention and visuospatial learning.

	Maximum Axial Strain	Maximum Lateral Strain	Maximum Shear Strain
WAISIVDigitSymbolSS	$r = -0.595, p < 0.001$	$r = -0.539, p < 0.001$	$r = -0.620, p < 0.001$
TMTBT	$r = -0.501, p < 0.001$	$r = -0.509, p < 0.001$	$r = -0.528, p < 0.001$
RCFTCopyTime	$r = 0.524, p < 0.001$	$r = 0.509, p < 0.001$	$r = 0.489, p < 0.001$

Table 4.1: Significant correlations of each sub-test score to maximum strain indices for all patients ($n = 51$).

Correlation coefficients and significance values of maximum axial, lateral and shear strain indices with each sub-test score for symptomatic patients and asymptomatic patients are listed in Table 4.2 and Table 4.3, respectively. In a similar manner, only significant correlations with the absolute value of $r > 0.5$ and $p < 0.05$ were listed. When compared to the results obtained with all patients, WAISIVDigitSymbolSS has significant correlations with maximum strain indices for both symptomatic and asymptomatic patients. Compared to the correlations obtained with all patients, TMTBT is only correlated significantly with maximum strain indices for asymptomatic patients, while RCFTCopyTime is only correlated significantly with maximum strain indices for

symptomatic patients. Correlations with maximum strain indices are also significant with RCFT30DelayT for symptomatic patients. Note that the highest correlation coefficient of -0.77 was obtained with WAISIVDigitSymbolSS for asymptomatic patients.

	Maximum Axial Strain	Maximum Lateral Strain	Maximum Shear Strain
WAISIVDigitSymbolSS	$r = -0.522, p = 0.002$	$r = -0.509, p = 0.003$	$r = -0.556, p = 0.001$
RCFTCopyTime	$r = 0.616, p < 0.001$	$r = 0.622, p < 0.001$	$r = 0.608, p < 0.001$
RCFT30DelayT	$r = -0.441, p = 0.012$	$r = -0.554, p = 0.001$	$r = -0.435, p = 0.014$

Table 4.2: Significant correlations of each sub-test score to maximum strain indices for symptomatic group (n = 31).

	Maximum Axial Strain	Maximum Lateral Strain	Maximum Shear Strain
WAISIVDigitSymbolSS	$r = -0.752, p < 0.001$	$r = -0.674, p < 0.001$	$r = -0.768, p < 0.001$
TMTBT	$r = -0.590, p = 0.006$	$r = -0.655, p = 0.001$	$r = -0.635, p = 0.002$

Table 4.3: Significant correlations of each sub-test score to maximum strain indices for asymptomatic group (n = 20).

Correlation coefficients and significance values for maximum axial, lateral and shear strain indices with each sub-test score and for each specific group are listed in Table 4.4 through Table 4.7. Similar to the results shown previously, only significant correlations with the absolute value of $r > 0.5$ and $p < 0.05$ were listed. Note that WAISIVDigitSymbolSS has significant correlations with maximum strain indices for all groups. ANMLT has significant correlations with maximum strain indices for the

diabetes group, while TMTAT has significant correlations with maximum strain indices for hypertension group and smoker group. TMTBT and RCFTCopyTime are also significantly correlated with maximum strain indices for diabetes group, hypertension group and smoker group.

	Maximum Axial Strain	Maximum Lateral Strain	Maximum Shear Strain
ANMLT	$r = -0.312, p = 0.275$	$r = -0.543, p = 0.042$	$r = -0.346, p = 0.222$
WAISIVDigitSymbolSS	$r = -0.576, p = 0.029$	$r = -0.472, p = 0.085$	$r = -0.641, p = 0.012$
TMTBT	$r = -0.640, p = 0.012$	$r = -0.632, p = 0.013$	$r = -0.643, p = 0.011$
RCFTCopyTime	$r = 0.275, p = 0.338$	$r = 0.534, p = 0.046$	$r = 0.432, p = 0.119$

Table 4.4: Significant correlations of each sub-test score to maximum strain indices for diabetes group (n = 14).

	Maximum Axial Strain	Maximum Lateral Strain	Maximum Shear Strain
WAISIVDigitSymbolSS	$r = -0.589, p < 0.001$	$r = -0.548, p < 0.001$	$r = -0.629, p < 0.001$
TMTAT	$r = -0.487, p < 0.001$	$r = -0.541, p < 0.001$	$r = -0.455, p = 0.002$
TMTBT	$r = -0.563, p < 0.001$	$r = -0.561, p < 0.001$	$r = -0.547, p < 0.001$
RCFTCopyTime	$r = 0.586, p < 0.001$	$r = 0.597, p < 0.001$	$r = 0.552, p < 0.001$

Table 4.5: Significant correlations of each sub-test score to maximum strain indices for hypertension group (n = 43).

	Maximum Axial Strain	Maximum Lateral Strain	Maximum Shear Strain
WAISIVDigitSymbolSS	$r = -0.575, p < 0.001$	$r = -0.589, p < 0.001$	$r = -0.609, p < 0.001$

Table 4.6: Significant correlations of each sub-test score to maximum strain indices for hyperlipidemia group (n = 40).

	Maximum Axial Strain	Maximum Lateral Strain	Maximum Shear Strain
WAISIVDigitSymbolSS	$r = -0.597, p < 0.001$	$r = -0.515, p = 0.001$	$r = -0.600, p < 0.001$
TMTAT	$r = -0.464, p = 0.004$	$r = -0.531, p < 0.001$	$r = -0.455, p = 0.005$
TMTBT	$r = -0.515, p = 0.001$	$r = -0.524, p < 0.001$	$r = -0.518, p < 0.001$
RCFTCopyTime	$r = 0.601, p < 0.001$	$r = 0.588, p < 0.001$	$r = 0.596, p < 0.001$

Table 4.7: Significant correlations of each sub-test score to maximum strain indices for smoker group (n = 37).

4.4 Discussion

In this chapter, we have shown that a relationship exists between maximum strain indices and cognitive function. Overall, WAISIVDigitSymbolSS, which evaluates speeded motor function, has significant correlation with maximum strain indices for each specific group and for all patients combined. RCFTCopyTime and RCFT30DelayT from Rey Complex Figure Test, which evaluates visuospatial learning and delayed verbal memory, demonstrated significant correlations with maximum strain indices only for symptomatic patients. TMTBT, which evaluates motor, executive function and visual

attention, from the Trail-Making Test showed significant correlations with maximum strain indices only for asymptomatic patients. This is consistent with the correlations obtained with specific component scores in RBANS [4] in Chapter 3 [5]. In Chapter 3, we have shown that significant correlations were obtained with immediate memory for both the symptomatic and asymptomatic group. Maximum strain indices were correlated significantly with visuospatial/constructional and delayed memory only for symptomatic patients, and with attention only for asymptomatic patients. No significant correlation was observed with language.

The only significant correlation with language in this chapter was observed in the diabetes group, since ANMLT evaluates language and executive function. For patients with vascular risk factors including diabetes, hypertension, hyperlipidemia and smoking, significant correlations were also obtained mainly with WAISIVDigitSymbolSS, TMTAT, TMTBT and RCFTCopyTime.

4.5 Conclusions

In summary, we demonstrate that maximum strain indices in carotid plaque as vascular biomarkers may be associated with specific cognitive function. Although the etiology of cognition impairment is still uncertain, our results suggest that the decline of motor function, speeded motor function, executive function, visual attention and visuospatial learning may be associated with embolization indicated by high strain indices in carotid plaque.

4.6 References

1. Hachinski, V., Iadecola, C., Petersen, R.C., Breteler, M.M., Nyenhuis, D.L.,

- Black, S.E., Powers, W.J., DeCarli, C., Merino, J.G., Kalaria, R.N., Vinters, H.V., Holtzman, D.M., Rosenberg, G.A., Wallin, A., Dichgans, M., Marler, J.R., and Leblanc, G.G., *National Institute of Neurological Disorders and Stroke-Canadian Stroke Network vascular cognitive impairment harmonization standards*. *Stroke*, 2006. **37**(9): p. 2220-41.
2. Di Legge, S. and Hachinski, V., *Vascular cognitive impairment (VCI): progress towards knowledge and treatment*. *Dement Neuropsychol*, 2010. **4**: p. 1.
 3. McCormick, M., Varghese, T., Wang, X., Mitchell, C., Kliewer, M.A., and Dempsey, R.J., *Methods for robust in vivo strain estimation in the carotid artery*. *Phys Med Biol*, 2012. **57**(22): p. 7329-53.
 4. Randolph, C., Tierney, M.C., Mohr, E., and Chase, T.N., *The Repeatable Battery for the Assessment of Neuropsychological Status (RBANS): preliminary clinical validity*. *J Clin Exp Neuropsychol*, 1998. **20**(3): p. 310-9.
 5. Wang, X., Mitchell, C.C., Varghese, T., Jackson, D.C., Rocque, B.G., Hermann, B.P., and Dempsey, R.J., *Improved correlation of strain indices with cognitive dysfunction with inclusion of adventitia layer with carotid plaque*. *Ultrasonic Imaging*, doi:10.1177/0161734615589252.

Chapter 5 : Receiver Operating Characteristic Analysis of Strain Indices as a Classifier for Cognitive Impairment

5.1 Introduction

In this chapter¹, we combine cognition results obtained from a newer group of patients in Chapter 4 with the earlier group that we had reported in Chapter 3 [1-2], and evaluate correlations between strain indices and cognitive function, as well as the feasibility of using strain indices to classify patients with cognitive impairment. Vascular cognitive decline may be caused by micro-emboli generated from carotid plaque instability [3]. We have previously shown that maximum strain indices in carotid plaque were significantly correlated with cognitive function [1-2]. In this chapter, we examine correlations with a larger sample size, along with performance evaluation of these maximum strain indices to possibly predict cognitive impairment.

Ultrasound based strain imaging and cognition assessment were conducted on 75 human subjects. We use either a Repeatable Battery for the Assessment of Neuropsychological Status (RBANS) [4] or National Institute of Neurological Disorder and Stroke-Canadian Stroke Network (NINDS-CSN) Vascular Cognitive Impairment

¹This chapter is adapted from Wang, X., Jackson, D.C., Mitchell, C.C., Varghese, T., Wilbrand, S.M., Rocque, B.G., Hermann, B.P., and Dempsey, R.J., *Classification of symptomatic vs. asymptomatic patients with cognitive decline using non-invasive carotid plaque based strain indices as biomarkers*. Ultrasound Med Biol, submitted.

Harmonization Standards [5] as a test protocol for a standardized cognitive assessment. Z-scores are tabulated to normalize cognition measures obtained from these two tests. Radiofrequency (RF) echo signals for ultrasound strain imaging are acquired on the carotid arteries using either a Siemens Antares with a VFX 13-5 linear array transducer or a Siemens S2000 with an 18L6 linear array transducer. The same hierarchical block-matching motion tracking algorithm [6] developed in our laboratory is utilized to estimate accumulated axial, lateral, and shear strain indices in carotid plaque with inclusion of adventitia regardless of the ultrasound system and transducer used. Correlations of z-score to the maximum strain indices are performed with Pearson's correlation coefficients (r) and significance values (p) obtained. Maximum strain indices are also utilized to predict cognitive impairment using receiver operating characteristic (ROC) analysis.

5.2 Materials and Methods

5.2.1 Data acquisition

Ultrasound imaging and corresponding cognition tests were performed on 75 patients (44 male and 31 female) with significant plaque prior to carotid endarterectomy (CEA) procedure at the University of Wisconsin-Madison Hospitals and Clinics. Patients participated in the study after providing informed consent using a protocol approved by the University of Wisconsin-Madison Institutional Review Boards (IRB). The age of the patients ranged from 43 to 85, with a mean and standard deviation of 68.65 ± 9.23 respectively. The first group of 24 patients participated in the study before 2011, and a second group of 51 patients participated since 2011.

Ultrasound RF echo signal data was acquired, along with clinical B-mode images and color-flow Doppler images on these patients. A Siemens Antares ultrasound system (Siemens Ultrasound, Mountain View, CA, USA) equipped with a VFX 13-5 linear array transducer was used to acquire ultrasound data on the first group of 24 patients, while a Siemens S2000 ultrasound system (Siemens Ultrasound, Mountain View, CA, USA) equipped with an 18L6 linear array transducer was used on the second group of 51 patients. Although different transducers and different ultrasound systems were utilized, the transmit frequency was set to 11.4 MHz for both transducers and on both systems. The sampling frequency of 40 MHz was also the same for both ultrasound systems with a single transmit focus set at the depth of the plaque.

5.2.2 Strain indices estimation

We used the same strain estimation algorithm on all patients regardless of the ultrasound system. Plaque regions with adventitia were segmented by a radiologist/research sonographer for end-diastole frames using the Medical Imaging Interaction Toolkit (MITK), as shown in Figure 5.1. Segmentations were done on B-mode images reconstructed from RF data. Clinical B-mode images and color-flow Doppler images were also used to help determine plaque borders. The segmented regions were automatically tracked over two complete cardiac cycles using a hierarchical block-matching motion tracking algorithm developed in our laboratory [6], using the segmented end-diastolic frame as the initial frame of the sequence. For optimal motion tracking purpose, a dynamic frame skip method was utilized with a short frame skip during systole and a long frame skip during end-diastole [6].

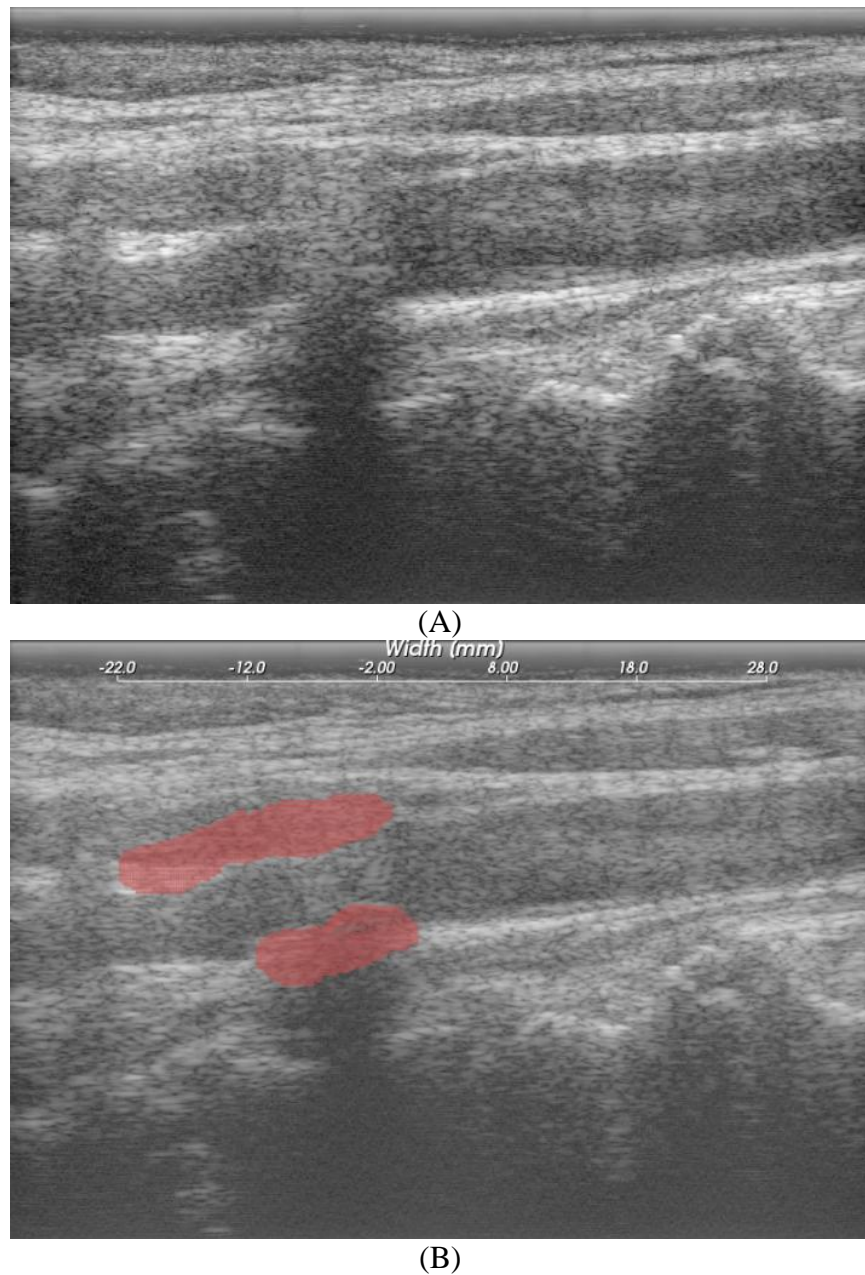


Figure 5.1: B-mode image reconstructed from RF data (A) and segmented plaque with adventitia on the B-mode image (B).

Displacements between consecutive frames were tracked utilizing normalized cross-correlation analysis with recursive Bayesian regularization over three iterations [7], and filtered with a 3×3 pixel median filter. Accumulated displacements over a cardiac cycle were then utilized to estimate strain by applying a modified least squares fit over a 7 pixel

length. Strain images computed inside the segmented region were overlaid on the corresponding B-mode images. Maximum accumulated strain over two cardiac cycles was then located in the strain image and averaged over the surrounding 10-20 data points to reduce noise artifacts. The absolute value of the maximum strain over a cardiac cycle was used in our analysis.

5.2.3 Cognition assessment

Cognition assessment was also performed before the CEA procedure on each patient. Different cognition test protocols were conducted for the two groups of patients. The first group of 24 patients were assessed using Repeatable Battery for the Assessment of Neuropsychological Status (RBANS), which provides an total score for overall cognition status, as well as five sub-scores for specific cognitive abilities including immediate memory, visuospatial/constructional, language, attention and delayed memory [4]. The second group of 51 patients were assessed using National Institute of Neurological Disorders and Stroke-Canadian Stroke Network (NINDS-CSN) Vascular Cognitive Impairment Harmonization Standards 60-minute protocol, which consists of several scores evaluating executive/activation, visuospatial, language/lexical retrieval, memory/learning, neuropsychiatric/depression symptoms, and pre-morbid status [5].

To standardize and normalize the cognition scores, a z-score was generated for every patient from the two independent groups of patients assessed with the different protocols. For the first group of 24 patients, the z-scores represented the standardized score for RBANS Total score. For the second group of 51 patients, the z-score was calculated for each sub-test, and then averaged across all sub-tests. In this way, we combined the cognition evaluation for the two groups of patients using z-scores.

5.2.4 Statistics and ROC analysis

Ultrasound imaging and cognition assessment were conducted separately and were blinded to each other. Maximum strain indices were correlated to the standardized z -score using a Pearson's correlation coefficient r and a significance level of $p < 0.05$ using a two-tailed t -test. Correlation analysis were performed in each group of patients separately, and also in all patients combined. Patients were also divided into symptomatic and asymptomatic groups based on clinical criteria. Stroke and transient ischemic attack (TIA) were the clinical symptoms that were utilized for classifying a patient as symptomatic. Among the 75 patients, 47 patients were symptomatic, 27 patients were asymptomatic and one patient was questionable based on clinical findings.

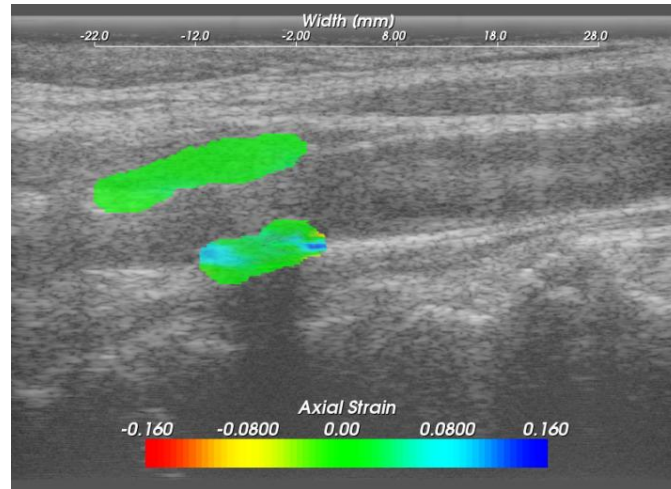
ROC analysis was performed to evaluate the efficacy of high strain indices to predict cognitive impairment. Patients were divided into 2 groups using $z = 0$ as a threshold; namely a lower cognition group with $z < 0$ and a higher cognition group with $z \geq 0$. The lower cognition group was assigned to the positive category, and the higher cognition group assigned to the negative category. Maximum axial, lateral and shear strain indices were used as predictors, as well as a combination of two of them, and a combination of all three indices. Using a 10-fold cross-validation logistic regression as classifier, ROC analysis for the single features and combined features were performed using Weka 3 (Version 3.7.12, Machine Learning Group at the University of Waikato) [8]. Sensitivity and specificity for both single features and combined features were also computed. ROC curves were fitted using parameters [9] generated with ROC-kit software (Version 0.9.1 beta, Metz ROC Software at the University of Chicago). The area under curve (AUC) and the upper and lower bounds of a 95% confidence interval (CI) were also estimated using

ROC-kit.

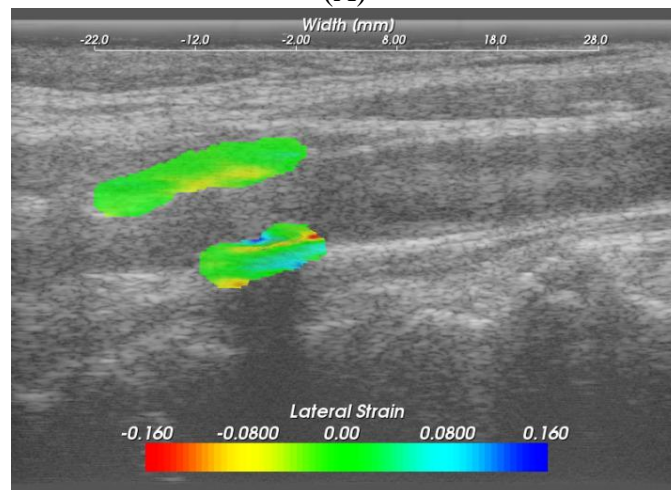
5.3 Results

5.3.1 Correlation study

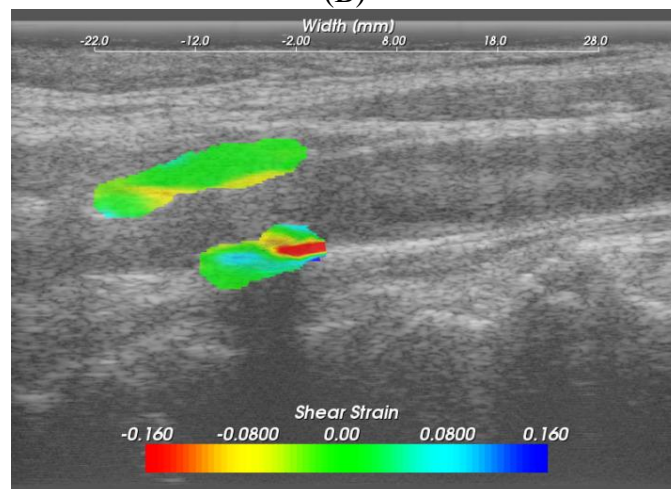
Figure 5.2 shows typical axial, lateral and shear strain images overlaid on B-mode images for the plaque segmented in Figure 5.1. The magnitude and direction of strains are also depicted on the color bar. Positive strain represents expansion of the vessel wall and plaque, while negative strains represent compression. The distribution and variation of strain inside the plaque indicates plaque heterogeneity. Note that the composition or tissue type of plaque changes from region to region within a single plaque. Higher strains are observed at the vessel wall - plaque interface close to adventitia, especially for shearing strains.



(A)



(B)



(C)

Figure 5.2: Axial (A), lateral (B) and shear (C) strain images in the segmented region overlaid on the B-mode image.

Figure 5.3 presents plots of correlations of z-scores with maximum axial, lateral and shear strain indices for all patients, and for symptomatic and asymptomatic groups separately. A linear fit was performed for all patients, and also for the two groups respectively. Correlation coefficients and significance values for all patients, the two groups of patients recruited at different time periods, and the symptomatic group and asymptomatic group are shown in Table 5.1. Since z-score represent the standardized RBANS Total score for the first group of 24 patients, the correlation coefficients and significance values are the same as reported previously [2]. Overall the z-score decreases with increasing strain indices, indicating that higher strain indices are associated with lower cognitive function. The correlation coefficient reduces when the two groups of patients were combined. However, all correlations remain significant, with $p < 0.05$.

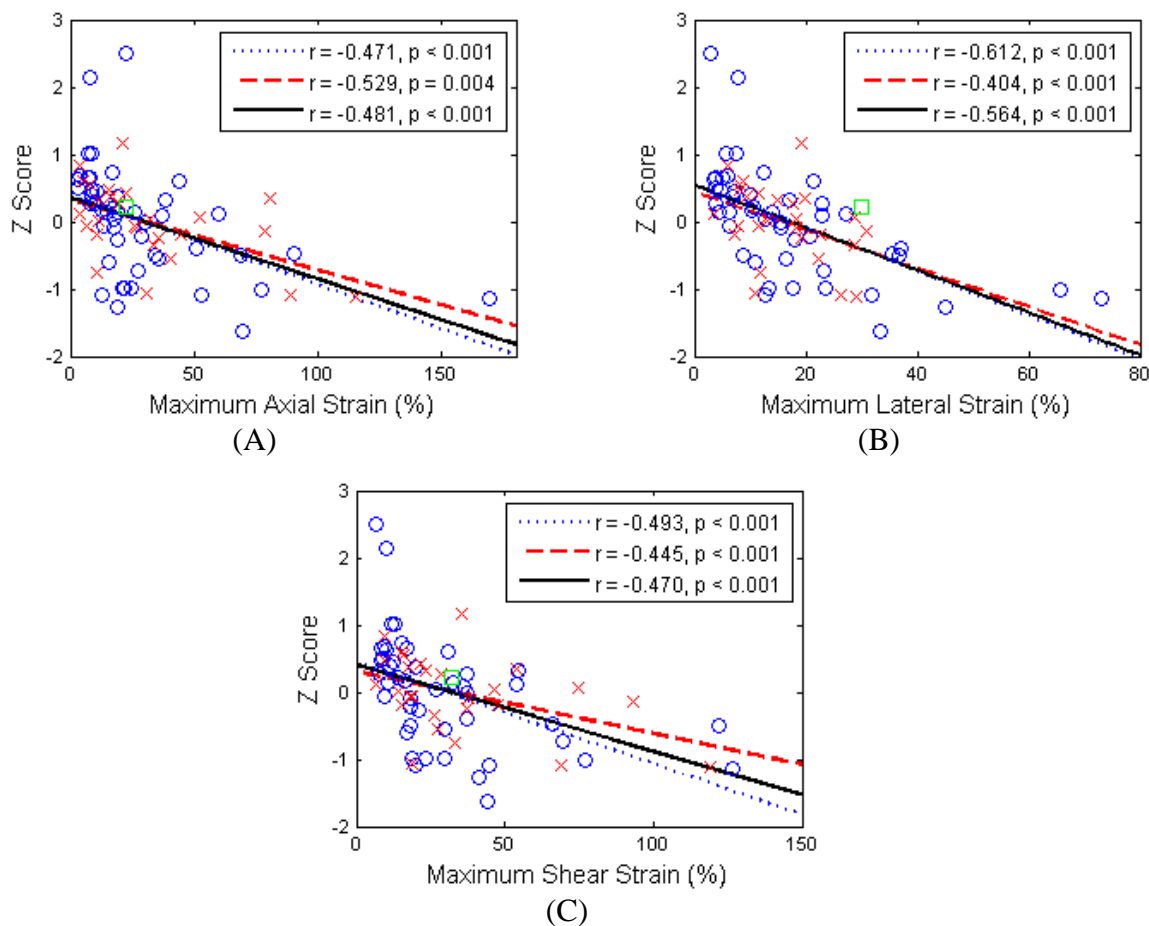


Figure 5.3: Linear least-squares fits of the z-scores with maximum axial strain (A), maximum lateral strain (B) and maximum shear strain (C). \circ = Symptomatic, \times = asymptomatic, \square = questionable, the dotted line represents the linear fit for symptomatic, dashed line the linear fit for asymptomatic, and the solid line denotes the linear fit for all patients.

	Axial Strain	Lateral Strain	Shear Strain
All (n=75)	$r = -0.481, p < 0.001$	$r = -0.564, p < 0.001$	$r = -0.470, p < 0.001$
First group (n = 24)	$r = -0.581, p = 0.003$	$r = -0.656, p < 0.001$	$r = -0.717, p < 0.001$
Second group (n = 51)	$r = -0.597, p < 0.001$	$r = -0.592, p < 0.001$	$r = -0.590, p < 0.001$
Symptomatic (n=47)	$r = -0.471, p < 0.001$	$r = -0.612, p < 0.001$	$r = -0.493, p < 0.001$
Asymptomatic (n=27)	$r = -0.529, p = 0.004$	$r = -0.404, p < 0.001$	$r = -0.445, p < 0.001$

Table 5.1: Correlation of z-score to maximum strain indices.

5.3.2 ROC analysis

Figure 5.4 presents a three-dimensional scatter plot of the maximum axial, lateral and shear strain indices against each other for the lower cognition group ($z < 0$) and the higher cognition group ($z \geq 0$). The strain indices were log-scaled to clearly visualize variations in the indices between individual patients. LSMAS in the axes represents log-scaled maximum axial strain, LSMLS represents log-scaled maximum lateral strain, LSMSS represents log-scaled maximum shear strain. Although some overlap exist between the two groups, we can observe that the lower cognition group tends to have higher strain indices, while the higher cognition group tends to cluster in the region with

lower strain indices range, suggesting the possibility of using maximum strain indices to differentiate between the lower cognition group and the higher cognition group, respectively.

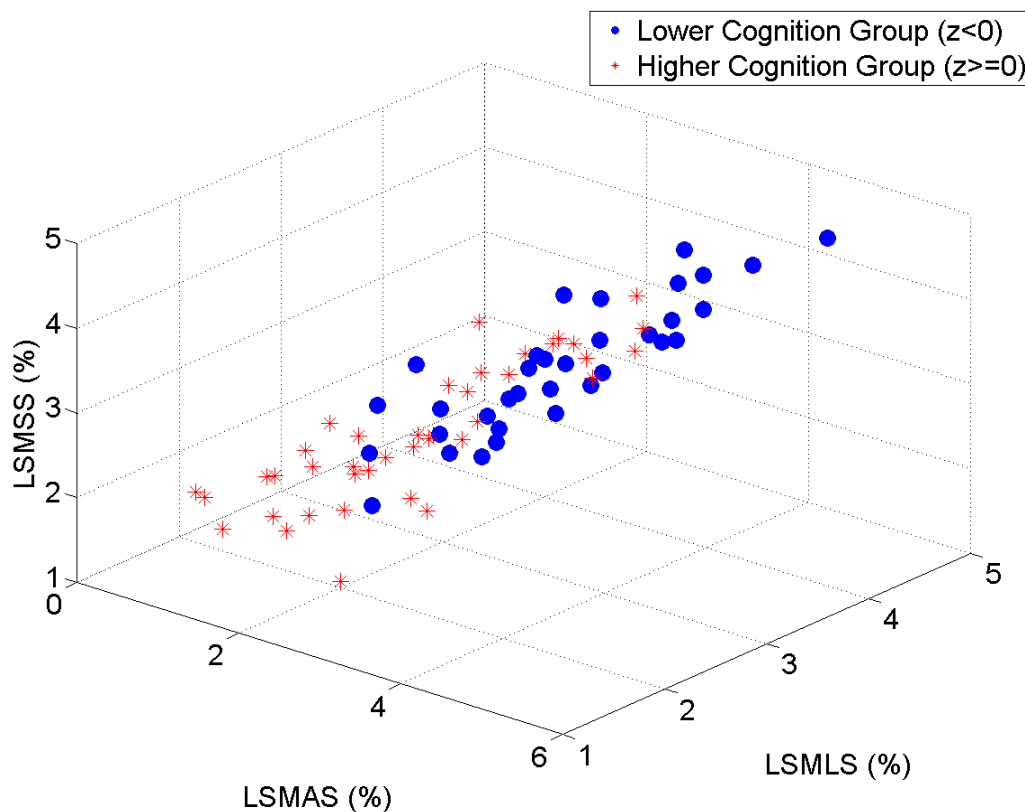


Figure 5.4: Three-dimensional scatter plot of maximum axial, lateral and shear strain indices plotted against each other. \circ = Higher cognition group ($z < 0$), $*$ = lower cognition group ($z \geq 0$).

Figure 5.5 through 5.7 presents three-dimensional scatter plots of the z-scores and two of the maximum strain indices against each other for the symptomatic group and asymptomatic group. The strain indices were log-scaled to clearly visualize variations in the indices between individual patients. LSMAS in the axes represents log-scaled maximum axial strain, LSMLS represents log-scaled maximum lateral strain, LSMSS

represents log-scaled maximum shear strain.

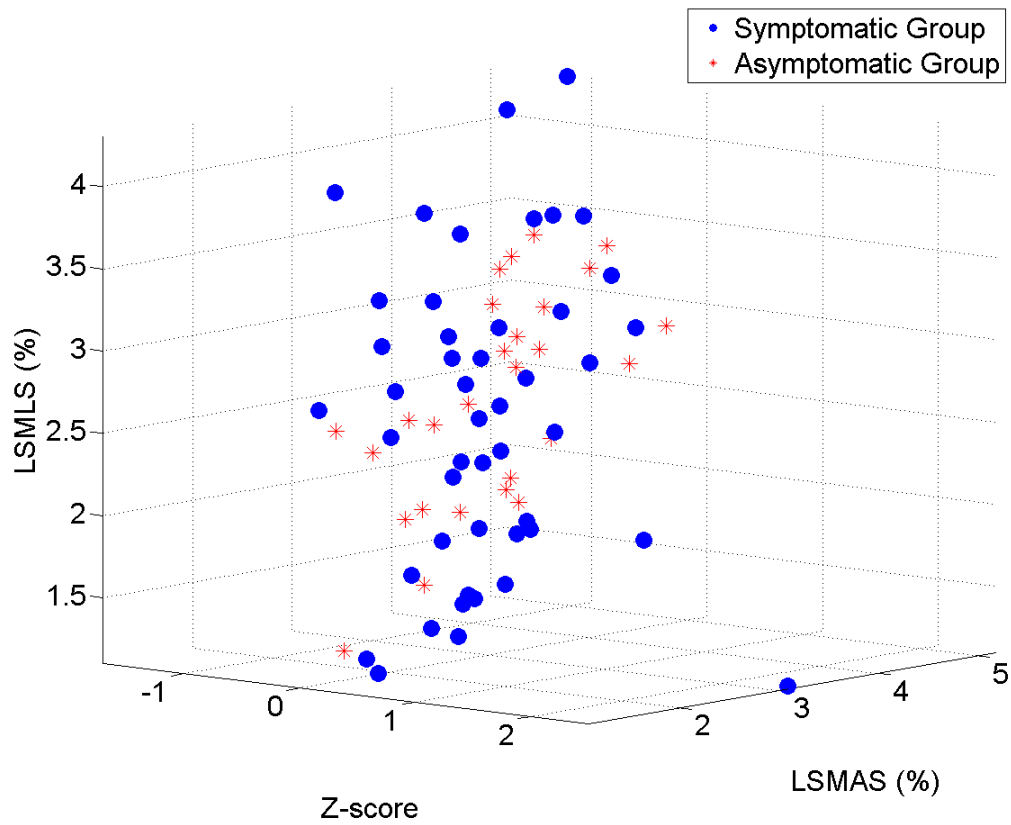


Figure 5.5: Three-dimensional scatter plot of z-score, maximum axial strain and maximum lateral strain plotted against each other. \circ = Symptomatic group, $*$ = asymptomatic group.

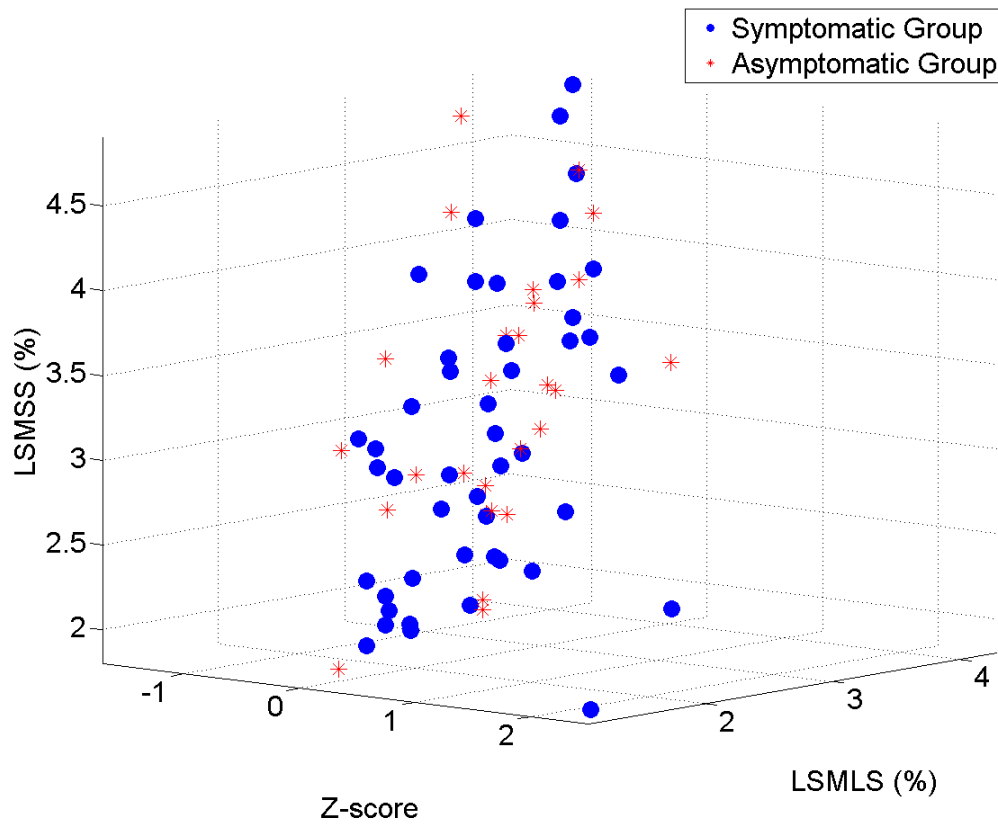


Figure 5.6: Three-dimensional scatter plot of z-score, maximum lateral strain and maximum shear strain plotted against each other. \circ = Symptomatic group, $*$ = asymptomatic group.

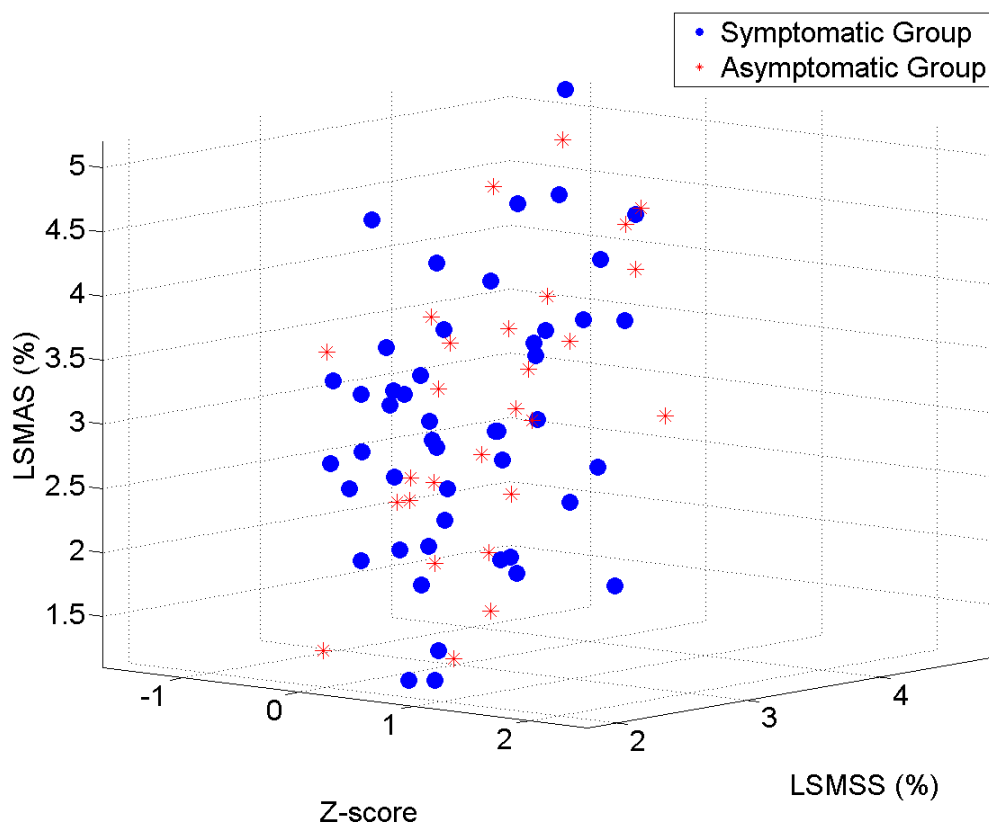
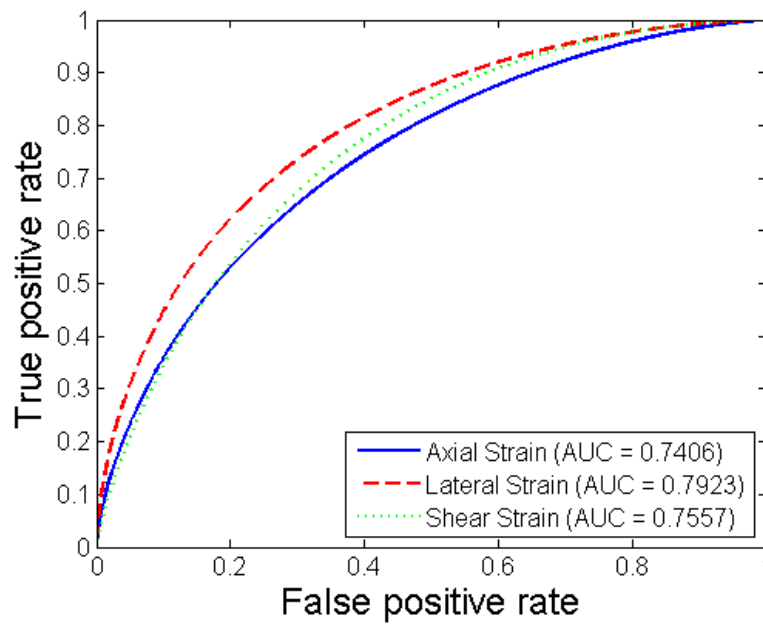
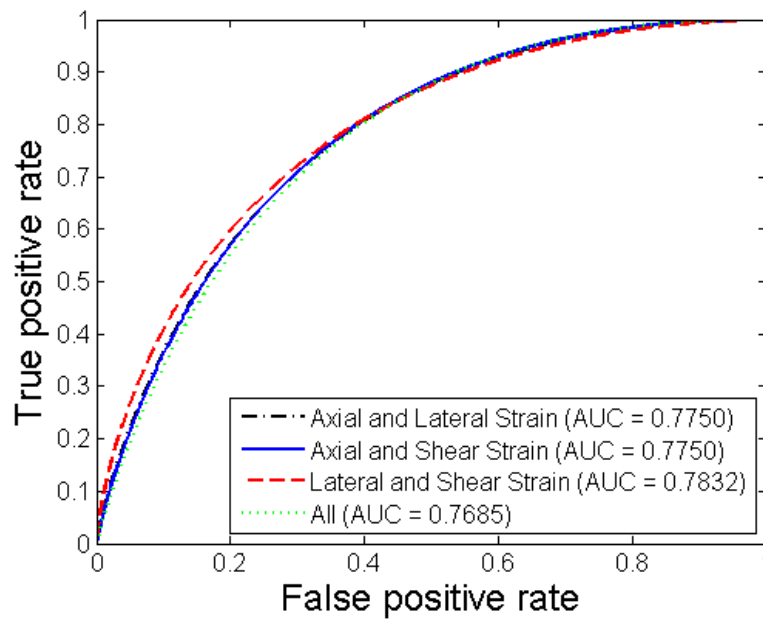


Figure 5.7: Three-dimensional scatter plot of z-score, maximum shear strain and maximum axial strain plotted against each other. \circ = Symptomatic group, $*$ = asymptomatic group.

Figure 5.8 depicts the comparisons of ROC curves for the maximum axial, lateral and shear strain indices individually and in combination to predict cognition decline for all patients. The sensitivity, specificity, AUC and 95% CI for each classifier are listed in Table 5.2. The AUC values for the seven individual and group of indices lie between 0.75 and 0.8, suggesting a good detection performance. Lateral strain indices exhibit the best performance with an AUC of 0.79. However, there was no significant improvement with the combination of strain indices, indicating that the strain indices are not completely independent of each other.



(A)



(B)

Figure 5.8: ROC curves using individual strain indices or features (A) and combined features (B) for all patients.

	Sensitivity	Specificity	AUC	95% (CI _{upper} -CI _{lower})
Axial Strain	0.667	0.633	0.7406	0.8382-0.6191
Lateral Strain	0.693	0.675	0.7923	0.8781-0.6785
Shear Strain	0.653	0.622	0.7557	0.8503-0.6358
Axial and Lateral Strain	0.653	0.632	0.7750	0.8647-0.6587
Axial and Shear Strain	0.640	0.601	0.7750	0.8648-0.6587
Lateral and Shear Strain	0.707	0.686	0.7832	0.8710-0.6683
All	0.680	0.649	0.7685	0.8600-0.6507

Table 5.2: Sensitivity, specificity, area under curve (AUC) and 95% confidence intervals (CI) for individual features and combined features for all patients.

Similar ROC analyses were also conducted for the symptomatic patients only and for the asymptomatic patients only. The ROC curves for symptomatic group and for asymptomatic group are illustrated in Figure 5.9 and Figure 5.10, respectively. The sensitivity, specificity, AUC and 95% CI for symptomatic group and for asymptomatic group are listed in Table 5.3 and Table 5.4, respectively. For the symptomatic group, the AUC values improve to be between 0.78 and 0.85. Lateral strain individually, and the combination of lateral and shear strain provide the best performance with an AUC of 0.85. For the asymptomatic group, the AUC values are not as high, between 0.59 and 0.69. Among all classifiers, lateral strain indices provide the best performance with an AUC of 0.68. The comparison between different groups of patients indicates that the performance of maximum strain indices to predict cognition impairment is better for

symptomatic patients. Similarly, there was no significant improvement with the combination of features, for both symptomatic and asymptomatic patient groups as observed for the entire group of patients.

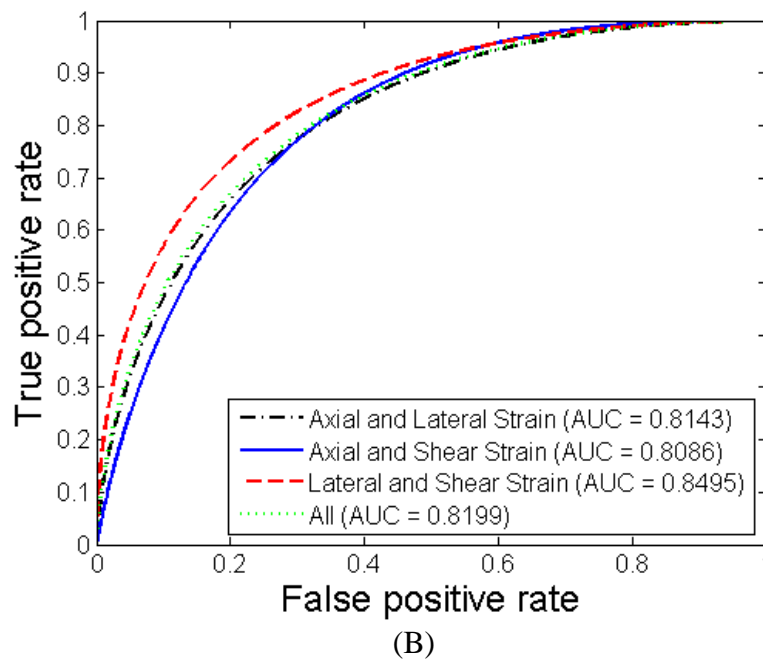
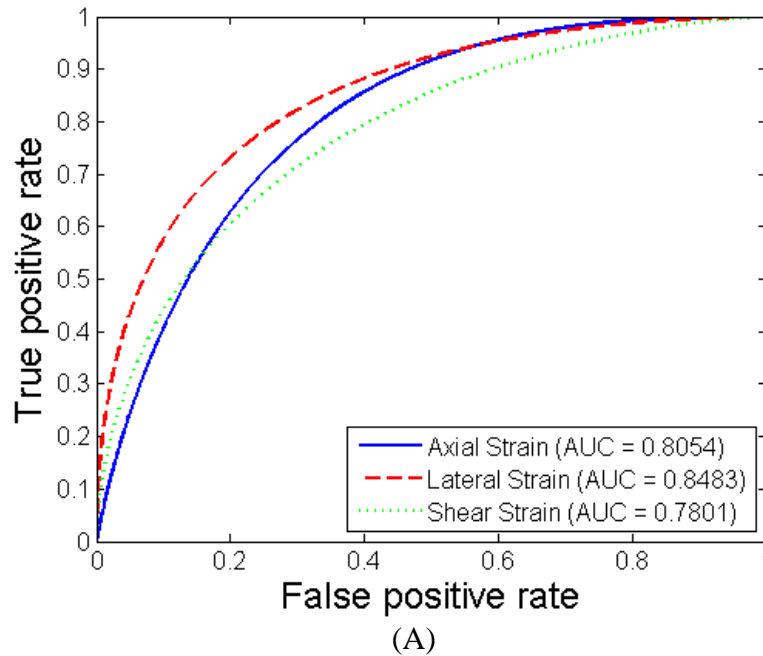


Figure 5.9: ROC curves using individual features (A) and combined features (B) for symptomatic patients.

	Sensitivity	Specificity	AUC	95% (CI_{upper} - CI_{lower})
Axial Strain	0.681	0.641	0.8054	0.9051-0.6596
Lateral Strain	0.723	0.703	0.8483	0.9326-0.7133
Shear Strain	0.638	0.607	0.7801	0.8892-0.6267
Axial and Lateral Strain	0.723	0.703	0.8143	0.9105-0.6714
Axial and Shear Strain	0.681	0.641	0.8086	0.9069-0.6640
Lateral and Shear Strain	0.723	0.694	0.8495	0.9333-0.7147
All	0.723	0.694	0.8199	0.9143-0.6781

Table 5.3: Sensitivity, specificity, area under curve (AUC) and 95% confidence intervals (CI) for individual features and combined features for symptomatic patients.

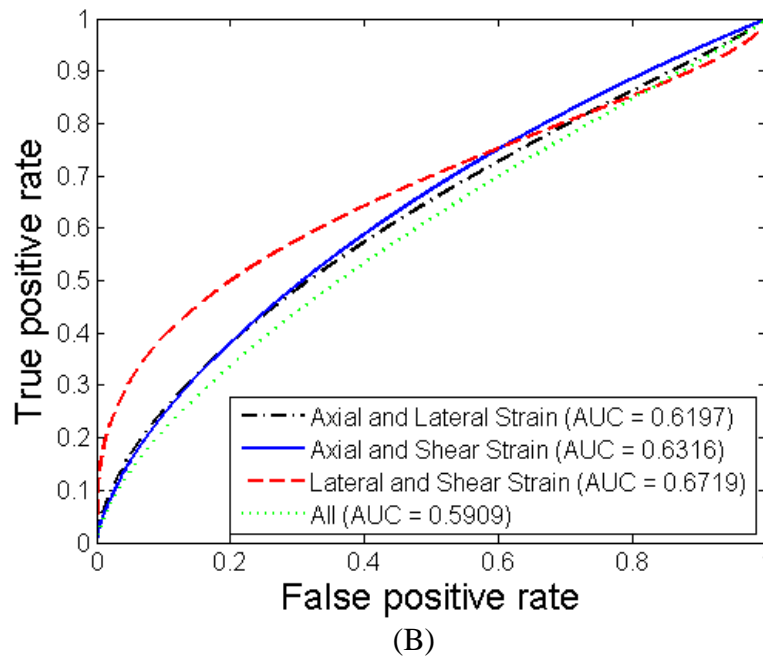
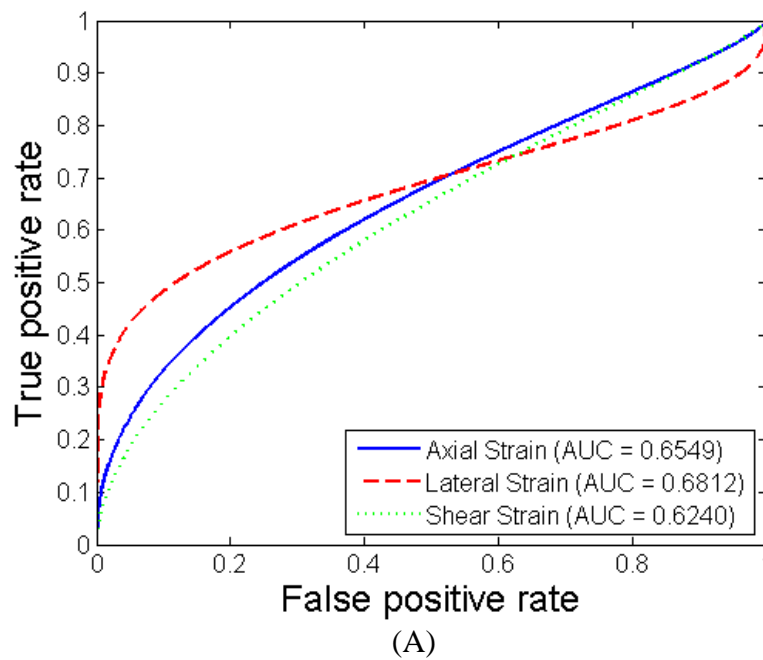


Figure 5.10: ROC curves using individual features (A) and combined features (B) for asymptomatic patients.

	Sensitivity	Specificity	AUC	95% (CI _{upper} -CI _{lower})
Axial Strain	0.667	0.652	0.6549	0.8330-0.4329
Lateral Strain	0.630	0.629	0.6812	0.8582-0.4483
Shear Strain	0.593	0.583	0.6240	0.8115-0.4007
Axial and Lateral Strain	0.667	0.663	0.6197	0.8058-0.4000
Axial and Shear Strain	0.667	0.652	0.6316	0.8141-0.4125
Lateral and Shear Strain	0.667	0.663	0.6719	0.8458-0.4490
All	0.741	0.732	0.5909	0.7834-0.3721

Table 5.4: Sensitivity, specificity, area under curve (AUC) and 95% confidence intervals (CI) for individual features and combined features for asymptomatic patients.

5.4 Discussion

In this chapter, we have shown that the evaluation of cognitive function represented using z-scores possess significant correlations with the maximum strain indices. The primary reason for combining the two groups of patients was to obtain a larger sample size and thereby a more robust prediction model. The negative association indicates that patients with higher strain indices tend to have lower cognitive function, which is also supported by what was observed in the three-dimensional scatter plot for the lower cognition group and the higher cognition group, respectively. This is consistent with our hypothesis that micro-emboli that may lead to cognitive impairment could be generated from rupture of vulnerable plaque that manifest with increased strain, since higher strain suggests larger deformation and increased probability of plaque rupture. Despite the

statistically significant correlation described in this chapter, examination of a larger number of patients is essential to further establish this relationship.

Note that correlation of cognitive function with the maximum lateral strain indices is much higher for symptomatic patients than asymptomatic patients. This is consistent with our hypothesis that plaque in symptomatic patients may have ruptured already, resulting in increased lateral strain with possible fissures than the possibly intact plaque in asymptomatic patients. For asymptomatic patients, the plaque might still be intact, thus the fibrous cap may limit the deformation of plaque in the lateral direction. However, softer plaque regions with increased strain or deformation in asymptomatic plaque may eventually break off and generate emboli.

Overall, we demonstrated the feasibility of classifying and determining patients at higher risk of cognitive impairment using maximum strain indices. The improved performance of high strain indices that predict cognition impairment in symptomatic patients than that in asymptomatic patients is as expected, since asymptomatic patients are patients devoid of possible clinical symptoms, suggesting there might be other contributions to cognition decline, in addition to embolization. Comparison of ROC curves for symptomatic patients and asymptomatic patients reveal that the etiology of cognitive decline might be different for symptomatic patients and asymptomatic patients. Carotid plaque instability might be an important etiology of vascular cognitive decline for symptomatic patients.

We have shown previously that it is essential to include adventitia into plaque segmentation, since higher shearing strain might occur at the interface of plaque and vessel wall [2]. In this chapter we also observed higher strains at the border of plaque and

at the vessel wall - plaque interface, especially in the shear strain images. The fact that all correlations are significant when we include adventitia in the strain analysis further proves the feasibility of the plaque-with-adventitia segmentation method, and supports theories of the importance of the vessel wall - plaque interface in the pathophysiology of embolic disease.

5.5 Conclusions

In summary, we demonstrated significant correlations between maximum strain indices and cognitive function, and the feasibility of using these maximum strain indices to predict cognitive decline. The significant correlation ($p < 0.05$) and high AUC values visualized in the ROC curves suggest that strain indices obtained in the plaque with the inclusion of adventitia may assist in the characterization of vulnerable plaque and identification of plaque prone to rupture. Ultrasound strain imaging can therefore play an important role in the prediction of embolism from vulnerable plaque and resulting cognitive impairment.

5.6 References

1. Wang, X., Jackson, D.C., Varghese, T., Mitchell, C.C., Hermann, B.P., Kliewer, M.A., and Dempsey, R.J., *Correlation of cognitive function with ultrasound strain indices in carotid plaque*. *Ultrasound Med Biol*, 2014. **40**(1): p. 78-89.
2. Wang, X., Mitchell, C.C., Varghese, T., Jackson, D.C., Rocque, B.G., Hermann, B.P., and Dempsey, R.J., *Improved correlation of strain indices with cognitive dysfunction with inclusion of adventitia layer with carotid plaque*. *Ultrasonic Imaging*, doi:10.1177/0161734615589252.
3. Carr, S., Farb, A., Pearce, W.H., Virmani, R., and Yao, J.S., *Atherosclerotic plaque rupture in symptomatic carotid artery stenosis*. *J Vasc Surg*, 1996. **23**(5): p. 755-65; discussion 765-6.
4. Randolph, C., Tierney, M.C., Mohr, E., and Chase, T.N., *The Repeatable Battery for the Assessment of Neuropsychological Status (RBANS): preliminary clinical*

- validity*. J Clin Exp Neuropsychol, 1998. **20**(3): p. 310-9.
5. Hachinski, V., Iadecola, C., Petersen, R.C., Breteler, M.M., Nyenhuis, D.L., Black, S.E., Powers, W.J., DeCarli, C., Merino, J.G., Kalaria, R.N., Vinters, H.V., Holtzman, D.M., Rosenberg, G.A., Wallin, A., Dichgans, M., Marler, J.R., and Leblanc, G.G., *National Institute of Neurological Disorders and Stroke-Canadian Stroke Network vascular cognitive impairment harmonization standards*. Stroke, 2006. **37**(9): p. 2220-41.
 6. McCormick, M., Varghese, T., Wang, X., Mitchell, C., Kliewer, M.A., and Dempsey, R.J., *Methods for robust in vivo strain estimation in the carotid artery*. Phys Med Biol, 2012. **57**(22): p. 7329-53.
 7. McCormick, M., Rubert, N., and Varghese, T., *Bayesian regularization applied to ultrasound strain imaging*. IEEE Trans Biomed Eng, 2011. **58**(6): p. 1612-20.
 8. Hall, M., Frank, E., Holmes, G., Pfahringer, B., Reutemann, P., and Witten, I.H., *The WEKA data mining software: an update*. ACM SIGKDD explorations newsletter, 2009. **11**(1): p. 10-18.
 9. Brown, C.D. and Davis, H.T., *Receiver operating characteristics curves and related decision measures: A tutorial*. Chemometrics and Intelligent Laboratory Systems, 2006. **80**(1): p. 24-38.

Chapter 6 : Statistics of Strain Indices versus Plaque Study Patients and Volunteers

6.1 Introduction

In this chapter, we perform a statistical analysis on the strain indices among all human subjects and volunteers. We compare histogram and scatter plots of maximum axial, lateral and shear strain indices for groups stratified by clinical findings based on specific vascular risk factors when compared to normal controls.

Vascular risk factors for atherosclerosis, vascular dementia and Alzheimer's disease includes diabetes, hypertension, hyperlipidemia, and tobacco smoking [1]. Patients with hypertension were reported to have larger carotid plaque area, when compared to individuals with normal blood pressure [2]. Hypertension and dyslipidemia were found to coexist with the more vulnerable plaque in Chinese patients with type 2 diabetes [3]. Lower values of high-density lipoprotein (HDL) cholesterol were related to echolucent carotid plaques in Japanese patients with type 2 diabetes [4]. Smoking was found to greatly increase the risk of atherosclerosis, although the effect of smoking may vary among individuals [5]. Cigarette smoking was associated with both hyperechoic calcified plaques and echolucent or hypoechoic soft plaques, where the latter plaques are generally classified as vulnerable plaques prone to rupture [6].

Estimated strain indices in carotid plaque were also compared to the strain estimated in the carotid vessel wall. Paini et al. conducted a study on the strain gradient in plaque

and adjacent CCA wall [7]. He found that patients with a negative strain gradient, namely sites with plaque that had lower radial strain values than that of the CCA wall, were more likely to have type 2 diabetes and dyslipidemia, and thus more prone to plaque rupture. We compare the strain indices obtained in patients with arterial strain indices estimated in the vessel wall of volunteers.

6.2 Materials and Methods

6.2.1 Data acquisition on human subjects

Ultrasound strain imaging was performed on 94 patients with significant plaque prior to an carotid endarterectomy (CEA) procedure at the University of Wisconsin-Madison Hospitals and Clinics. Patients participated in the study after providing informed consent using a protocol approved by the University of Wisconsin-Madison Institutional Review Boards (IRB). The first group of 36 patients participated in the study before 2011, and a second group of 58 patients participated since 2011. The 94 patients comprised of 54 male patients and 38 female patients. Clinical information was missing for 2 of the patients. The patients' age ranged from 43 to 87, with a mean and standard deviation of 69.45 ± 9.34 respectively. The patients' BMI ranged from 18.1 to 45.62, with a mean and standard deviation of 28.53 ± 4.60 respectively.

Ultrasound radiofrequency (RF) echo signal data, along with clinical B-mode images and color-flow Doppler images, were acquired on these patients. A Siemens Antares ultrasound system (Siemens Ultrasound, Mountain View, CA, USA) equipped with a VFX 13-5 linear array transducer was used to acquire ultrasound data on the first group of 36 patients, while a Siemens S2000 ultrasound system (Siemens Ultrasound, Mountain

View, CA, USA) equipped with an 18L6 linear array transducer was used on the second group of 58 patients. Although different transducers and different ultrasound systems were utilized, the transmit frequency was set to 11.4 MHz for both transducers and on both systems. The sampling frequency of 40 MHz was also the same for both ultrasound systems with a single transmit focus set at the depth of the plaque.

We used the same segmentation method and strain estimation algorithm on all patients regardless of the ultrasound system. Details of our algorithm were presented in Chapter 5. Maximum accumulated strain over two cardiac cycles was then located in the strain image and averaged over surrounding 10-20 data points to reduce noise artifacts. The absolute value of the maximum strain over a cardiac cycle was used in our analysis. The corresponding minimum strain was then obtained in the same cardiac cycle. Peak-to-peak strain was defined as the difference between maximum and minimum strain.

6.2.2 Data acquisition on human volunteers

Ultrasound strain imaging was performed on the bilateral vessel walls of 26 human volunteers with or without plaque. Patients participated in the study with informed consent using a protocol approved by the University of Wisconsin-Madison Institutional Review Boards (IRB). Among 26 volunteers, 11 were male, and 15 female. The volunteers' age ranged from 48 to 78, with a mean and standard deviation of 62.23 ± 7.46 respectively.

Ultrasound radiofrequency (RF) echo signal data was acquired, along with clinical B-mode images and color-flow Doppler images using a Siemens S2000 ultrasound system (Siemens Ultrasound, Mountain View, CA, USA) equipped with an 18L6 linear

array transducer. The acquisition environment for human volunteers was the same with that for patients. A rectangular region of interest (ROI) within the vessel wall was segmented by a research sonographer on three end-diastole frames using the Medical Imaging Interaction Toolkit (MITK) on B-mode images reconstructed from RF data. Clinical B-mode images and color-flow Doppler images were also used to help keep the ROIs identical in the three frames. We used the same strain estimation algorithm as that for patients. The absolute value of the maximum strain over a cardiac cycle was used in our analysis.

6.2.3 Statistical methods

The 92 patients were classified into two groups using different clinical criteria. Clinical information was missing for 2 patients. In the first classification, 92 patients were classified as symptomatic, asymptomatic or questionable based on clinical findings. 59 patients were symptomatic, 32 were asymptomatic, and 1 patient was questionable. Then, the patients were classified based on whether they possessed specific vascular risk factors including diabetes, hypertension, hyperlipidemia and tobacco usage. Among 92 patients, 25 patients were diabetic, 74 had hypertension, 75 had hyperlipidemia, and 73 were smokers, or previous smokers, or used other tobacco products.

Histograms and fitted curves, along with three-dimensional scatter plots of different strain indices for different groups were plotted in Matlab (Mathworks, Natick, MA, USA). Maximum axial, lateral and shear strain indices were used as individual predictors, as well as a combination of two of them, and a combination of all three indices. Using a 10-fold cross-validation logistic regression as classifier, sensitivity and specificity for both individual features and combined features were obtained using Weka 3 (Version

3.7.12, Machine Learning Group at the University of Waikato) [8].

6.3 Results

6.3.1 Strain indices histograms

Figure 6.1 shows the histograms for maximum and peak-to-peak axial, lateral and shear strain indices for all patients. Histograms were plotted using 50 bins. The curves were also fitted using the kernel smoothing function in Matlab. Note that for each strain histogram, the distribution of all patients has a peak and then a side lobe.

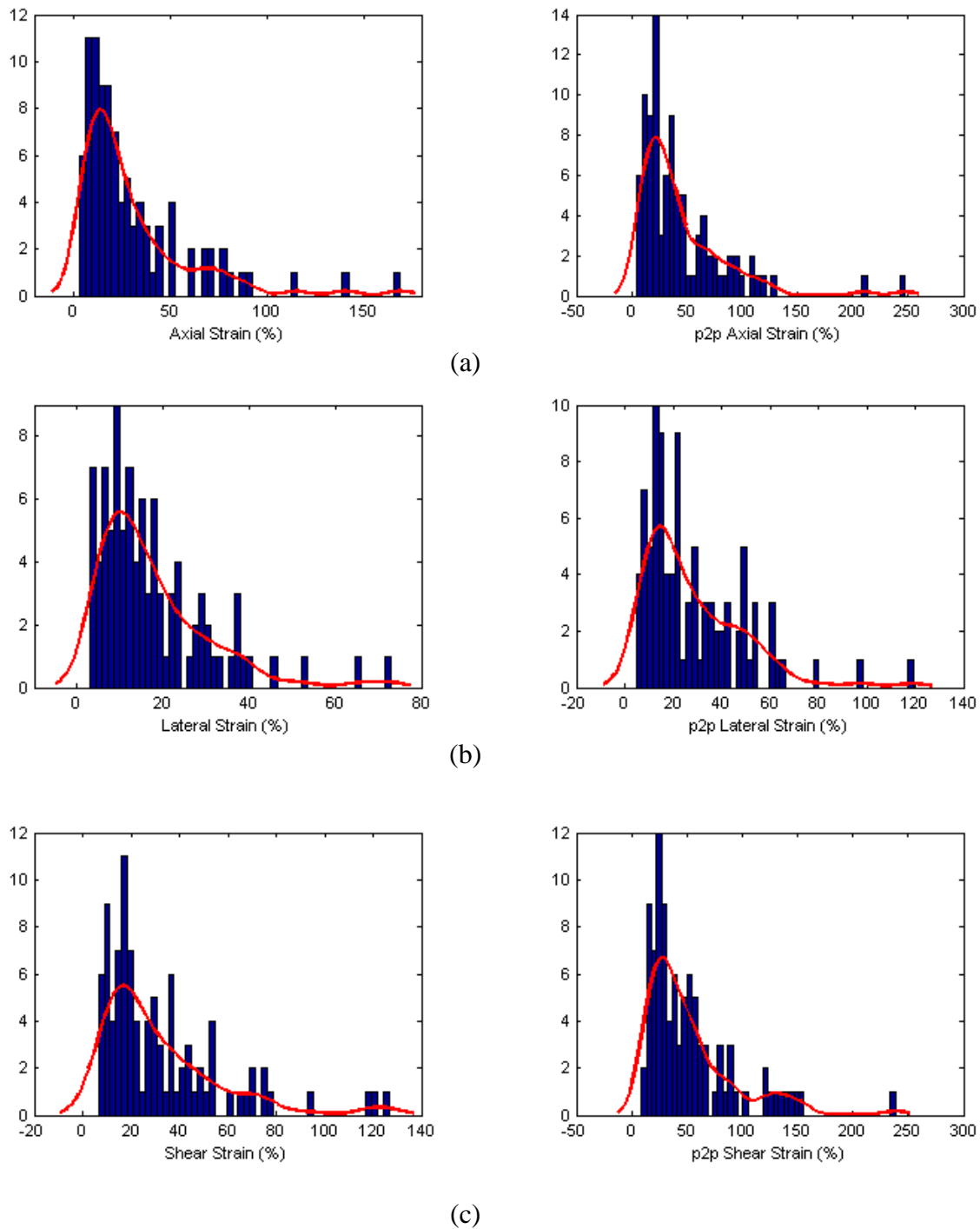
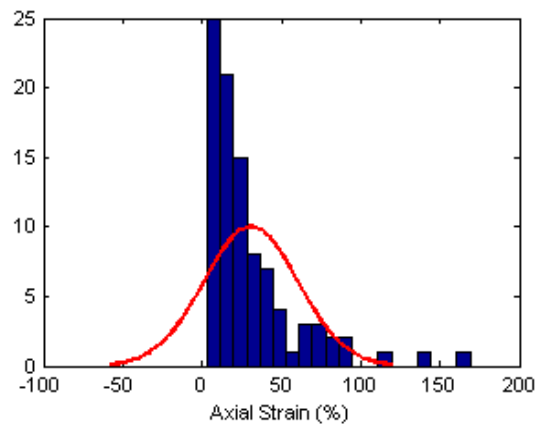


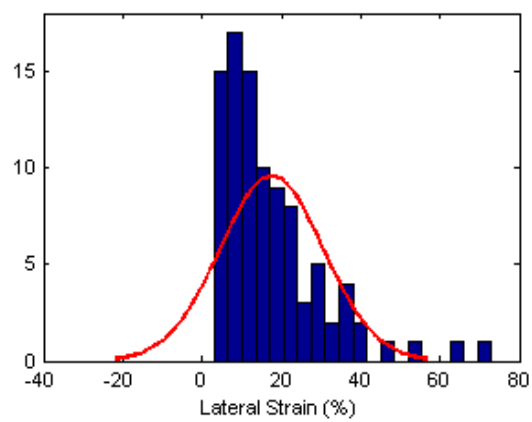
Figure 6.1: Histogram and fitted curve for maximum and peak-to-peak axial strain (a), lateral strain (b) and shear strain (c) for all patients.

A normal distribution fit was then applied to the maximum strain histograms plotted with 20 bins and is shown in Figure 6.2. Mean and standard deviation of the normal

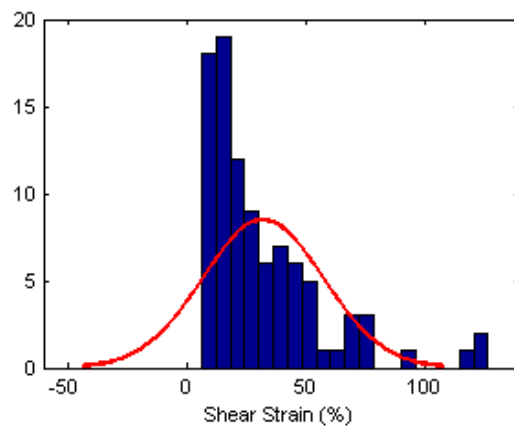
distribution for maximum axial, lateral and shear strain are listed in Table 6.1. Due to the side lobe, the normal distribution and the histogram do not match very well.



(a)



(b)



(c)

Figure 6.2: Normal distribution fitted histogram of maximum axial strain (a), lateral strain (b) and shear strain (c).

	Maximum Axial Strain	Maximum Lateral Strain	Maximum Shear Strain
Mean	30.765	17.542	32.222
Standard Deviation	29.526	13.053	25.287

Table 6.1: Mean and standard deviation of the normal distribution fit for maximum axial, lateral and shear strain indices.

6.3.2 Statistics of strain indices for different clinical groups

As mentioned before, 59 out of 94 patients were symptomatic, while 32 were asymptomatic. The rest are either questionable or lack clinical information. Thus the 59 patients were classified as the symptomatic group, and the 32 patients were classified as the asymptomatic group. Figure 6.3 through 6.5 presents the comparison of strain histograms for the two groups. Different distribution of the histogram can be observed between symptomatic and asymptomatic group with the same strain indices. Note that symptomatic group tends to have higher lateral strain compared to the asymptomatic group.

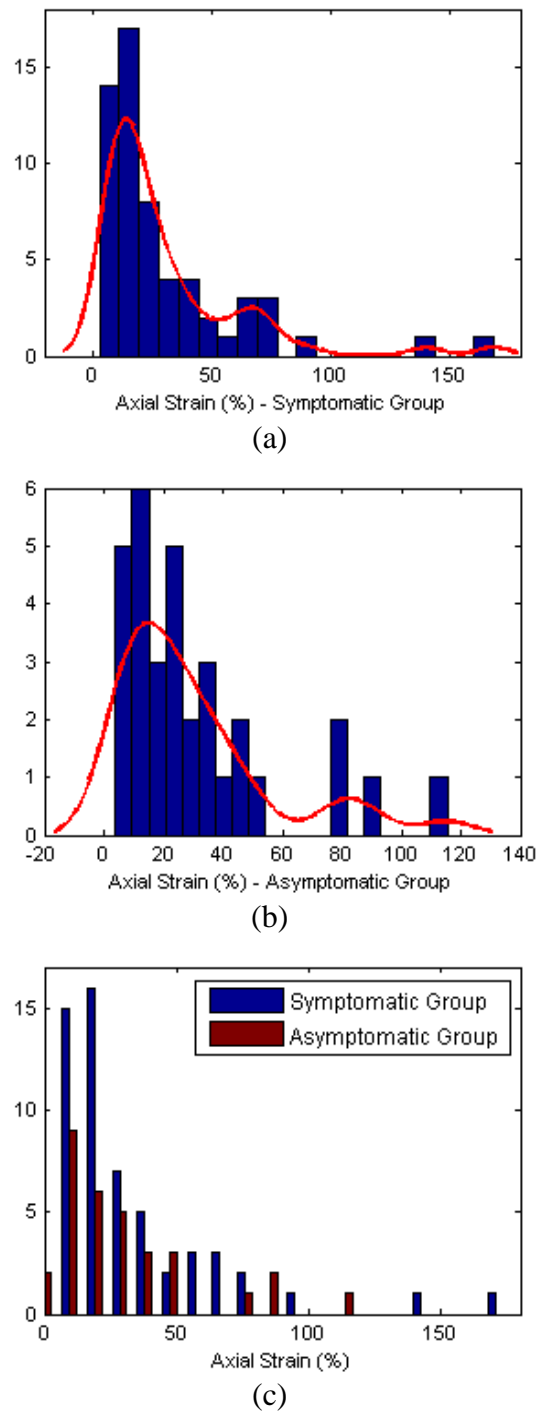
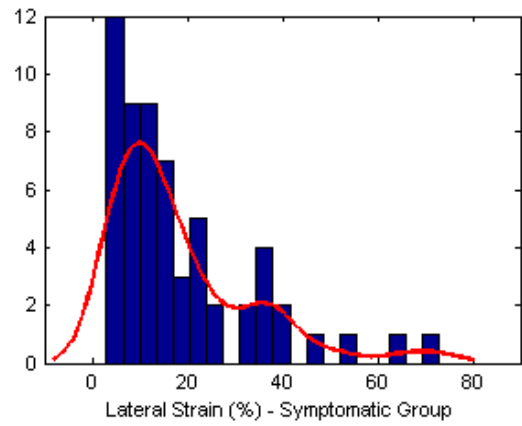
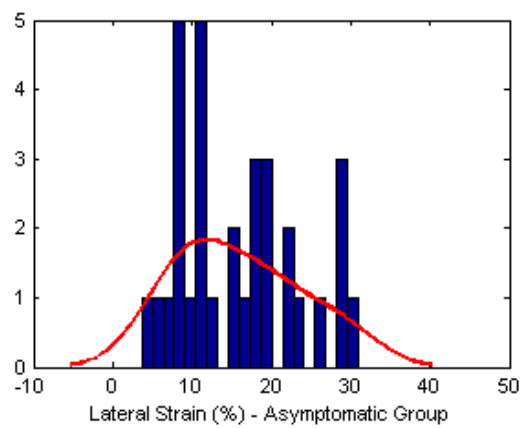


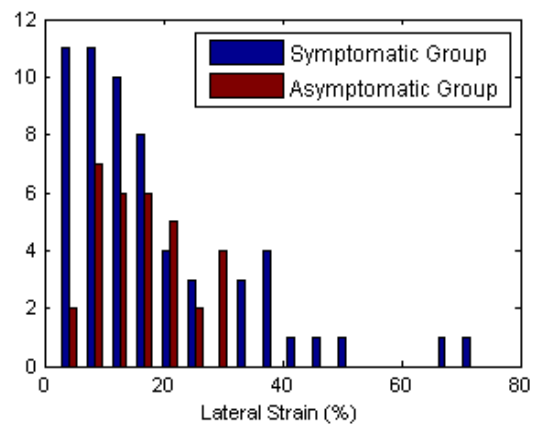
Figure 6.3: Comparison of histograms with fitted curve for maximum axial strain for symptomatic group and asymptomatic group.



(a)

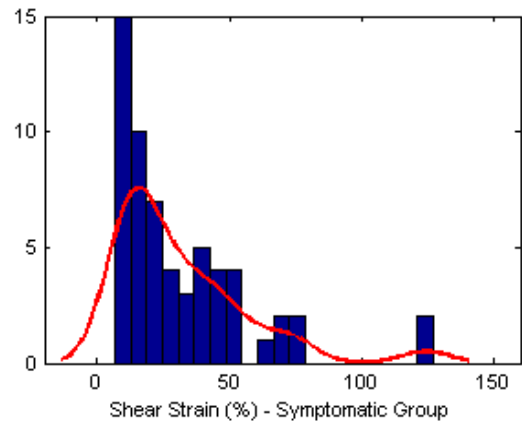


(b)

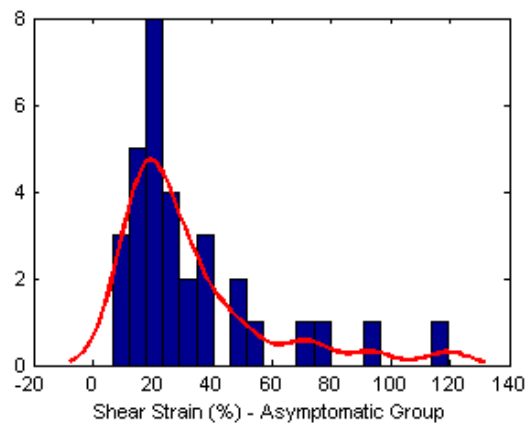


(c)

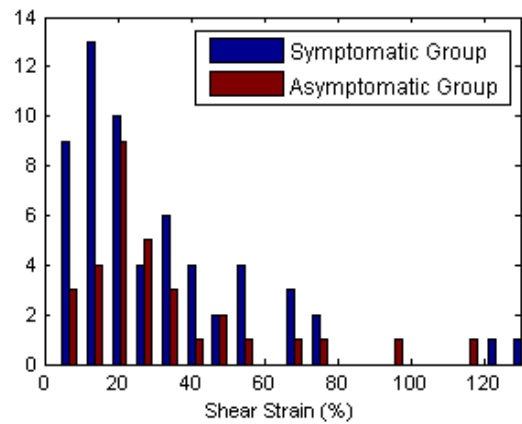
Figure 6.4: Comparison of histograms with fitted curve for maximum lateral strain for symptomatic group and asymptomatic group.



(a)



(b)



(c)

Figure 6.5: Comparison of histograms with fitted curve for maximum shear strain for symptomatic group and asymptomatic group.

Figure 6.6 depicts a three-dimensional scatter plot of the maximum axial, lateral and shear strain indices plotted against each other for the symptomatic group and the

asymptomatic group. The strain indices were log-scaled to clearly visualize variations in the indices between individual patients. LSMAS in the axes represents log-scaled maximum axial strain, LSMLS represents log-scaled maximum lateral strain, LSMSS represents log-scaled maximum shear strain. Although some overlap can be observed for the two groups, the strain indices of symptomatic group were distributed over a larger range when compared to the asymptomatic group. Maximum axial, lateral and shear strain indices individually and in combination were used as classifiers to differentiate symptomatic patients from asymptomatic patients. The sensitivity and specificity for each classifier with individual feature or combined features are listed in Table 6.2.

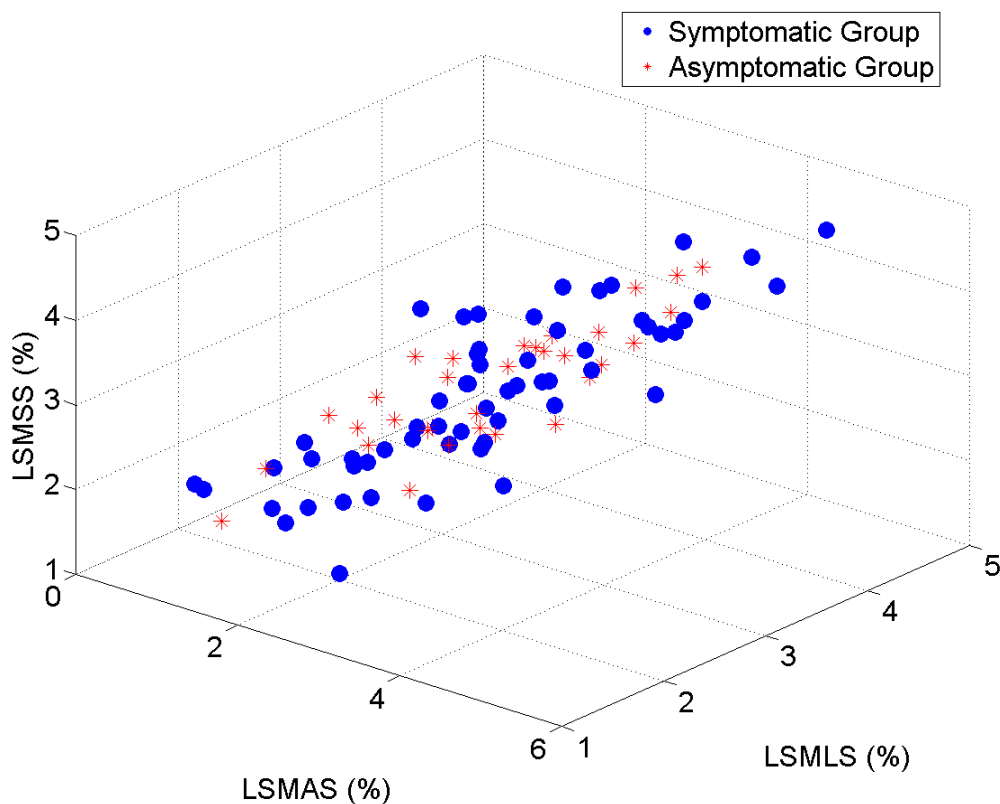
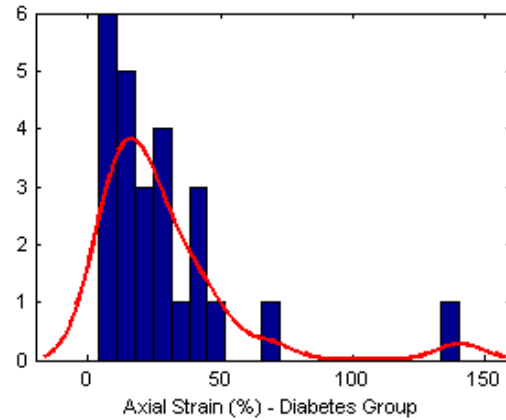


Figure 6.6: Three-dimensional scatter plot of maximum axial, lateral and shear strain indices plotted against each other. \circ = Symptomatic group, $*$ = asymptomatic group.

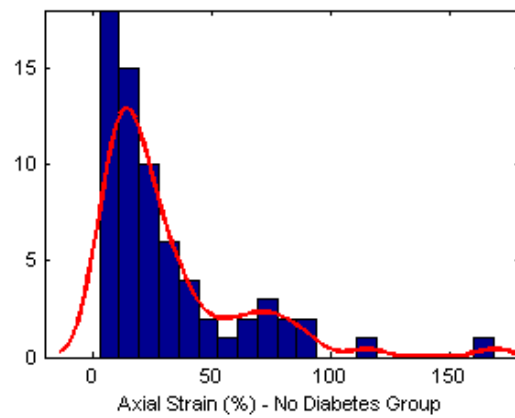
	Sensitivity	Specificity
Axial Strain	0.648	0.648
Lateral Strain	0.648	0.648
Shear Strain	0.637	0.654
Axial and Lateral Strain	0.648	0.648
Axial and Shear Strain	0.626	0.660
Lateral and Shear Strain	0.615	0.666
All	0.615	0.666

Table 6.2: Sensitivity and specificity for the classification of symptomatic patients for individual and combined features.

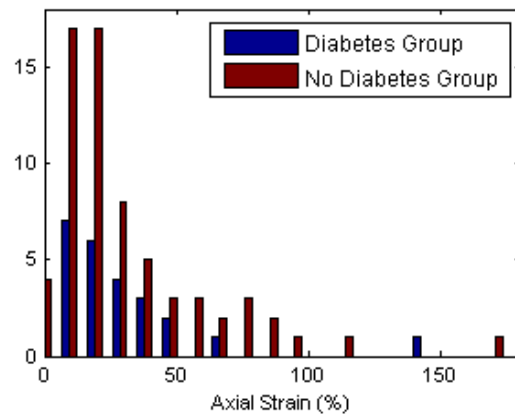
Since clinical information was missing for 2 patients, only 92 patients had clinical documentation of diabetes, hypertension, hyperlipidemia, or tobacco usage. Of these patients 25 out of 92 were diabetic, while the rest, i.e. 67 patients, were not diagnosed with diabetes. Figure 6.7 through 6.9 presents the comparison of strain histograms for the diabetes groups and no diabetes group. No significant difference can be observed for axial and shear strain, since high axial and shear strain also exist in the diabetes group. However, the diabetes group tends to have lower lateral strain.



(a)

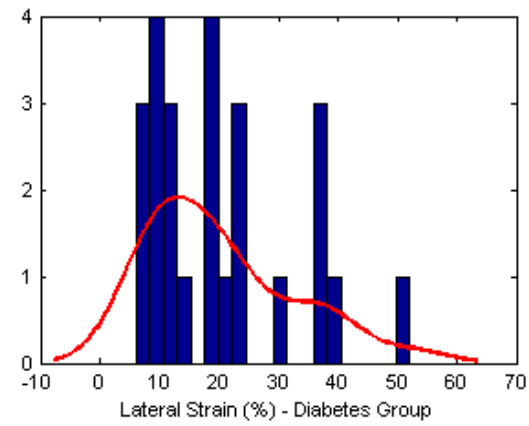


(b)

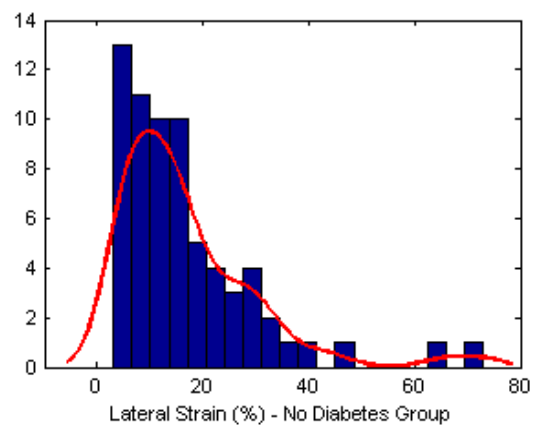


(c)

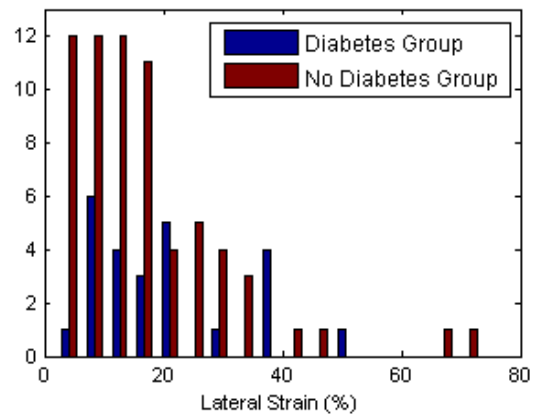
Figure 6.7: Comparison of histograms with fitted curve for maximum axial strain for diabetes group and the no diabetes group.



(a)



(b)



(c)

Figure 6.8: Comparison of histograms with fitted curve for maximum lateral strain for diabetes group and the no diabetes group.

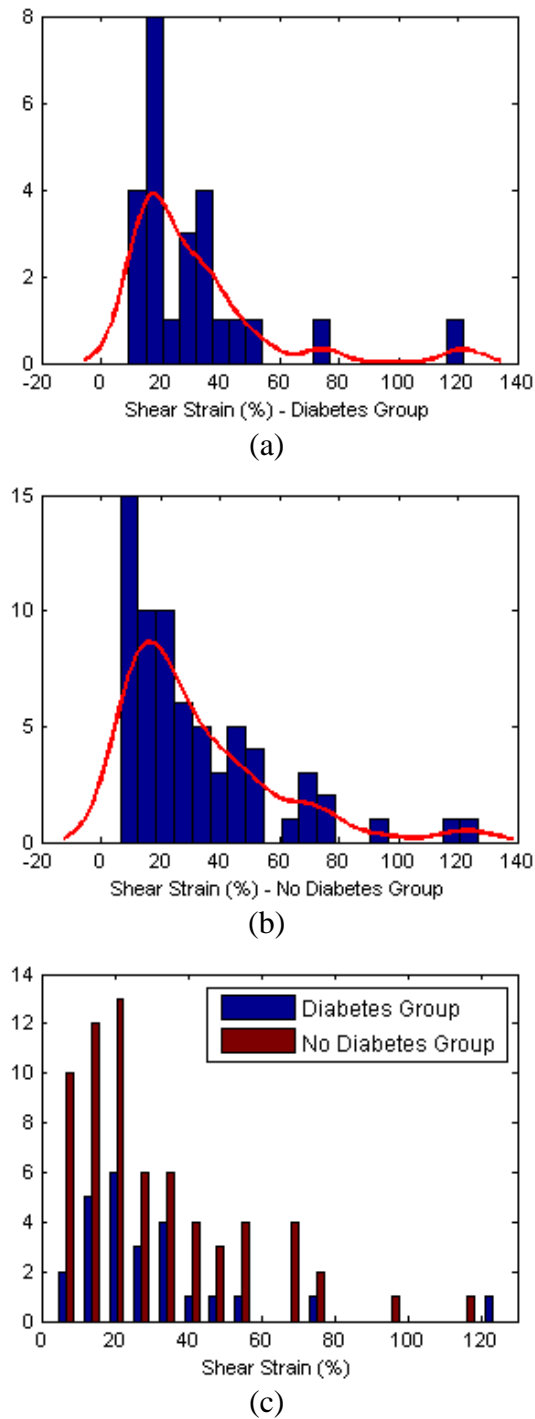


Figure 6.9: Comparison of histograms with fitted curve for maximum shear strain for diabetes group and the no diabetes group.

Figure 6.10 depicts a three-dimensional scatter plot of the maximum axial, lateral and shear strain indices against each other for the diabetes group and no diabetes group.

The strain indices were log-scaled to clearly visualize variations in the indices between individual patients. LSMAS in the axes represents log-scaled maximum axial strain, LSMLS represents log-scaled maximum lateral strain, LSMSS represents log-scaled maximum shear strain. No significant difference was observed, but the strain indices for patients in the no diabetes group is distributed more in the lower strain range than the diabetes group. Maximum axial, lateral and shear strain indices individually and in combination were used as classifiers to differentiate diabetic patients from patients without diabetes. The sensitivity and specificity for each classifier with individual feature or combined features are listed in Table 6.3. The sensitivity and specificity values are higher than that for classifying between the symptomatic group and asymptomatic group.

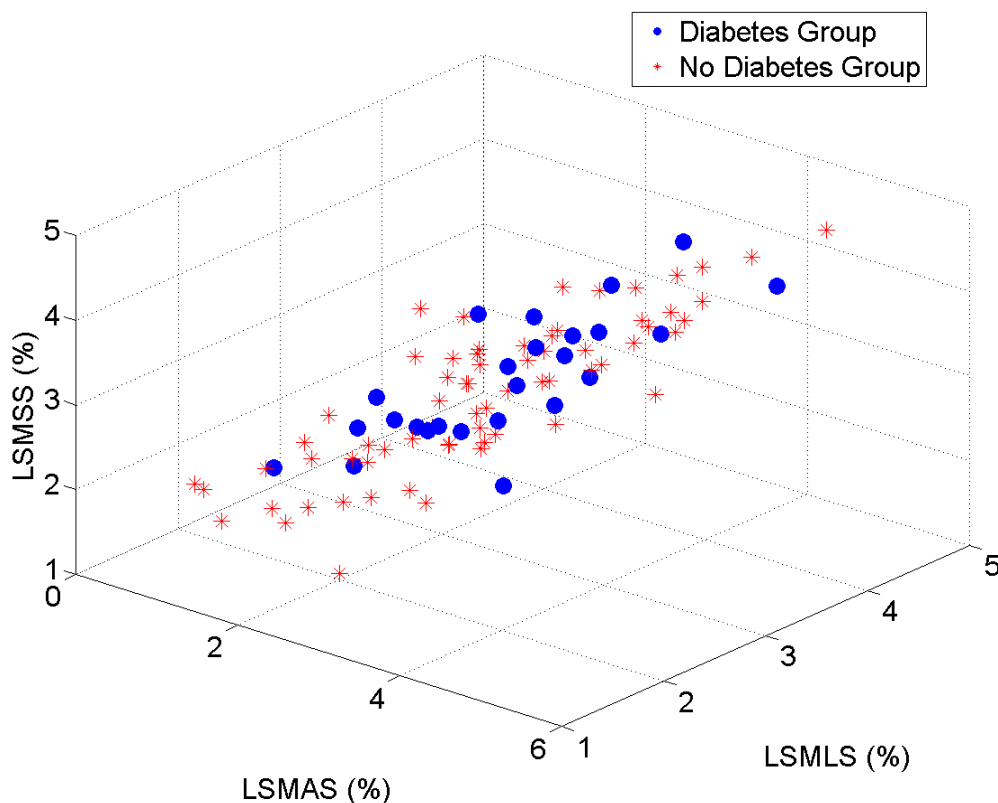
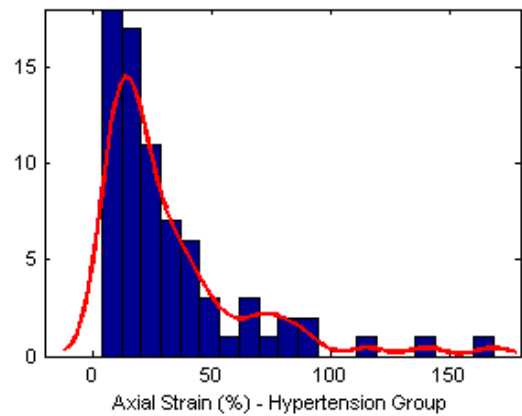


Figure 6.10: Three-dimensional scatter plot of maximum axial, lateral and shear strain indices plotted against each other. \circ = Diabetes group, $*$ = no diabetes group.

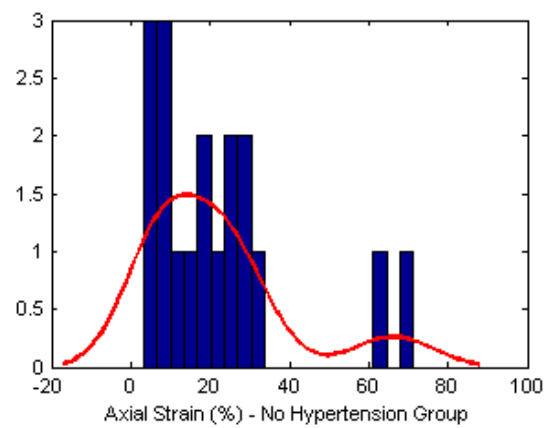
	Sensitivity	Specificity
Axial Strain	0.728	0.728
Lateral Strain	0.707	0.736
Shear Strain	0.728	0.728
Axial and Lateral Strain	0.728	0.678
Axial and Shear Strain	0.728	0.728
Lateral and Shear Strain	0.696	0.715
All	0.717	0.682

Table 6.3: Sensitivity and specificity of classification of patients with diabetes for individual features and combined features.

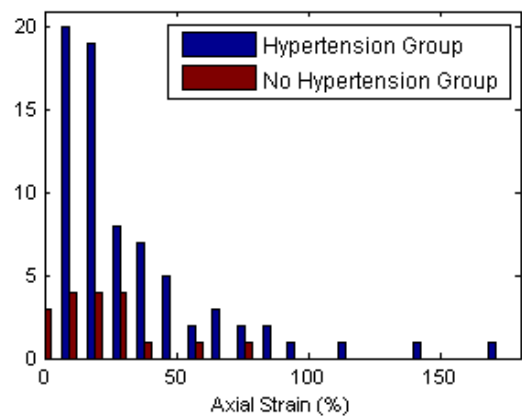
Among the 92 patients, 74 patients had hypertension or were treated for hypertension. Figure 6.11 through 6.13 presents the comparison of strain histograms for hypertension group with $n = 74$ and no hypertension group with $n = 18$. The hypertension group has more patients with higher axial, lateral and shear strain indices than the no hypertension group. The strain distribution in the histogram and smoothing curves are also different for the two groups.



(a)

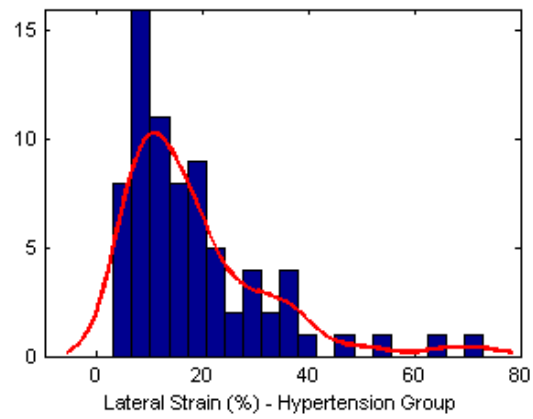


(b)

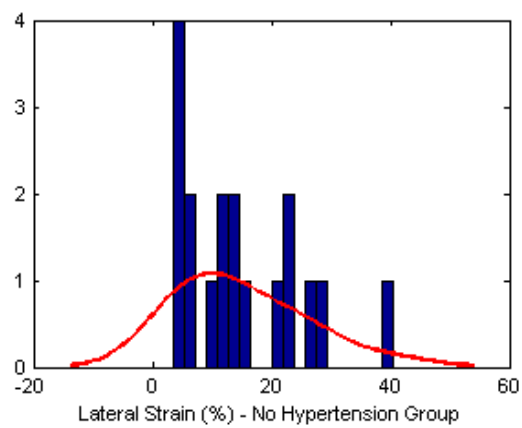


(c)

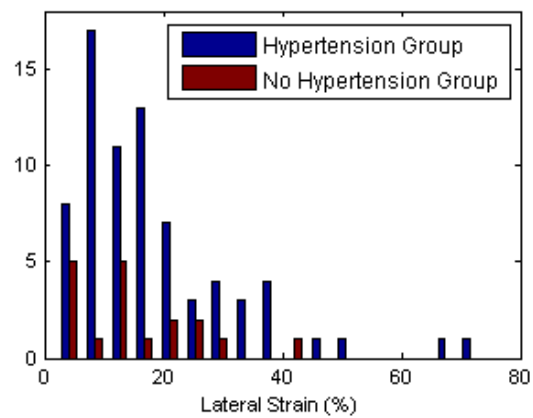
Figure 6.11: Comparison of histograms with fitted curve for maximum axial strain for hypertension and no hypertension group respectively.



(a)

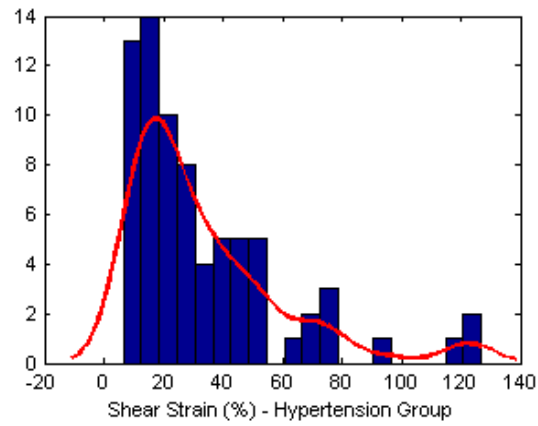


(b)

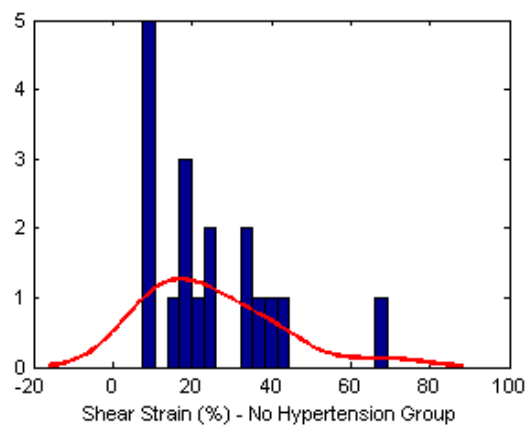


(c)

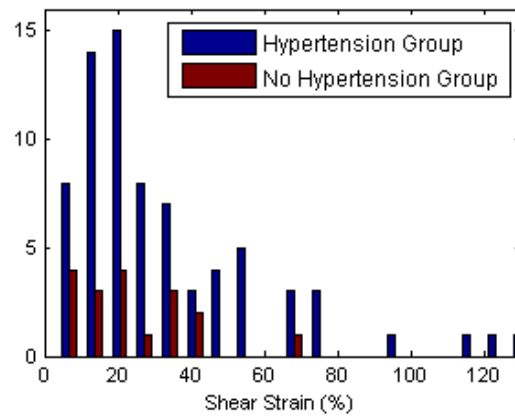
Figure 6.12: Comparison of histograms with fitted curve for maximum lateral strain for hypertension and no hypertension group respectively.



(a)



(b)



(c)

Figure 6.13: Comparison of histograms with fitted curve for maximum shear strain for hypertension and no hypertension group respectively.

Figure 6.14 depicts a three-dimensional scatter plot of the maximum axial, lateral and shear strain indices against each other for the hypertension group and no

hypertension group. The strain indices were log-scaled to clearly visualize variations in the indices between individual patients. LSMAS in the axes represents log-scaled maximum axial strain, LSMLS represents log-scaled maximum lateral strain, LSMSS represents log-scaled maximum shear strain. Similar to what we observed in the histogram comparison, the hypertension group tends to have more strain indices distributed in the high strain range. Maximum axial, lateral and shear strain indices individually and in combination were used as classifiers to differentiate the hypertension group from no hypertension group. The sensitivity and specificity for each classifier with individual feature or combined features are listed in Table 6.4. Both the sensitivity and specificity were above 0.8.

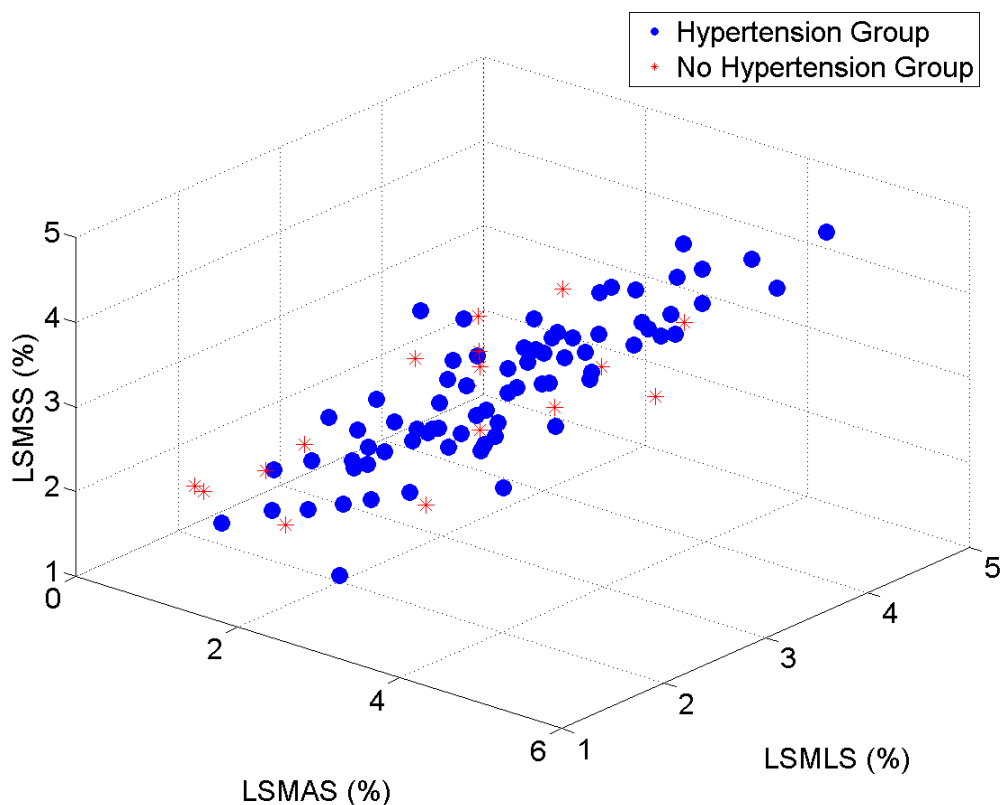
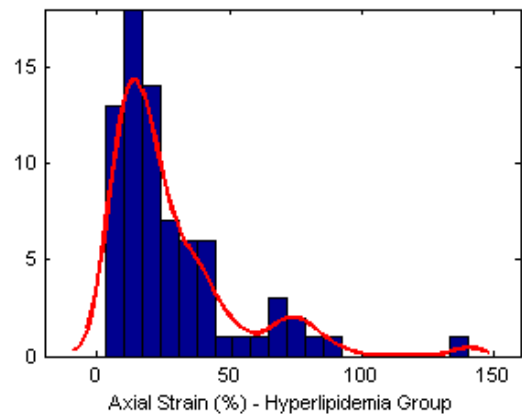


Figure 6.14: Three-dimensional scatter plot of maximum axial, lateral and shear strain indices plotted against each other. \circ = Hypertension group, $*$ = no hypertension group.

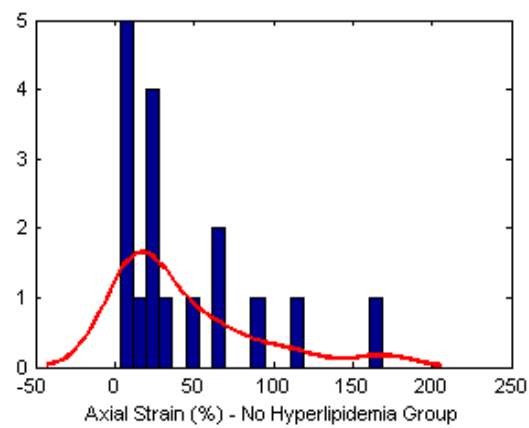
	Sensitivity	Specificity
Axial Strain	0.804	0.804
Lateral Strain	0.804	0.804
Shear Strain	0.804	0.804
Axial and Lateral Strain	0.804	0.804
Axial and Shear Strain	0.804	0.804
Lateral and Shear Strain	0.804	0.804
All	0.804	0.804

Table 6.4: Sensitivity and specificity of classification of patients with hypertension for individual features and combined features.

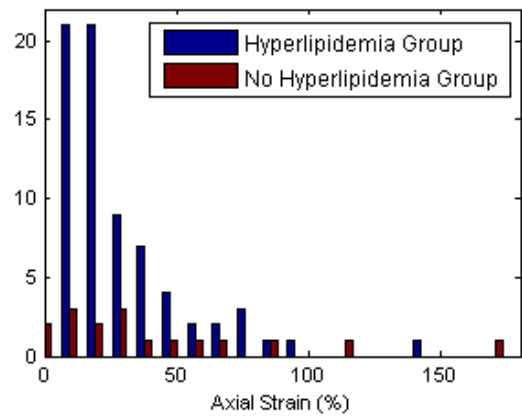
Similarly, 75 out of 92 patients are classified as belonging to the hyperlipidemia group, and the rest 17 were classified as no hyperlipidemia group. Figure 6.15 through 6.17 presents the comparison of strain histograms for the hyperlipidemia group and no hyperlipidemia group. Although the axial and lateral distribution are quite similar for the two groups, some difference in shear strain distribution can be observed.



(a)



(b)



(c)

Figure 6.15: Comparison of histograms with fitted curve for maximum axial strain for hyperlipidemia group and no hyperlipidemia group.

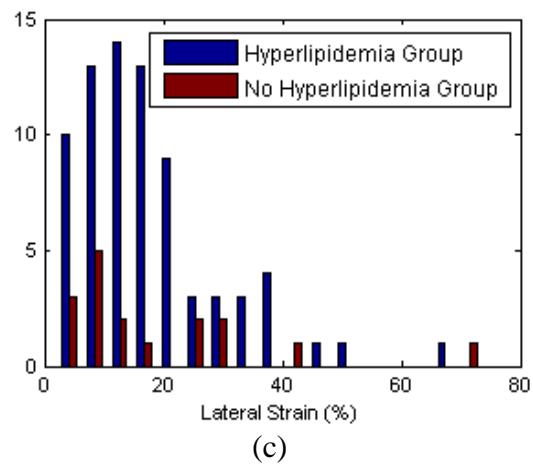
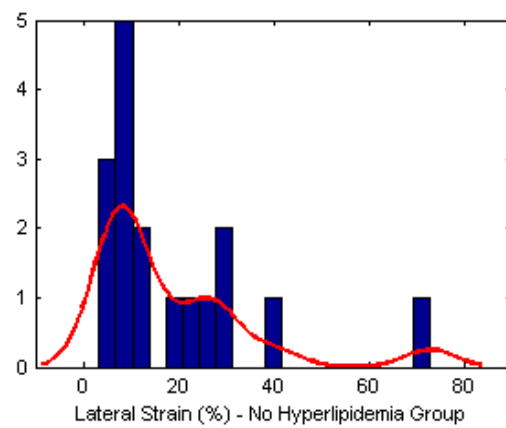
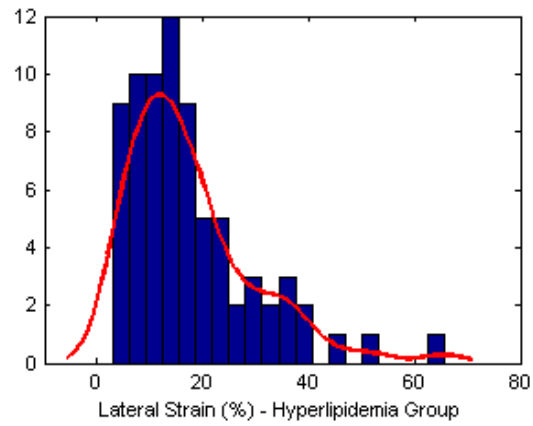
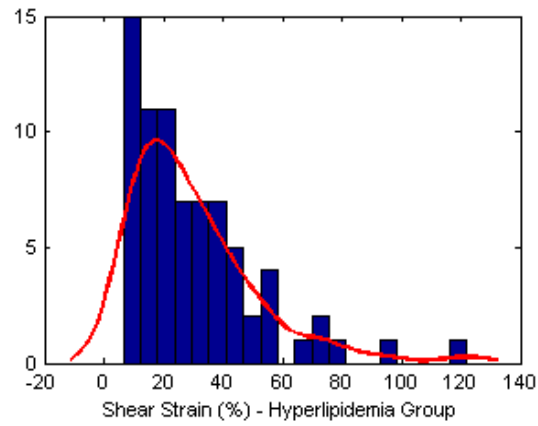
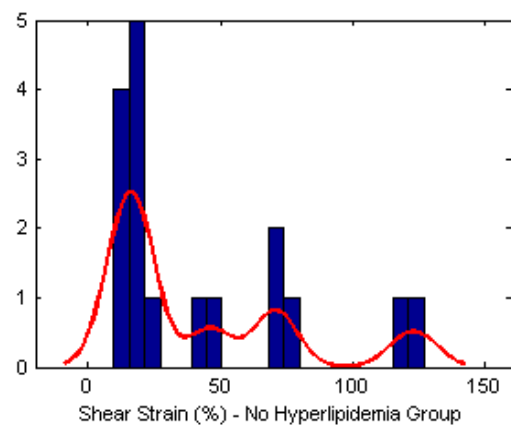


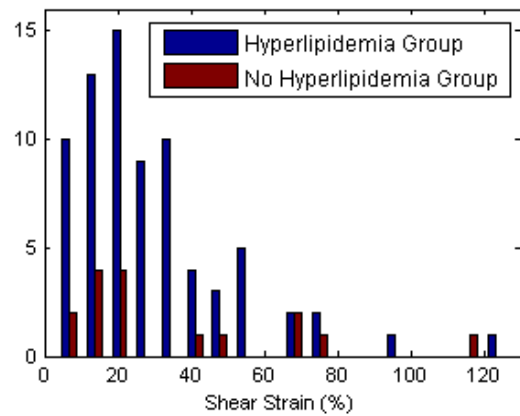
Figure 6.16: Comparison of histograms with fitted curve for maximum lateral strain for hyperlipidemia group and no hyperlipidemia group.



(a)



(b)



(c)

Figure 6.17: Comparison of histograms with fitted curve for maximum shear strain for hyperlipidemia group and no hyperlipidemia group.

Figure 6.18 depicts a three-dimensional scatter plot of the maximum axial, lateral and shear strain indices plotted against each other for the hyperlipidemia group and no

hyperlipidemia group. The strain indices were log-scaled to clearly visualize variations in the indices between individual patients. LSMAS in the axes represents log-scaled maximum axial strain, LSMLS represents log-scaled maximum lateral strain, LSMSS represents log-scaled maximum shear strain. Due to the much smaller sample size in the patients listed in the no hyperlipidemia group compared to the hyperlipidemia group, no significant difference of the two groups can be observed. Maximum axial, lateral and shear strain indices individually and in combination were used as classifiers to differentiate hyperlipidemia group from no hyperlipidemia group. The sensitivity and specificity for each classifier with individual feature or combined features are listed in Table 6.5. The sensitivity and specificity are also around 0.8.

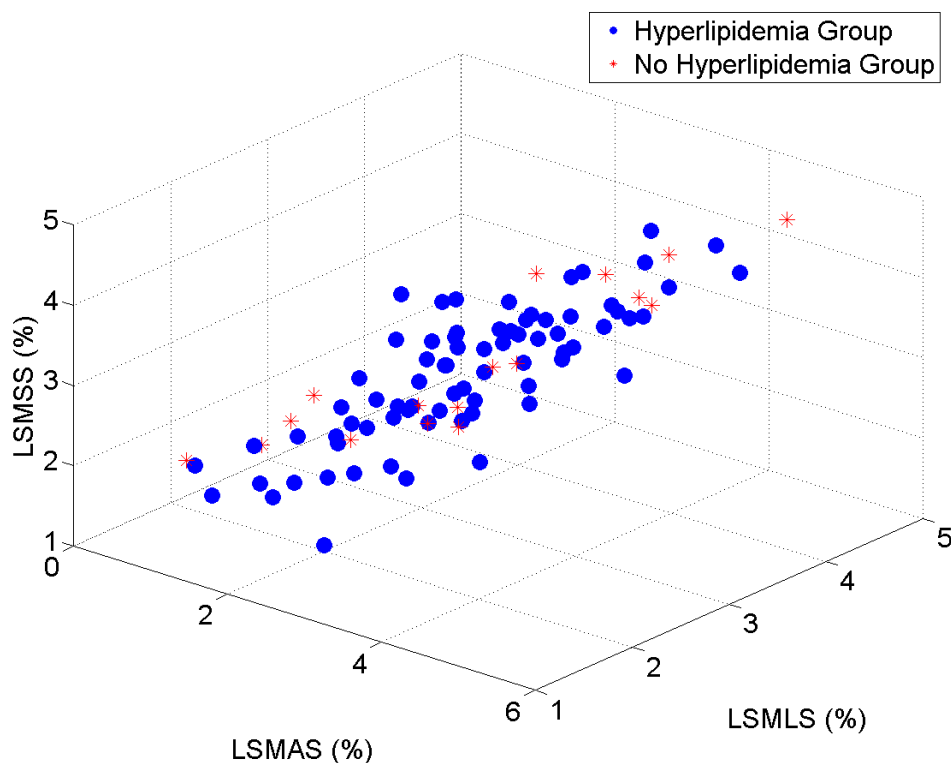
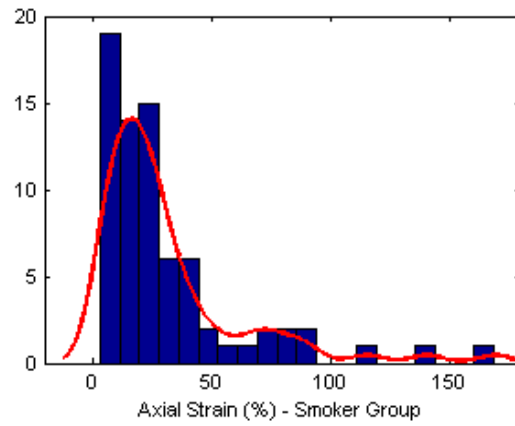


Figure 6.18: Three-dimensional scatter plot of maximum axial, lateral and shear strain indices plotted against each other. \circ = Hyperlipidemia group, $*$ = no hyperlipidemia group.

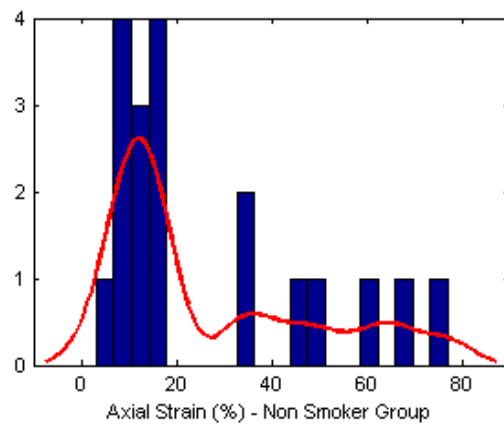
	Sensitivity	Specificity
Axial Strain	0.804	0.818
Lateral Strain	0.815	0.815
Shear Strain	0.804	0.818
Axial and Lateral Strain	0.815	0.770
Axial and Shear Strain	0.793	0.820
Lateral and Shear Strain	0.804	0.772
All	0.793	0.775

Table 6.5: Sensitivity and specificity of classification of patients with hyperlipidemia for individual features and combined features.

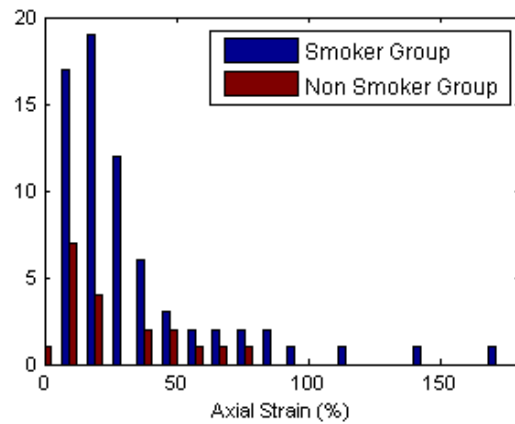
In the smoking group, 73 out of 92 patients were classified as smokers, while 19 were classified as non-smokers. Patients with previous smoking history or other tobacco usage are also classified as smokers in our analysis. Figure 6.19 through 6.21 presents the comparison of strain histograms for the two groups. The smoker group has higher axial and shear strain indices compared to the non-smoker group.



(a)

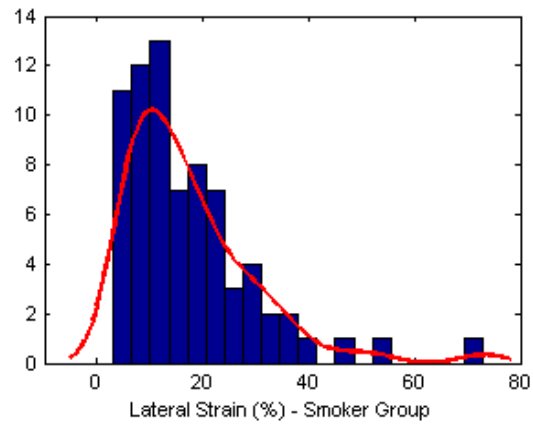


(b)

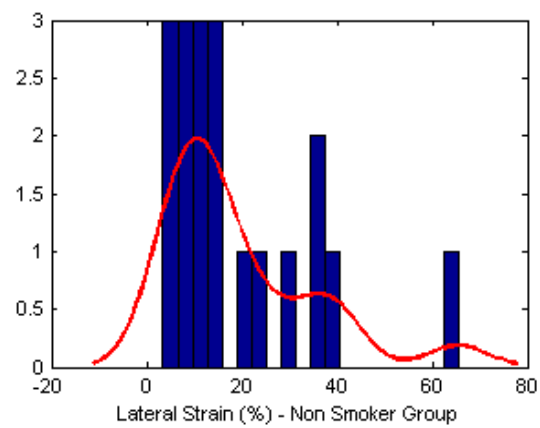


(c)

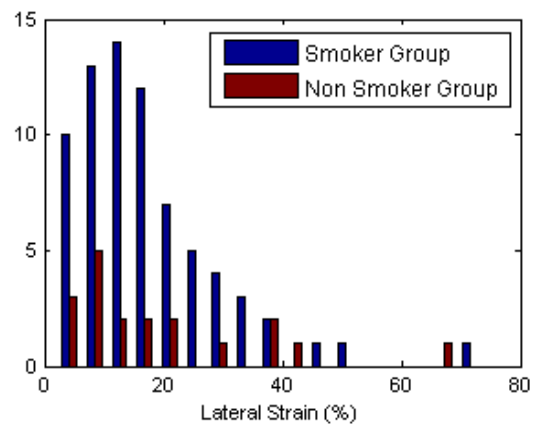
Figure 6.19: Comparison of histograms with fitted curve for maximum axial strain for smoker group and non-smoker group.



(a)

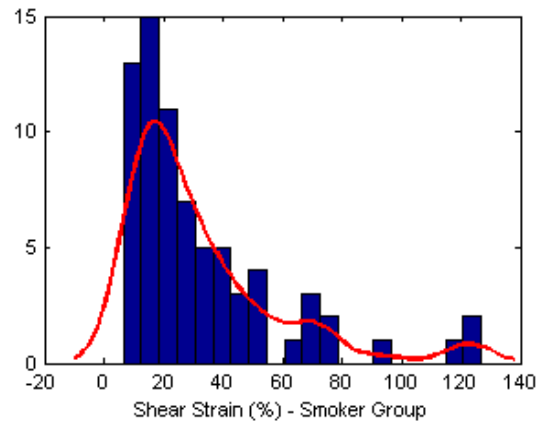


(b)

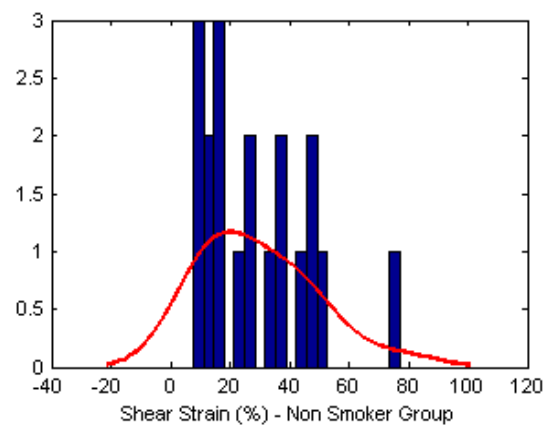


(c)

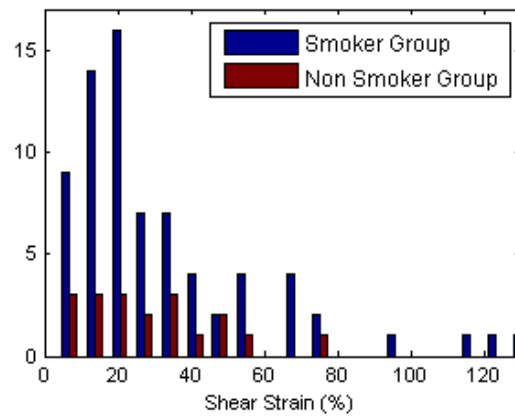
Figure 6.20: Comparison of histograms with fitted curve for maximum lateral strain for smoker group and non-smoker group.



(a)



(b)



(c)

Figure 6.21: Comparison of histograms with fitted curve for maximum shear strain for smoker group and non-smoker group.

Figure 6.22 depicts a three-dimensional scatter plot of the maximum axial, lateral and shear strain indices plotted against each other for the smoker group and the non-

smoker group. The strain indices were log-scaled to clearly visualize variations in the indices between individual patients. LSMAS in the axes represents log-scaled maximum axial strain, LSMLS represents log-scaled maximum lateral strain, LSMSS represents log-scaled maximum shear strain. Some overlap and no significant difference can be observed. Maximum axial, lateral and shear strain indices individually and in combination were used as classifiers to differentiate smokers from non-smokers. The sensitivity and specificity for each classifier with individual feature or combined features are listed in Table 6.6. The sensitivity and specificity are close to 0.8, but not high as those for patients clinically classified as belonging to the hypertension or hyperlipidemia groups.

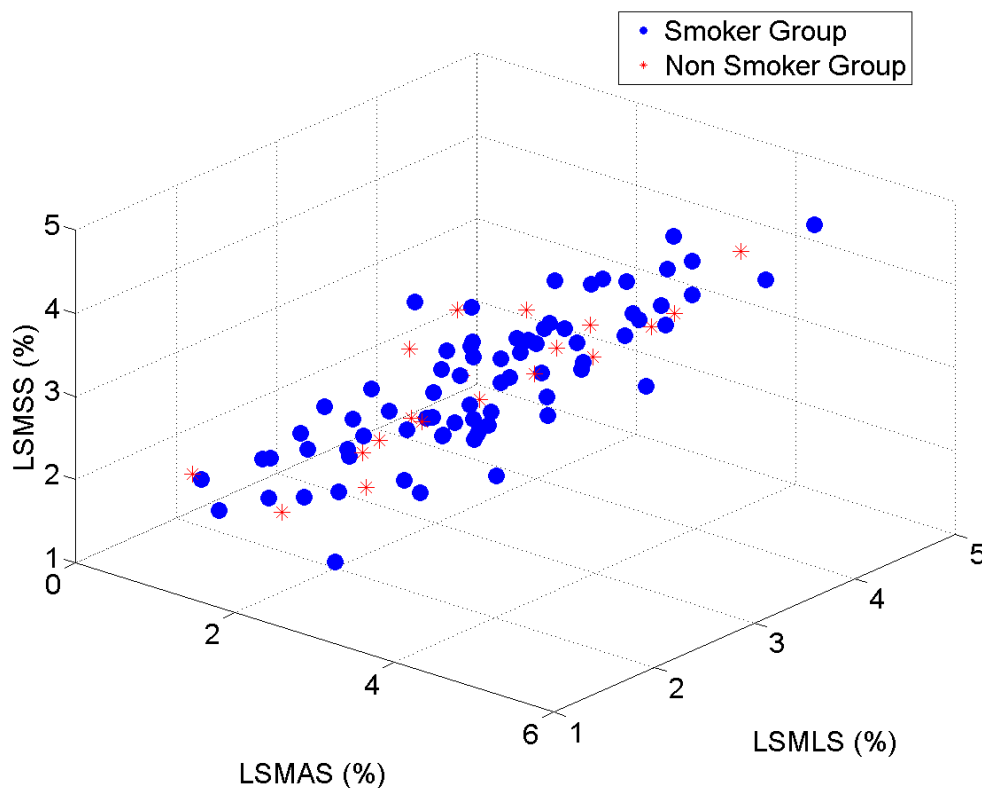


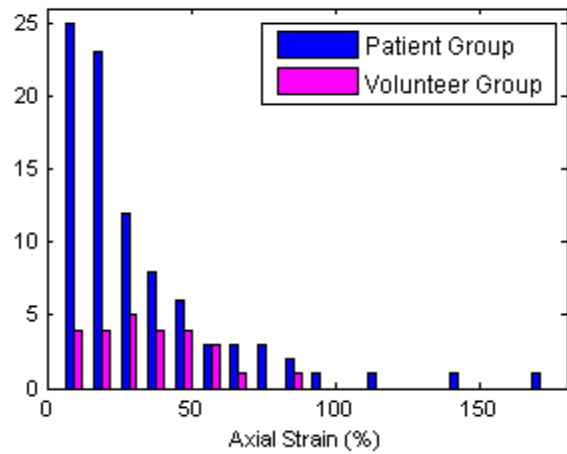
Figure 6.22: Three-dimensional scatter plot of maximum axial, lateral and shear strain indices plotted against each other. \circ = Smoker group, $*$ = non-smoker group.

	Sensitivity	Specificity
Axial Strain	0.793	0.793
Lateral Strain	0.793	0.793
Shear Strain	0.793	0.793
Axial and Lateral Strain	0.783	0.796
Axial and Shear Strain	0.793	0.793
Lateral and Shear Strain	0.783	0.796
All	0.783	0.796

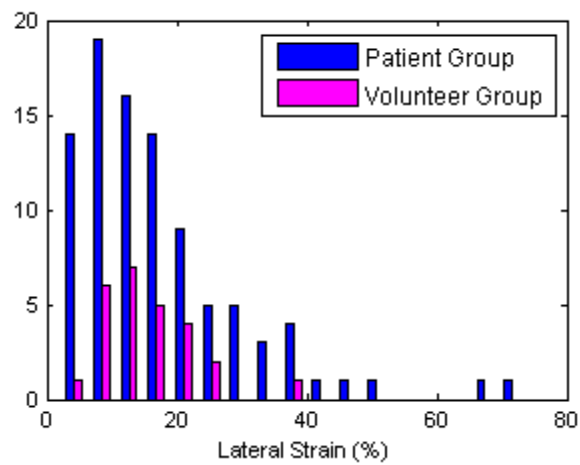
Table 6.6: Sensitivity and specificity of classification of patients with tobacco usage for individual features and combined features.

6.3.3 Comparison with human volunteers

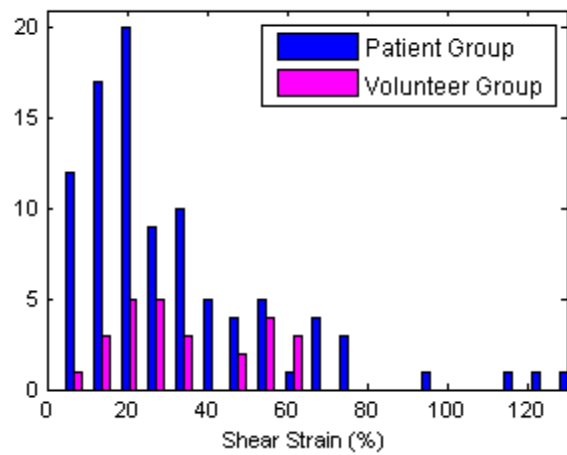
Figure 6.23 shows the comparison of histograms of the strain indices between patients and volunteers. For patients, the maximum strain was calculated within the plaque or adventitia. For volunteers, the maximum strain was estimated within the vessel wall, since there might be no plaque in the carotid artery of a healthy volunteer. Therefore, the comparison is between the strain in plaque and the strain in vessel wall. Plaque tends to have higher strain than vessel wall, in every strain histogram comparison.



(a)



(b)



(c)

Figure 6.23: Comparison of histograms for maximum axial strain (a), lateral strain (b) and shear strain (c) for patient group and volunteer group.

Figure 6.24 depicts a three-dimensional scatter plot of the maximum axial, lateral and shear strain indices plotted against each other for the patient group and volunteer group. The strain indices were log-scaled to clearly visualize variations in the indices between individual patients. LSMAS in the axes represents log-scaled maximum axial strain, LSMLS represents log-scaled maximum lateral strain, LSMSS represents log-scaled maximum shear strain. Note that vessel wall strain indices for volunteers tend to cluster in the middle range, with plaque strain being more widely distributed.

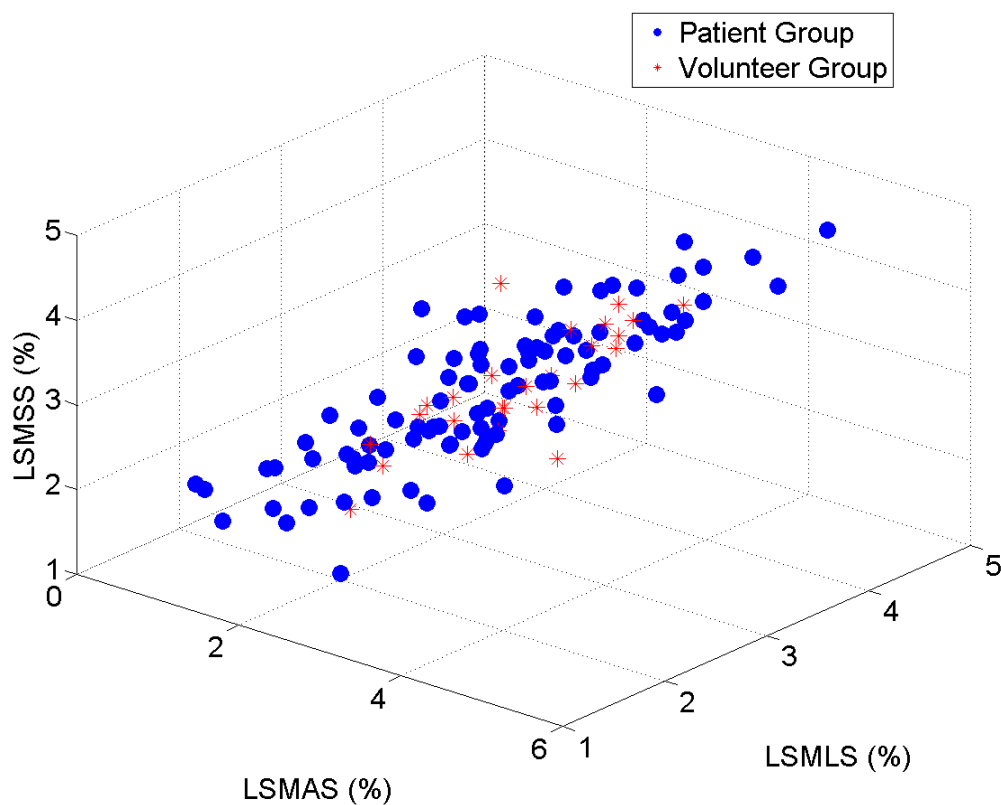


Figure 6.24: Three-dimensional scatter plot of maximum axial, lateral and shear strain indices plotted against each other. \circ = Patient group, $*$ = volunteer group.

Figure 6.25 shows bivariate histograms of age and maximum strain indices for patients and volunteers. The bars were colored according to height. The patient group has

larger range of both age and strain than the volunteer group.

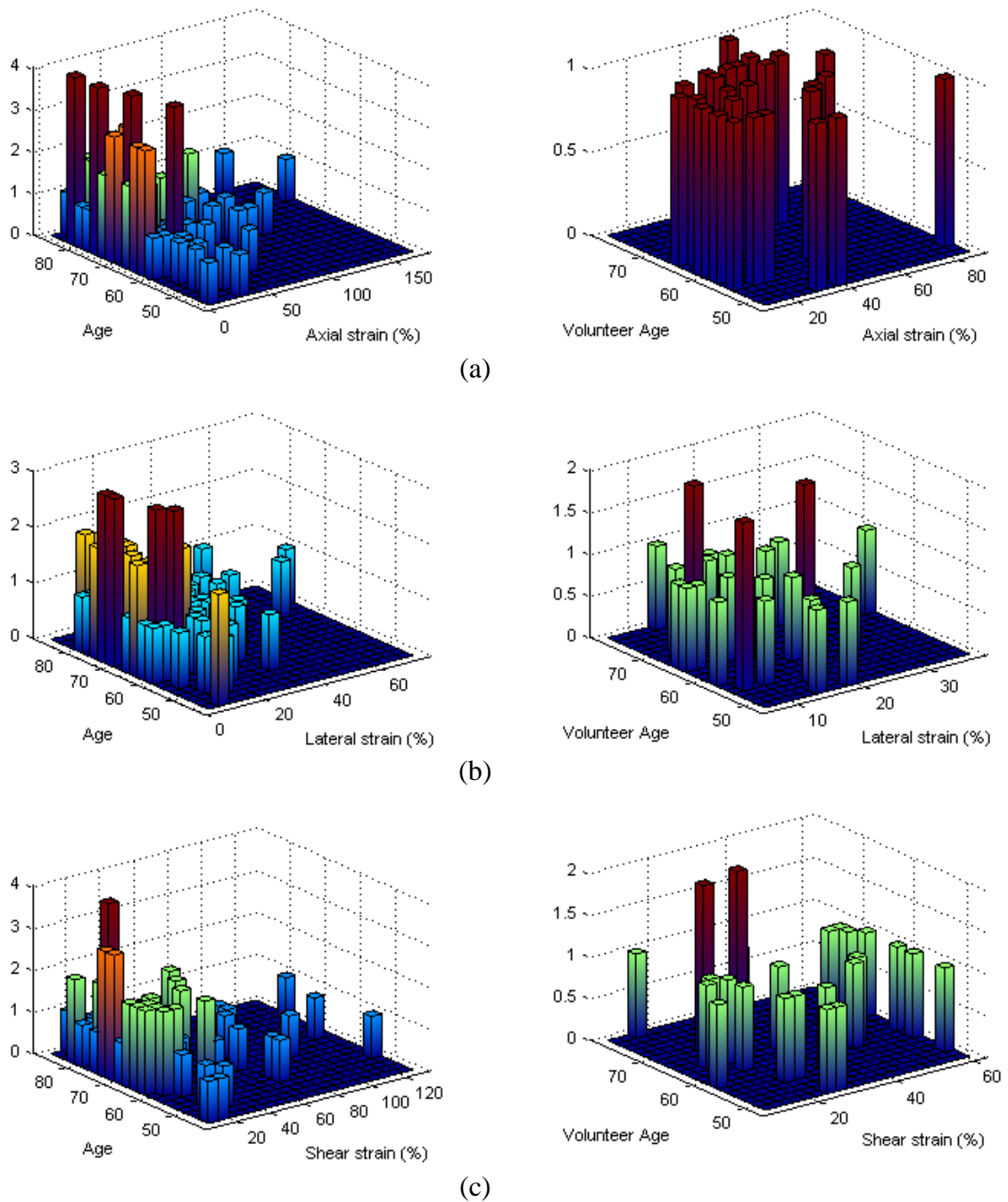


Figure 6.25: Bivariate histograms of age and maximum axial strain (a), lateral strain (b) and shear strain (c) for patient group and volunteer group.

To better visualize the relationship between strain and age, all 94 patients were

divided into five age groups, 40s (40-49), 50s (50-59), 60s (60-69), 70s (70-79) and 80s (80-89). Figure 6.26 depicts a three-dimensional scatter plot of the maximum axial, lateral and shear strain indices against each other for different age groups. The strain indices were log-scaled to clearly visualize variations in the indices between individual patients. LSMAS in the axes represents log-scaled maximum axial strain, LSMLS represents log-scaled maximum lateral strain, LSMSS represents log-scaled maximum shear strain. Most patients are in their 70s, and the 70s group is widely distributed with low strain values, and also some of the highest strain values.

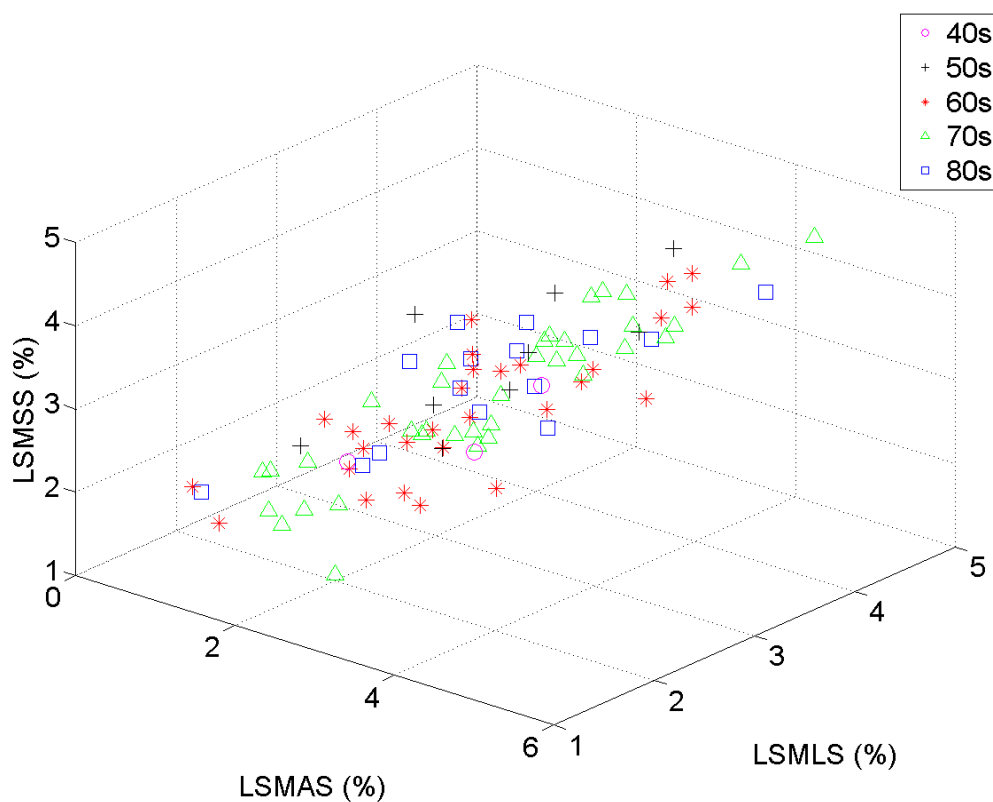


Figure 6.26: Three-dimensional scatter plot of maximum axial, lateral and shear strain indices plotted against each other. \circ = Patients in 40s, $+$ = patients in 50s, $*$ = patients in 60s, Δ = patients in 70s, \square = patients in 80s.

Similarly, all 26 volunteers were divided into four age groups, 40s (40-49), 50s (50-59), 60s (60-69), and 70s (70-79). Figure 6.27 depicts a three-dimensional scatter plot of the maximum axial, lateral and shear strain indices against each other for different age groups. The strain indices were log-scaled to clearly visualize variations in the indices between individual patients. LSMAS in the axes represents log-scaled maximum axial strain, LSMLS represents log-scaled maximum lateral strain, LSMSS represents log-scaled maximum shear strain. Different from the patients in 70s, volunteers in 70s have lower strain among all volunteers. That is to say the plaque strain is high for people in 70s, but the vessel wall strain is not as high due to arterial stiffening.

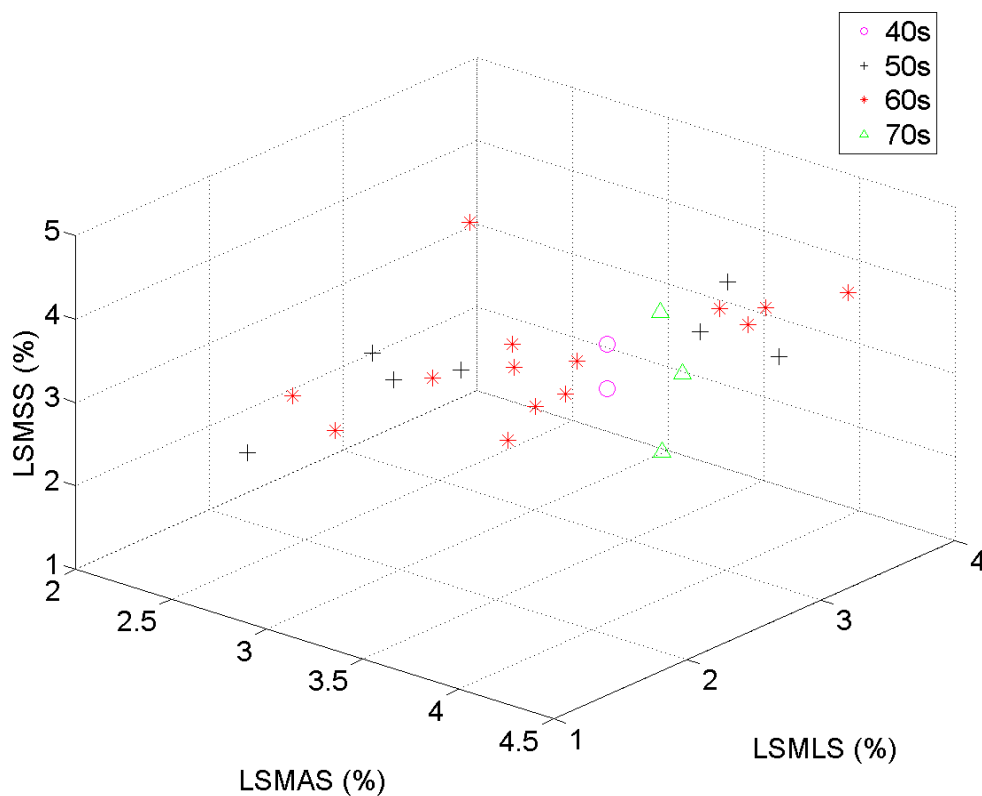


Figure 6.27: Three-dimensional scatter plot of maximum axial, lateral and shear strain indices plotted against each other. ○ = Patients in 40s, + = patients in 50s, * = patients in 60s, △ = patients in 70s.

6.4 Discussion

In this chapter we have illustrated the distribution in strain indices for patients and volunteers as well as for each specific risk factor group. In general no significant difference in the strain indices were observed in the comparison presented in this chapter, and the classification using strain indices versus clinical symptomology needs further study. In addition, due to the small sample sizes for both patients and volunteers, the trend in the distribution of the strain indices for each clinical group was difficult to discern.

The diabetes group was shown to have lower strain indices, suggesting that arterial stiffening may have happened in these patients. Patients with type 1 and type 2 diabetes have been compared to healthy controls and the results revealed that diabetes patients tend to have higher carotid intima-media thickness (IMT) and arterial stiffness [9-10].

The fact that patients in 70s showed high plaque strain and low vessel wall strain also leads to the assumption of arterial stiffening with age. Carotid arterial stiffening was reported to accelerate with aging in a study of 2650 participants [11]. The contributions of age-related arterial stiffening to cardiovascular disease has been extensively studied [12]. It has been shown that arterial stiffening may contribute to hypertension [13]. Variations in carotid artery stiffness with age were reported to be associated with hypertension in both male and female subjects, although contributions from hypertension differed between the sexes [14].

6.5 Conclusions

In summary, the results reveal different strain statistics of patients versus volunteers,

symptomatic versus asymptomatic patients, as well as patients with diabetes, hypertension, hyperlipidemia, tobacco usage versus normal controls. Although some trends could be observed, the relationships should be further examined in a larger number of patients and volunteers.

6.6 References

1. Gorelick, P.B., *Risk factors for vascular dementia and Alzheimer disease*. Stroke, 2004. **35**(11 Suppl 1): p. 2620-2.
2. Balashenko, N., Podpalov, V., Zhurova, O., and Podpalova, O., *Possible Impact on the Total Carotid Plaque Area in Patient with Arterial Hypertension*. Atherosclerosis, 2014. **235**(2): p. E232-E232.
3. Yuan, C., Lai, C.W., Chan, L.W., Chow, M., Law, H.K., and Ying, M., *Cumulative effects of hypertension, dyslipidemia, and chronic kidney disease on carotid atherosclerosis in Chinese patients with type 2 diabetes mellitus*. J Diabetes Res, 2014. **2014**: p. 179686.
4. Irie, Y., Katakami, N., Kaneto, H., Takahara, M., Sakamoto, K., Kosugi, K., and Shimomura, I., *The risk factors associated with ultrasonic tissue characterization of carotid plaque in type 2 diabetic patients*. J Diabetes Complications, 2014. **28**(4): p. 523-7.
5. Della-Morte, D., Wang, L., Beecham, A., Blanton, S.H., Zhao, H., Sacco, R.L., Rundek, T., and Dong, C., *Novel genetic variants modify the effect of smoking on carotid plaque burden in Hispanics*. J Neurol Sci, 2014. **344**(1-2): p. 27-31.
6. Yang, D., Iyer, S., Gardener, H., Della-Morte, D., Crisby, M., Dong, C., McLaughlin, C., Wright, C.B., Elkind, M.S., and Sacco, R.L., *Abstract T P141: Current Cigarette Smoking Is Associated With Echodensity of Carotid Plaque in the Northern Manhattan Study*. Stroke, 2015. **46**(Suppl 1): p. ATP141-ATP141.
7. Paine, A., Boutouyrie, P., Calvet, D., Zidi, M., Agabiti-Rosei, E., and Laurent, S., *Multiaxial mechanical characteristics of carotid plaque: analysis by multiarray echotracking system*. Stroke, 2007. **38**(1): p. 117-23.
8. Hall, M., Frank, E., Holmes, G., Pfahringer, B., Reutemann, P., and Witten, I.H., *The WEKA data mining software: an update*. ACM SIGKDD explorations newsletter, 2009. **11**(1): p. 10-18.
9. Sveen, K.A., Dahl-Jorgensen, K., Stensaeth, K.H., Angel, K., Seljeflot, I., Sell, D.R., Monnier, V.M., and Hanssen, K.F., *Glucosepane and oxidative markers in skin collagen correlate with intima media thickness and arterial stiffness in long-term type 1 diabetes*. J Diabetes Complications, 2015. **29**(3): p. 407-12.
10. Kozakova, M., Morizzo, C., Bianchi, C., Di Filippi, M., Miccoli, R., Paterni, M.,

- Di Bello, V., and Palombo, C., *Glucose-related arterial stiffness and carotid artery remodeling: a study in normal subjects and type 2 diabetes patients*. *J Clin Endocrinol Metab*, 2014. **99**(11): p. E2362-6.
11. Gepner, A.D., Korcarz, C.E., Colangelo, L.A., Hom, E.K., Tattersall, M.C., Astor, B.C., Kaufman, J.D., Liu, K., and Stein, J.H., *Longitudinal effects of a decade of aging on carotid artery stiffness: the multiethnic study of atherosclerosis*. *Stroke*, 2014. **45**(1): p. 48-53.
 12. Kohn, J.C., Lampi, M.C., and Reinhart-King, C.A., *Age-related vascular stiffening: causes and consequences*. *Front Genet*, 2015. **6**: p. 112.
 13. Weisbrod, R.M., Shiang, T., Al Sayah, L., Fry, J.L., Bajpai, S., Reinhart-King, C.A., Lob, H.E., Santhanam, L., Mitchell, G., Cohen, R.A., and Seta, F., *Arterial stiffening precedes systolic hypertension in diet-induced obesity*. *Hypertension*, 2013. **62**(6): p. 1105-10.
 14. Stern, R., Tattersall, M.C., Gepner, A.D., Korcarz, C.E., Kaufman, J., Colangelo, L.A., Liu, K., and Stein, J.H., *Sex differences in predictors of longitudinal changes in carotid artery stiffness: the Multi-Ethnic Study of Atherosclerosis*. *Arterioscler Thromb Vasc Biol*, 2015. **35**(2): p. 478-84.

Chapter 7 : Trans-cranial Doppler versus Ultrasound Strain Indices

7.1 Introduction

In this chapter, we provide a comparison of trans-cranial Doppler (TCD) and ultrasound strain indices described in previous chapters for predicting embolism and preventing potential silent strokes. Ultrasound strain indices may predict plaque prone to rupture and generate micro-emboli, which may be visualized during TCD monitoring. TCD monitoring has been utilized to detect intraprocedural micro-emboli during transapical transcatheter aortic valve implantation (TA-TAVI) [1], orthopedic surgery [2], and at the vertebrobasilar junction during vertebral artery dissection (VAD) [3].

TCD measures the velocity of blood flow in middle cerebral arteries (MCA), including peak systolic velocity (PSV), end-diastolic velocity (EDV) and mean velocity during a cardiac cycle. MCA velocities measured by TCD were compared to MRI findings in asymptomatic patients with internal carotid artery (ICA) stenosis [4], and during hypercapnia and hypocapnia [5]. TCD also provides a pulsatility index (PI), the difference between systolic and diastolic velocities divided by the mean velocity, which was also utilized for arterial disease studies in patients with stroke [6]. During the monitoring process, a high intensity transient signal (HITS) can occur in the recordings, which may reflect the propagation of micro-emboli [7-9] through the MCA. Clinical studies have shown that patients with HITS may have different clinical characteristics

including age and vascular risk factors from patients without HITS [10], and characteristics of HITS in symptomatic patients may also differ from those in asymptomatic patients [11]. HITS were associated with unstable lipid-rich carotid plaque and luminal thrombus in symptomatic patients prior to CEA [12]. In symptomatic patients with mild to moderate carotid artery stenosis, HITS was not associated with intraplaque hemorrhage and thin fibrous cap evaluated with MRI, suggesting TCD and MRI provide independent information on plaque vulnerability [13]. HITS has been reported to show high correlation with symptomatic carotid disease [14-15]. HITS was more likely to occur in patients with symptomatic lesions and high cholesterol in TCD monitoring after carotid artery stenting [16]. HITS may also suggest the presence of a right-to-left shunting in patients who suffer strokes with an undetermined etiology [17].

7.2 Materials and Methods

7.2.1 Data acquisition

TCD monitoring was conducted on 50 patients with significant plaque and scheduled for a carotid endarterectomy (CEA) procedure at the University of Wisconsin-Madison Hospitals and Clinics. Patients provided informed consent using a protocol approved by the University of Wisconsin-Madison Institutional Review Board (IRB) prior to the TCD and ultrasound study. 30 out of 50 patients were male, and 20 were female. The age of the patients ranged from 43 to 87, with a mean and standard deviation of 68.96 ± 9.37 respectively. The BMI of the patients ranged from 19.22 to 45.62, with a mean and standard deviation of 28.27 ± 5.02 respectively. TCD signals were monitored for one hour, followed by ultrasound strain imaging on carotid artery. Maximum PSV on bilateral

sides were obtained. PSV in proximal ICA, middle ICA and distal ICA were also acquired using Doppler Ultrasound.

During monitoring, the TCD system recorded Doppler waveforms of the blood flow velocity in the MCA, and labeled HITS with a “complex” waveform, which is the high resolution raw time domain Doppler data. Since HITS may reflect the progression of micro-emboli or a possible artifact, HITS recorded by the TCD system were filtered by physician and real HITS identified. A real HITS should satisfy all of the following criteria: the Doppler signal was less than 300 milliseconds, the amplitude of the signal was at least 3dB higher than the background blood flow signal, the signal was unidirectional within the velocity spectrum, and an audible “snap”, “chirp” or “moan” was present [18].

7.2.2 Statistical analysis

Strain indices were estimated previously, as described in Chapter 2 to Chapter 6. Since patients were scheduled for a CEA procedure, bilateral TCD and ultrasound data were acquired and labeled as surgical side or non-surgical side respectively. Maximum strain indices on the surgical side and non-surgical side were correlated to the PSV in MCA on the corresponding side using a Pearson’s correlation coefficient r and a significance level of $p < 0.05$ using a two-tailed t -test. To better understand the hemodynamics of ICA and MCA, PSV in different segments of ICA and the maximum PSV in ICA were also correlated to the PSV in MCA on the same side using a Pearson’s correlation coefficient r and a significance level of $p < 0.05$ using a two-tailed t -test.

7.3 Results

7.3.1 HITS

Among the 50 patients monitored, HITS were recorded on 13 patients (9 male and 4 female). The age of the patients with HITS ranged from 59 to 87, with a mean and standard deviation of 73.38 ± 8.86 respectively. The BMI of the patients ranged from 24.08 to 33.74, with a mean and standard deviation of 28.18 ± 2.87 respectively. Figure 7.1 shows a typical TCD display with the labeling of a classical HITS. The “complex” window shows the original Doppler quadrature data with two signals with a $\pi/2$ phase shift. This HITS was real since an audible chirp was present, and the signal was within 300 microseconds and unidirectional within the Doppler waveform. Also, the amplitude of the signal fluctuated significantly and was much higher than the background, with a classical “complex” shape for HITS. The large amplitude of the signal can also be observed from the high velocity represented in red color in the Doppler spectrum window denoted by the yellow arrow.

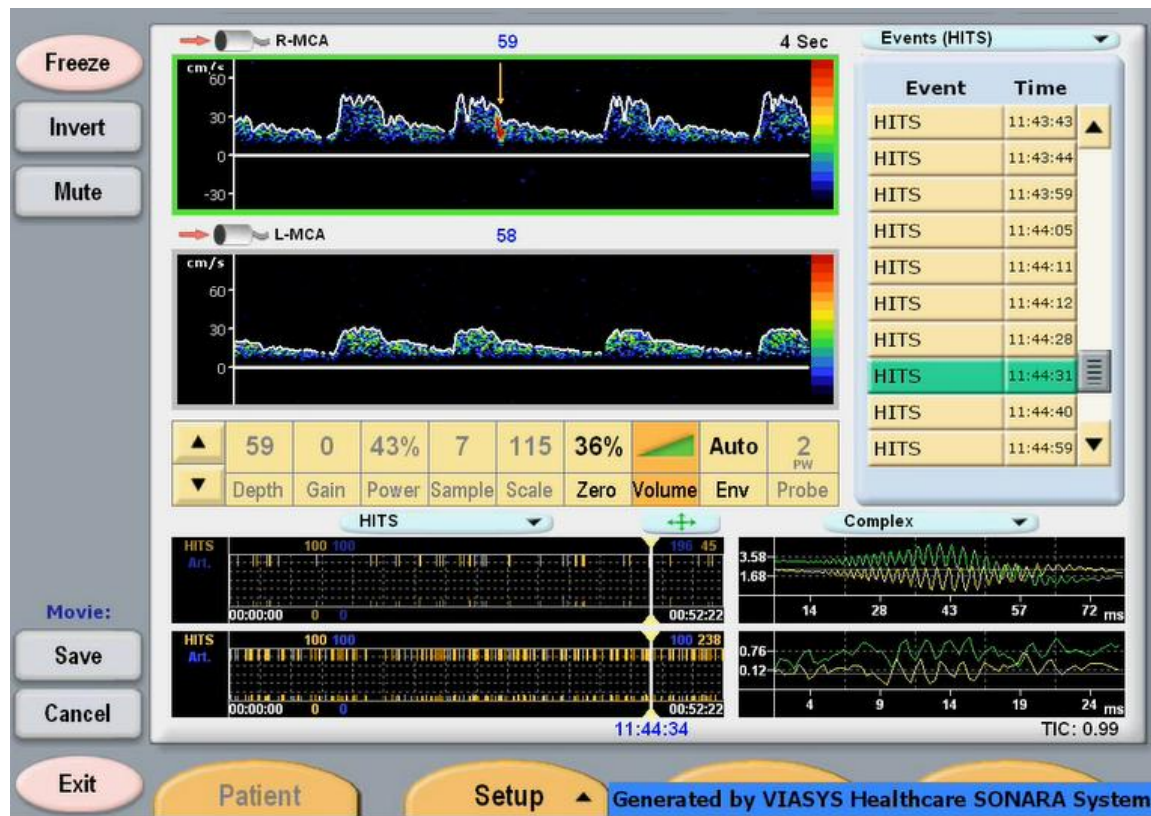


Figure 7.1: A classical HITS labeled on the TCD display.

7.3.2 Correlations of MCA velocities with strain indices and ICA velocities

The Pearson's correlation coefficient r and significance level p for correlations of maximum axial, lateral and shear strain indices with PSV in MCA for the 13 patients identified with HITS are listed in Table 7.1. The Pearson's correlation coefficient r is highest for the correlation of maximum lateral strain to MCA PSV on the surgical side, with p value also closest to become significant. Note that the correlations are not significant due to the fact that the sample size is rather small.

	Axial Strain	Lateral Strain	Shear Strain
surgical side (n = 12)	$r = 0.456, p = 0.132$	$r = 0.502, p = 0.092$	$r = 0.342, p = 0.273$
non-surgical side (n = 10)	$r = 0.295, p = 0.403$	$r = 0.477, p = 0.156$	$r = 0.060, p = 0.869$

Table 7.1: Correlations of maximum strain indices with MCA PSV on surgical side and non-surgical side for patients with HITS.

The Pearson's correlation coefficient r and significance level p for correlations of PSV in proximal ICA, middle ICA, distal ICA and the maximum of the three with PSV in MCA for the same 13 patients identified with HITS are listed in Table 7.2. Note that the correlations are rather weak. The highest correlation is the correlation of maximum ICA PSV with MCA PSV on the surgical side, with an r value close to 0.5 and the lowest p value.

	ICA-Proximal	ICA-Mid	ICA-Distal	Maximum of ICA
surgical side (n = 11)	$r = 0.438, p = 0.171$	$r = 0.397, p = 0.221$	$r = 0.354, p = 0.280$	$r = 0.474, p = 0.134$
non-surgical side (n = 9)	$r = 0.400, p = 0.279$	$r = 0.264, p = 0.488$	$r = -0.441, p = 0.226$	$r = -0.385, p = 0.298$

Table 7.2: Correlations of ICA PSV with MCA PSV on surgical side and non-surgical side for patients with HITS.

7.4 Discussion

In this chapter we demonstrated the feasibility of detecting micro-emboli using TCD on pre-op patients. On some of the patients, over 100 HITS identified by TCD system could be observed. It took a lot of time and effort in the differentiation of real HITS from artifact by human observers. More efficient implementations are needed for better automatic identification of real HITS [19].

The results revealed some trend in the association of maximum strain indices and maximum ICA PSV with MCA PSV on the surgical side of patients identified with HITS, although the correlations were not statistically significant due to the low patient number. The correlations for the non-surgical side were weaker as expected, since significant plaque is present on the surgical side, with blood flow velocities more affected by the micro-emboli generated by possible plaque rupture. Since, we did not observe a significant correlation, examination of a larger sample size is essential to establish any relationship. Also, human errors can occur since the values obtained were highly dependent on human operation. The placement of transducers may affect the measurements and result in lower velocities obtained than the true velocities.

Unstable plaques with high strain indices may also be associated with vascular mediated brain damage. In a recent analysis in our Plaque Study group, maximum strain indices in carotid plaque in ICA were correlated to white matter hyperintensities (WMH) [20]. WMH are the bright regions on T2 weighted brain MRI image, and are postulated to result from cumulative subclinical microvascular injury. Berman et al. [20] found that WMH total lesion volume, adjusted for age and gender, was positively correlated to maximum strain indices estimated in carotid plaque in the ICA.

7.5 Conclusions

In summary, we have shown that TCD is a sensitive detector of clinically silent micro-emboli. A relationship exists between maximum strain indices, maximum ICA velocity and maximum MCA velocity on the surgical side with significant plaque. Increased strains in carotid plaque in ICA are also significantly associated with an increase in WMH. Since HITS in TCD monitoring may reflect the existence of micro-emboli, correlation of strain indices to HITS would give us more insight into the ability of strain imaging for predicting the vulnerability or rupture of carotid plaques.

7.6 References

1. Erdoes, G., Huber, C., Basciani, R., Stortecky, S., Windecker, S., Wenaweser, P., Carrel, T., and Eberle, B., *The self-expanding Symetis Acurate does not increase cerebral microembolic load when compared to the balloon-expandable Edwards Sapien prosthesis: a transcranial Doppler study in patients undergoing transapical aortic valve implantation*. Plos One, 2014. **9**(10): p. e108191.
2. Silbert, B.S., Evered, L.A., Scott, D.A., Rahardja, S., Gerraty, R.P., and Choong, P.F., *Review of transcranial Doppler ultrasound to detect microemboli during orthopedic surgery*. AJNR Am J Neuroradiol, 2014. **35**(10): p. 1858-63.
3. Yamaoka, Y., Ichikawa, Y., Kimura, T., Sameshima, T., Ochiai, C., and Morita, A., *A novel method for transcranial Doppler microembolic signal monitoring at the vertebrobasilar junction in vertebral artery dissection patients*. J Neuroimaging, 2014. **24**(2): p. 191-4.
4. Marshall, R.S., Lazar, R.M., Pavol, M.A., Dharssi, S., Slane, K., and Asllani, I., *Abstract WP170: Hemodynamic Effects in Carotid Occlusion Using Arterial Spin Labeling and Transcranial Doppler*. Stroke, 2014. **45**(Suppl 1): p. AWP170-AWP170.
5. Coverdale, N.S., Gati, J.S., Opalevych, O., Perrotta, A., and Shoemaker, J.K., *Cerebral blood flow velocity underestimates cerebral blood flow during modest hypercapnia and hypocapnia*. J Appl Physiol (1985), 2014. **117**(10): p. 1090-6.
6. Barlinn, K., Kolieskova, S., Shahripour, R.B., Kepplinger, J., Boehme, A.K., Puetz, V., Bodechtel, U., Albright, K.C., and Alexandrov, A.V., *Abstract T P87: Does an Increased Pulsatility of the Intracranial Blood Flow Spectral Waveform on Transcranial Doppler (TCD) Point to Peripheral Arterial Disease in Stroke Patients?* Stroke, 2014. **45**(Suppl 1): p. ATP87-ATP87.

7. Spencer, M.P., Thomas, G.I., Nicholls, S.C., and Sauvage, L.R., *Detection of middle cerebral artery emboli during carotid endarterectomy using transcranial Doppler ultrasonography*. Stroke, 1990. **21**(3): p. 415-23.
8. Droste, D.W. and Ringelstein, E.B., *Detection of high intensity transient signals (HITS): how and why?* Eur J Ultrasound, 1998. **7**(1): p. 23-9.
9. Dittrich, R., Ritter, M.A., and Droste, D.W., *Microembolus detection by transcranial doppler sonography*. Eur J Ultrasound, 2002. **16**(1-2): p. 21-30.
10. Koffman, L., Ahmed, Z., Michael, R., Baus, L., Raber, L., and Katzan, I., *Abstract W MP70: Characteristics of Patients With Microemboli Detected With Transcranial Doppler Monitoring*. Stroke, 2014. **45**(Suppl 1): p. AWMP70-AWMP70.
11. Wu, X., Zhang, H., Liu, H., Xing, Y., and Liu, K., *Microembolic signals detected with transcranial doppler sonography differ between symptomatic and asymptomatic middle cerebral artery stenoses in Northeast China*. Plos One, 2014. **9**(2): p. e88986.
12. Van Lammeren, G.W., Van De Mortel, R.H., Visscher, M., Pasterkamp, G., De Borst, G.J., Moll, F.L., Vink, A., Tromp, S.C., and De Vries, J.P., *Spontaneous preoperative microembolic signals detected with transcranial Doppler are associated with vulnerable carotid plaque characteristics*. J Cardiovasc Surg (Torino), 2014. **55**(3): p. 375-80.
13. Truijman, M.T., de Rotte, A.A., Aaslid, R., van Dijk, A.C., Steinbuch, J., Liem, M.I., Schreuder, F.H., van der Steen, A.F., Daemen, M.J., van Oostenbrugge, R.J., Wildberger, J.E., Nederkoorn, P.J., Hendrikse, J., van der Lugt, A., Kooi, M.E., and Mess, W.H., *Intraplaque hemorrhage, fibrous cap status, and microembolic signals in symptomatic patients with mild to moderate carotid artery stenosis: the Plaque at RISK study*. Stroke, 2014. **45**(11): p. 3423-6.
14. Bazan, R., Braga, G.P., Bazan, S.G., Hueb, J.C., Leite, J.P., and Pontes-Neto, O.M., *Abstract T P170: Risk Stratification in Acute Ischemic Stroke by Transcranial Doppler in a Multiethnic Population: Role of Microembolic Signal*. Stroke, 2014. **45**(Suppl 1): p. ATP170-ATP170.
15. Bazan, R., Braga, G.P., Bazan, S.G., Hueb, J.C., Sobreira, M.L., Luvizutto, G.J., Leite, J.P., and Pontes-Neto, O.M. *Relation of Spontaneous Microembolic Signals to Stratification of Risk, Recurrence and Morbi-mortality of Ischemic Stroke by Transcranial Doppler: A Prospective Trial*. in Stroke. 2015: LIPPINCOTT WILLIAMS & WILKINS TWO COMMERCE SQ, 2001 MARKET ST, PHILADELPHIA, PA 19103 USA.
16. Piorkowski, M., Klaffling, C., Botsios, S., Zerweck, C., Scheinert, S., Banning-Eichenseher, U., Bausback, Y., Scheinert, D., and Schmidt, A., *Postinterventional microembolism signals detected by transcranial Doppler ultrasound after carotid artery stenting*. Vasa, 2015. **44**(1): p. 49-57.
17. Ahmed, Z.A., Koffman, L., Michael, R., Baus, L., Raber, L., and Katzan, I., *Abstract W P176: Relationship Between Right-to-Left Shunting and Microembolic*

- Signals on Transcranial Doppler Monitoring*. Stroke, 2014. **45**(Suppl 1): p. AWP176-AWP176.
18. *Basic identification criteria of Doppler microembolic signals. Consensus Committee of the Ninth International Cerebral Hemodynamic Symposium*. Stroke, 1995. **26**(6): p. 1123.
 19. Lin, F., Saglio, C., Almar, M., Guibert, B., and Delachartre, P. *Micro-embolic signal characterization based on long time Doppler time-frequency image processing and statistics*. in *Signal Processing (ICSP), 2014 12th International Conference on*. 2014: IEEE.
 20. Berman, S., Wang, X., Mitchell, C.C., Jackson, D.C., Wilbrand, S.M., Varghese, T., Vemuganti, R., Johnson, S.C., and Dempsey, R.J., *The relationship between carotid artery plaque stability and white matter ischemic injury*. Neuroimage Clin, submitted.

Chapter 8 : Estimation of Carotid Radial and Circumferential Strain

8.1 Introduction

In this chapter, we generate a Lagrangian description [1-2] of radial and circumferential strains over a cardiac cycle utilizing a Lagrangian polar strain generation framework previously developed in our lab. Originally designed for cardiac short axes views [3], the framework described in this chapter utilizes luminal or plaque borders and adventitia contours to generate a polar grid to follow arterial wall and plaque deformation over two cardiac cycles. Radial and circumferential components of displacement and strain in a polar coordinate system are readily generated from the geometrical arrangement of polar grid data points.

Polar strain, i.e. radial and circumferential strain described in a polar coordinate system has been investigated for vascular ultrasound strain imaging, usually with FEA based concentric wall models [4-5]. Hansen et al. [4] calculated radial strains using a transverse cross-section of a homogeneous vessel with a concentric lumen for evaluating angular compounding, using a single quasi-static compressional state with an applied pressure of 0.532 kPa. Richards et al. [5] designed a concentric FEA model for intravascular ultrasound (IVUS) and investigated 8 independent quasi-static radial and circumferential strain deformations ranging from 0.1% to 10%. They utilized a polar registration mesh for displacement interpolation. These studies, however, were mainly

focused on tissue deformations at selected time instances in a cardiac cycle, and not over a continuous deformation as described in this chapter.

In this chapter, we present radial and circumferential strain results in carotid artery over a cardiac cycle. The radial and circumferential strain indices are obtained using Lagrangian strain estimation using a polar grid between the inner lumen or plaque borders and the outer adventitia wall in cross-sectional scans of the carotid artery.

8.2 Materials and Methods

8.2.1 Data acquisition

Ultrasound imaging was performed on patients with significant plaque prior to carotid endarterectomy (CEA) procedure at the University of Wisconsin-Madison Hospitals and Clinics. Patients provided informed consent using a protocol approved by the University of Wisconsin-Madison Institutional Review Boards (IRB) to participate in the study. Ultrasound radiofrequency (RF) echo signal data was acquired on the cross-sectional view of the carotid artery, along with clinical B-mode images and color-flow Doppler images, using a Siemens S2000 ultrasound system (Siemens Ultrasound, Mountain View, CA, USA) equipped with an 18L6 linear array transducer. The transmit frequency was set to 11.4 MHz with a single transmit focus set at the depth of the plaque, and the sampling frequency was 40 MHz.

Plaque regions with adventitia were segmented by a research sonographer at two end-diastole frames using the Medical Imaging Interaction Toolkit (MITK), as shown in Figure 8.1. Segmentations were done on B-mode images reconstructed from RF data, and were intentionally demarcated as a closed loop. Clinical B-mode images and color-flow

Doppler images were used to help determine the plaque inner borders in the lumen since the RF reconstructed B-mode images are noisier when compared to clinical B-mode images of the same region. The segmented regions were automatically tracked over a complete cardiac cycle using a hierarchical block-matching motion tracking algorithm developed in our laboratory [6].

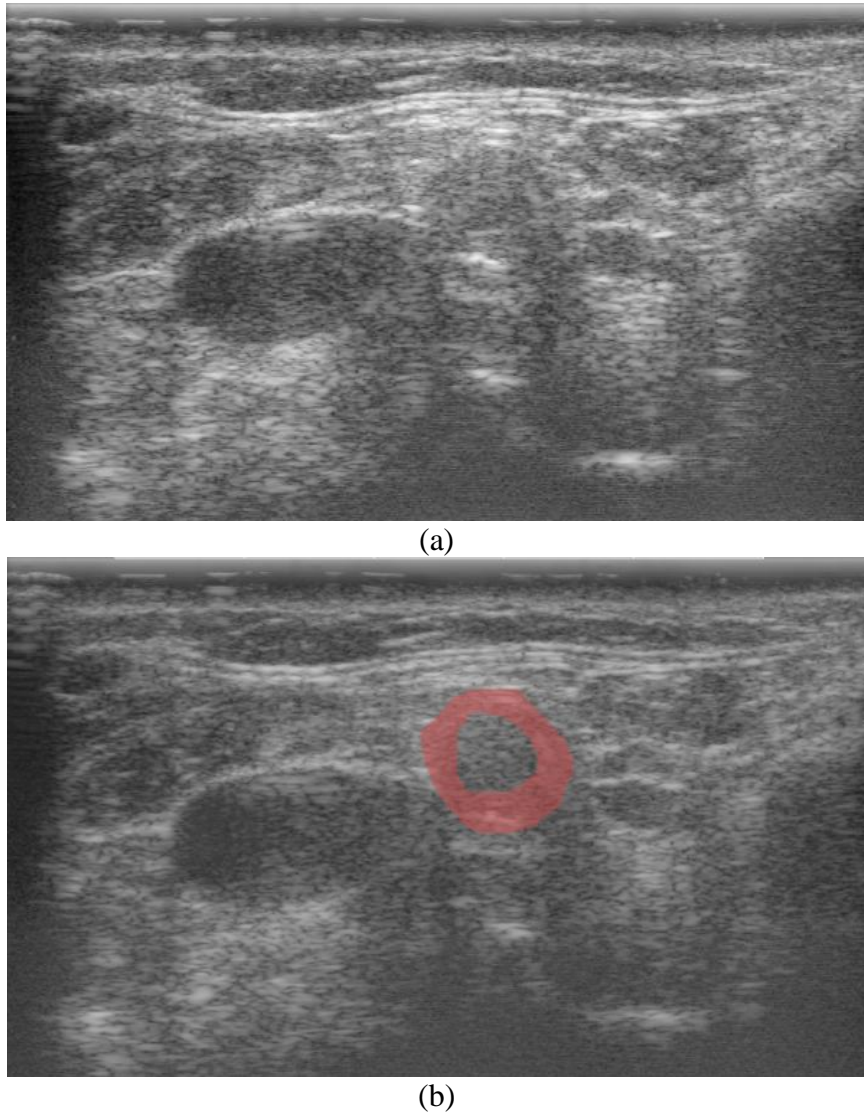


Figure 8.1: B-mode image reconstructed from RF data (a) and segmented plaque with adventitia on the B-mode image (b).

8.2.2 Polar grid generation

A frame work that generate radial and circumferential strains using Lagrangian deformation tracking algorithm [3] previously developed in our laboratory was adapted in this chapter. Here, inner and outer wall contour pairs over two cardiac cycles were generated using a hierarchical block-matching motion tracking algorithm [6] also developed in our laboratory. A centroid was then calculated from the donut-shaped carotid artery wall in cross-sectional view with the contour pair for each image frame. The contour pair was then divided in an equiangular fashion along the circumferential direction with equidistant points in the radial direction to generate a polar grid. In this study, contour lines were divided into 600 sections along the circumferential direction. In addition, 40 data points along the radial direction between the inner and outer carotid artery wall contours were generated for this study. These numbers were chosen to closely approximate the resolution of the estimated displacement field. Axial and lateral displacements were then overlaid onto the polar grid, with non-overlapping points filled in with bilinear interpolation.

8.2.3 Radial and circumferential displacement estimation

Accumulated axial and lateral displacements in a Cartesian coordinate system were previously computed with a hierarchical block-matching motion tracking algorithm [6] described in previous chapters. Radial and circumferential displacements were then estimated using a 2D rotation matrix \mathbf{M} , which defined as:

$$\mathbf{M} = \begin{bmatrix} \cos\theta & \sin\theta \\ -\sin\theta & \cos\theta \end{bmatrix} \quad (2)$$

where θ denotes the counter-clockwise angle measured from a pre-defined 0° line

crossing the centroid and a point on the polar grid. Radial and circumferential displacements in polar coordinates can be generated using:

$$\mathbf{D}^{\text{polar}} = \mathbf{M}\mathbf{D}^{\text{cartesian}} \quad (3)$$

where

$$\mathbf{D}^{\text{polar}} = \begin{pmatrix} d_r \\ d_\theta \end{pmatrix}$$

$$\mathbf{D}^{\text{cartesian}} = \begin{pmatrix} d_{\text{axial}} \\ d_{\text{lateral}} \end{pmatrix} \quad (4)$$

In Equation 4, d_r and d_θ denote the radial and circumferential displacement vector components for the polar coordinate system, while d_{axial} and d_{lateral} denote the displacement components for Cartesian coordinate system. Equation 3 finally reduces to:

$$d_r = \cos\theta * d_{\text{axial}} + \sin\theta * d_{\text{lateral}}$$

$$d_\theta = -\sin\theta * d_{\text{axial}} + \cos\theta * d_{\text{lateral}} \quad (5)$$

8.2.4 Radial and circumferential strain generation

After the polar displacement vector components were computed, radial and circumferential strains can be calculated using:

$$\varepsilon_{rr} = \frac{\partial d_r}{\partial r}$$

$$\varepsilon_{\theta\theta} = \frac{1}{r} \frac{\partial d_\theta}{\partial \theta} + \frac{d_r}{r} \quad (6)$$

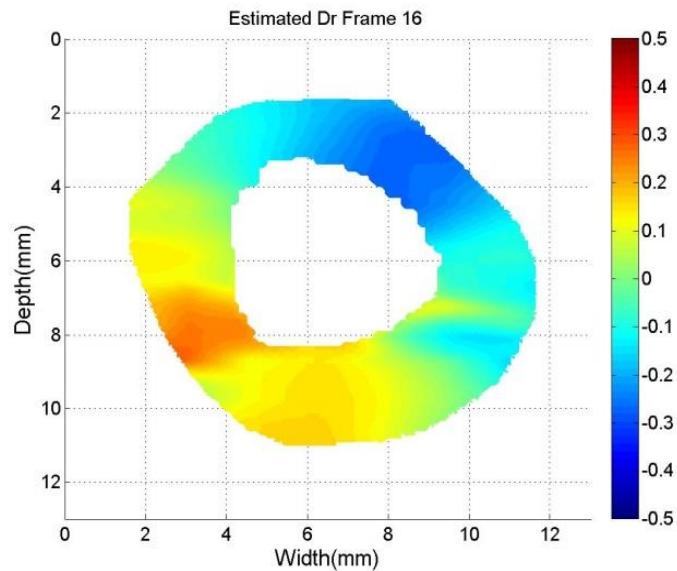
where r denotes the distance between the centroid and a computation point or particle. Note that the contribution of the radial displacement to circumferential strain comes from the elongation or shortening of carotid artery wall along the circumferential

direction when the radial deformation occurs. Along the radial direction, radial strains were computed using a 9-point least squares strain estimator (LSQSE) [7]. In a similar manner in the circumferential direction, $\frac{\partial d_\theta}{\partial \theta}$ was also computed with a 9-point LSQSE. Note that this was achievable because the polar grid is divided equi-distantly in the radial direction and equi-angularly in the circumferential direction.

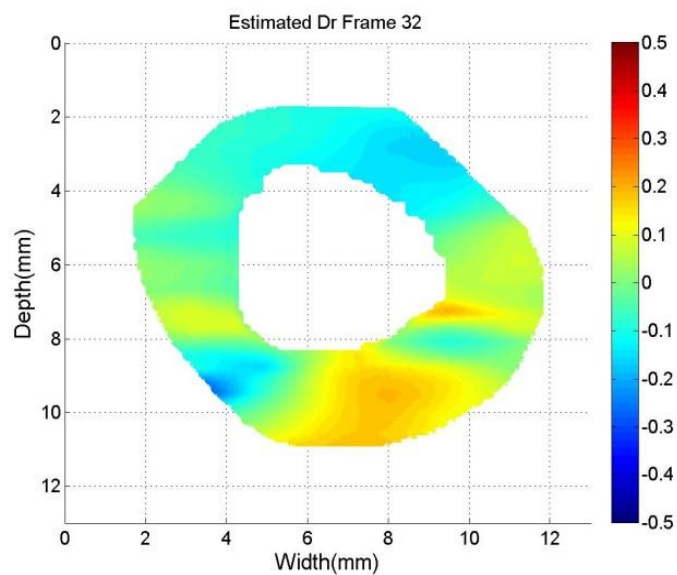
8.3 Results

8.3.1 Radial and circumferential displacements

Figure 8.2 shows typical accumulated radial displacement images at systole and end-diastole for the plaque demarcated in Figure 8.1. Positive radial displacements are depicted in a red color, indicating the motion is away from the centroid. Negative radial displacements are depicted in blue color, indicating the motion is towards the centroid. Radial displacement in maximum amplitude can be observed at systole, as shown in Figure 8.2 (a), while the amplitude of radial displacement decreases at end-diastole, as shown in Figure 8.2 (b). Note that the displacement doesn't go back to zero because the contour of the plaque with adventitia is not a perfectly symmetric loop with equally distributed mass.



(a)

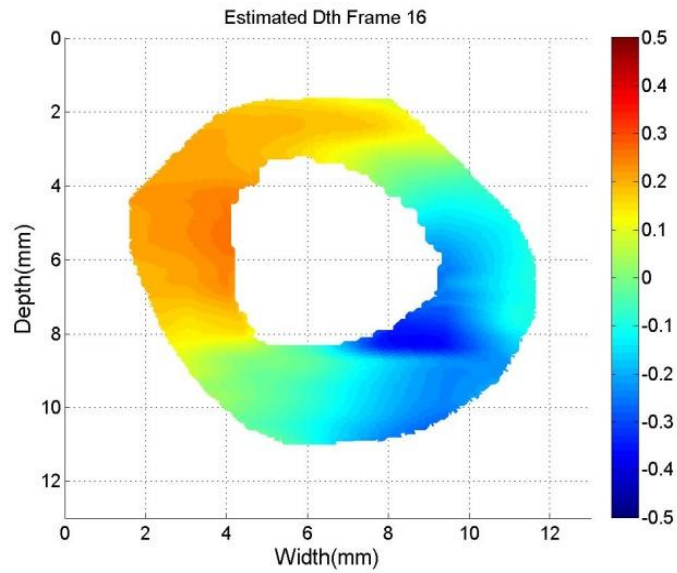


(b)

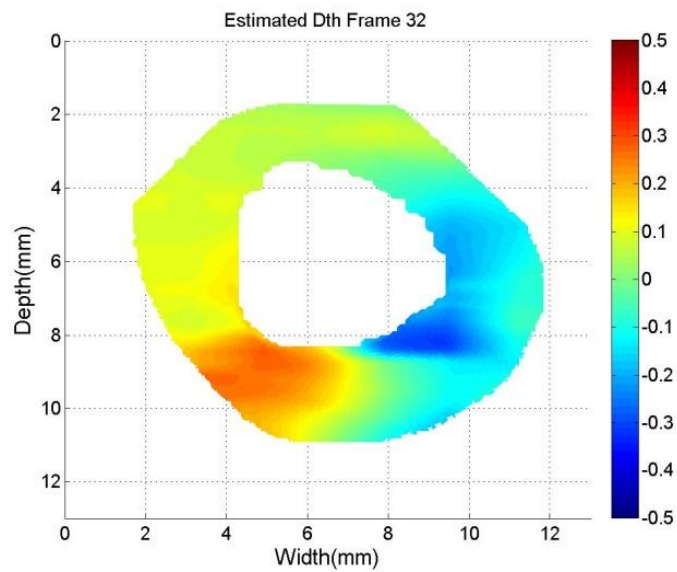
Figure 8.2: Radial displacement images at systole (a) and end-diastole (b) in the segmented region.

Figure 8.3 presents the corresponding accumulated circumferential displacement images at systole and end-diastole. Positive circumferential displacements are depicted in a red color, indicating that the motion is in a counter-clockwise direction. Negative

circumferential displacements are depicted in blue color, indicating the motion is in a clockwise direction.



(a)

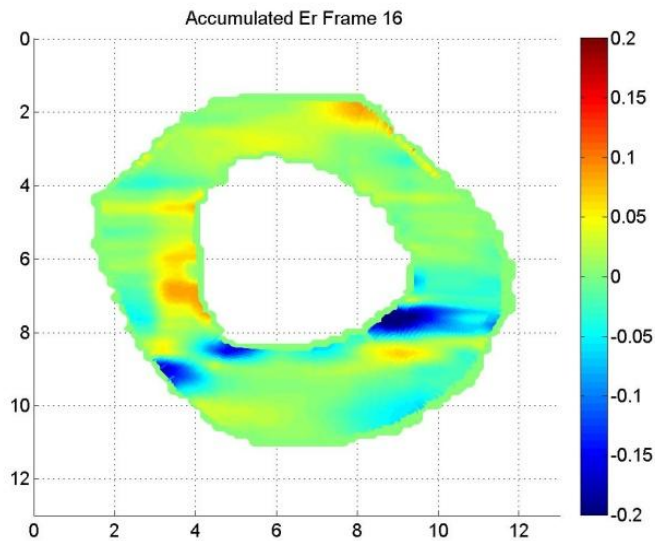


(b)

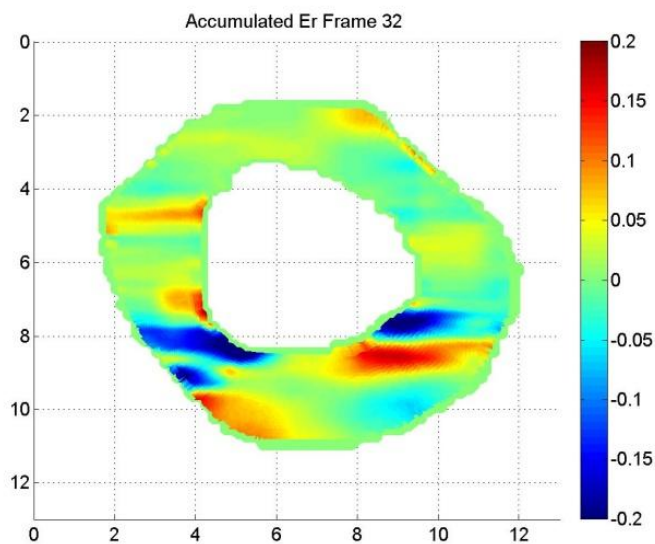
Figure 8.3: Circumferential displacement images at systole (a) and end-diastole (b) in the segmented region.

8.3.2 Radial and circumferential strain tensor images

Figure 8.4 exhibits the accumulated radial strain images at systole and end-diastole for the same plaque. Positive radial strains are depicted in a red color indicating expansion along the radial direction. Negative radial strains are depicted in a blue color indicating compression along the radial direction. The maximum strain can get as high as 20%, suggesting that regions with higher strain are more prone to rupture. Note that the radial strain distribution is not symmetrical. The distribution of the radial strain also suggests that the composition of plaque varies inside the plaque and adventitia region.



(a)

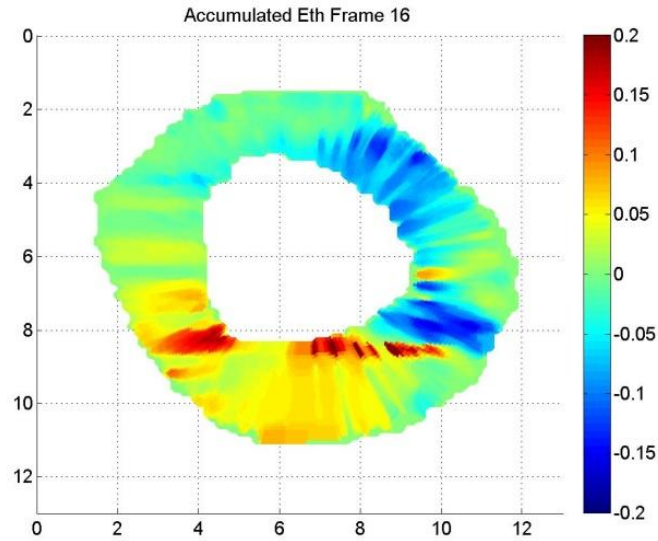


(b)

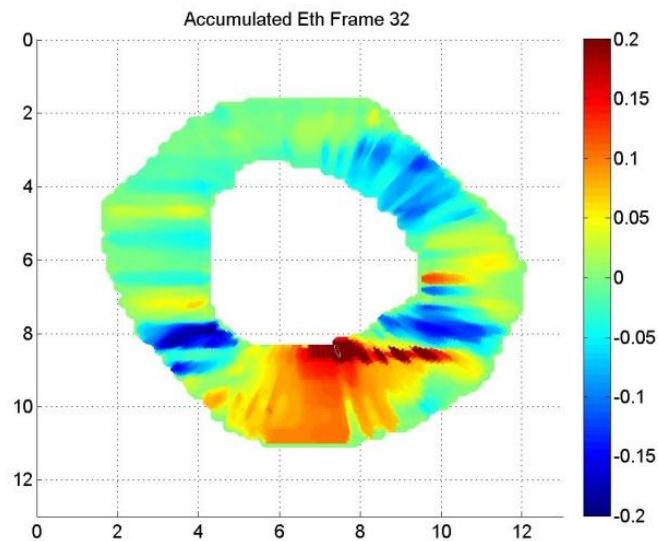
Figure 8.4: Radial strain images at systole (a) and end-diastole (b) in the segmented region.

Figure 8.5 demonstrates the corresponding accumulated circumferential strain images at systole and end-diastole. Positive circumferential strains are depicted in a red color indicating expansion along the circumferential direction. Negative circumferential

strains are depicted in blue color indicating compression in circumferential direction. Similarly the distribution of circumferential strain is not symmetrical, as expected.



(a)



(b)

Figure 8.5: Circumferential strain images at systole (a) and end-diastole (b) in the segmented region.

8.4 Discussion

In this chapter we present an algorithm developed for radial and circumferential strain estimation. We also showed the feasibility of utilizing this algorithm in cross-sectional scans of the carotid arteries with plaque in human subjects. Previous studies of radial and circumferential strain estimation on carotid or coronary plaque reported in the literature were mostly performed utilizing IVUS since it can provide better symmetry and image quality due to the higher transmit frequencies used [4, 8-13]. Strain imaging using in vivo transverse scanning planes for carotid strain imaging is challenging for several reasons. First, it is more difficult to distinguish plaque from the vessel wall and segment adventitia and plaque in a cross-sectional fashion on in vivo images. Secondly, determining a centroid value is complicated by the lack of symmetry in the presence of plaque. Thirdly, only parts of the plaque or vessel along the beam propagation direction, i.e. A-lines, provide good strain estimation results.

Note that the displacement and strain images look significantly different from that for a perfectly contracting and expanding vessel, for example, when compared to a simulated homogeneous vessel with a concentric lumen as shown in [4]. In our case, for the carotid artery with plaque the data loop segmented was not symmetrical because of the presence of plaque and inhomogeneity of human vessel wall tissue. The center of mass, or the centroid, was not at the center of the carotid artery. In addition, movement of the handheld transducer during data acquisition may introduce more motion artifacts for cross-sectional scans.

In previous chapters, we had two complete cardiac cycles when the carotid artery was studied along a longitudinal scan view. However, with cross-sectional views, we

found that it was difficult for the research sonographer to segment two complete cardiac cycles using MITK software. Significant mis-registration of the artery wall and plaque was found when going beyond a cardiac cycle. This may be due to the fact that the ultrasound transducer may not be perfectly perpendicular to the carotid artery during data acquisition. In the future, a 3D data acquisition might be helpful in obtaining more precision in the placement of the transducer. Besides, a lot of patients have arrhythmias, resulting in a short cardiac cycle followed by a long cardiac cycle or vice versa. This further adds to the difficulty in segmentation of the end diastolic frames. Therefore, in this study, we only estimated radial and circumferential strain indices over a cardiac cycle.

Another concern regarding the segmentation of plaque is that the inner contour is difficult to segment on the reconstructed B-mode images for the research sonographer. To ensure the accuracy and consistency of border determination, we also need a verification and validation system for the segmentation of plaque. Future work including automatic segmentation could help solve the problem and facilitate the process.

8.5 Conclusions

In summary, our preliminary results demonstrate the feasibility of in vivo radial and circumferential strain estimation in cross-sectional views of the carotid artery with plaque.

8.6 References

1. Lai, W.M., Rubin, D., and Krempl, E., Introduction to Continuum Mechanics. 4 ed. 2009: Elsevier.
2. Haupt, P. and Kurth, J.A., Continuum Mechanics and Theory of Materials. 2002:

- Springer.
3. Ma, C. and Varghese, T., Lagrangian displacement tracking using a polar grid between endocardial and epicardial contours for cardiac strain imaging. *Medical physics*, 2012. 39(4): p. 1779-92.
 4. Hansen, H.H., Lopata, R.G., Idzenga, T., and de Korte, C.L., An angular compounding technique using displacement projection for noninvasive ultrasound strain imaging of vessel cross-sections. *Ultrasound Med Biol*, 2010. 36(11): p. 1947-56.
 5. Richards, M.S. and Doyley, M.M., Non-rigid image registration based strain estimator for intravascular ultrasound elastography. *Ultrasound Med Biol*, 2013. 39(3): p. 515-33.
 6. McCormick, M., Varghese, T., Wang, X., Mitchell, C., Kliwer, M.A., and Dempsey, R.J., Methods for robust in vivo strain estimation in the carotid artery. *Phys Med Biol*, 2012. 57(22): p. 7329-53.
 7. Kallel, F. and Ophir, J., A least-squares strain estimator for elastography. *Ultrason Imaging*, 1997. 19(3): p. 195-208.
 8. de Korte, C.L., Cespedes, E.I., van der Steen, A.F., Pasterkamp, G., and Bom, N., Intravascular ultrasound elastography: assessment and imaging of elastic properties of diseased arteries and vulnerable plaque. *Eur J Ultrasound*, 1998. 7(3): p. 219-24.
 9. de Korte, C.L., Pasterkamp, G., van der Steen, A.F., Woutman, H.A., and Bom, N., Characterization of plaque components with intravascular ultrasound elastography in human femoral and coronary arteries in vitro. *Circulation*, 2000. 102(6): p. 617-23.
 10. de Korte, C.L., van der Steen, A.F., Cepedes, E.I., Pasterkamp, G., Carlier, S.G., Mastik, F., Schoneveld, A.H., Serruys, P.W., and Bom, N., Characterization of plaque components and vulnerability with intravascular ultrasound elastography. *Phys Med Biol*, 2000. 45(6): p. 1465-75.
 11. de Korte, C.L. and van der Steen, A.F., Intravascular ultrasound elastography: an overview. *Ultrasonics*, 2002. 40(1-8): p. 859-65.
 12. Hansen, H.H., Lopata, R.G., Idzenga, T., and de Korte, C.L., Full 2D displacement vector and strain tensor estimation for superficial tissue using beam-steered ultrasound imaging. *Phys Med Biol*, 2010. 55(11): p. 3201-18.
 13. Hansen, H.H., Lopata, R.G., and de Korte, C.L., Noninvasive carotid strain imaging using angular compounding at large beam steered angles: validation in vessel phantoms. *IEEE Trans Med Imaging*, 2009. 28(6): p. 872-80.

Chapter 9 : Characterization of Carotid Plaque with Histology and Quantitative Ultrasound

9.1 Introduction

In this chapter¹, we propose a novel approach to characterize localized plaque regions with heterogeneous tissue directly to their histology. Most atherosclerotic plaques are heterogeneous, making it difficult to classify them in the clinic as calcified or lipidic plaques. Ultrasound is a noninvasive option for imaging superior shallow vessels such as the carotid artery. Conventional ultrasound B-mode images are commonly used clinically, but they are not sufficient to determine heterogeneous plaque composition, since they are primarily utilized to differentiate plaque from normal tissue [1].

Quantitative ultrasound (QUS) has been used to assess acoustic properties of tissue, using parameters such as the integrated attenuation and integrated backscatter coefficient, since differences in acoustic properties may reflect differences in tissue composition [2]. QUS has been widely used to characterize and classify plaque with the classification often compared to pathology patterns [3-9]. Experimental evaluations using parameters such as the integrated attenuation, attenuation coefficient and integrated backscatter have been reported [4-5, 7-12]. Most of these studies utilized intravascular ultrasound (IVUS), utilizing higher frequency transducers. Virtual histology based intravascular ultrasound

¹This chapter is adapted from Wang, X., Salamat, M.S., Varghese, T., and Dempsey, R.J. *Carotid plaque characterization with histology and quantitative ultrasound*. in *Ultrasonics Symposium (IUS), 2014 IEEE International*. 2014: IEEE.

(VH-IVUS) technology at 45 MHz has been validated to have an accuracy of greater than 88% in indentifying different tissue types when compared to histology as the gold standard [3]. Integrated backscatter based intravascular ultrasound (IB-IVUS) systems have also shown good performance in characterizing coronary plaques when compared to histological diagnoses [4]. IB-IVUS has been compared to VH-IVUS at 40 MHz using histology as the gold standard, and the former has been shown to provide higher diagnostic accuracy than the latter [5]. IB-IVUS has been used to detect lipidic and fibrous tissue in carotid and coronary plaques [10]. Attenuated plaques in IVUS and near-infrared spectroscopy (NIRS) detected lipid-rich plaques in human coronary arteries were compared with histopathology and showed improved accuracy in predicting the necrotic core or large lipid pool when the two technologies were combined together [6].

Fewer studies however, have utilized non-invasive external ultrasound transducers to assess acoustic properties of plaques. Bridal et al. measured the integrated attenuation, attenuation slope and integrated backscatter from 5 MHz up to 56 MHz, and estimated the attenuation coefficient for dense collagen region to be 2.8 ± 0.6 dB/cm/MHz, and the attenuation coefficient for media beneath the lipid region to be 1.9 ± 0.3 dB/cm/MHz at 37.5 MHz. The integrated attenuation calculated was 97 ± 20 dB/cm for media, 107 ± 33 dB/cm for dense collagen, 142 ± 51 dB/cm for collagen-lipidic region, 139 ± 53 dB/cm for lipid, and 245 ± 93 dB/cm for calcifications at 30 to 50 MHz [7-9]. In our laboratory, Shi et al. reported on the attenuation coefficient for calcified and soft regions of *ex vivo* carotid plaque in the frequency range of 2.5 to 7.5 MHz. Calcified regions were reported with attenuation coefficients between 1.4 - 2.5 dB/cm/MHz, while for softer regions the attenuation coefficients ranged from 0.3 - 1.3 B/cm/MHz [11-12].

In this chapter, 3D attenuation volumes for *ex vivo* carotid plaque in a higher frequency range are generated and correlated to 3D histology volumes. We will compare and correlate calcified, fibrous and lipid regions within heterogeneous plaque using a region-to-region registration with histology and QUS imaging. Different regions such as the lumen, calcified, lipid and fibrous regions were segmented by a pathologist and digitally color-coded into the 3D histology volumes. Similar tissue types from the 3D histology volume were then compared to the estimated 3D attenuation coefficient obtained using QUS methods.

9.2 Materials and Methods

9.2.1 Attenuation estimation

Six atherosclerotic plaque samples were obtained from three independent patients following carotid endarterectomy procedures (CEA) at the University of Wisconsin-Madison Hospitals and Clinics. Patients provided informed consent prior to the CEA procedure. Excised intact CEA plaque specimens were then imaged *ex vivo* immediately after surgery. The study was conducted under a protocol approved by the University of Wisconsin-Madison Institutional Review Board (IRB).

A VisualSonics Vevo 770 ultrasound system equipped with a RMV710B high frequency transducer was used to image four of the excised plaque tissue. Plaque specimens were scanned in a water bath, suspended between two catheters on either end. The transducer was connected to a 3D motion table and immersed in degassed distilled water. The center frequency of the transducer was 25 MHz, with a frequency bandwidth up to 37.5 MHz. The transducer has an axial resolution of 70 μm and a lateral resolution

of 140 μm . Two-dimensional radiofrequency (RF) data was collected for each cross-section of the plaque, and the motor stepped over the length of the plaque to form a three-dimensional (3D) RF data volume. Each acquisition consisted of 250 beam lines with 2128 samples. The axial dimension of the beam line was 3.9 mm, with a lateral spacing of 60 μm . In the elevational direction, frames were separated by 100 μm to 200 μm depending on the dimensions of the plaque specimen, which ranged from 20 mm to 40 mm. Up to 250 frames were collected and rendered into a 3D volume.

A Siemens S2000 ultrasound system equipped with an 18L6 linear array transducer was used to image two other excised plaque tissue. The experimental setup was the same with the other two plaque specimen. The transmit frequency of the transducer was 11.4 MHz with a single transmit focus set at the depth of plaque. The total depth of the B-mode image was 4 cm, and the lateral width was 3.8 cm that included 508 A-lines. RF data was digitized at a 40 MHz sampling frequency. The plaque was scanned longitudinally, with a frame separation of 500 μm in the elevational direction. RF data was acquired and rendered into a 3D volume.

For each 2D image frame, an attenuation coefficient image was obtained from RF data using a reference phantom method [13]. A well-characterized high frequency tissue-mimicking (TM) reference phantom manufactured in our laboratory [14] was imaged immediately after scanning the plaque sample with the same transducer and time-gain compensation (TGC) settings. In the reference phantom method, the ratio of the power spectrum of the sample and reference phantom is utilized. This ratio is approximately equal to the product of the ratio of the backscatter coefficient and ratio of attenuation coefficient, as shown in (1):

$$\frac{S_s(f, z)}{S_r(f, z)} = \frac{B_s(f)}{B_r(f)} \cdot \frac{A_s(f, z)}{A_r(f, z)} \quad (1)$$

where f denotes frequency and z denotes depth. $S_s(f, z)$ represents the power spectrum of the sample, and $S_r(f, z)$ represents the power spectrum of the reference phantom. $B_s(f)$ is the backscatter coefficient of the sample, depending on frequency f , and $B_r(f)$ is the backscatter coefficient of the reference phantom. $A_s(f, z)$ represents total attenuation of the sample, accounting for both frequency f and depth z , and $A_r(f, z)$ represents total attenuation of the reference phantom.

The attenuation coefficient can be modeled as shown in (2):

$$A(f, z) = \exp(-4\beta fz) \quad (2)$$

where β denotes the attenuation coefficient, independent of frequency f and depth z .

Taking the logarithm of the power spectral ratio, the attenuation coefficient is obtained by performing a linear regression against depth and frequency, as shown in (3).

$$\ln \frac{S_s(f, z)}{S_r(f, z)} = \ln \frac{B_s(f)}{B_r(f)} - 4(\beta_s - \beta_r) fz \quad (3)$$

where β_s is the attenuation coefficient of the sample, and β_r is the already known attenuation coefficient of the reference phantom.

Attenuation coefficient was estimated in each region of interest (ROI). The ROI size was 2 mm \times 2 mm. The ROIs had 85% overlap on each other. Along the frequency spectrum, the frequencies were separated by 0.2 MHz. The kernel of the depth utilized was 6 mm. The power spectrum was estimated using multitaper method.

Using this method, for each RF frame, a 2D attenuation map was generated. 2D attenuation images were then stacked and rendered into a 3D volume. Figure 9.1 presents rendered results of both the attenuation coefficient estimates and the 3D B-mode volume.

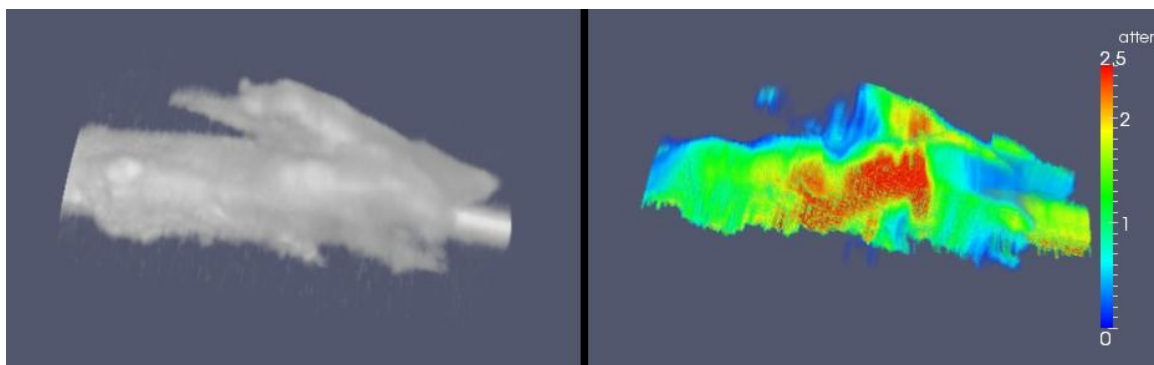


Figure 9.1: 3D B-mode and QUS attenuation coefficient volumes for a plaque specimen.

9.2.2 Histology reconstruction

After high-frequency ultrasound imaging and RF data acquisition, the plaque specimens were fixed in formalin and returned to the pathology department on the same day for histology sectioning. Plaque tissues were longitudinally sectioned in 5 μm thickness, and sections separated by 100 μm were selected for analysis and 3D histology reconstructions. Typically between 20 to 60 histology slides were obtained for each plaque specimen based on its dimensions. A PathScan Enabler IV was used to scan and digitize the 2D histopathology images from the histology glass slides. Each histology slide was digitized into a 9967×5832 image. The 2D digitized grayscale histology images obtained were then registered and reconstructed into a 3D volume using a cross-correlation based registration algorithm in Matlab (Mathworks, Natick, MA, USA).

Registration of the histology images were performed using the following steps. Possible transformations between consecutive histology images included translation,

rotation and deformation. Since some of the plaque specimens were calcified and sometimes the tissue could get torn apart when sectioned, no quantification of this deformation could be performed and only translation and rotation were done to align the 2D histology images. First, a fixed point in every 2D histology image was manually chosen and all these points were aligned to form an axis. The general procedure followed was to choose the tip of the flow divider, which is typically depicted in the longitudinally sectioned histological image of plaque specimens. Then rotations were performed for each histology image about this axis. For each rotation angle in increment of one degree, a cross-correlation coefficient was calculated between this 2D histology image and the previously aligned image. The rotation angle that provided the highest peak value of the normalized cross-correlation coefficient was selected and the current histology image was then rotated to that angle. After this iterative procedure was performed on all the 2D histology images with respect to the one immediately preceding it, all the 2D histology images were thus aligned to the first histology slide or image.

Different regions such as the lumen, calcified, lipid and fibrous regions were then segmented by a pathologist and digitally color-coded into the 3D histology data. Figure 9.2 presents an example of a slide of the original histology data and corresponding color-coded pathology classification of the same plaque sample presented in Fig. 9.1. As illustrated in Fig. 9.2, calcified regions were color-coded in red, lipidic regions color-coded in yellow, and fibrous regions colored in light blue. The lumen was colored in blue, same as the background color.

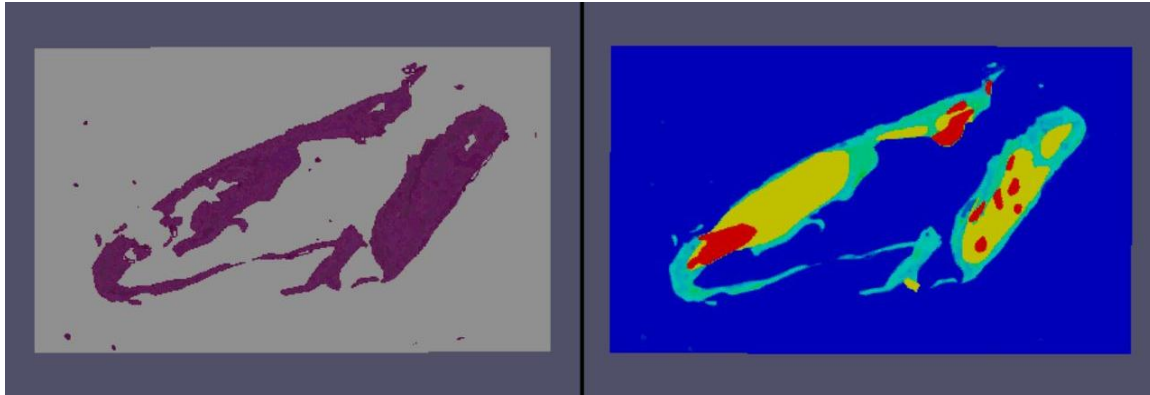


Figure 9.2: Pathology microscopic slides and color-coded segmentation of different plaque regions.

9.3 Direct Comparison of QUS to histology

9.3.1 Alignment of attenuation volumes to histology

Our results indicate that calcified, fibrous and lipidic regions in the two volumes showed good correlation with attenuation results, as illustrated in Figure 9.3. From the figure, we can observe that calcified regions delineated on the histology volume correspond to the high attenuation coefficient region in the 3D attenuation coefficient volume, while lipidic regions tend to have lower attenuation coefficient values. Fibrous regions in histology correlate to the lowest attenuation coefficient value.

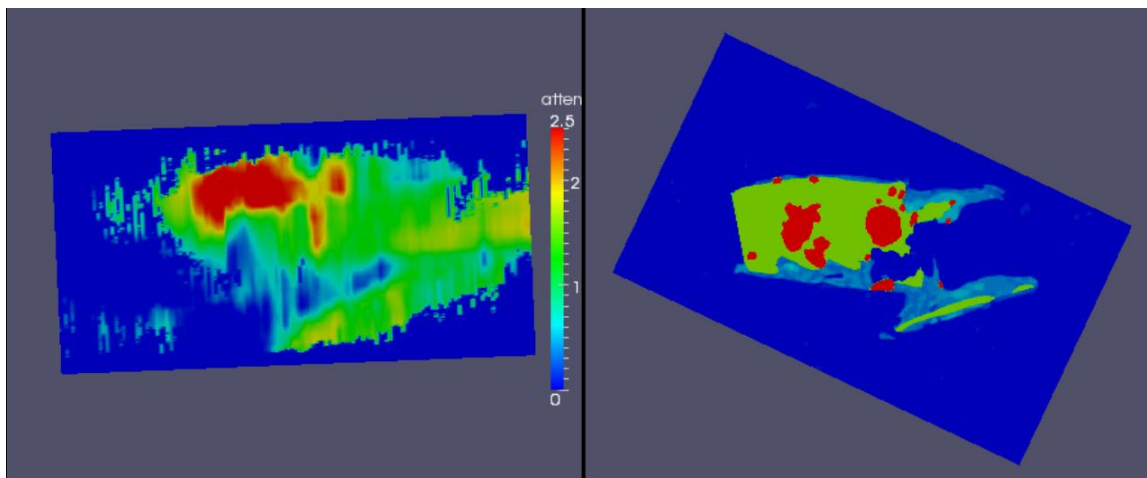


Figure 9.3: Alignment of attenuation images with color-coded histology slides for the previously shown sample.

The same procedure were performed on additional plaque specimens and the average attenuation coefficient in each region obtained. Comparison of attenuation image with histology slide for a second specimen is presented in Figure 9.4. Similar to the results for the first sample, different regions in attenuation images correspond well with color-coded histology regions.

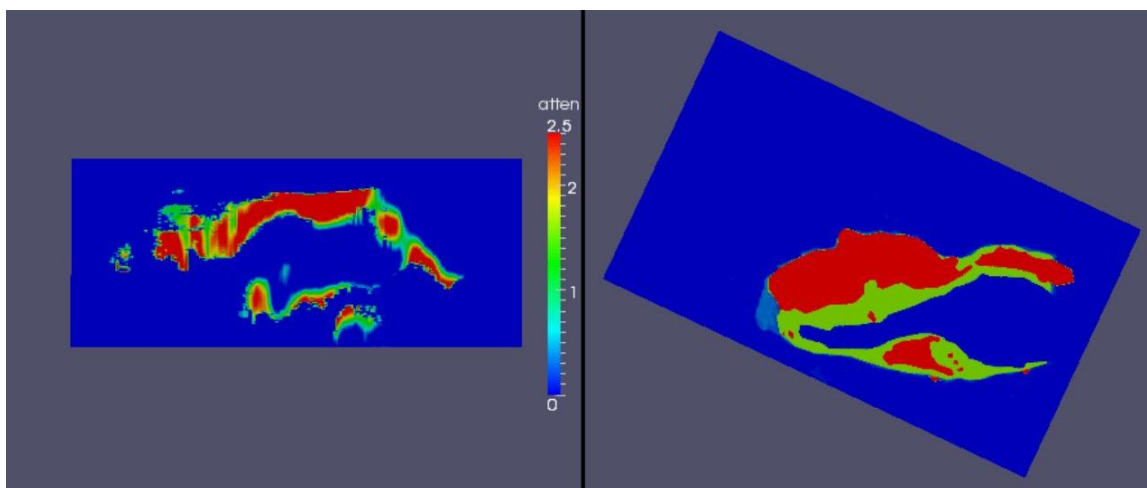


Figure 9.4: Alignment of attenuation images with color-coded histology slides for another sample.

9.3.2 Attenuation coefficients in different regions

A summary of the mean and standard deviation of calculated mean attenuation coefficient and its standard deviation in different regions for the six plaque samples are presented in Table 9.1.

	Attenuation Coefficient (dB/cm/MHz)		
	calcified	lipid	fibrous
<i>Sample 1</i>	2.48 ±0.33	1.47 ±0.53	0.86 ±0.22
<i>Sample 2</i>	2.42 ±0.20	1.79 ±0.42	0.88 ±0.29
<i>Sample 3</i>	2.41 ±0.40	1.52 ±0.43	0.80 ±0.11
<i>Sample 4</i>	2.39 ±0.43	1.52 ±0.58	0.77 ±0.31
<i>Sample 5 (S2000)</i>	2.36 ±0.74	1.75 ±0.62	0.86 ±0.34
<i>Sample 6 (S2000)</i>	2.32 ±0.43	1.55 ±0.48	0.78 ±0.42
<i>Mean ± Standard Deviation</i>	2.40 ±0.38	1.60 ±0.49	0.83 ±0.22

Table 9.1: Attenuation coefficients in different regions.

9.4 Discussion

Our results show that the attenuation coefficient values in different regions were consistent with those reported in literature [8, 12]. Therefore, the reference phantom

method provides comparable mean attenuation estimates in the higher frequency range and for the smaller plaque dimensions.

Heterogeneous plaques are difficult to characterize in the clinic since they cannot be precisely classified as calcified, lipidic or fibrous plaques. In this study we show that the generated 3D high-frequency parametric attenuation coefficient images may be a useful tool for plaque characterization. To date, no previous work has reconstructed and compared similar regions identified on 3D histology volumes to 3D attenuation coefficient maps in carotid plaque. With a 3D volume, different compositions within the plaque can be better identified and understood, and correlations can be made between irregular shapes in pathology images and corresponding ultrasound and QUS images. 3D attenuation and histology volumes provide a promising way to characterize plaque within localized regions with different heterogeneous tissue types. For future work, it might be useful to register and correlate the 3D histology volume to 3D *in vivo* ultrasound image volumes, which in turn could be registered to the high-frequency 3D *ex vivo* ultrasound volume to quantify the composition of plaque tissue.

9.5 Conclusions

This chapter compared and correlated localization and registration of calcified, fibrous and lipidic regions within heterogeneous plaque using 3D histology and quantitative ultrasound imaging. Our results indicate that calcified, lipidic and fibrous regions in the two volumes showed a good correlation. This work demonstrates a direct correlation between histopathology and quantitative ultrasound (QUS) imaging characterization of plaque. Using 3D histology volumes, different tissue composition within the plaque can be better identified and characterized. It provides a promising way

for direct localization of plaque regions and structures, and for improved determination of plaque composition.

9.6 References

1. Noritomi, T., Sigel, B., Swami, V., Justin, J., Gahtan, V., Chen, X., Feleppa, E.J., Roberts, A.B., and Shirouzu, K., *Carotid plaque typing by multiple-parameter ultrasonic tissue characterization*. *Ultrasound Med Biol*, 1997. **23**(5): p. 643-50.
2. Barzilai, B., Saffitz, J.E., Miller, J.G., and Sobel, B.E., *Quantitative ultrasonic characterization of the nature of atherosclerotic plaques in human aorta*. *Circ Res*, 1987. **60**(3): p. 459-63.
3. Campos, C.M., Fedewa, R.J., Garcia-Garcia, H.M., Vince, D.G., Margolis, M.P., Lemos, P.A., Stone, G.W., Serruys, P.W., and Nair, A., *Ex vivo validation of 45 MHz intravascular ultrasound backscatter tissue characterization*. *Eur Heart J Cardiovasc Imaging*, 2015.
4. Okubo, M., Kawasaki, M., Ishihara, Y., Takeyama, U., Kubota, T., Yamaki, T., Ojio, S., Nishigaki, K., Takemura, G., Saio, M., Takami, T., Minatoguchi, S., and Fujiwara, H., *Development of integrated backscatter intravascular ultrasound for tissue characterization of coronary plaques*. *Ultrasound Med Biol*, 2008. **34**(4): p. 655-63.
5. Okubo, M., Kawasaki, M., Ishihara, Y., Takeyama, U., Yasuda, S., Kubota, T., Tanaka, S., Yamaki, T., Ojio, S., Nishigaki, K., Takemura, G., Saio, M., Takami, T., Fujiwara, H., and Minatoguchi, S., *Tissue characterization of coronary plaques: comparison of integrated backscatter intravascular ultrasound with virtual histology intravascular ultrasound*. *Circ J*, 2008. **72**(10): p. 1631-9.
6. Kang, S.J., Mintz, G.S., Pu, J., Sum, S.T., Madden, S.P., Burke, A.P., Xu, K., Goldstein, J.A., Stone, G.W., Muller, J.E., Virmani, R., and Maehara, A., *Combined IVUS and NIRS detection of fibroatheromas: histopathological validation in human coronary arteries*. *JACC Cardiovasc Imaging*, 2015. **8**(2): p. 184-94.
7. Bridal, S.L., Fornes, P., Bruneval, P., and Berger, G., *Parametric (integrated backscatter and attenuation) images constructed using backscattered radio frequency signals (25-56 MHz) from human aortae in vitro*. *Ultrasound Med Biol*, 1997. **23**(2): p. 215-29.
8. Bridal, S.L., Fornes, P., Bruneval, P., and Berger, G., *Correlation of ultrasonic attenuation (30 to 50 MHz and constituents of atherosclerotic plaque*. *Ultrasound Med Biol*, 1997. **23**(5): p. 691-703.
9. Bridal, S.L., Beyssen, B., Fornes, P., Julia, P., and Berger, G., *Multiparametric attenuation and backscatter images for characterization of carotid plaque*. *Ultrason Imaging*, 2000. **22**(1): p. 20-34.

10. Kawasaki, M., *An integrated backscatter ultrasound technique for the detection of coronary and carotid atherosclerotic lesions*. *Sensors (Basel)*, 2015. **15**(1): p. 979-94.
11. Shi, H., Varghese, T., Dempsey, R.J., Salamat, M.S., and Zagzebski, J.A., *Relationship between ultrasonic attenuation, size and axial strain parameters for ex vivo atherosclerotic carotid plaque*. *Ultrasound Med Biol*, 2008. **34**(10): p. 1666-77.
12. Shi, H., Varghese, T., Mitchell, C.C., McCormick, M., Dempsey, R.J., and Kliewer, M.A., *In vivo attenuation and equivalent scatterer size parameters for atherosclerotic carotid plaque: preliminary results*. *Ultrasonics*, 2009. **49**(8): p. 779-85.
13. Yao, L.X., Zagzebski, J.A., and Madsen, E.L., *Backscatter coefficient measurements using a reference phantom to extract depth-dependent instrumentation factors*. *Ultrason Imaging*, 1990. **12**(1): p. 58-70.
14. McCormick, M.M., Madsen, E.L., Deaner, M.E., and Varghese, T., *Absolute backscatter coefficient estimates of tissue-mimicking phantoms in the 5-50 MHz frequency range*. *J Acoust Soc Am*, 2011. **130**(2): p. 737-43.

Chapter 10 : Conclusions and Future Work

10.1 Contributions of this Dissertation

Characterization of carotid plaque vulnerability using strain imaging and quantitative ultrasound was presented in this dissertation. Relationships between ultrasound strain indices, cognition and embolization were investigated to show the importance of carotid plaque characterization.

Since ultrasound strain indices may assist in the identification of plaques prone to rupture, which in turn causes emboli; it plays an important role in characterizing plaque and detecting vulnerability of plaque. The results also demonstrate the feasibility and advantage of the plaque-with-adventitia segmentation method over the plaque-only segmentation method. The vessel wall-plaque interface was shown to be an important region for increased plaque instability, especially utilizing the shear strain indices.

Overall cognitive function, and specific cognitive function test scores for motor function, speeded motor function, executive function, visual attention and visuospatial learning, were found to have significant associations with maximum strain indices in carotid plaque. The results demonstrated that maximum strain indices in carotid plaque as vascular biomarkers may be significantly associated with cognitive function through embolization, and the feasibility of using these maximum strain indices to predict cognitive impairment. Ultrasound strain imaging can therefore assist in the identification of plaque prone to rupture, as well as prediction of embolism from vulnerable plaque and

resulting cognitive impairment. Since silent stroke is strongly linked with cognitive impairment and difficult to diagnose or predict clinically, ultrasound strain imaging have clinical significance in preventing potential silent strokes.

Evaluation of variation in the strain indices in patients versus volunteers, symptomatic versus asymptomatic patients, as well as patients with diabetes, hypertension, hyperlipidemia, tobacco usage versus normal controls were also evaluated. This will help assess the correlation of plaque strain indices to clinical symptomology and each specific vascular risk factor.

In a few patients. clinically occult micro-emboli that did not produce clinical symptoms were visualized using TCD. Associations between maximum strain indices, maximum ICA velocity and maximum MCA velocity on the surgical side of patients with significant plaque were evaluated. Increased strains in carotid plaque in ICA were also significantly associated with an increase in WMH. Since the existence of micro-emboli may be reflected in TCD monitoring, correlation of strain indices to TCD would provide us with the ability to indicate strain imaging feasibility for predicting plaque prone to rupture.

The feasibility of *in vivo* radial and circumferential strain estimation in cross-sectional views of the carotid artery with plaque was demonstrated. Radial and circumferential strain in cross-sectional views would give us a more straightforward and intuitive interpretation of deformation and this noninvasive ultrasound approach would be more clinically friendly when compared to IVUS based approaches.

Localization and registration of calcified, fibrous and lipidic regions within heterogeneous plaque using 3D histology and quantitative ultrasound imaging was

performed. Calcified, lipidic and fibrous regions in the 3D histology volume and 3D attenuation coefficient volume showed good correlation. Heterogeneous tissue composition within the plaque would be better identified and characterized using a direct correlation between histopathology and QUS characterization of plaque.

10.2 Future Directions

Arterial strain in the carotid vessel wall of a limited number of volunteers in the general population has been investigated. A study on a larger number of volunteers over a large age range is essential to demonstrate variations in the strain indices with age. Another approach that could be pursued would be utilization of strain estimation in the vessel wall of the common carotid artery (CCA) in patients for normalization of the estimated strain in plaque in the same carotid artery. This will provide another feature to analyze, i.e. the strain ratio of plaque and CCA wall, subject to possibly similar blood pressures. This approach would take into account the mechanical stress that causes the deformation of carotid vessel wall, and also give us more insight into arterial stiffening.

Three-dimensional data acquisition in strain imaging might be helpful in obtaining more precision in the placement of the transducer and better geometry. It might be worthwhile to register and correlate 3D *in vivo* strain volumes to 3D histology volumes, which in turn could be registered to the high-frequency 3D *ex vivo* attenuation coefficient volumes to quantify composition of plaque tissue. Other approaches other than cross-correlation to facilitate registration of the 2D histological images to obtain the 3D volume should be explored. In addition to the attenuation coefficient, other QUS parameters such as the scatterer size and backscatter coefficient could also be estimated in 3D to obtain variations in these QUS parameters over the entire plaque volume.

An automatic segmentation method would be a logical next step for carotid plaque strain imaging. Automatic segmentation could help overcome some of the challenges with manual plaque segmentation and facilitate the process of strain imaging with reduced user interaction and also ensure improved consistency of plaque demarcation. Manual segmentation will require experienced operators to segment the plaque from the vessel wall and lumen.

Despite the statistically significant correlations described in this dissertation, examination of a larger number of patients and volunteers is essential to further establish the relationships illustrated in this dissertation.